Title

Multifactorial Investigation of Perovskite Solar Cell Degradation in Operation

Author

Biaou, Carlos Koladele

Publication Date

2020

Peer reviewed|Thesis/dissertation

Multifactorial Investigation of Perovskite Solar Cell Degradation in Operation

by

Carlos Koladélé Biaou

A dissertation submitted in partial satisfaction of the

requirements for the degree of

Doctor of Philosophy

in

Engineering - Applied Science & Technology

in the

Graduate Division

of the

University of California, Berkeley

Committee in charge:

Professor Vivek Subramanian, Co-chair
Professor Oscar Dubón, Jr., Co-chair
Professor Mark Asta
Professor Junqiao Wu

Fall 2020

Multifactorial Investigation of Perovskite Solar Cell Degradation in Operation

Abstract

Multifactorial Investigation of Perovskite Solar Cell Degradation in Operation

by

Carlos Koladélé Biaou

Doctor of Philosophy in Engineering - Applied Science & Technology

University of California, Berkeley

Professor Vivek Subramanian, Co-chair

Professor Oscar Dubón, Jr., Co-chair

In 2009, Kojima et al. introduced a perovskite solar cell delivering 3.8% power conversion efficiency (PCE). Then, in 2012, Henry Snaith's group demonstrated a solution-processed perovskite solar cell with a PCE of 10.9%. Ever since, a race for the highest PCE perovskite solar cells has taken over the photovoltaic research community with the latest confirmed maximum PCE, as of 2020, at 25.2%. However, to be realistically viable, perovskites need to overcome their problem with long-term stability. Numerous studies, both theoretical and experimental, have tackled the issue. Some involved looking solely at the effects of humidity, temperature or oxygen on the active layer, whereas others focused on the effects of UV light on the solar cell structure. These single factor studies provide invaluable insights on the degradation of perovskites. Yet, a more holistic approach is needed to understand the effects of salient primary factors along with confounding higher order factors on the degradation. The design of experiment (DOE) methodology is uniquely suited for this endeavor. Few studies have employed a multifactorial approach in perovskite investigations. In this work, we seek to provide a mechanistic understanding of the degradation of perovskite solar cells in operation by focusing on methylammonium lead triiodide ($CH_3NH_3PbI_3$ or $MAPbI_3$) and tracking over time its crystallographic (XRD), optical (UV-Vis), and electrical (IV) characteristics under various electric load and temperature conditions. Moreover, we also record the evolution of electronic defects via Photo-Induced Current Transient Spectroscopy (PICTS). Using these techniques, we found that two interaction factors (temperature $\times$ load & temperature $\times$ time) were significant in the degradation of the perovskite cells studied, which validates the importance of our holistic approach. Furthermore, we found that bands of trap states, initially highly localized deep within the band gap of the perovskite, widened over the exposure period and increasing temperature. We also found that the average trap activation energy for each band of trap states became shallower over the degradation period. These observations establish a mechanistic link between deep level traps and the evolution of the current-voltage characteristics, crystallite size, microstrain, and optical absorption.

To the Reader

Black Lives Matter.

Contents

List of Figures

List of Tables

Acknowledgments

Research does not happen in a vacuum. Mine is no different, for I would certainly not have completed this work without the guidance of my advisors Vivek Subramanian and Oscar Dubón. Vivek has been my advisor for all six years I've spent at Berkeley and has offered me independence, motivation, and confidence to pursue the areas of research that were most appealing to me. He has stuck with me in moments of doubt, and I am forever grateful to him for that. Oscar has been my co-advisor for the second half of my tenure at Berkeley. He was fundamental in opening up a new avenue of research within my project, and his inherent joy and decency is one I'll dearly miss moving forward. I'm also extending my thanks to Professors Mark Asta and Junqiao Wu for serving on my thesis committee and providing me timely feedback. I also thank, Professors Ali Javey, Ana Claudia Arias, Jeff Bokor, Sayeef Salahuddin, and Tsu-Jae King-Liu for their guidance in teaching me the fundamentals of the semiconductor field. Moreover, I extend my regards to Professors Kara Nelson, Armando Fox, Boubacar Kante, and John Canny in working in good faith with me in advancing diversity, equity, and inclusion efforts in the College of Engineering, and the EECS department.

This work would not have been successfully completed without my active collaboration with Matt McPhail and Kazutaka Eriguchi. Matt is one of the hardest workers I know and his drive, diligence and pragmatism have influenced and allowed me to build the framework of my academic journey at Berkeley. His selflessness in spending countless hours with me in the lab developing processes or fixing tools has been instrumental in my success. Kazutaka was a visiting scholar from the Sumco Corporation in Japan during my time at Berkeley. He helped me master the in-and-outs of deep level trap measurements and was key in helping me run the tool. His kindness is only matched by his expertise, and I'm humbled to have witnessed both.

I also kindly acknowledge my labmates, colloquially known as my academic family, from the Subramanian and Dubón Groups. From the Subramanian side, I thank, in addition to Matt McPhail, Nishita Deka, Raj Kumar, Will Scheideler, Seungjun Chung, Chi Chung (Alvin) Li, Jake Sporrer, Gerd Grau, Jeremy Smith, Andre Zeumault, Jake Sadie, Sarah Swisher, Jaewon Jang, Steve Volkman, Lance Go, Jean Manzano, Denniell Hurboda, Dawn Corpus, and Virgil Castillo. On the Dubón side, I extend my appreciations, in addition to Kazutaka Eriguchi, to Edy Cardona, Clarissa Towle, Anthony Salazar, Petra Specht, Daniel Paulo-Wach, Diana Sanchez, Andre Palacios, and Niharika Gupta.

I commend the amazing staff from the various entities within the College of Engineering who have supported me in my journey. In particular, I thank Meltem Erol, Sheila Humphreys, Tiffany Reardon, Marvin Lopez, Audrey Sillers, Kedrick Perry, Shirley Salanio, Susanne Kauer, Charlotte Jones, Ariana Castro, Ira Young, Catalina Estrada, and Daisy Hernandez.

I am lucky to have been part of an amazing entering class of physical device students, with whom I've enjoyed fruitful, joyful, and uplifting relationships with. These are Juan Pablo Llinas, Akshay Pattabi, Benjamin Osoba, Jodi Loo, Mahsa Sadeghi, Urmita Sikder,

Maggie Payne, and Alyssa Zhou, amongst many more. Beyond my class, I've met other amazing engineers and scientists with great character. They include, but are not limited to, Maite Goiriena Goikoetxea, Eneko Axpe, Dominic Labanowski, Justin Wong, Varun Mishra, Hani Gomez, Regina Eckert, Chrissy Stachl, Rosemarie de la Rosa, Eduardo Lupi, Hector Neira, Karina Chavarria, Miguel Rodriguez, Emma Regan, Maddie Gordon, and Rachel Woods-Robinson.

I give a special praise to the Black community at large on the Berkeley campus, but especially the Black Graduate Engineering and Science Students (BGESS) that I've had the honor and privilege to lead as president from 2017 to 2019. This group of brilliant students has provided community and support to Black STEM students for more than 3 decades now, and my years at the helm have helped shape and sharpen my values and views on blackness in STEM. As such, I thank the aforementionned Benjamin Osoba, Oladapo Afolabi, Casey Mackin, Franiece Bennett, Bria Crawford, Kene Akametalu, Chukwuebuka Nweke, Will Tarpeh, Cameron Rose, Regan Patterson, Nicole Ramsey, Willie Mae Reese, Ashia Wilson, Omoju Miller, Pierce Gordon, Rocky Sison-Foster, Meron Tesfaye, Amal El-Ghazaly, Liya Weldegebriel, Matthew Anderson, Devin Guillory, Marsalis Gibson, Oyinkansola Romiluyi, Tsegereda Esatu, Samee Ibraheem, Shafeeq Ibraheem, Christian White, Ean Hall, Gideon Ukpai, George Moore, Kwasi Amofa, Pelagie Elimbi Moudio, Caleb Bugg, Eve Mwangi, Gift Kiti, Grey Batie, Renaldo Williams, Nadia Ayad, Devante Horne, Theresa Oehmke, Soliver Fusi, Tayo Olukoya, and the many more Black students I've had the opportunity to cross paths with.

I thank my friends Chikesie Esione, Michael Teklu, Nasir Memudu, the late Najim Memudu, Olabode Buraimoh, Justus Adeleke, Armand Kana, Iniese Umah, Kwame & Braxton Boler, Jacqueline Loberiza & AJ Clayborne, Claudia Espinoza, and Lida Ramsey for their support ever since I've known them.

The National Science Foundation Graduate Research Fellowship, the Jack Kent Cooke Foundation Graduate Scholarship, and the UC Berkeley Chancellor's Fellowship were all funding source that alleviated the worries of any financial burden I may have encountered during my tenure at Berkeley.

Finally, to my family, I owe an immense debt of gratitude. Pursuing a PhD is a privilege as it effectively removes one from society to work on problems that may be very abstract. Having a supportive family makes this journey of self-doubt and tentativeness result in joy and pride. I therefore thank my mother, Justine, and father, Rogatien, for providing me the irrational confidence that I could accomplish anything I wanted so long as I worked diligently. To my siblings Angela, José, and Lynda, I only have love and admiration, for I have always looked up to them either from up close growing up, or afar while our lives are in different parts of the country and the globe.

None of the relationships I enjoy with the folks listed above fit neatly in the categories that I've summarily decided to present them in. They are often interwoven in various aspects of my life, which makes them ever so meaningful. I wouldn't have any other way.

Chapter 1

Introduction to Perovskite Solar Cells

1.1 Motivation

Our global energy access is not equitable. Today, 16% of the world's population still lacks access to electricity [1]. The situation in Africa is especially dire because roughly 600 million people living below the Sahara desert lack access to this commodity essential for fully participating in the 21st century's technology age. For the Africans with access to electricity, its nature is unreliable. Constant power outages due to the demand vastly outweighing the supply, especially in rural areas, are a hindrance to economic development [2]. Solar powered mini-grids can greatly accelerate this expansion while providing a sustainable alternative to the diesel-powered generators commonly used in Africa [3].

Our global energy diet is not sustainable. One of the latest Statistical Review of World Energy by BP shows a rapid growth in energy demand and carbon emissions over the past few years. Indeed, the global primary energy grew by 2.9% in 2018 — the fastest growth seen since 2010. At the same time, carbon emissions from energy use grew by 2.0%, also the fastest expansion for many years, with emissions increasing by around 0.6 gigatonnes. That's roughly equivalent to the carbon emissions associated with increasing the number of passenger cars on the planet by a third [4]. The rise in energy consumption in 2018 appears to be related to weather effects. In particular, there was an unusually large number of hot and cold days across many of the world's major demand centers (US, China and Russia), with the increased demand for cooling and heating services helping to explain the strong growth in energy consumption [5]. To a very large extent, the growth in carbon emissions is simply a direct consequence of the increase in energy growth. Relative to the average of the previous five years, growth in energy demand and carbon emissions were 1.5% and 1.4% higher in 2018, respectively. This is worrisome, especially if the link between the growing levels of carbon in the atmosphere and the types of weather patterns observed in 2018 was not just correlational, but causal. Indeed, this would raise the possibility of a vicious cycle: increasing levels of carbon leading to more extreme weather patterns, which in turn trigger stronger growth in energy (and carbon emissions) as households and businesses seek to offset

their effects. Thankfully, the rise in renewable energy last year helped curb the growth of carbon emission with only 0.5% increase in 2019 [6]. Hence, there's a dire need for an aggressive adoption of solar and other renewable energies to sustain both the global energy demand and the environment. Perovskites can reduce the adoption cost.

In this chapter, we will show the potential of perovskite solar cells. First, we will briefly discuss the evolution of their study over the years by focusing on power conversion efficiency milestones between 2009 and 2020. Second, we will present the general characteristics of the perovskite material by focusing on its crystal structure and optoelectronic properties. Third, we will describe the main fabrication techniques used for building the solar cells and discuss their advantages and drawbacks. Fourth, we will discuss the usefulness of perovskite in building tandem cells with silicon and its economic advantages. Finally, we will discuss the main issues that prevent perovskites from currently achieving their market viability.

1.2 Brief History

1.2.1 2009

Perovskite solar cells started garnering the attention of the scientific community starting with a report [7] from the Miyasaka Research Group from Toin University of Yokohama, Japan. Approaching the problem from a dye-sensitized cell point of view, they were seeking an alternative to two types of sensitizers:

- First, organic sensitizers because of their low absorption coefficients and narrow absorption bands often limiting their light harvesting ability and,
- Second, inorganic quantum dots such as CdS, CdSe, PbS, InP, and InAs because of significant losses in light conversion and charge separation at the semiconductor-sensitizer interface resulting in low quantum conversion and photovoltaic generation.

This led them to investigate organic-inorganic hybrid lead halide perovskite compounds $CH_3NH_3PbX_3$ (X = Br, I) as visible-light sensitizers in photoelectrochemical cells. These compounds revealed themselves to be very attractive options for their unique optical [8], electrical [9] and excitonic [10] properties. Indeed, $CH_3NH_3PbI_3$ was shown to have an optical absorption coefficient of $\sim 10^5$ cm^{-1} at the absorption band edge, and a low exciton biding energy of 37 meV, while $CH_3NH_3PbBr_3$ exhibited a conductivity of $2x10^{-5}$ S/cm at room temperature. With these appealing materials, they built a sandwich-type open cell by combining the $CH_3NH_3PbX_3$ with a mesoporous layer of TiO_2 to form the photoelectrode (anode) and using a Pt-coated FTO glass as the counter electrode (cathode) with insertion of a 50 μm thick separator film. The gap between the electrodes was filled with an organic electrolyte solution containing lithium halide and halogen as a redox couple. The results were the first perovskite solar cells made with a PCE of 3.13% and 3.81% for $CH_3NH_3PbBr_3$ and $CH_3NH_3PbI_3$, respectively (See Figure 1.1 and Table 1.1).

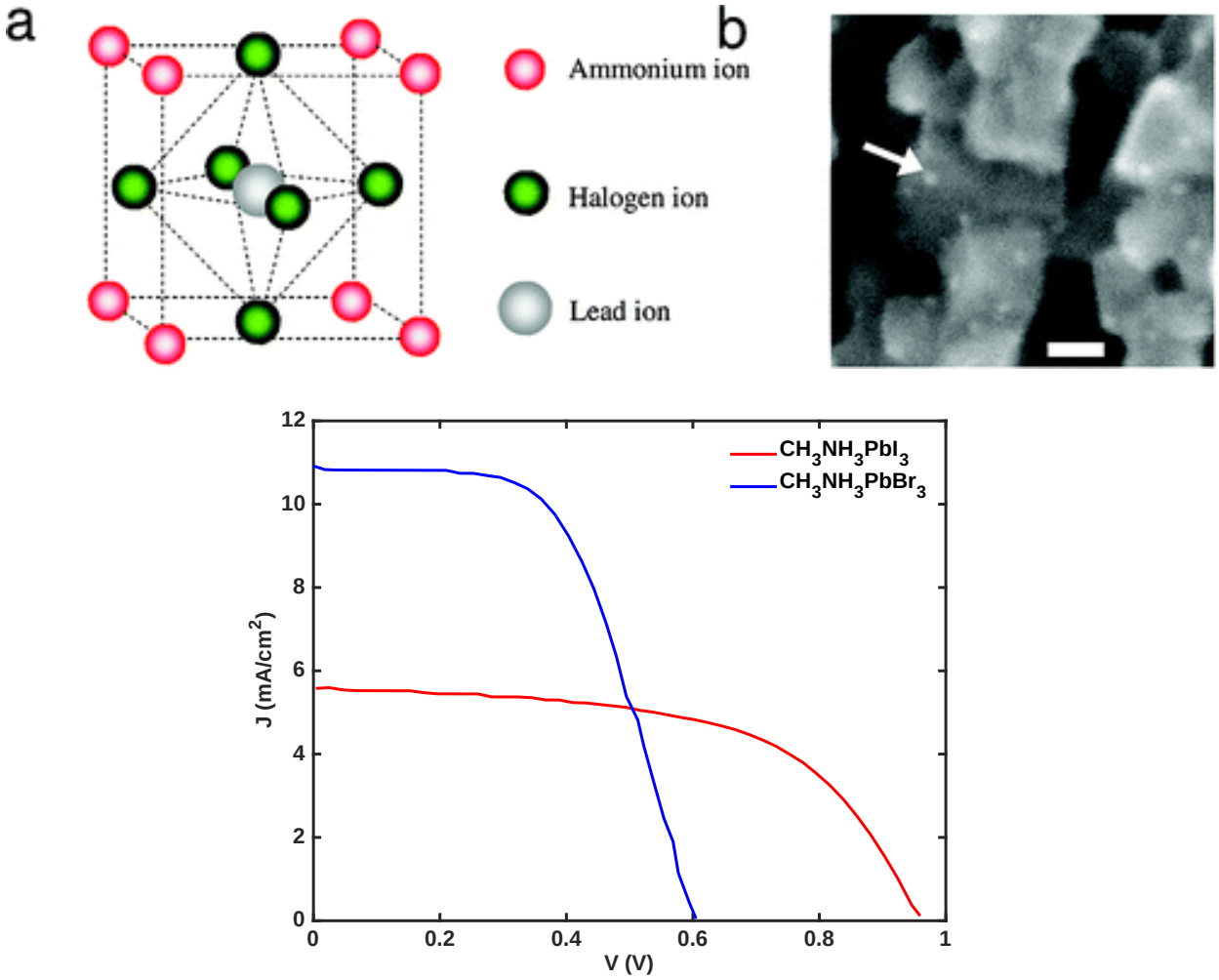

Figure 1.1: [**Top**] (**a**) Crystal structure of perovskite compounds. (**b**) SEM image of particles of nanocrystalline $CH_3NH_3PbBr_3$ deposited on the TiO_2 surface. The arrow indicates a particle, and the scale bar shows 10 nm. [**Bottom**] IV characteristics of perovskite under illumination [7].

Perovskite Type	J_{SC} (mA/cm^2)	V_{OC} (V)	FF	PCE (%)
$CH_3NH_3PbBr_3$	5.57	0.96	0.59	3.13
$CH_3NH_3PbI_3$	11.0	0.61	0.57	3.81

Table 1.1: Photovoltaic characteristics of perovskite cells of effective area 0.24 cm^2 [7].

1.2.2 2012

A few years later, Miyasaka collaborated with Henry Snaith's group at Oxford University to improve the aforementioned cell design and further characterize its performance. This collaboration [11] has put perovskite on the fast track to be the leading research topic in the photovoltaic (PV) community with a reported PCE of 10.9% and a more compact architecture than the one previously described. Working with a $CH_3NH_3PbI_2Cl$ structure, chosen for its relative air stability, they observed that this absorber material has a 1.55 eV band gap and could generate more than 1.1 V of open-circuit photovoltage as a single junction device. The cell was fabricated by sequentially spin-coating, on top of a fluorine tin oxide (FTO) coated glass substrate, a compact layer of TiO_2, a mesoporous oxide layer (TiO_2 or Al_2O_3) as the transparent n-type electron transport material or scaffold, the perovskite absorber, and 2,2',7,7'-tetrakis-(N,N-di-p-methoxyphenylamine)9,9'-spirobifluorene (spiro-OMeTAD) as the transparent p-type hole conductor. A layer of silver was thermally evaporated on top to serve as the anode, whereas the FTO was used as the cathode (See Figure 1.3). The measured current-voltage characteristics, shown in Figure 1.2 and Table 1.2, revealed that switching the mesoporous TiO_2 with Al_2O_3 resulted in higher V_{OC} and PCE. The paper posits that the photocarriers generated in the Al_2O_3-based cells remained in the perovskite phase until collected at the compact TiO_2 layer for electrons and must hence be transported throughout the film thickness in the perovskite. As a consequence, it was apparent that the perovskite layer could function as both absorber and n-type component, transporting electronic charge out of the device. To probe its effectiveness at charge transport, Lee et al. [11] performed small-perturbation transient photocurrent decay measurements [12]. The cells were exposed to simulated sunlight and "flashed" with a small red light pulse; in such experiments, the decay rate of the transient photocurrent signal is approximately proportional to the rate of charge transport out of the photoactive layer. As shown in Figure 1.4, the charge collection in the Al_2O_3-based devices was faster than in the TiO_2 sensitized devices by a factor of more than 10, indicating faster electron diffusion through the perovskite phase than through the n-type TiO_2.

This study also garnered a lot of interest because this cell was fully solution-processable, low-cost, and offered the promise of forming multi-junction cells with silicon down the road due to its excellent visible to near-infrared absorptivity.

Mesoporous oxide layer	J_{SC} (mA/cm^2)	V_{OC} (V)	FF	PCE (%)
TiO_2	17.8	0.80	0.53	7.6
Al_2O_3 - Champion	17.8	0.98	0.63	10.9
Al_2O_3 - High V_{OC}	15.4	1.13	0.45	7.8

Table 1.2: Photovoltaic characteristics of perovskite-based cells with various mesoporous oxide layers and of effective area 0.09 cm^2 [11].

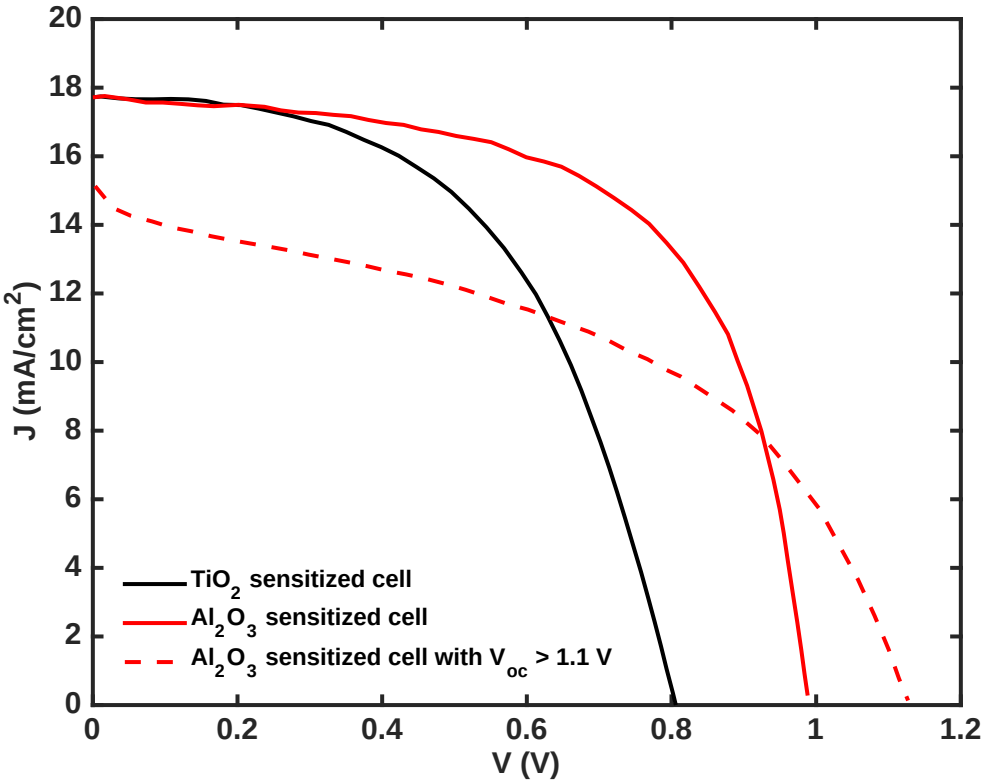

Figure 1.2: Current density-voltage characteristics under simulated AM1.5 100W/cm^2 illumination for perovskite cells with various mesoporous layers [11].

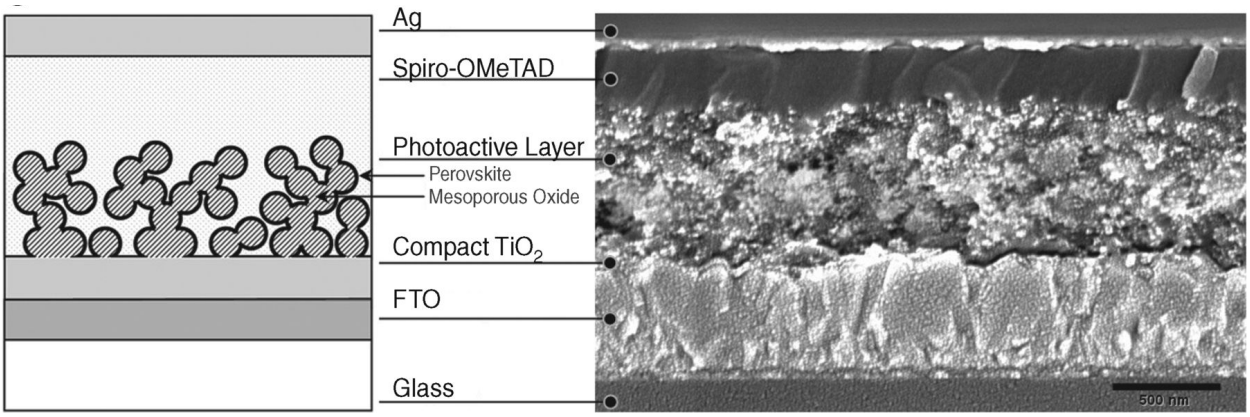

Figure 1.3: [**Left**] Schematic representation of full device structure, where the mesoporous oxide is either Al_2O_3 or anatase TiO_2. [**Right**] Cross-sectional SEM image of a full device incorporating mesoporous Al_2O_3 [11].

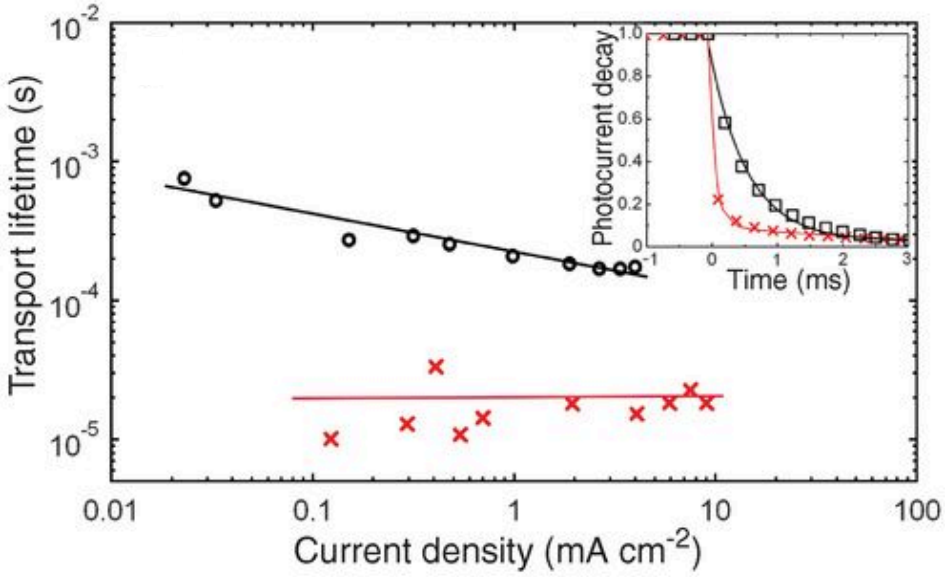

Figure 1.4: Charge transport lifetime determined by small-perturbation transient photocurrent decay of perovskite-sensitized TiO_2 cells (black circles) and Al_2O_3 cells (red crosses), both with lines to aid the eye. Inset shows normalized photocurrent transients for Al_2O_3 cells (red trace with crosses every 7th point) and TiO_2 cells (black trace with circles every 7th point), set to generate 5 mA/cm^2 photocurrent from the background light bias [11].

1.2.3 2016

With the passage of a few more years, perovskites were known for their immense potential yet failure to last long under atmospheric conditions. Indeed, numerous formulations of the ABX_3 structure have been tested to improve the PCE and environmental stability. $MAPbI_3$ (1.56 eV) perovskites raised concerns with respect to their structural phase transition at 55°C [13], degradation upon contact with moisture, and thermal stability [14]. Mixed halide perovskites such as $MAPbBr_xI_{3-x}$ raised the issue of light-induced trap-state formation and halide segregation [15]. $FAPbI_3$, though having a band gap of 1.43 eV [16], which is closer to the single-junction optimum of ∼1.33 eV [17], lacks structural stability at room temperature as it can crystallize either into a photoinactive, non-perovskite hexagonal δ-phase ("yellow phase") or a photoactive perovskite α-phase ("black phase") [13, 18, 19], which is sensitive to solvents or humidity [20]. $CsPbBr_3$ exhibits excellent thermal stability but does not have an ideal band gap for PVs (2.32 ± 0.02 eV) [21]. $CsPbI_3$ has a better band gap of 1.73 eV [22] and good emissive properties [23] but crystallizes in a photoinactive, orthorhombic δ-phase ("yellow phase") at room temperature, and the photoactive perovskite phase ("black phase") is only stable at temperatures above 300°C [22]. Consequently, Grätzel's group at École Polytechnique Fédérale de Lausanne (EPFL) published a study in 2016 that addressed those issues [24]. They posited that the road to high efficiency and stability perovskites will involve the use of mixed organic/inorganic cations (methy-

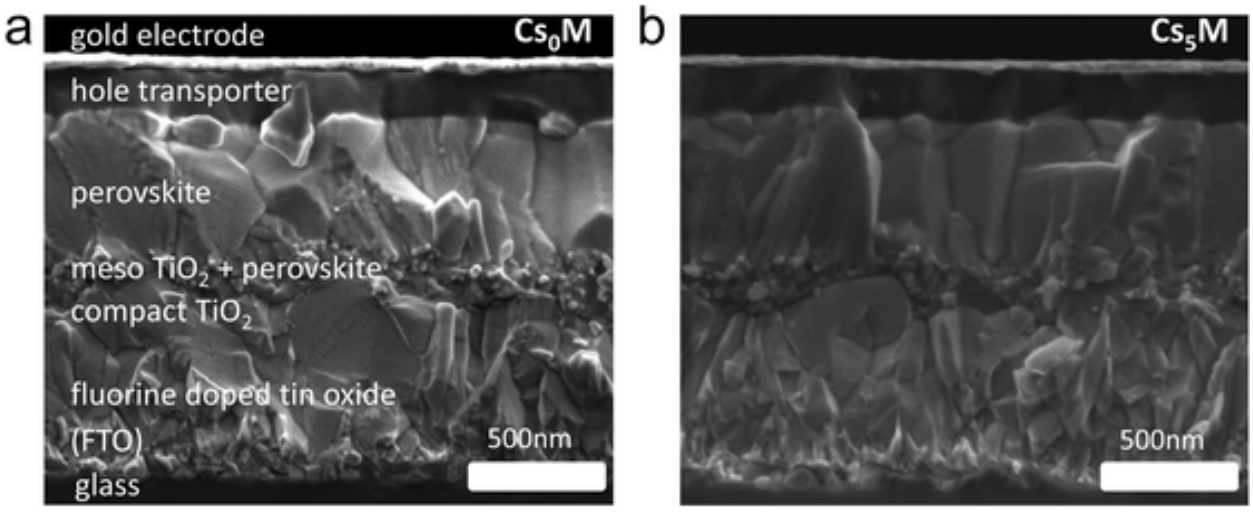

Figure 1.5: Cross-sectional SEM of (**a**) Cs_0M and (**b**) Cs_5M devices [24].

lammonium (MA), formamidinium (FA), cesium (Cs)...) and mixed halides. They argued that these types of formulations would exploit the benefits of the individual components while reducing their drawbacks. Therefore, they investigated triple cation perovskites of the generic form $Cs_x(MA_{0.17}FA_{0.83})_{(100\text{-}x)}Pb(I_{0.83}Br_{0.17})_3$, abbreviated Cs_xM for convenience, where x is in percentage. The solar cell architecture used was a stack of glass/FTO/compact TiO_2/Li-doped mesoporous TiO_2/perovskite/spiro-OMeTAD/gold (See Figure 1.5). All the layers were sequentially spin-coated and annealed on top of the FTO glass substrate, except for the gold layer, which was thermally evaporated. An optimum for efficiency, consistency and stability was reached for $x = 5\%$. Salida et. al [24] contend that the integration of the smaller Cs on the MA/FA combination leads to a lowering of the effective Cs/MA/FA cation radius in the new perovskite compound. This shifts the tolerance factor, an indicator of the stability and distortion of a crystal structure [25], towards a cubic lattice structure that matches the black perovskite phase. The photoactive black phase is thus entropically stabilized at room temperature. The introduction of Cs has improved all the current-voltage characteristics (See Figure 1.6 & Table 1.3) and stability of the illuminated perovskite cell (See Figure 1.7). This study illustrates the salience of stability, reproducibility and process control in the development of perovskite solar cells.

Perovskite	n	J_{SC} (mA/cm^2)	V_{OC} (mV)	FF	PCE (%)
Cs_0M	40	21.06 ± 1.53	1121 ± 25	0.693 ± 0.028	16.37 ± 1.49
Cs_5M	98	22.69 ± 0.75	1132 ± 25	0.748 ± 0.018	19.20 ± 0.91

Table 1.3: Summary of Figure 1.6.

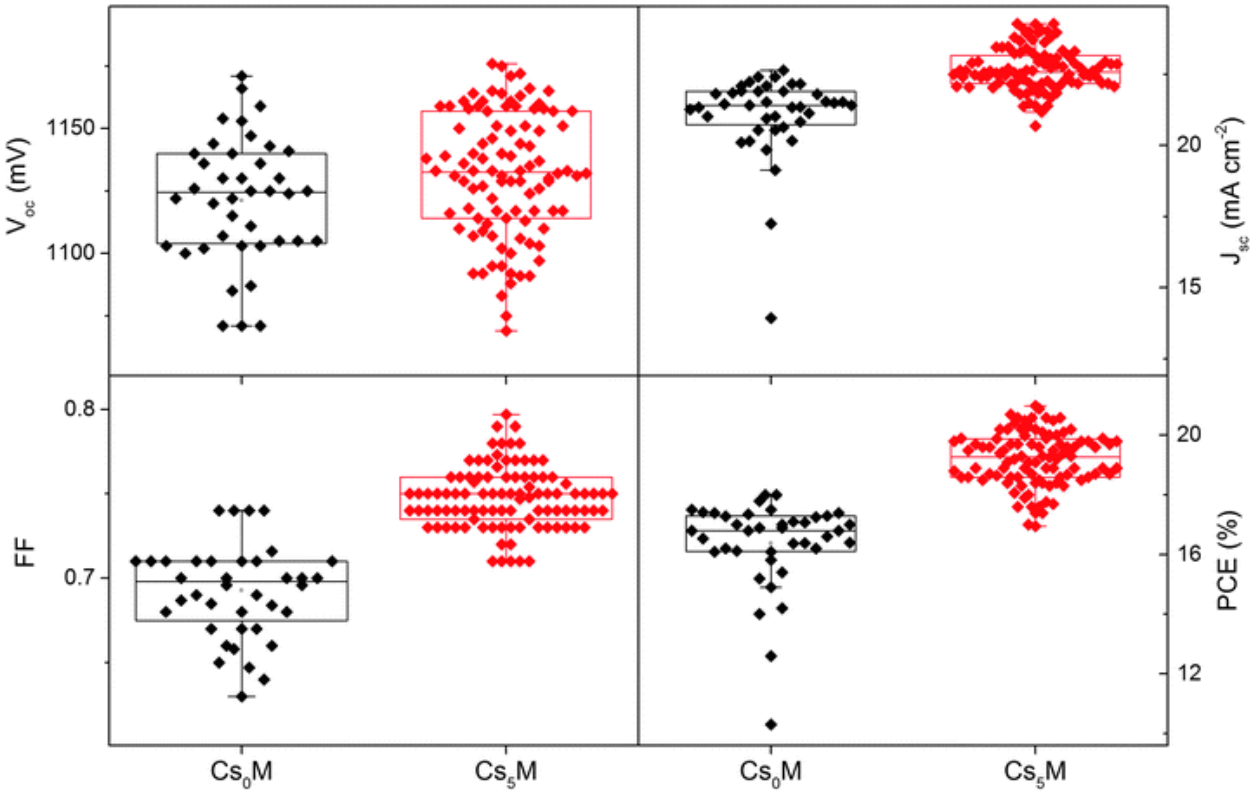

Figure 1.6: Statistics of Cs_xM devices as collected over 18 different batches [24].

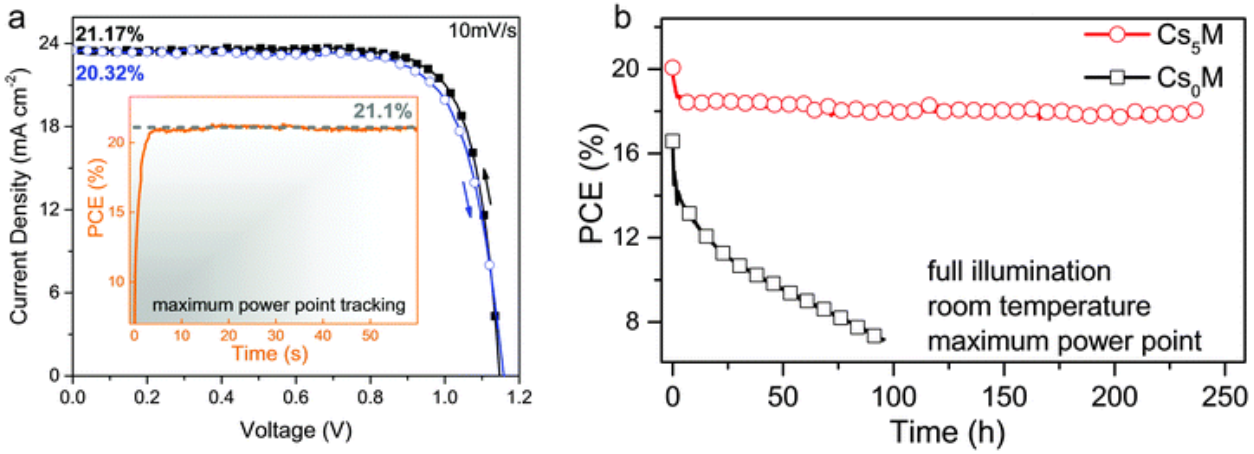

Figure 1.7: JV and stability characteristics (**a**) current-voltage scans for the best performing Cs_5M device showing PCEs exceeding 21%. The inset shows the power output under maximum power point (MPP) tracking for 60s, starting from forward bias. (**b**) Aging for 250 h of a high performance Cs_5M and Cs_0M devices in a nitrogen atmosphere held at room temperature under constant illumination and MPP tracking [24].

1.2.4 2020

Nowadays, the state-of-the-art single junction perovskite solar cell has a certified efficiency of 25.2% according to the National Renewable Energy Laboratory (NREL) [26]. This feat has been achieved jointly by the Massachusetts Institute of Technology (MIT) and the Korea Research Institute of Chemical Technology (KRICT). No further details are available at this time about the record device, but this is reflective of the current era of secrecy surrounding major breakthroughs in perovskite research. Companies such as Oxford PV and Swift Solar are banking on making significant improvements in scalability and stability of perovskites to create a marketable product. One can only speculate that the new record device employs mixed cation and halides along with a high quality fabrication technique such as chemical vapor deposition to reduce interfacial traps. Nonetheless, progress in this field that started just a decade ago has been nothing but remarkable (See Figure 1.8). The PCE levels achieved are on par with commercial silicon cells, and the last hurdles to clear are to scale the cell size and reach long-term stability.

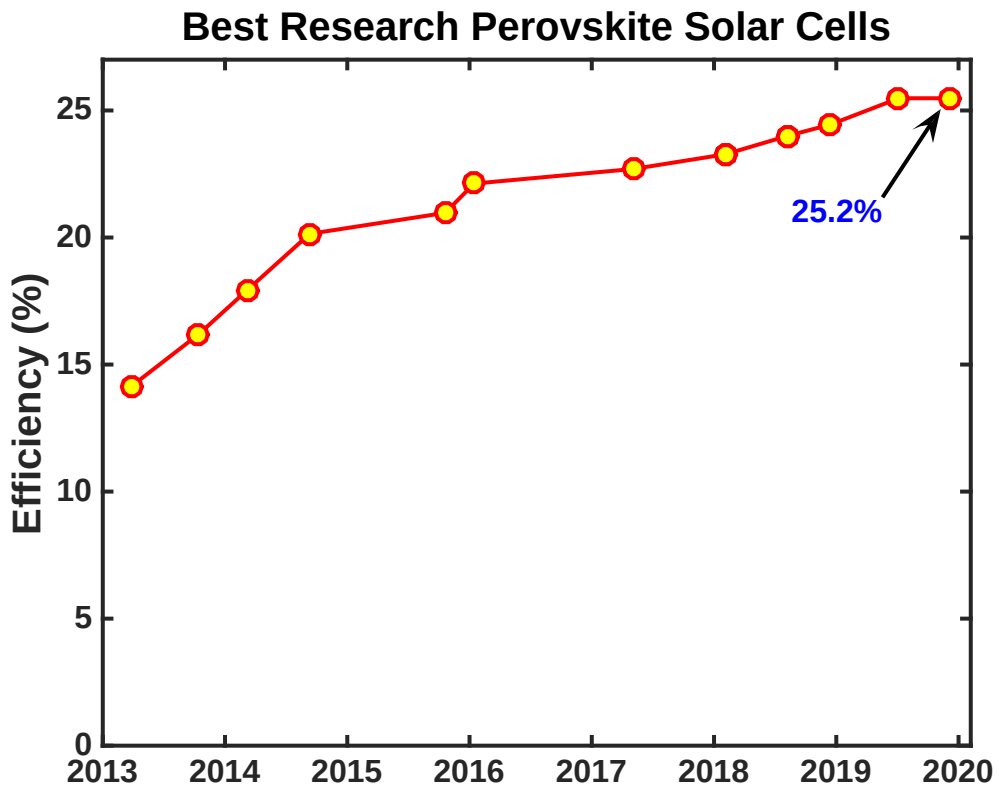

Figure 1.8: Record cells over time as certified by NREL [26].

In the next section, we will discuss the general characteristics of perovskites that have allowed for this steady improvement in power conversion efficiency over time.

1.3 General Characteristics

1.3.1 Crystal Structure

The term perovskite merely refers to a large family of crystalline ceramics with the ABX_3 crystal structure resembling that of calcium titanium oxide ($CaTiO_3$), which was discovered by German mineralogist Gustavus Rose and named after fellow Russian mineralogist Count Lev Alekseyevich von Perovski [27]. The A site refers to a larger cation, B a smaller cation, and X an anion bonding A and B together. This structure is based on a mixed fcc packing of three X anions and one A cation. This partitions the fcc array to yield a 12-fold cuboctahedral coordination of the X anions about the larger A cation. The B cations are octahedrally coordinated by the X anions. The structure is usually illustrated as an idealized cubic structure but is more commonly tetragonal or orthorhombic because of tilting of the octahedra or Jahn-Teller distortions. In Figure 1.9, the B cations occupy the body center, the A cations occupy the cube vertices, and the X anions decorate the face centers. By definition, many set of compounds could be used to form a perovskite. Henceforth, we will focus on describing the characteristics of $MAPbI_3$ as it is the compound of interest in this work.

Poglitsch and Weber deduced the temperature dependent crystal structure of $MAPbI_3$ from temperature dependent Guinier-Simon photographs of the powdered crystal [28]. The results are summarized in Table 1.4. $MAPbI_3$ forms a tetragonal structure at room temperature (space group $I4/m$ or $I4/mcm$). The transition to the cubic phase (T_c = 327.4 K) is accomplished by a slight distortion of the PbI_6 octahedra around the c axes. The MA^+ cation cannot be fixed there, suggesting that its position might be an eightfold disordered one. Lowering the temperature of the cubic phase causes the transition to a phase with tetragonal symmetry. This first transition preserves the disordered character of the MA^+ cation. The crystals formed have a strong tendency toward adopting the elongated rhombic dodecahedron (rhombo-hexagonal dodecahedron) shape (See Figure 1.10) [13]. The second transition from the tetragonal symmetry to an orthorhombic symmetry reduces the disordering of the MA^+ cation occupation. It gets a fixed position in the orthorhombic phase of $MAPbI_3$ (space group $Pna2_1$) [28]. $MAPbI_3$ tends to remain stable in air for months yet is affected by humidity and loses its crystalline luster after a couple of weeks. However, Stoumpos et al. affirm that this is only a surface effect since the bulk properties of the material are retained [13]. Figure 1.11 shows simulated and experimental data of X-ray diffraction (XRD) patterns for $MAPbI_3$ crystals in the tetragonal β-phase. It shows that the main peaks are at $2\theta \approx 14°(110), 28.5°(220), 31.5°(210), 40.5°(224)$, and $43°(314)$.

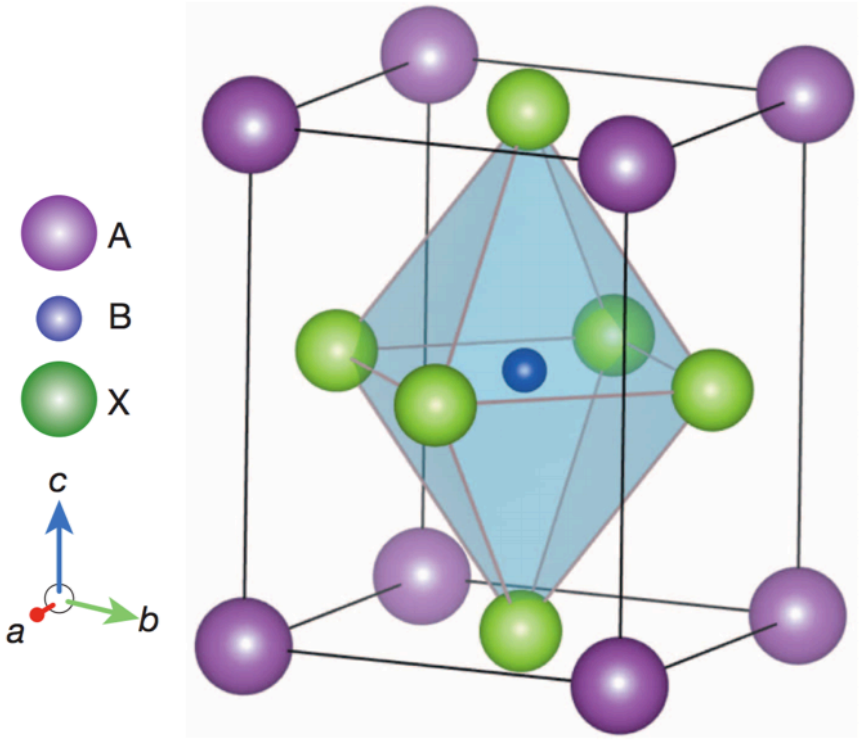

Figure 1.9: Perovskite crystal Structure of the form ABX_3 [29].

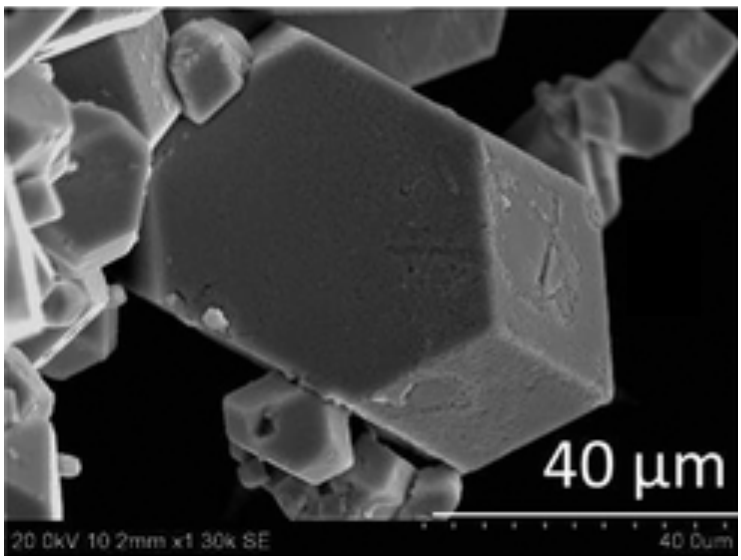

Figure 1.10: Typical SEM of the crystal structure of $MAPbI_3$ post-solution processing [13].

Phase	Temperature (K)	Crystal System	Space Group	Lattice (pm)	Volume (10^6 pm^3)
α	> 327.4	cubic	$Pm3m$	a = 632.85(4)	253.5
β	162.2-327.4	tetragonal	$I4/mcm$	a = 885.5(6) c = 1265.9(8)	992.6
γ	< 162.2	orthorhombic	$Pna2_1$	a = 886.1(2) b = 858.1(2) c = 1262.0(3)	959.5

Table 1.4: Temperature dependent structural data of $MAPbI_3$ [28].

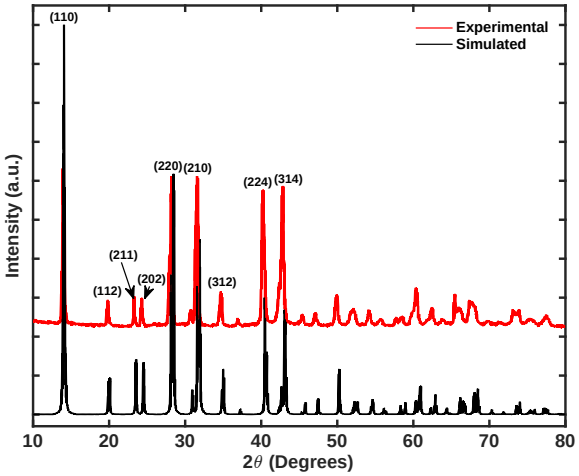

Figure 1.11: Typical XRD pattern of $MAPbI_3$ crystals in the β-phase prepared via solution processing (Adapted from [13, 30]).

1.3.2 Optoelectronics

Lin et al. sought to accurately determine the optical constants (refractive index n and extinction coefficients k) for planar perovskites [31]. To achieve this, they used a combination of spectroscopic ellipsometry, total transmittance, and near-normal incidence reflectance measurements. This is a non-trivial exercise for dispersive materials like perovskites, yet the constants were deduced by using an iterative self-consistency check employing an adapted form of the Kramers-Kronig relationship. Figure 1.12 presents n and k for $MAPbI_3$. Three different spectral regions appear: $\lambda < 500$ nm with the very strong absorption characteristic of PbI_2, 500 nm $< \lambda <$ 800 nm with moderate absorption (comparable with the absorption of typical organic semiconductors), and $\lambda > 800$ nm with minimal absorption. It is noteworthy that k, which is a dimensionless representation of the absorption coefficient, shows two sharp edges with onsets at $\sim$ 500 nm (reminiscent of PbI_2) and $\sim$ 750nm (the optical gap of $MAPbI_3$).

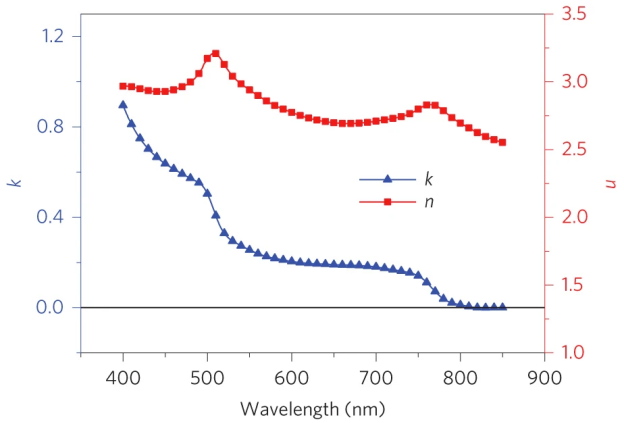

Figure 1.12: Refractive index n and extinction coefficient k of $MAPbI_3$ at RT [31].

Energy is generated by exciting an electron from the ground state unto an excited state via the absorption of a photon. Such an excited state can be regarded as an electron and a hole bound together by an electrostatic force. An electron-hole pair bound as described is called an exciton. Having a low exciton binding energy relative to thermal energy ($\sim$ 26 meV at RT) in any photovoltaic material is extremely important because it eases the creation of free electron-hole pair at room temperature thus maximizing the photocurrent generated. Using magnetoabsorption spectra, Hirasawa et al. extracted the exciton binding energy of $MAPbI_3$ to be 37 meV [10]. Miyata et al. measure the value to be 16 meV in the low-temperature orthorhombic phase using very high-field interband magnetoabsorption [32]. Moreover, other studies have shown that the diffusion length of free carriers in $MAPbI_3$ are above 100 nm [33, 34] and above 1 μm for other perovskite formulations [33]. The low exciton binding energies and long diffusion lengths are a few of the reasons why perovskites are favorable materials for solar cells.

Figure 1.13 shows the electronic band structure of $MAPbI_3$ as calculated from first principles using the GW approximation [35]. It reveals a direct band gap of 1.57 eV, which is in good agreement with experimental values determined at 4K to be 1.66 eV in the same study. The authors claim the small difference between the calculated and measured values of the band gap arise from the absence of electron-phonon interactions in the *ab initio* calculations. Interestingly, the extracted band structure also reveals the presence of another electronic transition with an onset energy of 1.95 eV, which could influence the shape of the absorption onset for its proximity to the band edge.

Maintaining the general characteristics presented in this section are important in ensuring the stability of perovskite solar cells. Indeed, any drastic change in ambient temperature can result in a phase change of the perovskite, which can be deleterious to its photovoltaic properties (See Table 1.4). This phase change can also affect its absorption properties and even its band gap. Therefore, we track these properties in this study to gain a mechanistic understanding of the degradation of perovskite solar cells in operation. In the next section, we will discuss the fabrication techniques used to build the solar cells.

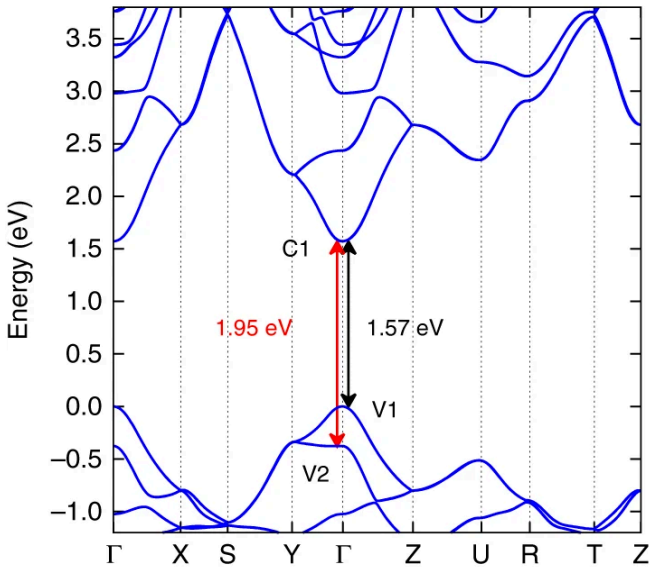

Figure 1.13: First-principles calculations of the band structure of $MAPbI_3$ calculated using the GW approximation. The black arrowed line shows the direct band transition from the first valence band (V1) to the first conduction band (C1) at 1.57 eV. The red arrowed line shows the transition from the second valence band (V2) to C1 at 1.95 eV [35].

1.4 Fabrication Techniques

Several methods have been applied to the fabrication of perovskite solar cells. They include spin coating [11], dip coating [36], 2-step interdiffusion [37], chemical vapor deposition [38], spray pyrolysis [39], atomic layer deposition [40], ink-jet printing [41], gravure printing [42], and thermal evaporation [29, 43]. We will highlight three and offer the trade-offs associated with each.

1.4.1 Spin-Coating

The spin-coating process involves drop casting a given volume of perovskite precursor onto a substrate and spinning it at high speeds to allow the centripetal force and the surface tension of the precursor to create an even coverage. The substrate is then annealed to evaporate the remaining solvent, promote crystallization, and form the absorber film. This technique is widely used in the development phase of perovskites for its simplicity in achieving uniform films. The disadvantage is that it is inherently a batch process and cannot be properly scaled for industrial use due to limitations in area scaling, and costs associated with the process. Lee et al. spun their $CH_3NH_3PbI_2Cl$ perovskite from a precursor solution in N,N-dimethylformamide (DMF) [11]. The substrate was a semitransparent FTO-coated glass with a compact layer of TiO_2 that acted as anode. In between the perovskite and the compact TiO_2 layer was a porous oxide film (either TiO_2 or Al_2O_3) fabricated from sol-gel

processed sintered nanoparticles. The precursor solution was infiltrated into the porous oxide mesostructure via spin-coating and was dried at 100°C, which enabled the perovskite to form via self-assembly of the constituent ions. A dark coloration, characteristic of the photoactive β-phase of perovskites, was observed only after annealing. With respect to the perovskite coating process, many considerations went into effectively infiltrating the mesoporous layer. If the concentration of the solution is low enough and the solubility of the cast material high enough, the material will completely penetrate the pores as the solvent evaporates. Typically, the material forms a "wetting" layer upon the internal surface of the mesoporous film that uniformly coats the pore walls throughout the thickness of the electrode. The degree of "pore filling" can be controlled by varying the solution concentration. If the concentration of the casting solution is high, then maximum pore filling occurs, and any "excess" material forms a "capping layer" on top of the filled mesoporous oxide.

Li et al. used a conjugated polymer-assisted growth to form a perovskite-polymer layer [44]. PbI_2 and methylammonium iodide (MAI) were dissolved in dimethyl sulfoxide (DMSO) : γ-butyrolactone. The perovskite solution was spun in a first spin step, then drops of chlorobenzene with or without conjugated polymer was added during the second step to accelerate crystallization. Figure 1.14 summarizes the spin coating process, Figure 1.15 shows the films' morphology and Figure 1.16, the respective current-voltage characteristics.

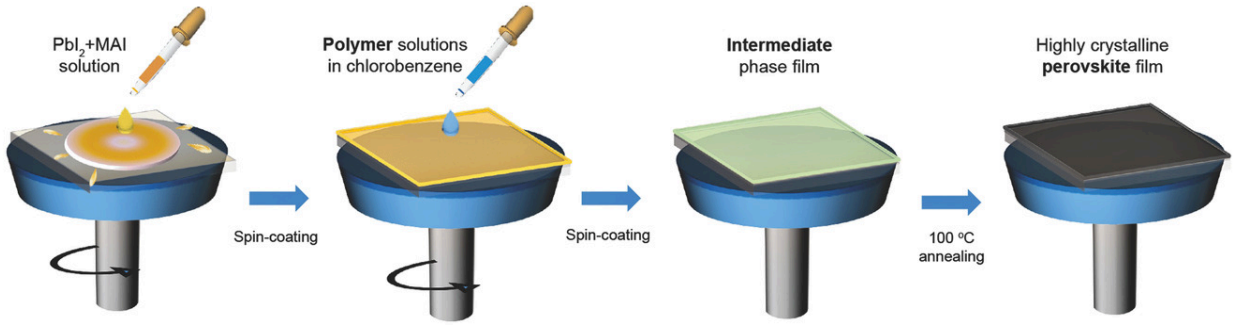

Figure 1.14: Spin-coating process for fabricating perovskite films with an antisolvent [44].

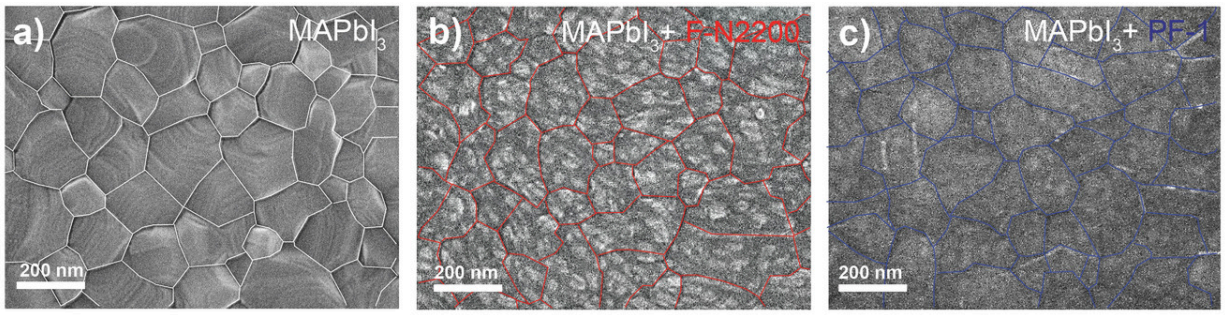

Figure 1.15: SEM of (**a**) pristine, (**b**) with n-type polymer F-N220, (**c**) with p-type polymer PF-1 spin-coated perovskite films [44].

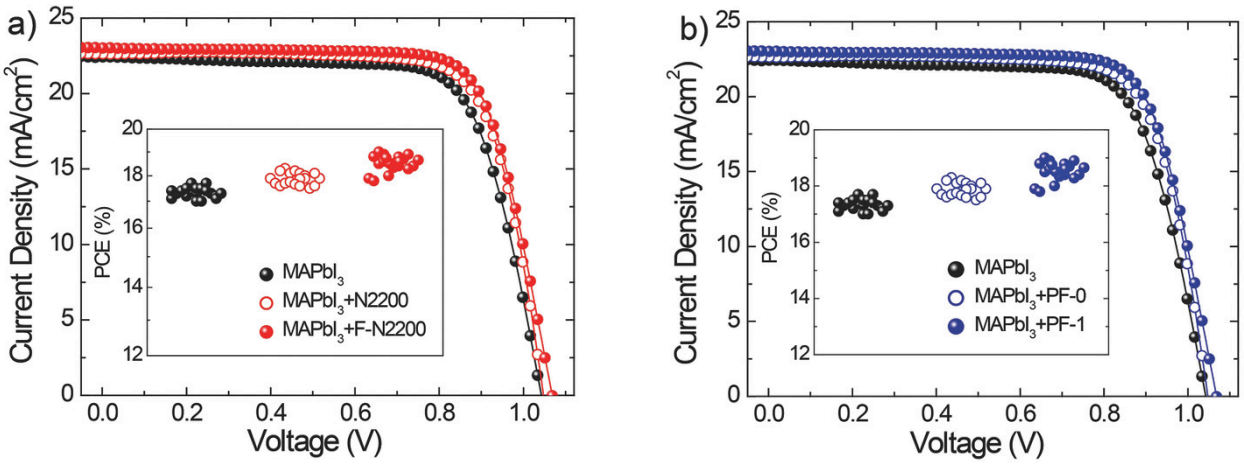

Figure 1.16: Current-voltage curves of optimized spin-coated perovskite solar cells with and without (**a**) N2200, F-N2200; (**b**) PF-0 and PF-1 measured under AM1.5 simulated sunlight. The inset pictures show the PCE distribution based on corresponding 20 devices [44].

1.4.2 Vapor Deposition

A technique better suited to preparing layered multi-stack thin films over large areas is vapor deposition. It is a mature technique used in the glazing industry, the liquid-crystal display industry, the thin-film solar cell industry, etc. it can lead to full optimization of electronic contacts at interfaces through multilayers with controlled levels of doping [45], as is done in the crystalline silicon 'heterojunction with thin intrinsic layer' solar cell [46], and in thin film solar cells [47]. Charge-collection interfaces can be carefully tuned via vapor deposition, and multi-junction architectures are simpler to achieve [48].

Liu et al. sought to understand and optimize the properties of the vapor deposited perovskite absorber layer [29]. To that end, they deposited it via a dual-source evaporation system with ceramic crucibles (organic light-emitting diode sources) in a nitrogen-filled glove box. The vapor deposited perovskite devices were fabricated on FTO-coated glass. A compact layer of TiO_2 was spun on the FTO-coated glass with a mildly acidic solution of titanium isopropoxide in ethanol prior to the deposition of the perovskite. The substrates were placed in a holder above the sources containing the precursors with the TiO_2-coated FTO facing down towards the sources. The organic CH_3NH_3I and inorganic $PbCl_2$ precursor salts were placed in the sources. Once the pressure in the chamber was pumped down below 10^{-5} mbar, the two sources were heated slightly above their desired deposition temperatures for a few minutes to remove volatile impurities before simultaneously evaporating the materials at a molar ratio of 4:1. The holder was rotated during evaporation to ensure uniform coating (See Figure 1.17). The perovskite films were optimized for best device performance by varying the deposition rates and periods for both sources in order to control the stoichiometric composition of the perovskite. Once the deposition was completed, the films were annealed in a nitrogen environment prior to spinning the hole transport material

and evaporating the silver as the top contact to complete the device.

Once fabricated, the vapor deposited perovskites were compared to spin-coated ones. Figure 1.18 summarizes the topological and cross-sectional comparison, whereas Figure 1.19 shows the current-voltage characteristics. The vapor deposited films are extremely uniform with crystalline features on the length scale of hundreds of nanometers. In contrast, the solution processed films appear to coat the substrate only partially, with crystalline 'platelets' on the length scale of tens of micrometers. The cross-sectional images show that the vapor deposited film is uniform with larger grains sizes while the solution processed one is smooth but with peaks and valleys. The IV characteristics, further summarized in Table 1.5, show a significantly improved performance from the vapor deposited devices as opposed to the solution processed ones.

These results were harbingers for the commercialization of perovskites. Because vapor deposition of perovskite layers is entirely compatible with conventional processing methods for silicon wafer-based and thin-film solar cells, the infrastructure could already be in place to scale up this technology [29].

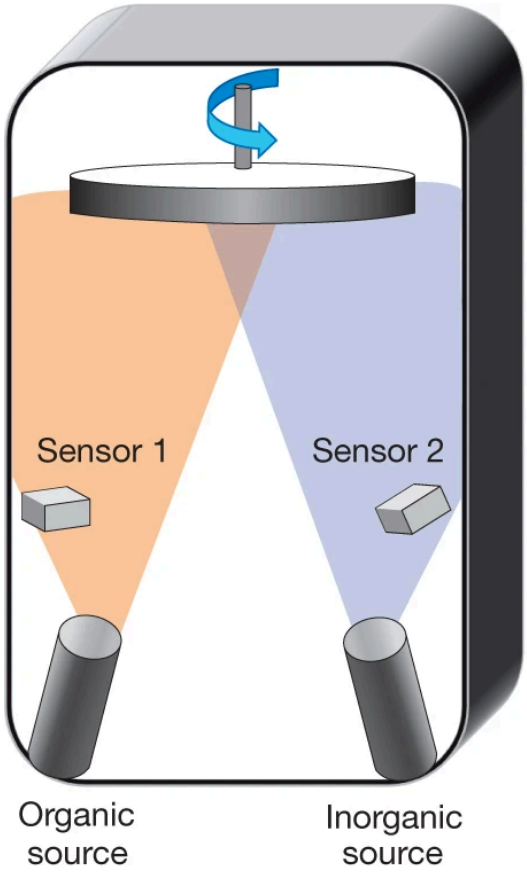

Figure 1.17: Dual source thermal evaporation system for depositing the perovskites [29].

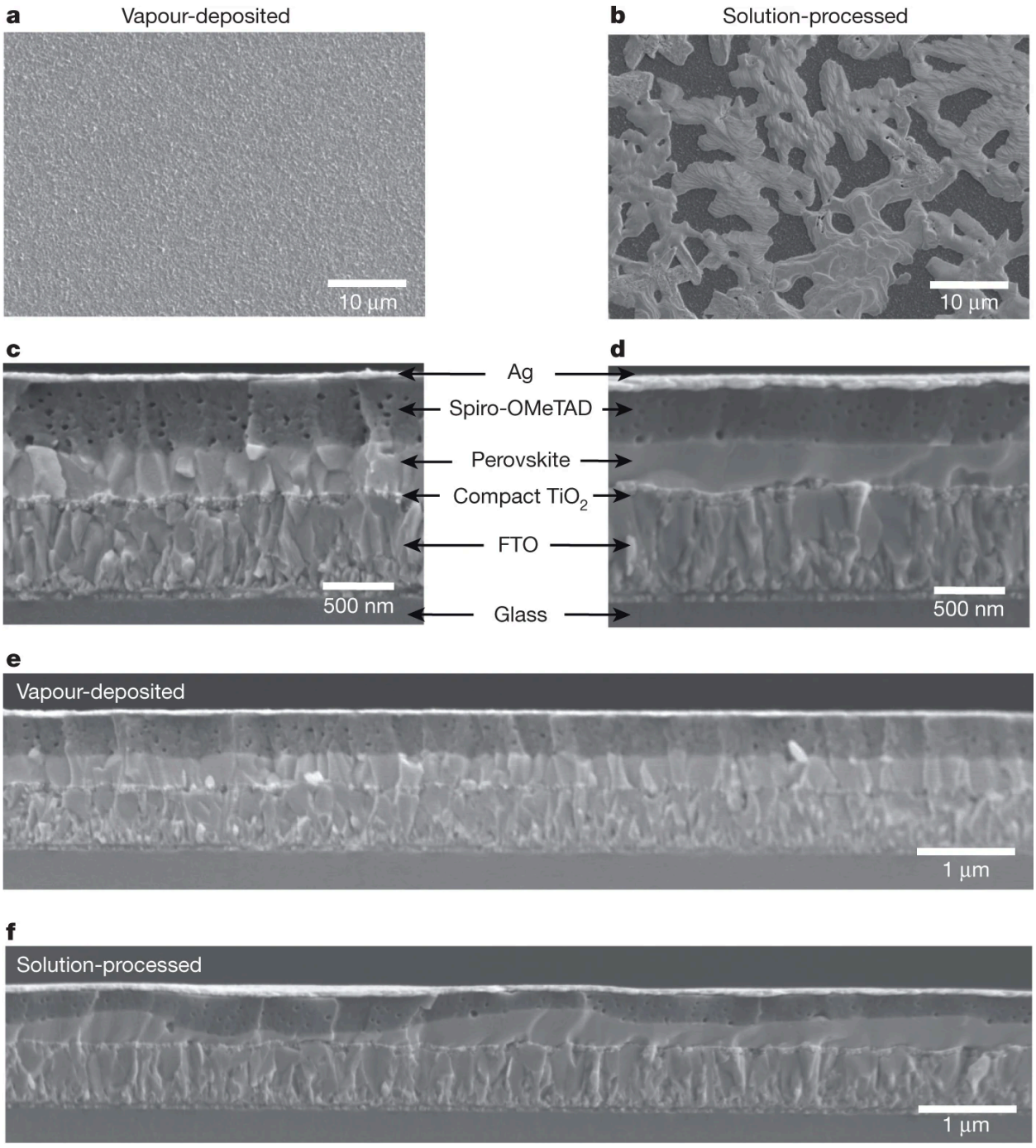

Figure 1.18: SEM top views of (**a**) a vapor deposited perovskite film and (**b**) a solution-processed film. Cross-sectional SEM of complete solar cells constructed from a vapor deposited perovskite (**c**–high mag, **e**–low mag) and a solution processed one (**d**–high mag, **f**–low mag) [29].

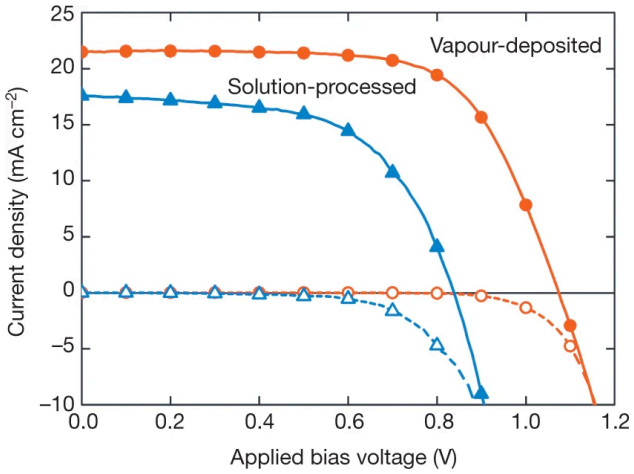

Figure 1.19: IV characteristics of champion cells for each technique measured under simulated AM1.5 sunlight of 101 mA/cm^2 irradiance (solid lines) and in the dark (dashed lines) [29].

Deposition Technique	J_{SC} (mA/cm^2)	V_{OC} (V)	FF	PCE (%)
Vapor Deposited (Champion)	2.15	1.07	0.67	15.4
Vapor Deposited (avg±s.d.)	18.9±1.8	1.05±0.03	0.62±0.05	12.3±2.0
Solution Processed (Champion)	17.6	0.84	0.58	8.6

Table 1.5: Solar cell performance parameters from Figure 1.19. The averages and standard deviations were extracted from a batch of 12 vapor deposited devices [29].

1.4.3 Gravure Printing

Gravure printing is uniquely suited for the manufacturing of perovskite solar cells because it is a high throughput roll-to-roll technique. To print, the ink is dropcasted onto the patterned roller to fill the recessed cells. As the roller spins, it draws excess ink onto the surface and into the cells. Then, the doctor blade scrapes the roller before it makes contact with the substrate, removing the excess ink from the non-printing areas and leaving the cells the right amount of ink required. Next, the substrate gets sandwiched between the impression roller and the engraved roller, which results in the ink transfer from the recessed cells to the substrate. Once in contact with the substrate, the ink's surface tension pulls the ink out of the cell and transfers it to the substrate. The thin film newly formed is finally dried. Unlike spin coating, gravure printing has no centrifugal force acting on the perovskite to accelerate its drying, and the inclusion of an antisolvent treatment to promote crystallization would significantly reduce the throughput. Using an airblade to direct the flow of a nitrogen gas in a wide and thin stream over the deposited perovskite film will help spread it across the substrate, accelerate drying, and promote supersaturation (See Figure 1.20) [42]. Optimizing the scan speed of the substrate, the flow rate of the nitrogen gas, and the substrate temperature during scan has shown promising results (See Figure 1.21).

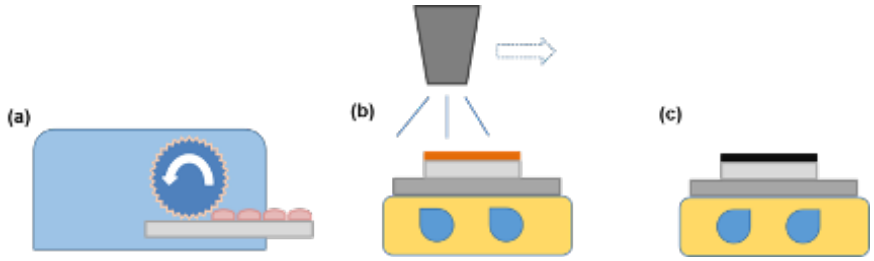

Figure 1.20: Schematic illustration of gravure printing perovskites using an airblade. (**a**) The ink is gravure printed onto the substrate, (**b**) moved to a hotplate where an airblade with flowing N_2 is scanned over the film, and (**c**) the film is moved to an annealing hotplate [42].

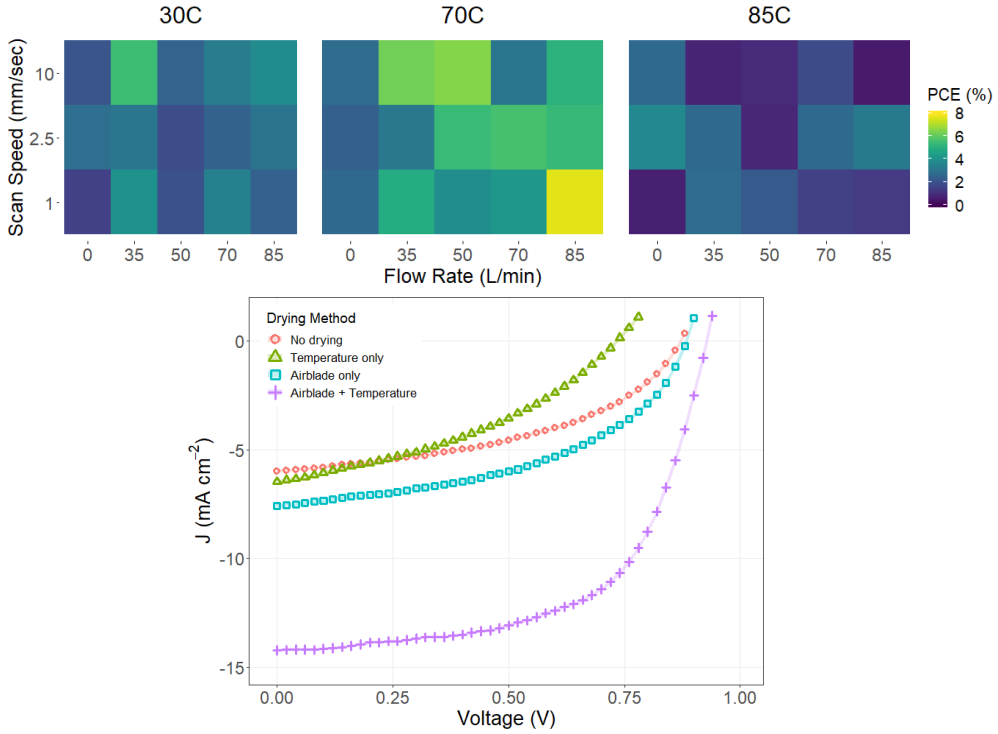

Figure 1.21: [**Top**] Heat map of PCE from gravure printed devices, dried via airblade under different substrate temperatures (30, 70, 85°C), flow rate, and scan speed conditions. [**Bottom**] JV characteristics of four drying method combinations [42].

1.4.4 Processing Environment

Uncontrolled processing environments with high humidities will result in poor film quality and useless photovoltaic activity. Some experiments [49] have shown that processing $MAPbX_3$ perovskites in air of relative humidity (RH) greater than 40% result in orange/brown film coloration post-spin, then reverting back to a bright yellow upon annealing and finally dark brown/grey post-heating. These are all signs of films with poor device per-

formance. Raga et al. show that annealing perovskite films in air with 50% RH is comparable with ones annealed in a dry nitrogen environment [50]. The current-voltage characteristics of those devices are shown in Figure 1.22. Raga et al. believe that at 50% RH, annealing will completely remove water from the film regardless of the environment. In general, studies concur in the need of controlling the processing humidity [51, 52, 53].

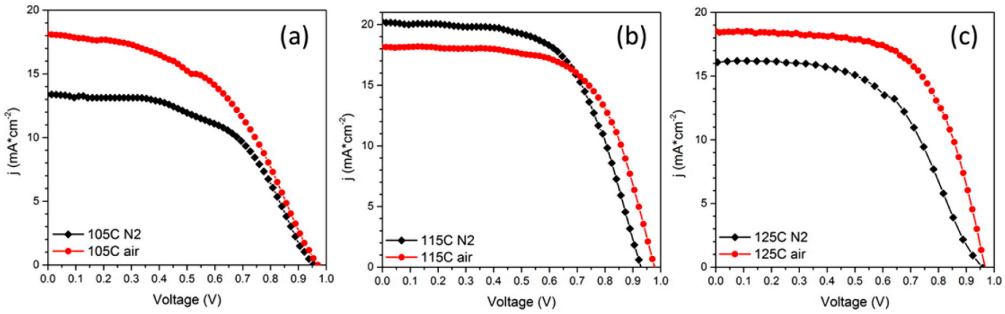

Figure 1.22: Representative current-voltage curves for cells annealed at increasing temperature in N_2 and air with 50% RH [50].

1.5 Perovskite-Silicon Tandem Solar Cells

Several architectures exist for forming perovskite solar cells. Thus far, we have shown the extensive work that has been done on raising the efficiency of single junction cells. Because the field has consistently achieved fairly high efficiencies, tandem cells with silicon have gained some steam with the ultimate commercialization in sight. Within the tandem world, there are many pathways to the integration of perovskites with silicon. We will focus here on a 2-terminal (2T) monolithic integration.

A monolithic architecture allows for having a compact, fully vertically integrated structure where current is collected at each electrode similarly to a single junction device. A successful tandem device will exploit the optimal optical absorption regions for each photoactive material in the structure. In the case of perovskites and silicon, the former is excellent at absorbing light closer to the red region of the spectrum, whereas the latter is better closer to the blue region. A detailed balance analysis [54] shows that crystalline silicon has a close to optimum band gap for a bottom cell in a two-semiconductor tandem device while the band gap of the perovskite top cell can be adjusted closer to the top cell optimum of 1.7 eV [55, 56]. Another criteria to consider in making a tandem cell is process compatibility. So far, mostly silicon heterojunction (SHJ) bottom cells are used due to the well-passivated c-Si wafer surface, which leads to high open circuit voltages [57]. Perovskites with the *p-i-n* top cell architecture prevailed over *n-i-p*, for the temperature limitations of the SHJ cell (200°C) prevented the use of high temperature processes such as the sintering of mesoporous TiO_2 [58]. It was shown that by depositing a SnO_2 buffer layer in the top contact via ALD, the absorption losses were mitigated in the n-type top contact of the *p-i-n* top cell architecture

[59]. Köhnen et al. pushed the envelope further by making more adjustments [60]. To strike a balance between conductivity and transparency of the indium zinc oxide (IZO) top electrode, the oxygen concentration was fine-tuned during sputtering. Then, a SnO_2 buffer layer was deposited via ALD to enable an effective electron-selective contact for the *p-i-n* top cell. Finally, the thicknesses of the nc-SiO_x:H, perovskite absorber, and IZO front electrode were optimized for maximum output power. The cross-sectional SEM in Figure 1.24 shows the textured backside of the bottom cell, which is a rear-junction SHJ solar cell with a planar front side. To improve light incoupling into the bottom cell, n-doped nc-SiO_x:H was used to create an electron-selective contact with proper refractive index interfacing with a thin indium tin oxide (ITO) layer as recombination site to interconnect both sub-cells. The perovskite top cell with *p-i-n* architecture is built in the following layer sequence with light entering the top cell from the LiF side: ITO/PTAA/perovskite/C_{60}/SnO_2/IZO/LiF. Poly[bis(4-phenyl)(2,4,6-trimethylphenyl)amine] (PTAA) and C_{60} are the anode and cathode, respectively. The perovskite absorber, $Cs_{0.05}(MA_{0.83}FA_{0.17})_{0.95}Pb(I_{0.83}Br_{0.17})_3$, was spin-coated using an antisolvent. SnO_2, deposited via ALD, is a barrier and buffer layer to the top contact as it prevents both moisture and oxygen penetration, both known to be deleterious to perovskites. A silver metal frame around the cell area was thermally evaporated to form the busbar without grid fingers. Finally, thermally evaporated LiF serves as the anti-reflective coating. The current-voltage characteristics in Figure 1.23 show a PCE of 26%. This is still shy of the detailed balance theoretical limit of ∼40% PCE [54], so there is room for improvement. Reports by Oxford PV show that their tandem cell has reached a certified 28% PCE, but no further detailed were made available [61].

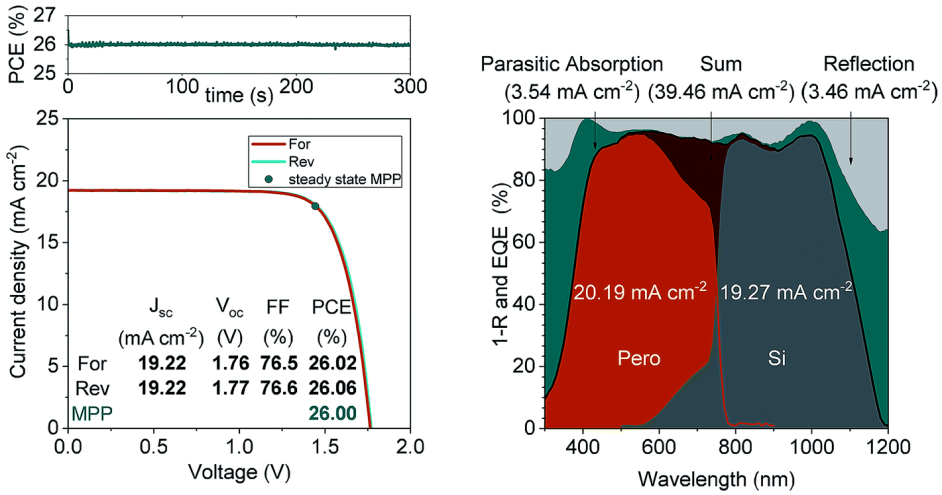

Figure 1.23: [**Left**] J-V characteristics of the optimized tandem solar cell with the performance metrics and a 5 min MPP-track. [**Right**] External quantum efficiency (EQE) and 1-reflectance (1-R) spectra of the same device. The integrated current densities are 20.19 mA/cm^2 and 19.27 mA/cm^2 for the perovskite and silicon sub-cells, respectively. Additionally, the integrated loss currents from parasitic absorption and 1-R are shown [60].

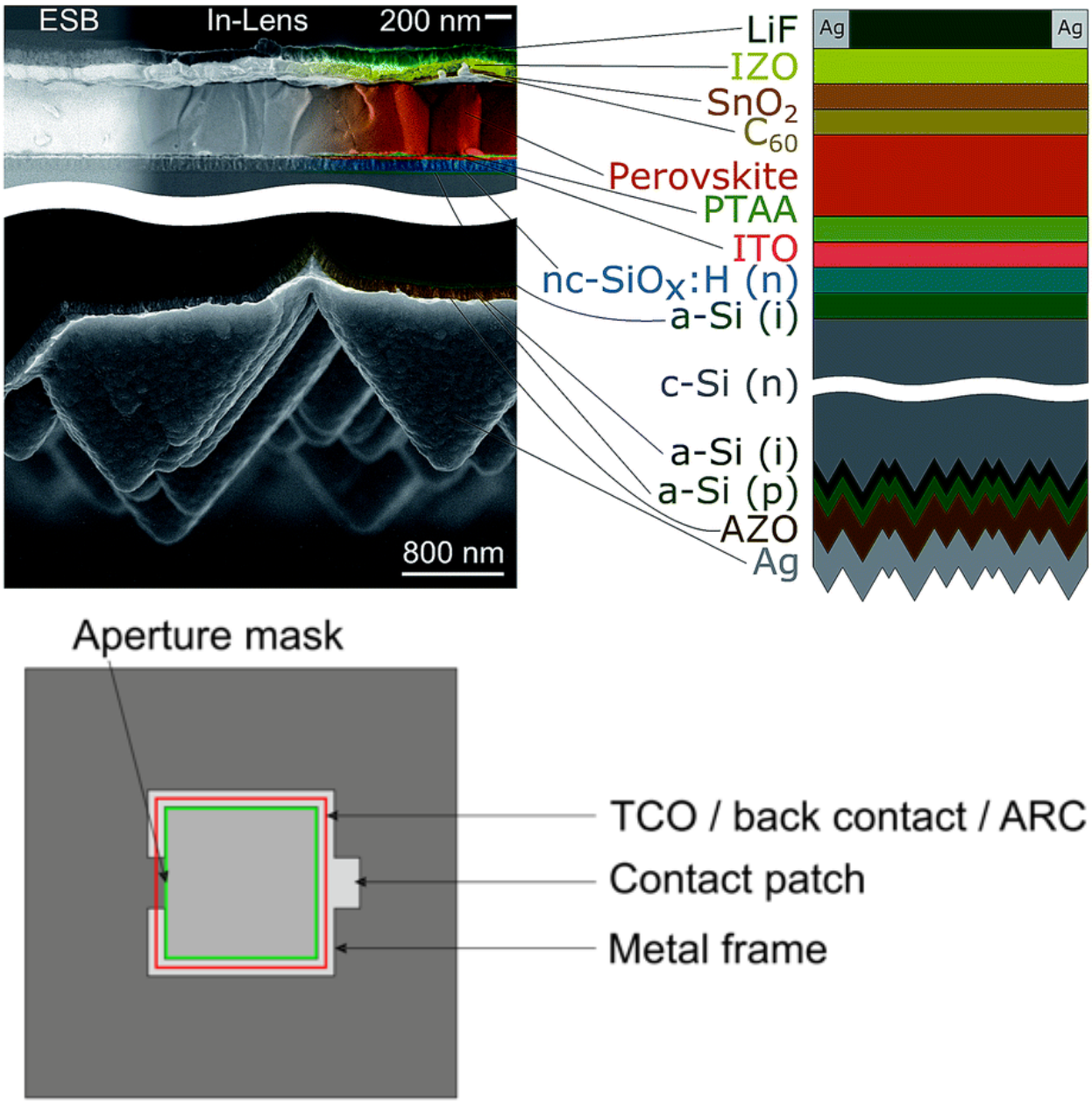

Figure 1.24: [**Top**][**Left**] Colored cross-sectional SEM image of the top cell (upper panel) and back side of the bottom cell (lower panel) of a typical monolithic tandem solar cell. The left side of the top cell is recorded with an energy selective backscattered (ESB) detector, the right side with an in-lens detector. Note that the scale bars in the top and bottom panels are different as indicated. [**Right**] Schematic device layout of the tandem architecture. [**Bottom**] Top view schematic design of the tandem solar cell [60].

1.6 Economics

As we master perovskite technology, it is important to understand which factors matter in its viability as a commercial product. We will focus on a key economic metric in the introduction of new generation technology in the world of cleantech and examine how perovskite solar cells fit in that paradigm. Additionally, we explore the market entry routes in Appendix B.

1.6.1 Levelized Cost of Electricity (LCOE)

The levelized cost of energy or electricity (LCOE) is a measure of the average net present cost of electricity generation for a generating plant over its lifetime. As such, it calculates the present value of the total cost of building and operating a power plant over an assumed lifetime. The LCOE allows for the comparison of different technologies of unequal life spans, project size, capital cost, risk, return, and capacities [62]. In short, it is an effective measure of the net cost of a given generating technology and a tool to fairly compare it to others. A simplified formula for LCOE is given by [63]:

$$LCOE = \frac{\sum_{t=1}^{n} \frac{I_t + M_t + F_t}{(1+d)^t}}{\sum_{t=1}^{n} \frac{E_t}{(1+d)^t}}$$

I_t is the investment expenditures (\$) in year t, M_t, the operations and maintenance (O&M) expenditures (\$) in year t, F_t, the financing expenditures (\$) in year t, E_t, the electricity generated (kWh) in year t , d, the discount rate, and n, the lifetime of the system (years). For a PV plant with a fixed solar array capacity, $E_t = P \times S \times (1 - L) \times (1 - r)^t$, where P is the rated power of the solar array, S is the annual solar isolation at the installed location, L is a constant loss factor for the array due to shading, soiling, DC connection, and AC conversion, and r is the system degradation rate [64]. The upfront investment for the initial installation (I_0) is the major cost component of a PV system. This initial cost includes the PV modules, inverters, other balance-of-system (BOS) equipment (*e.g.* racking, wiring, and tracking), installation labor, project overhead costs (*e.g.* permitting, environmental studies, and designing), grid interconnection, land fees, and taxes. The O&M cost includes an annual cost to maintain the normal operation of the system and the costs for repairing and replacing broken modules and inverters. The financial cost includes project debt interest, tax, insurance, incentives, and internal return of capital investment.

Li et al. performed a LCOE analysis on four different types of modules: traditional silicon cells, planar perovskite cells, silicon/perovskite tandem cells, and perovskite-perovskite tandem cells (See Figure 1.25) [65]. Their findings, summarized in Figure 1.26, show that, at equal lifetimes and efficiencies, any module containing perovskite is cheaper than the traditional silicon module. Song et al. further emphasize that point by analyzing the manufacturing of a hypothetical single junction perovskite module (See Figure 1.27) in Wichita, Kansas [64]. Figure 1.28 shows that for a ~ 15 years lifetime, the LCOE of a module of PCE $> 10\%$ would be lower than 10¢/kWh, the average price of electricity in the US in 2017.

These projections show that with decent lifetimes and efficiencies, perovskite solar modules can be disruptive in the solar generation market. Because of its cheaper manufacturing and materials cost, upstart businesses and industry staples have kept a keen eye on the progress of perovskites.

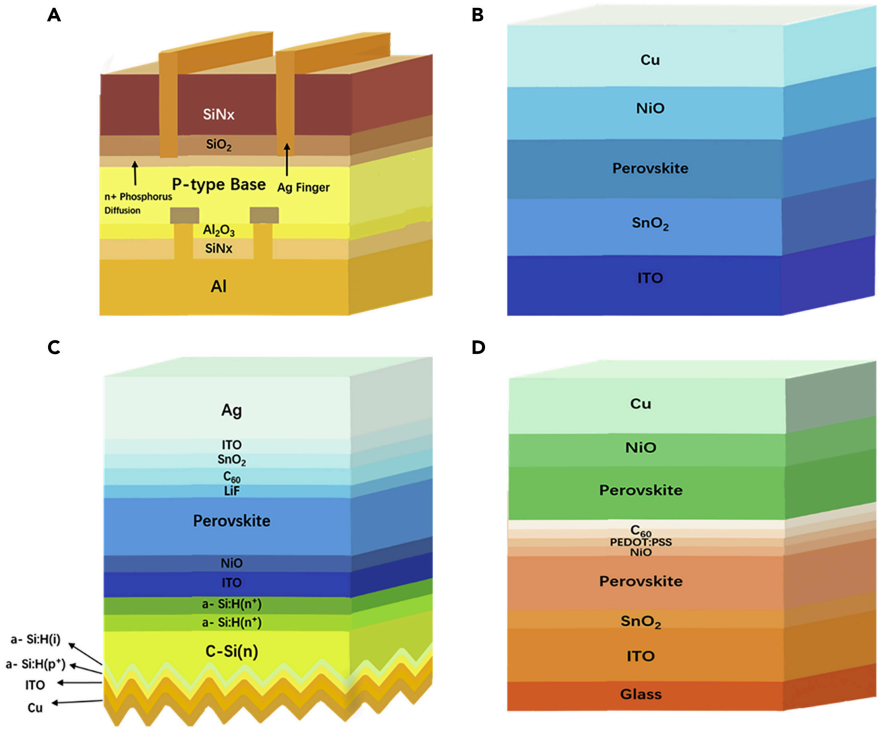

Figure 1.25: Module **A**: Traditional silicon cell; Module **B**: Planar perovskite; Module **C**: Silicon/perovskite tandem; Module **D**: Perovskite/perovskite tandem [65].

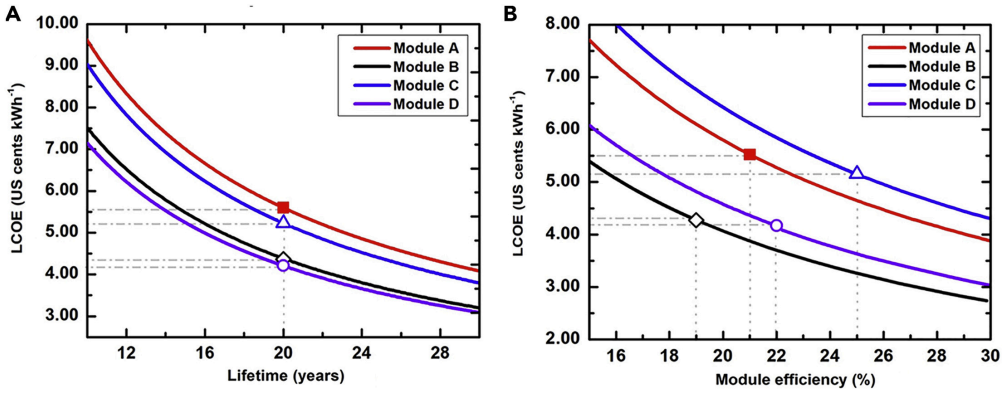

Figure 1.26: LCOE sensitivity analysis as functions of module (**A**) lifetime and (**B**) efficiency. The markers indicate the assumed conditions [65].

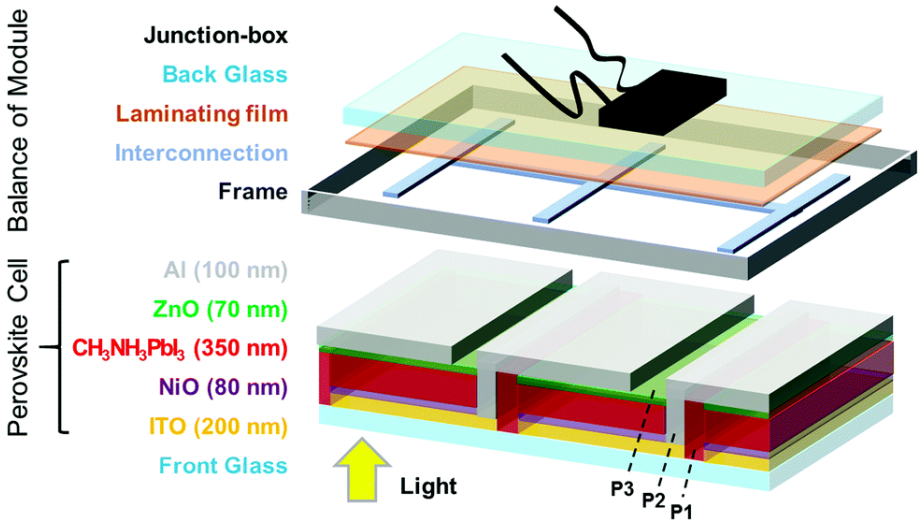

Figure 1.27: Structure of a monolithically integrated perovskite solar module. P1, P2 & P3 represent laser scribing processes to separate the transparent electrode, perovskite absorber, and metal contact, respectively, to form cells that can be integrated into a module [64].

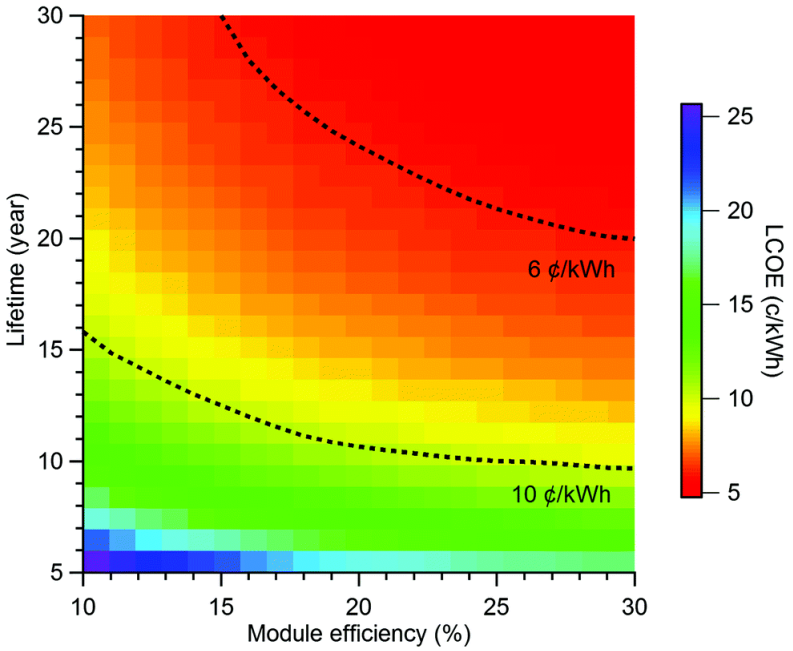

Figure 1.28: LCOE for perovskite PV module with different module efficiencies and lifetimes. The 6¢/kWh U.S. Sunshot goal [66] and 10¢/kWh average cost of electricity in the U.S. in 2017 are presented on the dotted curves [64].

1.7 Issues

1.7.1 Scalability

The state-of-the-art PCE for perovskite stands as 25.2% [26]. However, Park and Zhu remark in their review of scalability of perovskites that all record-efficiency devices have been achieved using substrates with active areas as small as 0.1 cm^2 [67]. For commercialization, it is necessary for large-scale (> 800 cm^2) modules to achieve such high PCEs. To date, most modules have had smaller areas and are often termed submodules (200-800 cm^2) or minimodules (< 200 cm^2) [68]. A PCE of 17.25% was certified in 2018 for a minimodule (seven series cells) manufactured by Microquanta with a designated illumination area of 17.277 cm^2 [68]. A lower PCE of 11.6% was also reported in 2018 by Toshiba for a submodule (44 series cells) with an area of 802 cm^2 [68]. The V_{OC} per cell was 1.07 V for both the minimodule and submodule, whereas a large difference in the J_{SC} per cell was found upon increasing the size, decreasing from 20.66 mA/cm^2 for the minimodule to 14.36 mA/cm^2 for the submodule. Increasing the J_{SC} with the device size is, therefore, a challenge. To overcome it, techniques, summarized in Table 1.6, need to be optimized to uniformly coat a large area with full coverage (no pinholes) and good crystallographic properties. An optimized blade coating process was shown to produce a 57.2 cm^2 module with PCE 14.6% [69]. Slot-die coating was used to produce a 149.5 cm^2 module with a PCE of 11.2% [70]. One of the most stable module structures was screen-printed over a 49 cm^2 area and achieving 10.4% PCE [71]. Beyond solution processing, a fully vapor-based scalable deposition method has been developed for preparing a 91.8 cm^2 module with a PCE $\sim 10\%$ [72]. These accomplishments in increasing module efficiency and size are impressive, yet there is still room for improvement. Park and Zhu project that perovskite module will reach a limit of $\sim 22\%$ at the 1 m^2 scale [67].

Method	Material	Largest Coating Area (cm^2)	PCE (%)	Refs
D-bar	$MAPbI_3$	20×20	~ 17	[73]
Blade	$MAPbI_3$	6×15	20.3 (14.8 for a 57.8 cm^2 module)	[69]
Slot Die	$MAPbI_3$	-	~ 12	[74]
Spray	$MAPbI_3$	7.5×7.5	16.4	[75]
Stamping	$MAPbI_3$	10×10	20	[76]
	$FAPbI_3$	10×10	18	[76]
Vacuum evaporation	$FAPbI_3$	8×8	14.2	[77]

Table 1.6: Summary of coating technologies for large-area perovskite films. Unless otherwise stated, the PCE values were measured for small-area cells using pieces of large-area coated perovskite films [67].

1.7.2 Toxicity

An important downside of perovskites in their current form is that they contain heavy metals – mainly lead. The PV community is very much aware of the toxicity issues associated with the Pb content of highly performing perovskite solar cells and of the strain this imposes on the public perception and acceptance of the technology [78]. The development of low-toxicity Pb-free materials is of course always preferred in the solar cell market if performance is not too compromised. Ideal Pb-free candidates as solar cell absorbers should have low toxicity, narrow direct band gaps, high optical-absorption coefficients, high mobilities, low exciton-binding energies, long charge carrier lifetimes, and good stability. There are several candidates, showcased in Figure 1.29 [79], that have attractive properties with Sn-based perovskites attracting the most attention. Indeed, the representative methylammonium tin iodide ($MASnI_3$), formamidinium tin iodide ($FASnI_3$), and cesium tin iodide ($CsSnI_3$) have direct band gaps of ~ 1.20, ~ 1.41, and ~ 1.3 eV [13], respectively, which are narrower than their Pb counterparts and closer to the detailed balance optimum [17]. After exposure to atmospheric conditions, the Sn-based perovskites degrade to Sn^{4+} becoming SnO_2, which is more environmentally friendly than the Pb by-products. A cursory look at the fundamental physical properties of Sn-based perovskites reveals a similarity to Pb-based ones [13], which would suggest that, at least in principle, these materials should be able to match the efficiencies of $APbI_3$ structures. First reports in 2013 showed a PCE of $\sim 6\%$ [80], whereas the latest reports, as of 2019, exhibited a PCE of 9.6% [81]. The Sn-based devices usually have high J_{SC}'s (up to $25 mA/cm^2$) because of their low band gaps, yet their average V_{OC} is ~ 0.5 V, which is much lower than the 1.1 V for Pb-based perovskites [80]. This is due to the self-oxidization process transforming Sn^{2+} into Sn^{4+}. The latter acts as a p-type dopant in the structure resulting in too high of a carrier concentration and very high photocarrier recombination.

Despite the metal content per square meter of solar panel being only a few hundred milligrams, the potential occupational and non-occupational exposure associated with the large-scale implementation of the Pb-based perovskites should be treated with caution. Indeed, upon moderate exposure to external stimuli such as humidity, oxygen, elevated temperature, or their combination, these perovskites tend to degrade into harmful compounds carrying heavy metals, which may readily leach into the environment as a result of the structural failure of a photovoltaic module [84]. Until a non-toxic and high performing perovskite compound is found and optimized, the safe deployment of this technology relies entirely on adopting precautionary measures against contamination at each stage of the device's life, from fabrication to disposal/recycling [85].

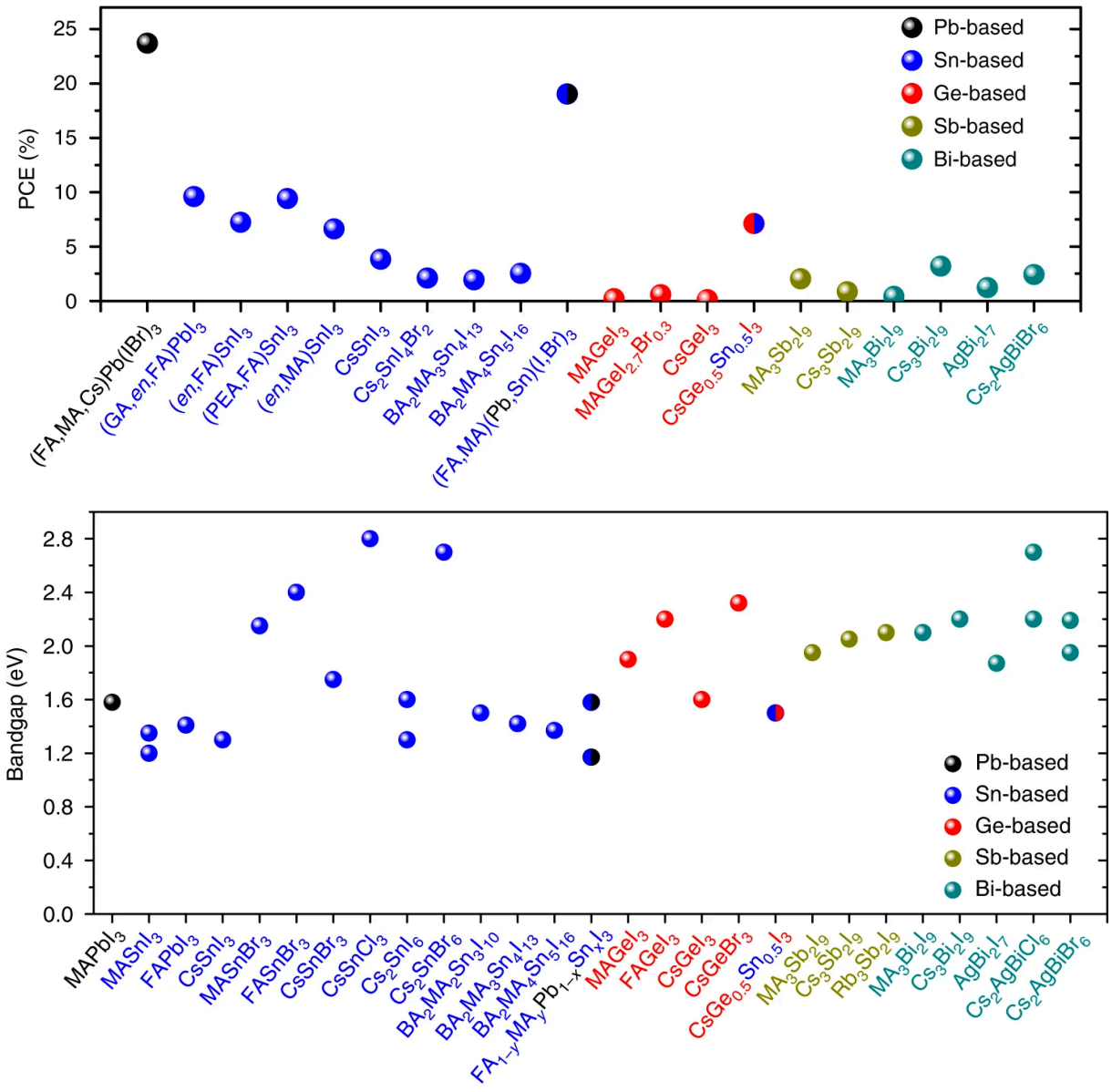

Figure 1.29: [**Top**] Record efficiencies of representative solar cells using Pb, Sn, Ge, Sb, and Bi-based perovskites [80, 81, 82, 83]. [**Bottom**] Band gaps of perovskites as potential solar cell materials. Suitable materials should have direct band gaps between 1.1 and 2.0 eV [79].

Figure 1.30 summarizes the risks associated to and controls for the processing of perovskite solar module over their lifetime with a focus on the fabrication, use and decommissioning portions given that the raw material extraction and synthesis of starting products follow well-established procedures [85]. In essence, it shows that the use of proper personal protective equipment (PPE) during fabrication and decommissioning minimizes the occupational hazards. It also shows that proper encapsulation with 100% reliability in the containment of degradation products from modules that lose their structural integrity during their useful life will ensure a safe deployment of perovskite solar modules.

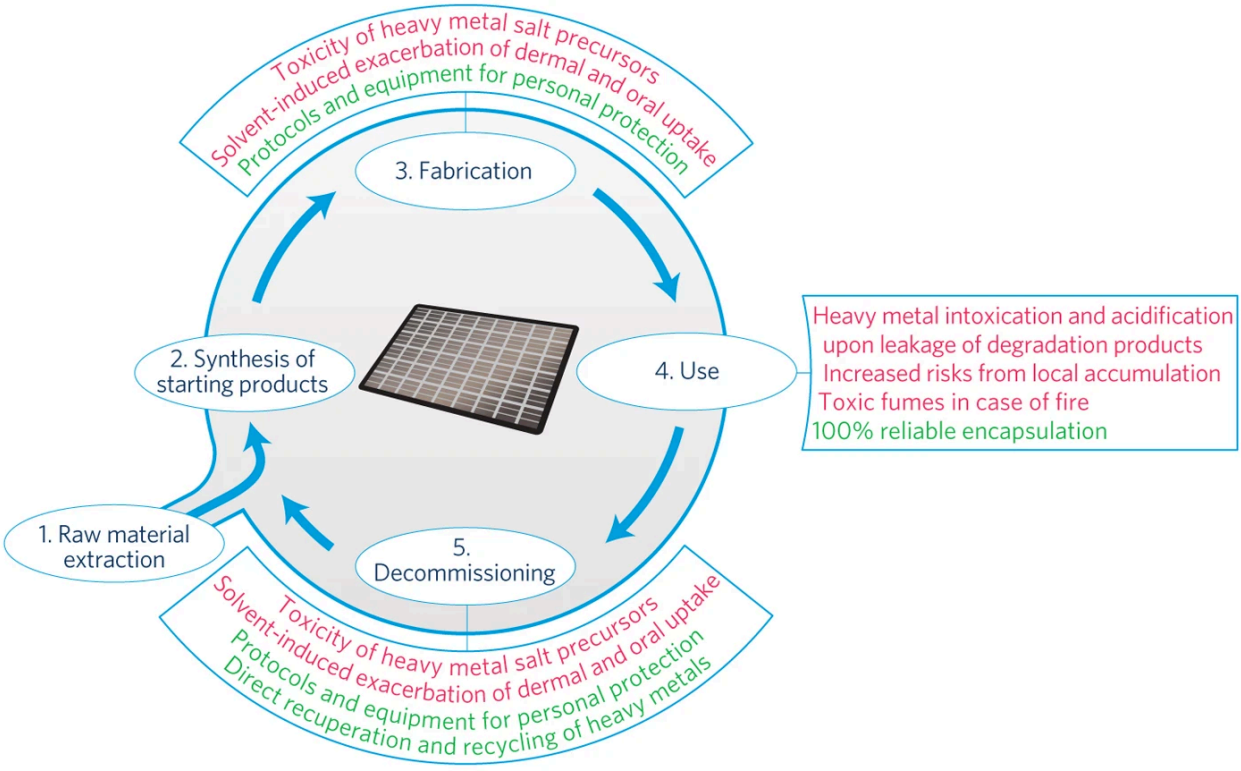

Figure 1.30: Concise schematic of the life cycle of perovskite solar cells, indicating the most important hazards (red) and strategies for their control (green). Safety protocols for phases one and two have already been established and are not described here [85].

1.7.3 Stability

The major remaining problem with perovskite solar cells is their instability under normal operating conditions, which is hampering their marketability [86, 87]. The economic analysis in Section 1.6 shows that we must guarantee high efficiency perovskites beyond 15 years at least, ideally between 20-25 years. The gold standard industrial test stipulates that solar devices should drop no more than 10% in PCE under a damp heat test (85°C, 85% RH) for 1000 h [88]. Perovskite solar cells are on their way to that milestone but not quite there yet. The sources of degradation (See Figure 1.31) are manifold but can be summarized in six categories: intrinsic properties, moisture, temperature, electric field, oxygen, and UV light [89]. $MAPbI_3$ is unstable because of the relative volatility of MAI, which evolves out of the film while heated, which is only exacerbated in contact with moisture and atmospheric air [13, 84]. $FAPbI_3$ perovskites have a narrower band gap than $MAPbI_3$ and show better thermal stability [18], but are structurally unstable because of the large size of the FA^+ cation. The trend has thus been towards mixed cations to improve both the thermal and structural stability of the perovskite. Table 1.7 recapitulates the performance of degrading perovskites in the literature. Unfortunately, few high efficiency cells have passed the aforementioned damp heat test [90]. Because the issues of degradation and stability is central to this work, we will take a deeper dive on the state of perovskite degradation research in the next chapter.

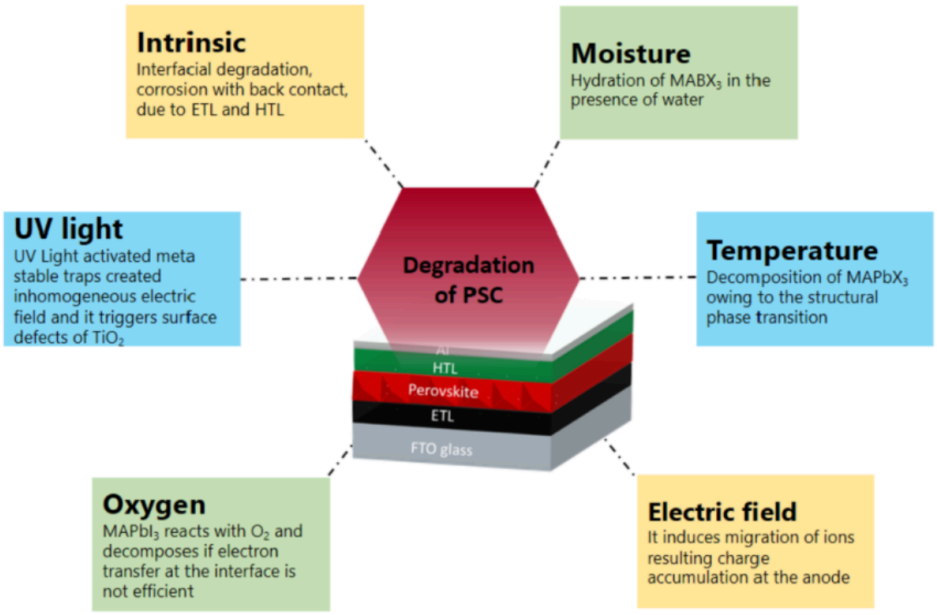

Figure 1.31: Summary of the degradation factors of perovskite solar cells [89].

Degradation Factor	Test Conditions	Device Configuration	PCE (%)	Loss in PCE (%)	Stability Period (hrs)	Refs
Humidity	Unsealed devices stored in the dark with $< 30\%$RH	FTO/TiO_2-Cl/$MAPbI_3$/ Spiro-OMeTAD/Au	21	4	2000	[91]
	Exposed to air at $\sim 55\%$RH	FTO/doped C_{60}/mixed perovskite/ Spiro-OMeTAD/Au	17.6	20	650	[92]
	Exposed to air at RH$\sim 55\%$	ITO/PEDOT:PSS/$MAPbI_3$/ PCBM/EFGnPs-F/Al	14.3	10	30 days	[93]
Illumination	Unencapsulated in N_2 at 25°C & UV	FTO/LBSO/$MAPbI_3$/PTAA/Au	21.2	< 10	120	[94]
		FTO/TiO_2/$MAPbI_3$/PTAA/Au	19.6	~ 50	120	
	Encapsulated in open air & UV	FTO/LBSO/$MAPbI_3$/NiO/Au	-	6.7	1000	
		FTO/TiO_2/$MAPbI_3$/NiO/Au	-	100	1000	
	N_2, white LED (1 Sun), 60°C	FTO/c-TiO_2/m-TiO_2/mixed perovskite/ Spiro-OMeTAD-SWCNT	15.0	20	580	[95]
Temperature	Sealed holder at 45°C	FTO/c-TiO_2/m-TiO_2/perovskite/ Spiro-OMeTAD/Au	14.6[a] 15.95[b]	40 > 50	300	[96]
	Sealed in ambient air, 55°C, 1 Sun	FTO/c-TiO_2/m-TiO_2/perovskite/ ZrO_2/Carbon	11.9[c] 10.10[d]	0 0	12,000	
Environment	N_2 at RT & constant light	FTO/c-TiO_2/m-TiO_2/Cs_5M/HTL/Au	21.2	< 10	250	
		FTO/c-TiO_2/m-TiO_2/Cs_0M/HTL/Au	-	80	250	
Illumination + Temperature	N_2 at high temp & constant light	ITO/c-TiO_2/m-TiO_2/perovskite/ PTAA/Au	20.6	10	160	[97]

Table 1.7: Summary of perovskite stability studies. [a]With 3% AVAI (5-Ammonium valeric acid iodide); [b]3D perovskite; [c]Module; [d]Cell [89].

1.8 Thesis Organization

This thesis uses a multivariate approach to the study of perovskite solar cell degradation to uncover relevant interaction factors and provide a mechanistic understanding of the underlying processes. This work seeks to fill a gap in knowledge that single factor studies alone cannot do by using the design of experiment (DOE) methodology. It provides a structured framework for varying multiple inputs to gain insights on their impact on the measured responses. The significance of factors and their interactions is revealed by a p-test, and the correlation between multiple responses can also be extracted. We use the DOE approach here to understand the connections between deep level traps and electrical, crystallographic, and optical characteristics.

In Chapter 2, we will survey the literature on perovskite solar cell degradation by first focusing on single factor studies, then multifactorial studies. When discussing single factor studies, we will explain the effects of four extrinsic factors (moisture, temperature, UV light, and oxygen) on perovskites and describe means to prevent them individually. The multifactorial studies discussion will be on the two published works known to date on perovskite degradation. The first studied the impact of operating conditions on the PCE, whereas the second screened intrinsic and extrinsic factors to optimize the device architecture for stability.

In Chapter 3, we will detail the DOE theory and methodology. We will describe its basic guidelines and explain the principles behind a factorial design. Then, we will explain how we employed that methodology to our work in the selection of factors to vary and the relevance of the responses tracked. We also present and discuss the results of the DOE in uncovering the relevance of interaction factors.

In Chapter 4, we will discuss how to track deep level trap in degrading perovskites. We will first describe their kinetics before describing how to measure them using various techniques including photo-induced conductivity transient spectroscopy (PICTS). We will also describe the evolution of deep level traps in our study and their nature.

In Chapter 5, we will engage in an informed analysis of the correlation between deep level traps and the electrical, crystallographic, and optical characteristics of the perovskites. We will provide a mechanistic explanation highlighting the underlying processes behind these connections.

Finally, in Chapter 6, we will summarize our findings by first highlighting the significant higher order interaction we've uncovered. Then, we will re-emphasize the importance of controlling deep level traps and pinning them deep within the band gap to improve the stability of the cells. Finally, we will provide new avenues to explore with this type of multifactorial framework.

Chapter 2

Survey of Degradation Studies

Extensive work is currently underway to solve the long-term stability problem for perovskite solar cells, their most pressing issue. As highlighted in Section 1.7.3, previous studies have allowed us to identify six principal degradation factors and their effects on the device. Subsequent studies have usually isolated and solved each of those problems individually by engineering new perovskites and/or encapsulating the whole device. Few studies treat the problem holistically. Henceforth, systematic investigations are sine qua non as they allow for an understanding of the interactions between degradation factors and trade-offs in the performance of the perovskite photovoltaics. In this chapter, we a fortiori seek to review two general categories of works: **single factor studies**, which focus on studying the effects of a unique extrinsic degradation factor at a time, and **multifactorial studies**, ones that use a systematic approach in analyzing multivariate degradation factors.

2.1 Single Factor Studies

2.1.1 Moisture

One of the main degradation pathways of perovskites is moisture induced. Indeed, it is a chemical process in which water is a catalyst to hydrolyze the perovskite due to its polar nature. The main by-products are PbI_2, CH_3NH_2I, and HI [89, 98, 99]. The decomposition reactions are described as follows:

$$CH_3NH_3PbI_3(s) \overset{H_2O}{\longleftrightarrow} PbI_2(s) + CH_3NH_3I(aq) \tag{2.1}$$

$$CH_3NH_3I(aq) \longleftrightarrow CH_3NH_2(aq) + HI(aq) \tag{2.2}$$

$$4HI(aq) + O_2(g) \longleftrightarrow 2I_2(s) + 2H_2O(l) \tag{2.3}$$

$$2HI(aq) \overset{h\nu}{\longleftrightarrow} H_2(g) + I_2(s) \tag{2.4}$$

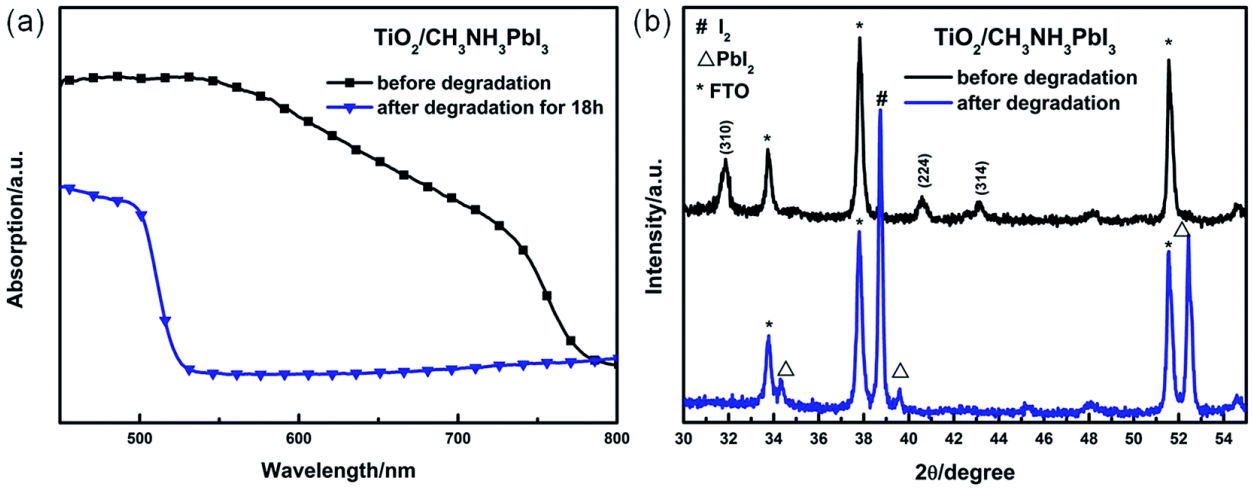

Figure 2.1: (**a**) UV-Vis absorption spectra of TiO_2/$MAPbI_3$ film before and after moisture degradation. (**b**) XRD patterns of TiO_2/$MAPbI_3$ films before and after moisture degradation [98].

It should be noted that oxygen and UV radiation are required for reactions 2.3 and 2.4. In fact, reaction 2.3 shows the degradation of HI via a redox reaction in the presence of oxygen, whereas reaction 2.4 highlights the decomposition of HI into H_2 and I_2 under UV radiation via a photochemical reaction. The consumption of HI, according to reactions 2.3 and 2.4, drives the degradation process forward. Because of the oxygen and moisture sensitivity of perovskites, most researchers elect to proceed with the fabrication process in an inert glove box. However, once assembled, $MAPbI_3$ solar cells brought to atmospheric conditions reportedly start to decompose at 55% RH, which is observable by a change in coloration from dark brown to bright yellow [100]. The passivation layer thus created inhibits the generation and transport of photocarriers, which reduces the ultimate PCE. The absorption of TiO_2/$MAPbI_3$ films between 530 nm and 800 nm greatly decreases after exposure to air at 35°C and 60% RH for 18h (See Figure 2.1**a**) [101]. XRD spectra of the same films reveal that the original peaks of $MAPbI_3$ all disappear post-exposure to moisture (See Figure 2.1**b**). The new peaks located at 34.3°, 39.5°, and 52.4° after degradation are attributed to the (102), (110), and (004) planes of hexagonal 2H polytype PbI_2, and another new peak at 38.7° is assigned to the (201) plane of orthorhombic I_2.

Frost et al. proposed a similar degradation pathway as the one described in reactions 2.1-2.4 for the decomposition of $MAPbI_3$ in presence of water from a simple acid-base reaction [99]. In Figure 2.2, a single water molecule (**a**) — a Lewis base — combines with $MAPbI_3$ and removes one proton from ammonium, leading to the formation of the intermediates $[(CH_3NH_3^+)_{n\text{-}1}(CH_3NH_2)PbI_3][H_3O^+]$. Then, the intermediates can decompose into HI (**b**), CH_3NH_2 (**c**), and finally into PbI_2 (**d**) by phase changes of hydrogen iodide (soluble in water) and methylammonium (volatile and soluble in water).

To improve the moisture stability, Noh et al. studied unencapsulated $MAPb(I_{1-x}Br_x)_3$ hybrid solar cells under ambient conditions with controlled humidity along the storage period

(See Figure 2.3) [100]. They found that all mixed halide perovskites were relatively stable during the first few days of the study at 35% RH. However, after a single day of exposure at 55% RH, the cells were stored back in a 35% RH environment, and their PCEs were re-measured. The subsequent measurements revealed that low Br-content perovskites degraded sharply, whereas the higher Br-content perovskites remained stable. They suggested that the substitution of larger I atoms with smaller Br atoms lead to the increase of the binding force between the organic and inorganic constituents, the decrease of the effective lattice constant, and the transition to a more compact and stable cubic phase.

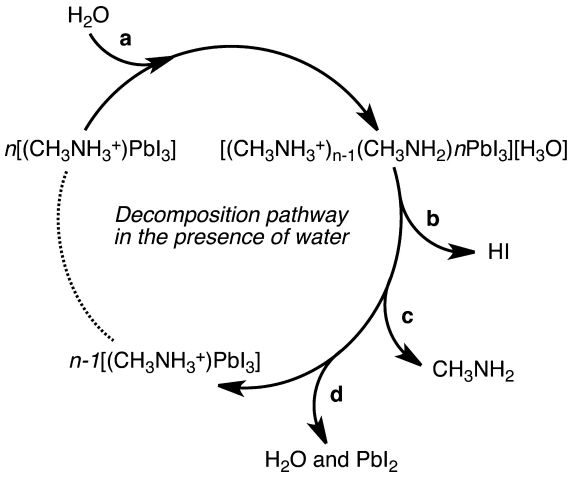

Figure 2.2: Possible decomposition pathway of perovskites in the presence of water [99].

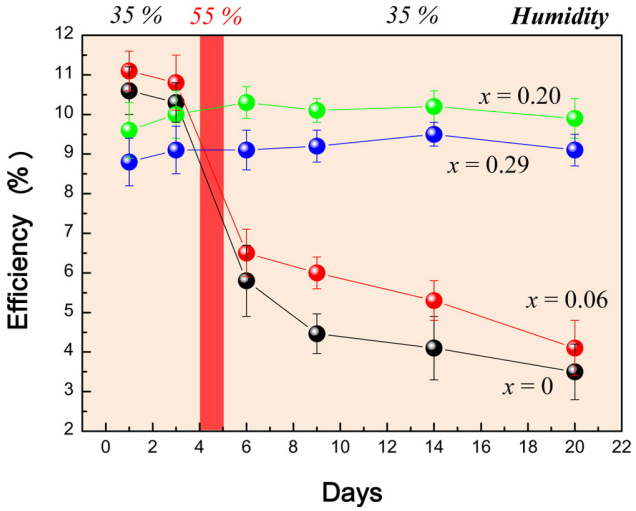

Figure 2.3: Stability of the PCE of $MAPb(I_{1-x}Br_x)_3$ with storage period in air, at room temperature, and without encapsulation. The humidity was maintained at 35% RH except for the fourth day when the cells were exposed to 55% RH [100].

2.1.2 Temperature

$MAPbI_3$ is highly sensitive to heat, as successive phase transitions occur from the lower temperature (T < 162.2 K) orthorhombic phase to the higher temperature (T > 327.4 K) ideal cubic phase, via the intermediate temperature (162.2-327.4 K) tetragonal phase [28]. Upon further temperature increase, the perovskite decomposes into the volatile CH_3NH_2 and HI compounds following this degradation reaction [89]:

$$CH_3NH_3PbI_3(s) \xrightarrow{Heat\uparrow} PbI_2(s) + CH_3NH_2(g) + HI(g) \tag{2.5}$$

Conings et al. sought to understand how temperature affects $MAPbI_3$ [84]. Hence, they spin-coated and annealed perovskite onto a glass/ITO/TiO_2 substrate, then degraded it for 24h at 85°C under three conditions: pure dry N_2, pure dry O_2, and ambient atmospheric air at 50% RH. The XRDs of each sample revealed the formation of PbI_2 and I_2 in only the $MAPbI_3$ degraded under ambient conditions (See Figure 2.5**a**). UV-Vis measurements also revealed that $MAPbI_3$ degraded in ambient conditions had the most significant loss in absorption (See Figure 2.5**b**). However, steady-state photoluminescence, measured at grazing incidence, thus more surface sensitive, showed a much reduced band gap luminescence, together with the emergence of a peak at 510 nm that signals the presence of PbI_2 (See Figure 2.5**c**). AFM and conductive AFM (c-AFM) topographs directly matched the presence of grains of PbI_2 and I_2 to a reduction in cross-sectional current, which magnitude was such that $I_{N_2} > I_{O_2} > I_{ambient}$ (See Figure 2.4). This shows that temperature degradation of perovskites is a process that starts at the surface before penetrating the bulk of the material and transforming it into its degradation by-products. The IV characteristics in Figure 2.6 show the detrimentality of high temperatures to the PCE of perovskites, dropping from $\sim 11\%$ for pristine cells to $\sim 3\%$ in ones degraded in ambient atmospheric air at 50% RH.

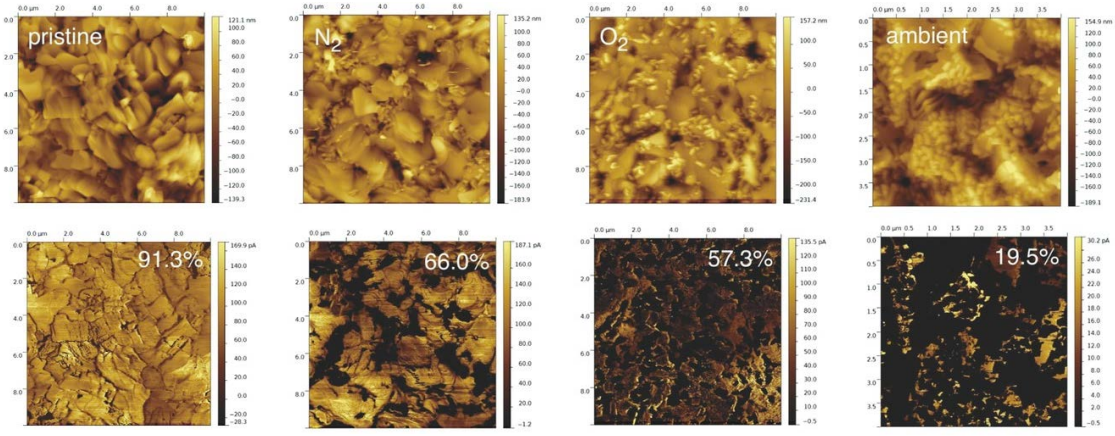

Figure 2.4: (**Top Row**) AFM and (**Bottom Row**) c-AFM images at V= 0.5 V of perovskite films subjected to 85°C for 24h in indicated atmospheres. The percentages on the c-AFM represent the fraction of the depicted area contributing to the measured current [84].

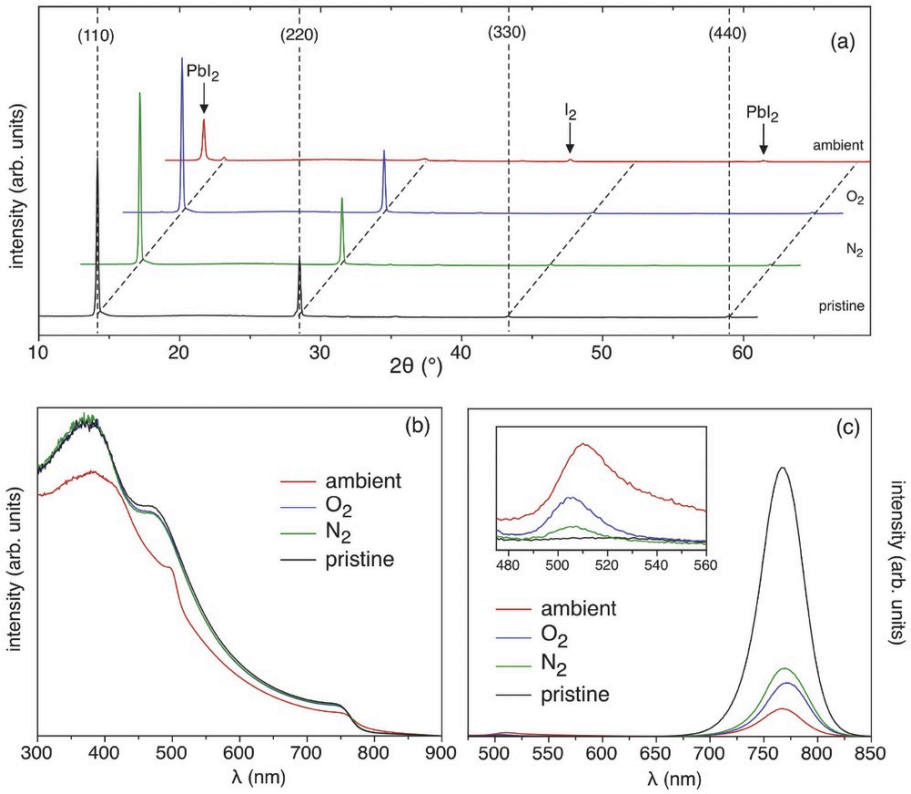

Figure 2.5: (**a**) XRD of ITO/TiO_2/perovskite samples that were subjected to 85°C for 24h in different atmospheres; Corresponding (**b**) absorption and (**c**) steady-state photoluminescence spectra (inset focuses on the wavelength range where PbI_2 is expected) [84].

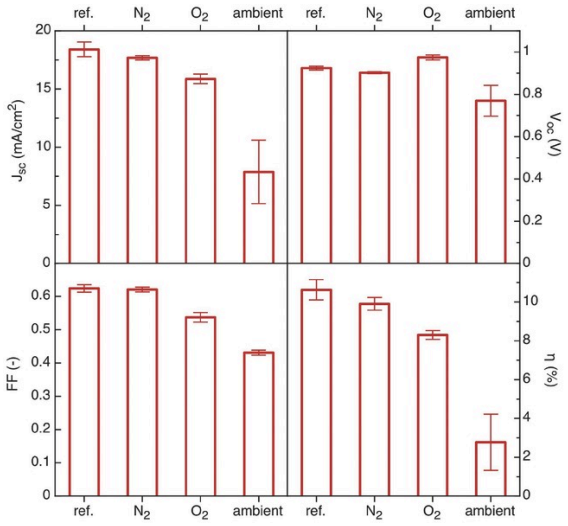

Figure 2.6: IV characteristics of solar cells prepared with perovskite layers that were subjected to a temperature of 85°C for 24h in different atmospheres. The error bars reflect the standard deviation for a batch of four solar cells [84].

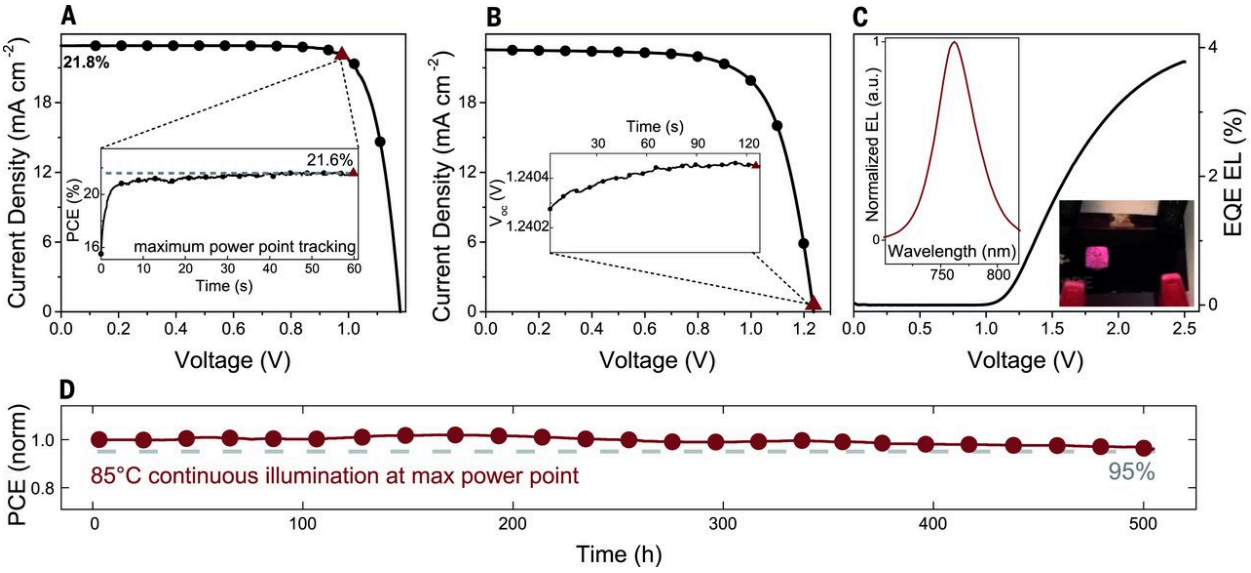

Figure 2.7: (**A**) J-V characteristics of the RbCsMAFA-based solar cell. The inset shows the scan rate-independent MPP tracking for 60 s. (**B**) J-V curve of the highest-V_{OC} device. The inset shows the V_{OC} over 120 s. (**C**) EQE electroluminescence (EL) as a function of voltage. The left inset shows the corresponding EL spectrum over wavelength. The right inset shows a perovskite solar cell. (**D**) Thermal stability test of a perovskite solar cell [102].

To improve the thermal stability, a focus has been on changing the A cation from the ABX_3 formulation of perovskites. Section 1.2.3 contains a discussion of cation selection. Saliba et al. proposed embedding the small and oxidation-stable rubidium cation Rb^+ into a "cation cascade" [102]. The RbCsMAFA mixture proved itself to have a combination of excellent electrical (PCE$\sim$ 22 %, $V_{OC}\sim$ 1.1 V) and optical properties (nonradiative recombination losses $>$ 1% at J_{SC}) as shown in Figure 2.7**A**-**C**. That cell was subsequently aged for 500 hours at 85°C under continous illumination with full intensity and maximum power point (MPP) tracking in a nitrogen atmosphere. The device retained 95% of its initial performance under those conditions (See Figure 2.7**D**).

2.1.3 UV Light

Perovskite solar cells are affected by UV light induced degradation especially at the junction between the electron transport layer (ETL) and the photoactive perovskite layer. TiO_2 is the material of choice for the ETL because of its high transparency and excellent electron transport properties. However, holes photogenerated in TiO_2 upon exposure to UV light react with the oxygen adsorbed at surface vacancies thereby acting as deep traps, leading to recombination [89]. This effect is especially pronounced in cells encapsulated from moisture and oxygen ingression [103]. Figure 2.8 shows this effect by comparing the degradation of variously encapsulated $MAPbI_3$ perovskite solar cells with TiO_2 ETL under 100 mW/cm^2

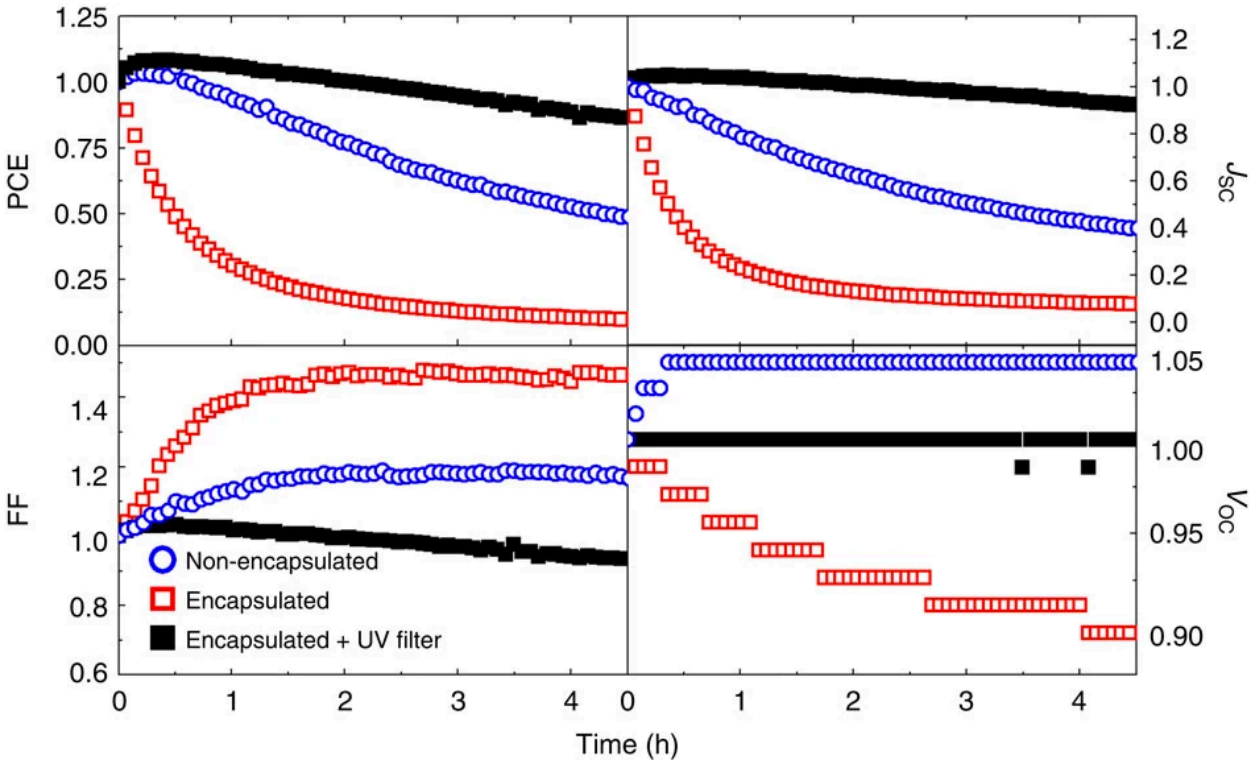

Figure 2.8: Evolution of the normalized solar cell performance parameters over 5h of AM1.5 100mW/cm^2 solar illumination for various encapsulation conditions [103].

simulated irradiance at 40°C. The possible decomposition reaction at the TiO_2/$MAPbI_3$ interface may be as [104]:

$$2I^- \longleftrightarrow I_2(s) + 2e^- \tag{2.6}$$

$$3CH_3NH_3^+ \longleftrightarrow 3CH_3NH_2(g) + 3H^+ \tag{2.7}$$

$$I^- + I_2(s) + 3H^+ + 2e^- \longleftrightarrow 3HI(g) \tag{2.8}$$

When UV light shines on the perovskite solar cells, TiO_2 gets excited and can extract electrons from I^-, resulting in I_2, which deconstructs the perovskite crystal (reaction 2.6). The electron extracted by the TiO_2 can return to its surface and allow reactions 2.7 and 2.8 to occur while emitting HI and CH_3NH_2. The loss of H^+ tends to shift reaction 2.8 to the right. To effectively prevent this degradation, Ito et al. deposited a Sb_2S_3 passivation layer between the TiO_2 and the perovskite layers [104].

2.1.4 Oxygen

The oxygen present in air is enough to turn $MAPbI_3$ perovskite from its pristine dark brown coloration to the photo-inactive bright yellow phase in just a few hours. Indeed, once the solar cell is exposed to air, oxygen molecules diffuse into the perovskite layer and get trapped into the iodine vacancies. Photogenerated electrons ionize the oxygen and produce highly reactive superoxide species. The latter attack the sample and extract H^+ from the photo-excited perovskite layer leading to the formation of PbI_2, H_2O, CH_3NH_2, and I_2. This efficient decomposition process of the perovskite layer is summarized in Figure 2.9 [105]. Aristidou et al. sought to improve the stability of the $MAPbI_3$ solar cell by inhibiting the superoxide formation at the iodide vacancies by defect passivation. Their investigation revealed that spin coating a solution of methylammonium iodide (MAI) onto the $MAPbI_3$ perovskite films filled the vacant iodide sites and extended the device's stability (See Figure 2.10) [105].

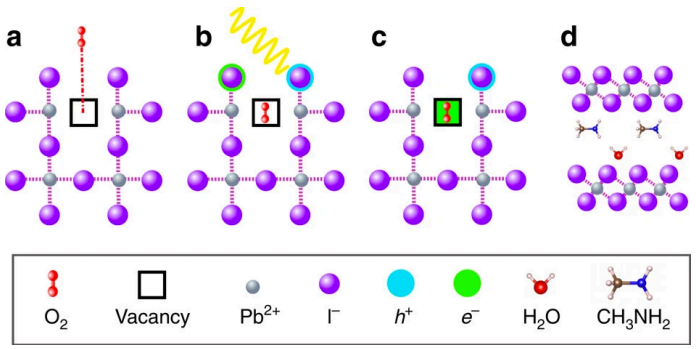

Figure 2.9: Schematic representation of the reaction steps of O_2 with $MAPbI_3$. (**a**) Oxygen diffusion and incorporation into the lattice, (**b**) photoexcitation of $MAPbI_3$ to create electrons and holes (**c**) superoxide formation from O_2, and (**d**) reaction and degradation into layered PbI_2, H_2O, I_2 and CH_3NH_2 [105].

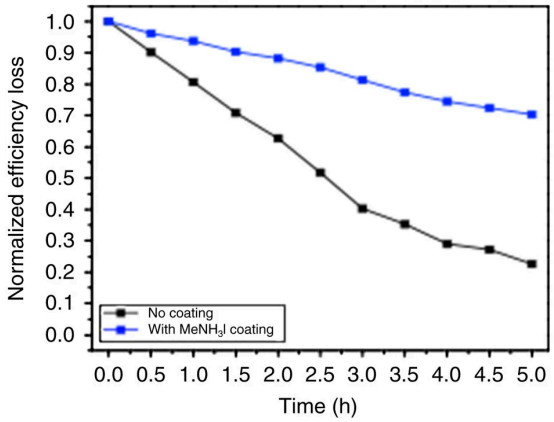

Figure 2.10: Normalized PCE loss for $MAPbI_3$ with/without a 10 mM treatment of MAI [105].

2.2 Multifactorial Studies

2.2.1 Systematic Analysis of the Operating Conditions' Impact on PCE

Understanding how primary extrinsic factors affect perovskite solar cells is an important step towards making them a viable product. Of greater value is the systematic understanding of their stability under operation, for it paints a realistic picture of the impact of multiple primary factors considered holistically. In 2018, Domanski et al. were the first to perform such an investigation and initiated a discussion on how to age perovskite solar cells and facilitate the development of consensus stability measurement protocols [106]. Their work focused on using state-of-the-art devices with a FTO/cp-TiO_2/mp-TiO_2/perovskite/Spiro-OMeTAD/Au architecture, where the perovskite is a Cs-containing 'triple cation.' All devices were used as fabricated and without any form of encapsulation. They started by comparing the illumination sources typically used in testing perovskite cells: UV-containing Xe light and UV-free white LED both calibrated to 1 sun power. Upon analysis, the degradation under either source was statistically indistinguishable, as the effect of UV light appeared to not be catastrophic for the degradation of the cells under inert conditions (See Figure 2.11). Consequently, they suggest using white LEDs to deconvolve the effects of UV. When focusing on atmospheric conditions, they show that illuminated cells exposed to oxygen and humidity sharply degrade unlike cells tested in inert nitrogen (See Figure 2.12). This observation shows that storage in dark, dry and inert conditions preserves the state of the cell, which is useful and practical information for experimentalists processing many cells.

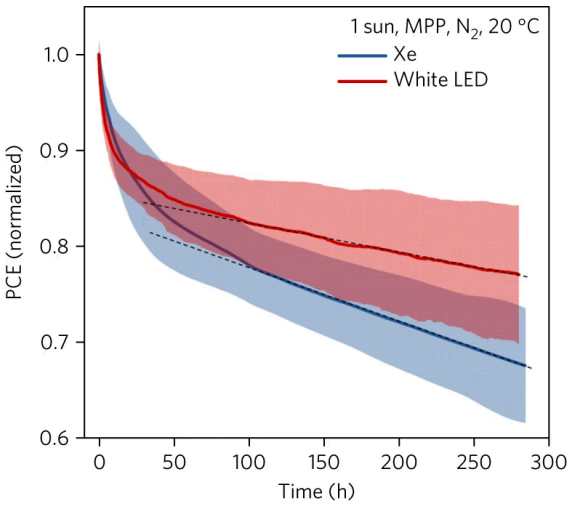

Figure 2.11: The effect of UV light on the stability of perovskites. Comparison of ageing 8 cells under an unfiltered Xe source and 13 under a UV-free white LED lamp. The values are normalized to the initial ones. The solid lines represent averages, while the shaded areas represent the standard deviations. The broken lines are guides to the eye [106].

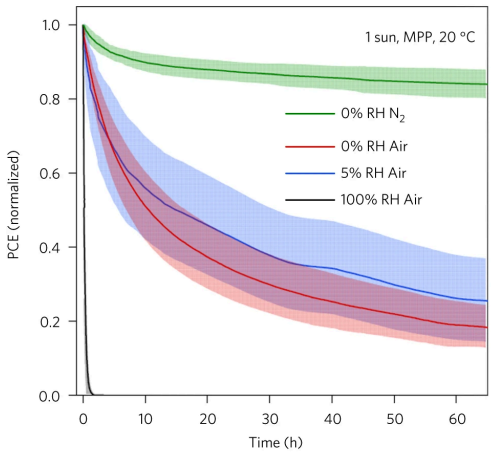

Figure 2.12: The effect of O_2 and H_2O on the stability of illuminated perovskites. Eight devices were aged under 5% and 100% RH air, six under 0% RH air, and thirteen under N_2. The values are normalized to the initial ones. The solid lines represent averages, while the shaded areas represent the standard deviations [106].

Domanski et al. also considered the effects of temperature on illuminated devices. They showed that lower temperature devices (-10°C to 20°C) exhibited an initial exponential decay in PCE followed by a slower linear decay that allowed the devices to remain operational. On the other hand, a cell maintained at higher temperature (65°C) degraded quickly and lost more than 80% of its initial PCE halfway through the degradation period. Temperature cycling between -10°C and 65°C performed on similar cells showed a slower degradation rate than at 65°C. This means that temperature shocks are not as deleterious as extended exposure to high temperatures (See Figure 2.13).

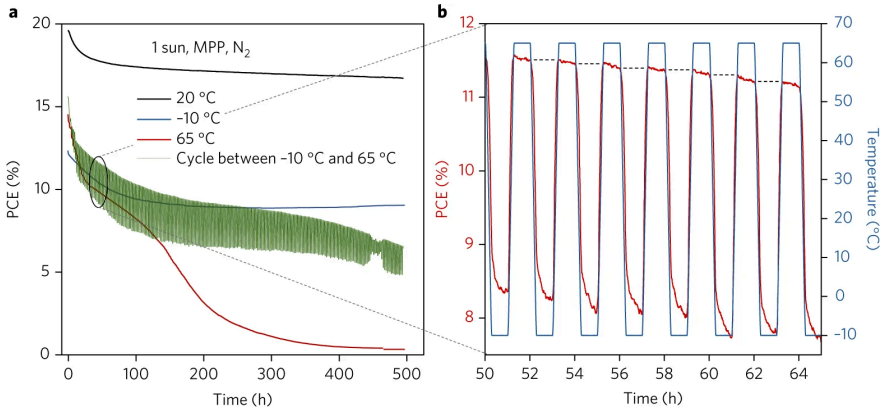

Figure 2.13: The effect of temperature on ageing. (**a**) The effects of temperature and temperature cycling (80 cycles) on the stability of illuminated perovskite solar cells. (**b**) A close-up of the trace of the temperature-cycled device [106].

To evaluate the role of electrical load on the degradation of perovskite solar cells, Domanski et al. aged a number of devices at open-circuit, short-circuit and maximum power point (MPP) conditions. They found that MPP tracking lead to a significantly slower decay than under open-circuit conditions (See Figure 2.14). At V_{OC}, the photogenerated carriers that are not extracted are possibly a source of degradation by accumulating radicals in the perovskite [107]. These results are important because they show that ageing without a load is very conservative and can be used as a worst case scenario, whereas the MPP tracking is a more realistic degradation scheme and can be used as a best case scenario for projections.

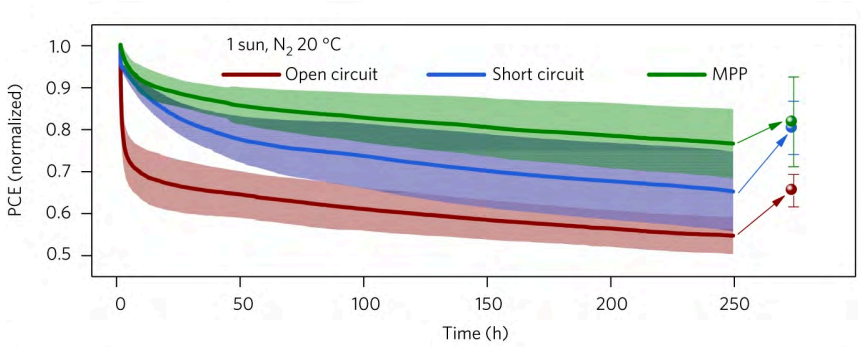

Figure 2.14: The effect of electrical load on PCE stability. The devices were held at the MPP, V_{OC} or J_{SC} during ageing period. The values are normalized to the initial ones. The solid lines represent averages, while the shaded areas represent the standard deviations. After 250h of ageing under illumination, the devices were stored in the dark for 24h before being re-measured [106].

Solar cells naturally undergo light cycling with the alternation of day and night, clear and cloudy skies, winter and summer. Figure 2.14 shows that storage in the dark for 24h helps recover some of the loss PCE after extended exposure to the elements. The effect on stability was more thoroughly evaluated by performing 23 light cycles and comparing the loss PCE to a cell under continuous illumination. No detrimental effect due to light cycling was observed (See Figure 2.15). The migration of cations is believed to induce this reversion in performance losses [108].

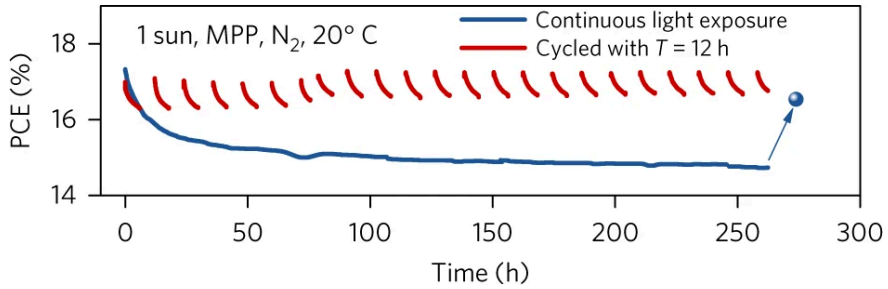

Figure 2.15: The effect of light cycling on ageing. One device was exposed to light continuously, while the other one was cycled with 6h light, 6h dark [106].

2.2.2 Screening Intrinsic and Extrinsic Factors

In 2019, Tyagi et al. examined 9 intrinsic and extrinsic degradation factors summarized in Table 2.1 [109]. Using the design of experiment (DOE) method, they undertook a multivariate analysis of perovskite solar cells' stability following the Plackett-Burman (PB) technique (more details on the DOE methodology will be provided in Chapter 3 as it is central to this work). This design allowed them to extract significant results from performing only 12 experiments as opposed to 512 that a full factorial run would require from a two-level design with 9 factors. Using transmission mode data of absorption measurements as the response for this screening experiment, they ranked the degradation factors by level of salience for two test cases: Time taken to reach 80% (T80%) of the original value (absorption of the perovskite layer) and 50% of the initial value (T50%). In this case, T80% is used as a proxy for the initial exponential decay, and T50%, for the slow linear degradation (See Figures 2.11-2.15). The rankings, shown in Figure 2.16, reveal that all but the halide choice, hole transport material (HTL), and UV were significant degradation factors for T80%, whereas all but the fabrication steps and electron transport layer (ETL) were significant for T50%. Using these results, Tyagi et al. built two devices representative of the best (Device A) and worst (Device B) architectures for long-term stability. Device A (NiO_x/$MAPbBr_2I$/$PC_{70}BM$/LiF/Ag) and Device B (PEDOT:PSS/$MAPbI_3$/$PC_{70}BM$/Ag) are compared in Figure 2.17 and confirm the results of the PB screening experiment.

	O_2	Humidity	UV Filter	T	Halide	HTL	ETL	Fabrication Step	Thickness
L	0%	< 5%	w/	45°C	$MAPbI_3$	PEDOT:PSS	w/o LiF	one-step	500 nm
H	20%	80%	w/o	65°C	$MAPbBr_2I$	NiOx	w/ LiF	two-step	280 nm

Table 2.1: Factors and levels used in the PB screening design [109].

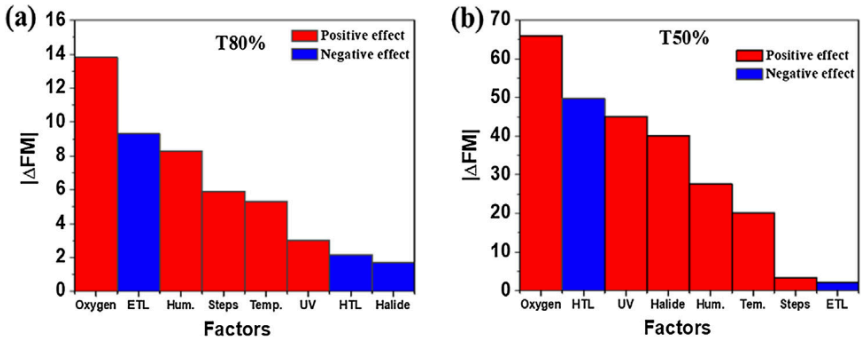

Figure 2.16: The absolute difference between the highest and lowest fitted means (|ΔFM|) showing the significance of factors for (**a**) T80% and (**b**) T50% values. A positive effect indicates that the 'L' level is preferred for higher stability [109].

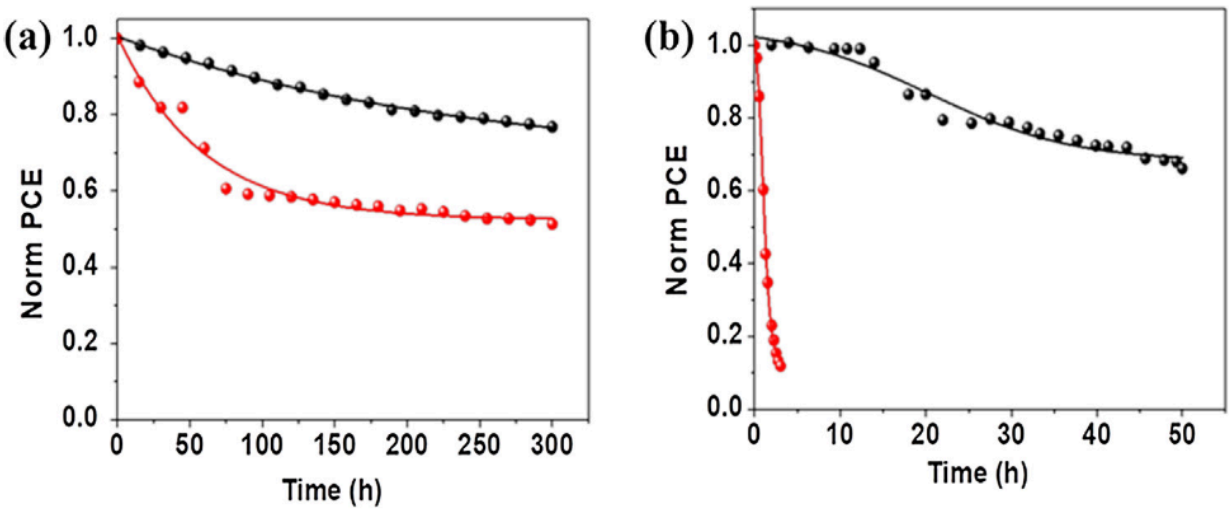

Figure 2.17: Normalized PCE as a function of time for Device A (black) and Device B (red) measured by (**a**) ISOS-D1 (stored in the dark and ambient temperature) and (**b**) ISOS-L2 (under continuous light exposure at 65°C) [109].

2.3 Summary

These multifactorial studies show the usefulness of a holistic approach to the investigation of degradation in perovskite solar cells. Indeed, they allow the ranking of various degradation factors by relevance and the significance of their confluence. Domanski et. al used the multifactorial approach to open a discussion in the perovskite solar cell community on how to appropriately carry out stability studies by using the most appropriate illumination, atmosphere, humidity, temperature, and electric load condition [106]. Tyagi et al. used DOE to optimize their device architecture for stability [109]. Moving forward, we use the multifactorial approach to uncover degradation mechanisms as they relate to deep level traps. We will discuss in detail the DOE methodology in the next chapter.

Chapter 3

Multifactorial Methodology with the Design of Experiments (DOE)

Observing a system is an integral part of understanding its inner workings. However, to fully grasp its dynamics, it is imperative to monitor its responses while methodically varying its inputs. Perovskite solar cells are no different, for they function as a system with tunable inputs and measurable outputs. The design of experiments (DOE) approach is well-suited at examining this type of multifactorial system. Hence, we will discuss in this chapter the principles of DOE in both the design and analysis of experiments and detail its application in the methodology of this work.

3.1 DOE Basic Guidelines

To use this statistical approach in designing and analyzing an experiment, it is important to have a clear vision of the problem to be studied, a method for data collection, and at least a qualitative understanding of the analysis. Table 3.1 summarizes the recommended procedure [110].

Steps	**Stages**
1. Recognition and statement of the problem	Pre-experimental
2. Selection of the response variable	Pre-experimental
3. Choice of factors, levels, and ranges	Pre-experimental
4. Choice of experimental design	Pre-experimental
5. Performing the experiment	Experimental
6. Statistical analysis of the data	Post-experimental
7. Conclusions and recommendations	Post-experimental

Table 3.1: Guidelines for designing experiments [110].

3.1.1 Recognition and Statement of the Problem

Though seemingly obvious, this step requires thoughtfulness because succinctly identifying the problem requiring experimentation is no easy task, neither is developing a clear and generally accepted statement of the problem. In a research lab, this is usually an ongoing conversation between the principal investigator(s) and lab researcher(s) based on literature reviews and/or prior experiments. In industry, it may require input from more stakeholders: engineering, quality assurance, manufacturing, marketing, management, customer, and operations. The problem tends to fit within one of these broad categories [110]:

- **Factor screening or characterization** for a new system or process to identify the most influential factors on the responses of interest;
- **Optimization** of a characterized system to extract the most desirable outcome from the most influential factors;
- **Confirmation** of the behavior of a characterized system to verify that its operation is consistent with theory or past experiments;
- **Discovery** of a novel system behavior from the addition of new factors or ranges of given factors;
- **Robustness** of a system to address questions of variability, stability or degradation of responses.

3.1.2 Selection of the Response Variable

Response variables should be rigorously chosen to accurately reflect the state of the system's features under study. Usually, the averages and standard deviations of the measured characteristics will serve as response variables. Well calibrated measurement systems ought to be used to carry out the experiments, and any known instrumental error should be factored in the measurement and analysis process. If the gauge of a measurement system is poor, each experimental unit should be measured several times and averaged for use as the observed response [110].

3.1.3 Choice of Factors, Levels, and Range

The factors influencing the performance of a system can be classified as either potential design factors or nuisance factors. The potential design factors are those that are intended to purposely vary during the experiment. Design factors, held-constant factors, and allowed-to-vary factors are some useful sub-categories. The design factors are the ones actually selected for the study. Held-constant factors are variables that may exert some effect on the response but are purposefully held constant, for they are not of interest in the study. Allowed-to-vary factors are the non-homogeneous supplies or materials that the design factors are applied

to. This batch-to-batch, unit-to-unit variability is often ignored because the randomization of samples tends to balance any significant effect it may have. Held-constant and allowed-to-vary factors are often assumed to be insignificant.

In contrast, nuisance or blocking factors may have a significant effect that must be accounted for, though they may not be the focus of the experiment designed. They are often classified as controllable, uncontrollable, or noise factors. A controllable nuisance factor is one whose levels may be set by the experimenter (time of experiment, days of the week, etc.). Should a nuisance factor be uncontrollable, yet measurable, an analysis of covariance can be used to compensate for it. On the other hand, when a factor can be minimized for the purposes of the study yet varies naturally and uncontrollably, it is called a noise factor.

Once the design factors are selected, their respective ranges must be thoughtfully chosen as well. Process knowledge is usually required for this and can be built from a combination of practical experience and theoretical understanding. Depending on the objectives of the experiment, few or many levels are chosen. In reality, the levels of given factors may be increased as knowledge of the system studied is furthered. A cause-and-effect or fishbone diagram illustrates the factors and responses of a system (See Figure 3.1) [110].

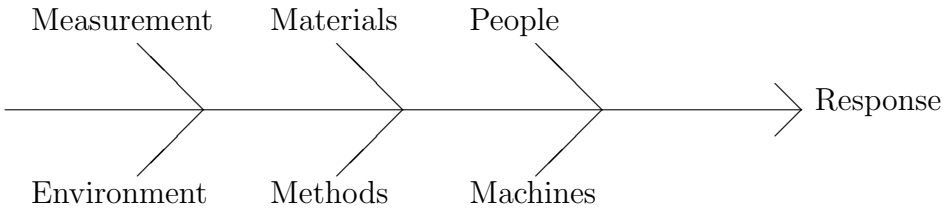

Figure 3.1: Sample fishbone diagram [110].

3.1.4 Choice of Experimental Design

Consideration is given to the sample size (number of replicates), the suitable run order for the experimental trials, and whether or not blocking or randomization restrictions are involved. Empirical models are also selected to describe the results. In many case, a first order or main effects model might suffice (See Equation 3.1). A common extension is to add an interaction term (See Equation 3.2). Depending on the objectives of the experiment and the number of factors at play, higher order interactions may be appropriate (See Equation 3.3).

$$y = \beta_0 + \beta_1 x_1 + \beta_2 x_2 + \epsilon \tag{3.1}$$

$$y = \beta_0 + \beta_1 x_1 + \beta_2 x_2 + \beta_{12} x_1 x_2 + \epsilon \tag{3.2}$$

$$y = \beta_0 + \beta_1 x_1 + \beta_2 x_2 + \beta_{12} x_1 x_2 + \beta_{11} x_1^2 + \beta_{22} x_2^2 + \epsilon \tag{3.3}$$

In these equations, y is the response, the x's are the design factors, the β's are unknown parameters to be estimated from the data in the experiment, and ϵ is the error term [110]. The choice of experimental design is usually aided by a software package like JMP [111].

3.1.5 Performing the Experiment

Properly planned experiments beget seamlessly run experiments. Attention must be given to following the experimental space designed and proper monitoring of the experimental process. Mistakes and errors could prove fatal in the analysis of the system.

3.1.6 Statistical Analysis of Data

Statistical analysis usually yields objective rather than subjective conclusions. Well-designed experiments do not require elaborate statistical analysis, and the empirical models from equations 3.1-3.3 are usually sufficient in describing the results. Residual analysis complements the models.

3.1.7 Conclusions and Recommendations

Once the data have been analyzed, practical conclusions can be drawn about the results, and recommendations for follow-up and/or confirmation studies can be made. Overall, the DOE process is iterative and strongly guided by well-designed experiments that allow to infirm or confirm various hypotheses about the system studied.

3.2 Factorial Design

3.2.1 Definitions and Principles

A factorial design is one in which, for each complete trial or replicate of the experiment, all possible combinations of the levels of the factors are investigated. In general, factorial designs are the most efficient for the study of the effects of two or more factors. For example, if there are a levels of factor A and b levels of factor B, each replicate contains all ab treatment combinations. When arranged in a factorial design, factors are often said to be crossed [110].

The effect of a factor is defined as the change in response produced by a change in the level of the factor. This is called the main effect, for it refers to the primary factors of interest in the experiment. The left of Figure 3.2 shows a simple two-factor factorial experiment with both design factors at two levels. The levels are coded as "low" and "high" and symbolized by "-" and "+," respectively. The main effect of factor A in this two-level design can be thought of as the difference between the average response at its low and high levels. Numerically, this is $A = (40 + 52)/2 - (20 + 30)/2 = 21$. So the main effect of factor A is +21, and +11 for B by using a similar approach. In some experiments, the difference in response between levels

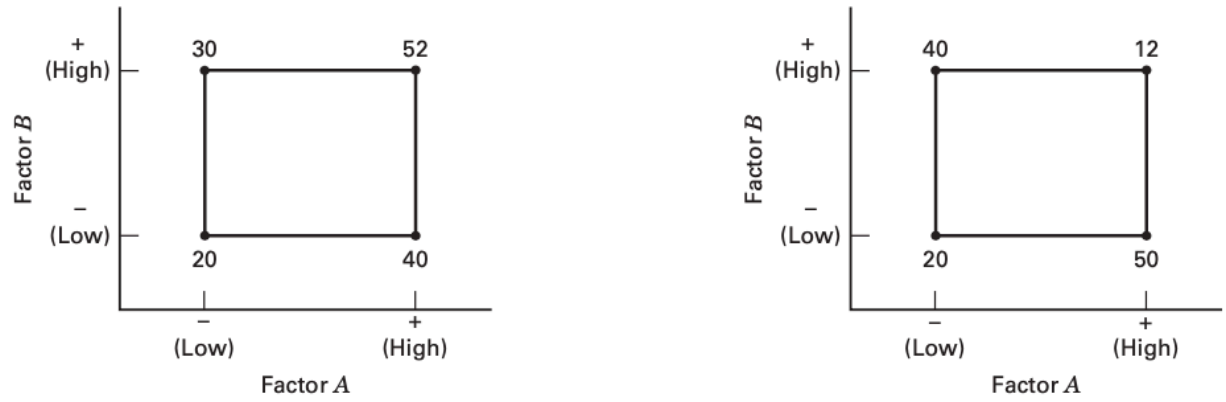

Figure 3.2: Two factor factorial experiment [**Left**] without and [**Right**] with interaction [110].

of one factor is not the same at all levels of the other factors. When this occurs, there is an interaction between the factors. On the right of Figure 3.2, the A effect is +30 and -28 at the low and high levels of B, respectively. Because the effect of A depends on the level chosen for factor B, there is an interaction between A and B. The magnitude of the interaction is the average difference in the two A effects, or $AB = (-28 - 30)/2 = -29$. Figure 3.3 shows a graphical illustration of these responses. The left plot shows non-intersecting lines, whereas the right one shows lines crossing — indicating the presence of an interaction [110].

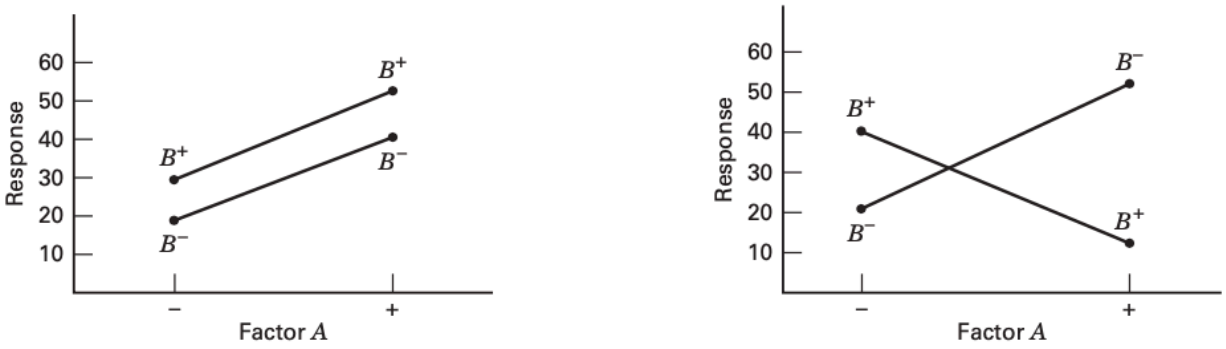

Figure 3.3: Factorial experiment responses [**Left**] without and [**Right**] with interaction [110].

A regression model akin to Equation 3.1 will be the basis for a quantitative representation of the responses. The β parameters are obtained via a least squares estimates. For an experiment with no interactions, the response surface plot will be a flat plane, and the contour plot will contain parallel lines (See Figure 3.4). However, if a significant interaction appears in the response model, then the response surface will be twisted, and the contour lines will be curved (See Figure 3.5). In some cases, the effect of the interaction between factors might be larger than the main effects themselves. Therefore, a significant interaction will often mask the significance of a main effect, which underlines the quintessence of multifactorial

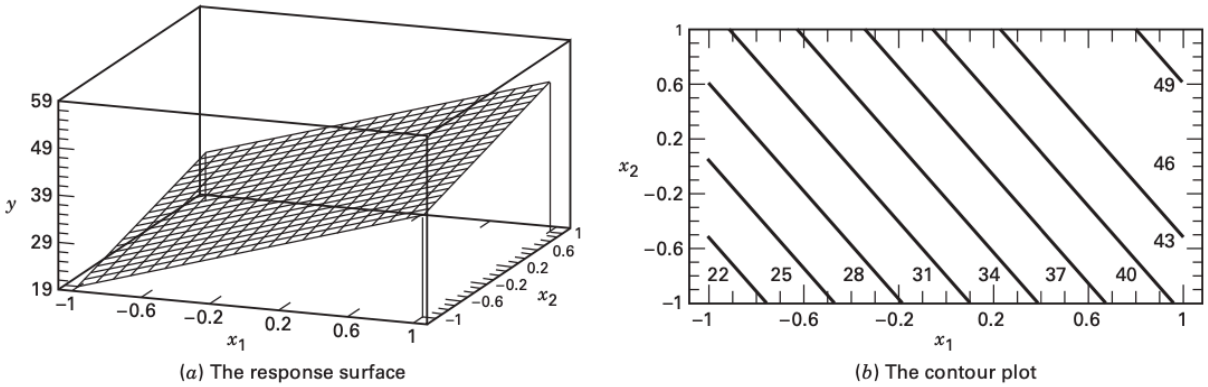

Figure 3.4: Response surface and contour plot for model $y = \beta_0 + \beta_1 x_1 + \beta_2 x_2 + \epsilon$ (without interaction) [110].

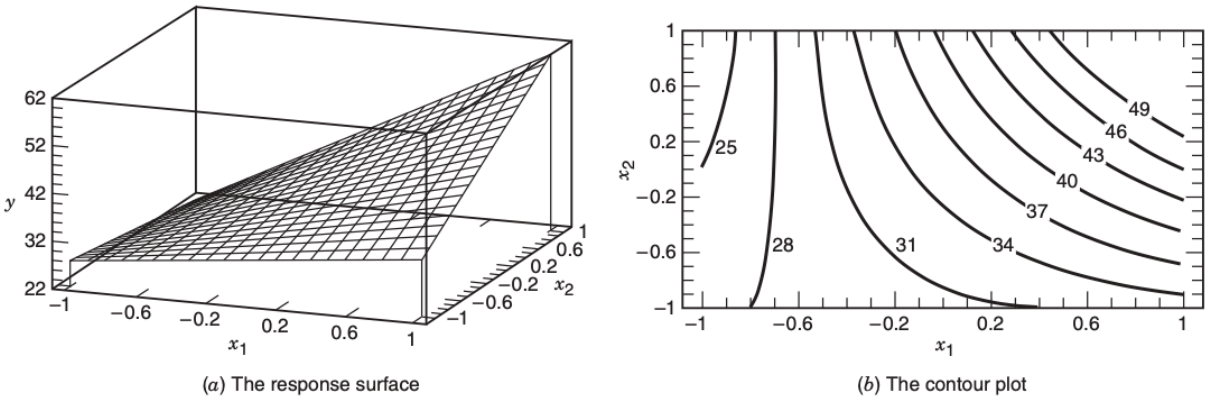

Figure 3.5: Response surface and contour plot for model $y = \beta_0 + \beta_1 x_1 + \beta_2 x_2 + \beta_{12} x_1 x_2 + \epsilon$ (with interaction) [110].

studies. Indeed, the DOE systematically evaluates the salience of interactions by examining the levels of one factor with the levels of the other factors fixed to draw conclusions [110].

3.2.2 Advantage of Factorials

The following example illustrates the advantage of factorial designs. Let A^-, A^+, B^-, and B^+ represent the levels of a two factor, two level experiment. Information on both factors could be obtained by varying the factors one at a time, as shown on the left of Figure 3.6. The effect of changing factor A is given by $A^+B^- - A^-B^-$, and the effect of changing factor B is given by $A^-B^+ - A^-B^-$. Because of experimental error, it is desirable to take replicates at each combination and estimate the effects of the factors using average responses. Thus, a total of six observations are required. Had a factorial experiment been performed, an additional combination, A^+B^+, would have been taken. Now, using just four observations,

two estimates of the A and B effects can be made, respectively. These two estimates of each main effect could be averaged to produce main effects that are just as precise as those from the single-factor experiment. Moreover, should an interaction be present, the one-factor-at-a-time design will fail to properly detect it. With only four total observations required, the factorial design is more efficient and accurate than the one-factor-at-a-time experiment and has a relative efficiency of $6/4 = 1.5$. Generally, this relative efficiency will increase as the number of factors increases (See right of Figure 3.6) [110].

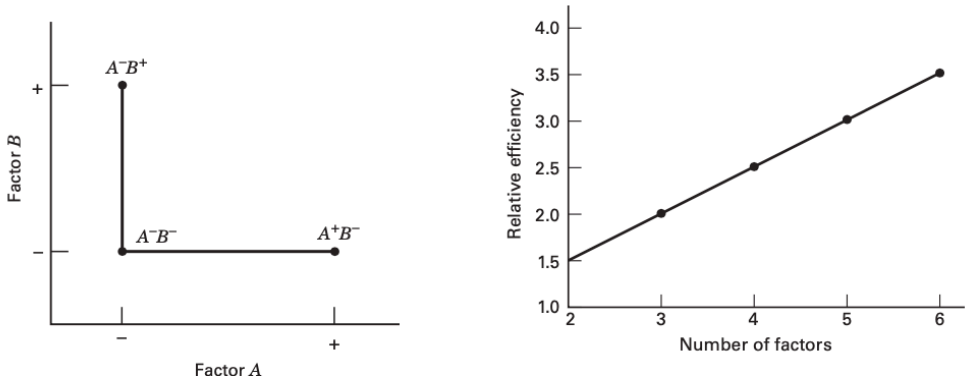

Figure 3.6: [**Left**] A one-factor-at-a-time experiment. [**Right**] Relative efficiency of a factorial design to a one-factor-at-a-time experiment (two-level factors) [110].

3.2.3 General 2^k Design

A 2^k factorial design is one with k factors, each at two levels. The statistical model for a 2^k design would include k main effects, $\binom{k}{2}$ two-factor interactions, $\binom{k}{3}$ three-factor interactions,..., and one k-factor interaction. Thus, the complete model would contain 2^k-1 effects for a 2^k design. The general approach to the statistical analysis of the 2^k design is summarized in Table 3.2. The process is highly iterative, and the advent of software packages like JMP has eased the speed and ease at which it is completed.

Steps
1. Estimate factor effects
2. Form initial model
3. Perform statistical testing
4. Refine model
5. Analyze residuals
6. Interpret results

Table 3.2: Analysis procedure for a 2^k design [110].

The first step is to estimate factor effects and examine their signs and magnitudes to get a preliminary sense of which factors and interactions are significant. Then, in forming the initial model for the experiment, a full factorial design is commonly chosen to get all of the main effects and interactions. In step 3, the significance of the latter is formally tested with an analysis of the variance. Refining the model in step 4 often consists of discarding any non-significant variables from the full model. Step 5 checks for the model's adequacy and assumptions in analyzing the residuals. The final step is to graphically and numerically represent the results and draw conclusions.

For even a moderate number of factors, the total number of runs in a 2^k factorial design is large — 32 for 2^5 design, 64 for 2^6, and so on. For convenience, a single replicate of the design is completed, which engenders the risk of fitting the model to noise. Indeed, if the response is highly variable, misleading conclusions may result from the experiment, should the levels be too close to one another (See Figure 3.7**a**). To ensure reliability, increasing the distance between the low and high factor levels is desirable (See Figure 3.7**b**).

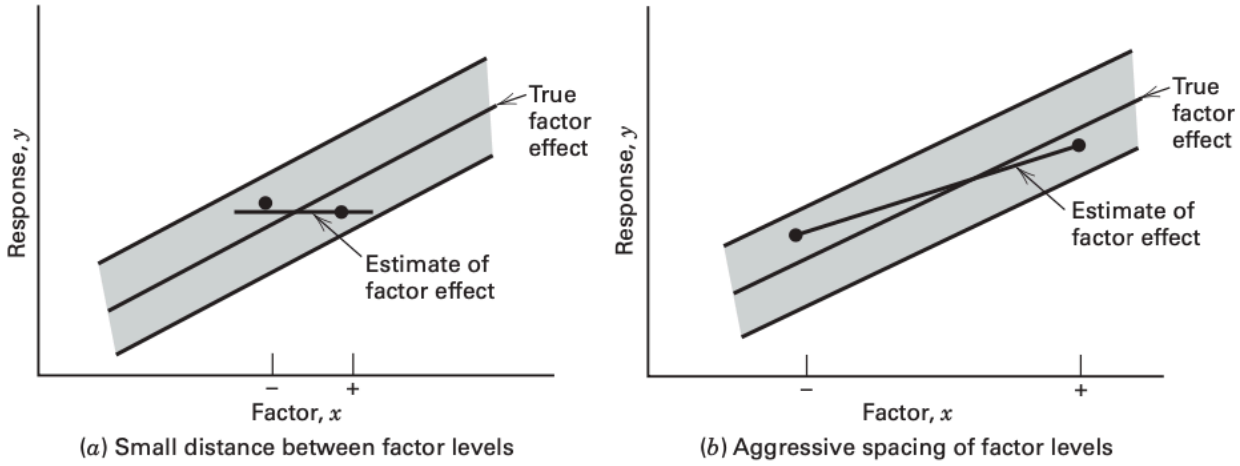

Figure 3.7: The impact of choice of factor levels in a design with a single replicate [110].

With only one replicate, there is no internal estimate of error. A normal probability plot of the estimates of the effects overcomes that problem [112]. The effects that are negligible are normally distributed, with mean zero and variance σ^2 and will tend to fall along a straight line on this plot, whereas significant effects will have nonzero means and will not lie along the straight line (See Figure 3.8**a**). Thus, the preliminary model will be specified to contain those effects that are apparently nonzero, based on the normal probability plot. The apparently negligible effects are combined as an estimate of error. It is important to note the drawbacks of normal probability plots. Indeed, should none of the effects be large enough, the plot may be ambiguous and hard to interpret. Should there be too few effects, the plot may also be of little help. To overcome this weakness, a half-normal plot, one of the absolute value of the effect estimates against their cumulative normal probabilities, can be employed. The straight line on the plot always passes through the origin and should also

pass close through the 50^{th} percentile data value (See Figure 3.8**b**). The half-normal plot is particularly effective when there only a few effect estimates.

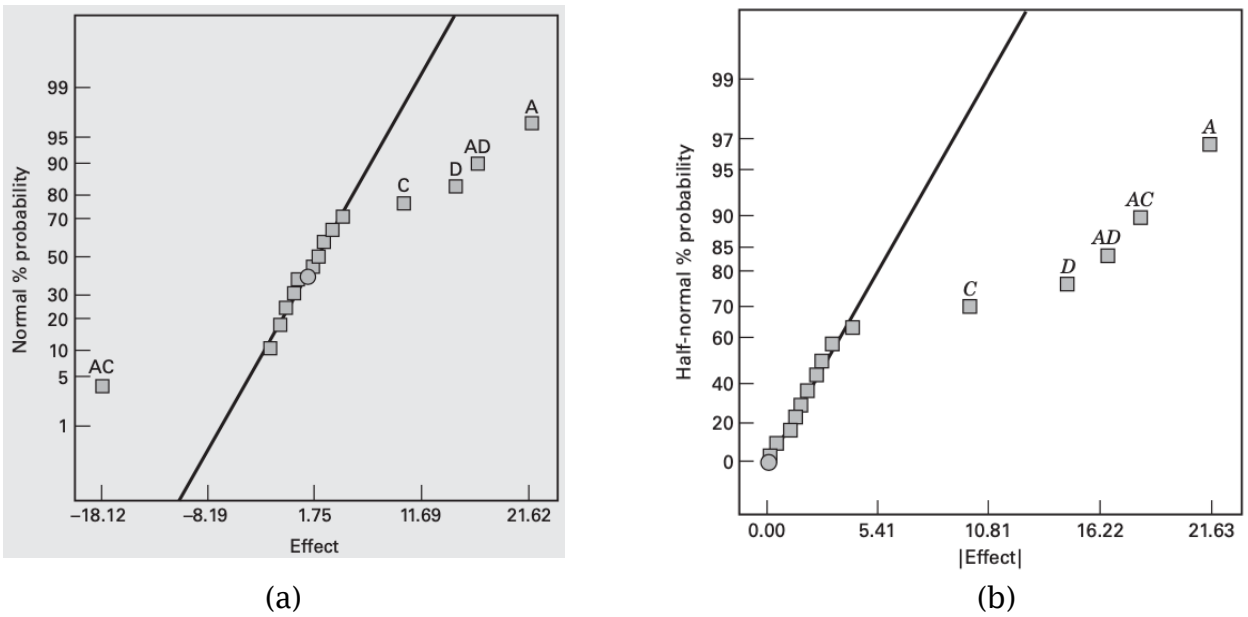

Figure 3.8: (**a**) Normal probability plot (**b**) Half-normal probability plot [110].

To complement the normal and half-normal probability plots and overcome their subjectivity, softwares like JMP use formal analysis procedures like Lenth's method, described next [113]. Suppose that there are m contrasts c_j of interest. If the design is an unreplicated 2^k factorial design, these contrasts correspond to the $m = 2^k - 1$ factor effect estimates. The basis of Lenth's method is to estimate the variance of a contrast from the smallest (in absolute value) contrast estimates. Let

$$s_0 = 1.5 \times median(|c_j|)$$

and

$$PSE = 1.5 \times median(|c_j| : |c_j| < 2.5s_0)$$

PSE is called the "pseudostandard error," and Lenth shows that it is a reasonable estimator of the contrast variance when there are only a few significant effects. The *PSE* is used to judge the significance of contrasts. An individual contrast can be compared to the margin of error

$$ME = t_{0.975,d} \times PSE$$

where $t_{0.975,d}$ is the 0.975th quantile of a t distribution on d degrees of freedom, defined as $d = m/3$. For inference on a group of contrasts, Lenth suggests using the simultaneous margin of error

$$SME = t_{\gamma,d} \times PSE$$

where the quantile of the t distribution used is $\gamma = (1 + 0.95^{1/m})/2$.

In JMP's implementation of Lenth's method, P-values for each factor and interaction are computed from a "real-time" simulation. It assumes that none of the factors in the experiment are significant and calculates the observed value of the Lenth statistic 10,000 times for this null model. Then, P-values are obtained by determining where the observed Lenth statistics fall relative to the tails of these simulation-based reference distributions. These P-values can be used as guidance in selecting factors for the model [110].

3.3 Studying Perovskite Degradation with a DOE Approach

This work's methodology is based on a 2^k factorial design from the design and analysis of experiments approach. Using the guidelines from Table 3.1, we detail steps 1 to 5 of our experimental procedure next, and discuss steps 6 & 7 in Chapters 5 and 6, respectively.

3.3.1 The Problem

In this work, we seek to provide a mechanistic understanding of the degradation of perovskite solar cells in operation by focusing on methylammonium lead triiodide ($CH_3NH_3PbI_3$ or $MAPbI_3$) and tracking over time its crystallographic (XRD), optical (UV-Vis), and electrical (IV) characteristics under various electrical load and temperature conditions. For the electrical characteristics, we do not limit ourselves to the typical current-voltage curves as we also record electronic defects via Photo-Induced Current Transient Spectroscopy (PICTS). Using these techniques, we seek to establish clear trends on the evolution of defects over a given degradation period, how they relate to other responses, and their significance in building a stability model.

3.3.2 Response Variables

There are four types of response variables we are tracking in this study:

- **Electrical/Photovoltaic Characteristics**: These are the four figures of merit that are extracted from a current-voltage curve of an illuminated solar cell under 1 sun irradiation. Explicitly, they are the short-circuit current (J_{SC}), the open-circuit voltage (V_{OC}), the fill factor (FF), and the power conversion efficiency (PCE). These metrics were chosen because they give a general representation of the state and performance of the solar cell at any given time, as explained in Appendix A.
- **Optical Characteristics**: We tracked two metrics here from a UV-vis absorption spectrum. Namely, the absorbance at 550 nm (A550) as a proxy for the general light absorption of the perovskite solar cell, and the absorption band edge (E_g) as a proxy for tracking any major change in band gap. A550 was chosen because it showed the most sensitivity to varying degradation conditions.

- **Crystallographic Characteristics**: The crystallite size (L) and microstrain ($\mu\epsilon$) are the two metrics we extracted from the XRD spectra, using Scherrer's equations [114], to evaluate changes in the crystal structure of the perovskite solar cells.
- **Electronic Defects**: Using PICTS, we followed the evolution of deep states in the perovskite solar cells. Specifically, we measured the traps' activation energy (E_a) and capture cross-section (σ_a). Deep level traps will be further discussed in Chapter 4.

3.3.3 Degradation Factors, Levels and Ranges

We have only considered the effects of temperature and electric load on perovskite over a determined degradation period. For the temperature, we have chosen two levels, 25°C and 55°C, that respectively represent room temperature and roughly the highest ambient temperature recorded on earth [115]. For the electric load conditions, we also chose two levels, open-circuit (OC) and maximum power point (MPP), as they represent the most and least conservative degradation scenarios, as discussed in Section 2.2.1. Exposure duration was the last factor, and the 5 periods chosen (0, 15, 45, 105, and 225min) captured the full degradation of unencapsulated $MAPbI_3$, as determined in our prior work [116].

3.3.4 Experimental Design

We chose an unreplicated $2^2 \times 5$ full factorial design and summarized it in Table 3.3.

	Factors			**Responses**									
	2 Levels		5 Levels	Photovoltaic				Crystal		Absorption		Traps	
Exp #	Temp.(°C)	Load	Time(min)	V_{OC}(V)	J_{SC}(mA/cm^2)	FF	PCE(%)	L(nm)	$\mu\epsilon$	A550	E_g(eV)	E_a(eV)	σ_a(cm^2)
1	25	OC	0	0.87	-20.58	0.48	8.58	48.16	0.19	1.74	1.58	0.96	5.9E-12
2	25	OC	15	0.85	-18.65	0.35	5.61	50.56	0.18	1.92	1.58	0.73	2.3E-14
3	25	OC	45	0.82	-23.27	0.44	8.47	39.86	0.22	2.45	1.58	0.75	1.4E-12
4	25	OC	105	0.74	-14.99	0.30	3.35	49.50	0.23	1.93	1.59	0.60	2.2E-16
5	25	OC	225	0.69	-2.56	0.21	0.36	57.35	0.18	1.66	1.59	0.70	2.2E-12
6	25	MPP	0	0.80	-18.04	0.35	5.04	40.37	0.21	1.54	1.59	0.95	4.3E-09
7	25	MPP	15	-	-	-	-	-	-	-	-	-	-
8	25	MPP	45	0.91	-22.87	0.44	9.21	49.79	0.19	2.18	1.58	0.80	5.0E-11
9	25	MPP	105	0.77	-7.62	0.30	1.74	90.58	0.14	1.82	1.59	0.75	1.9E-09
10	25	MPP	225	0.64	-2.50	0.26	0.40	57.56	0.16	1.58	1.59	0.58	8.0E-16
11	55	OC	0	0.87	-20.58	0.48	8.58	48.16	0.19	1.74	1.58	0.96	5.9E-12
12	55	OC	15	0.76	-8.78	0.36	2.26	57.94	0.14	2.68	1.58	0.78	1.6E-07
13	55	OC	45	0.76	-17.05	0.26	3.34	49.16	0.19	1.69	1.59	0.72	3.7E-13
14	55	OC	105	0.39	-7.46	0.38	1.09	87.44	0.15	1.20	1.59	0.77	2.7E-08
15	55	OC	225	0.57	-4.67	0.29	0.76	94.96	0.14	0.47	1.60	0.27	2.3E-14
16	55	MPP	0	0.80	-18.04	0.35	5.04	40.37	0.21	1.54	1.59	0.95	4.3E-09
17	55	MPP	15	-	-	-	-	-	-	-	-	-	-
18	55	MPP	45	0.80	-15.38	0.34	4.19	88.77	0.15	1.77	1.59	0.84	3.9E-10
19	55	MPP	105	0.80	-7.02	0.23	1.32	76.05	0.16	2.29	1.58	0.51	1.3E-16
20	55	MPP	225	0.66	-9.12	0.20	1.21	104.36	0.09	0.44	1.62	0.50	1.2E-14

Table 3.3: Experimental space for this work. All degradation was done at $< 5\%$ RH. The skipped experiments do not affect the significance of the results. The order presented here does not reflect the randomized data collection process and is only for the reader's convenience.

3.3.5 Experimental Details

All experiments were carried on $MAPbI_3$ perovskite solar cells, whose architecture is shown in Figure 3.9.

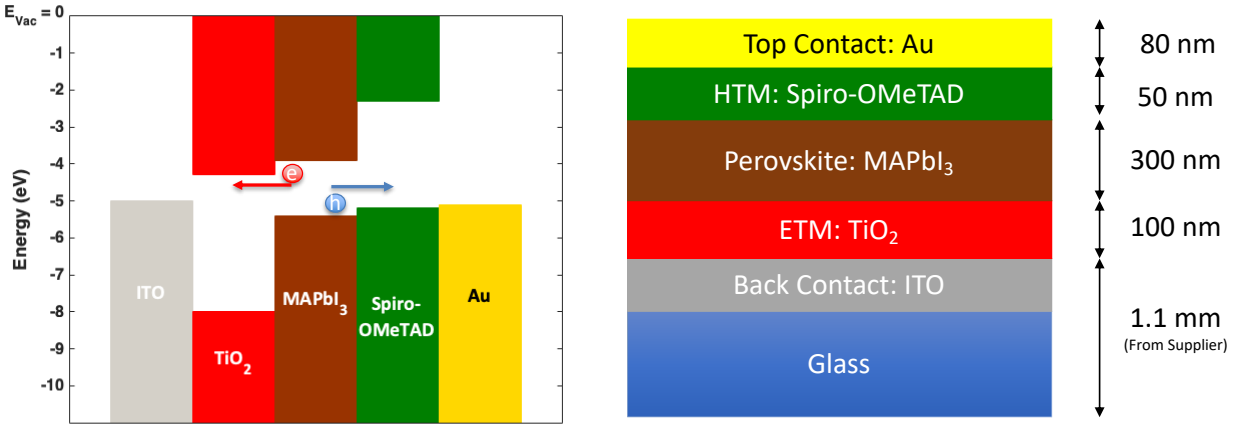

Figure 3.9: (**Left**) Band diagram and (**Right**) Architecture of the $MAPbI_3$ solar cell studied. ETM and HTM refer to electron transport material and hole transport material, respectively.

3.3.5.1 Sample Preparation

ITO coated glass (7 Ω/sq, MSE supplies) were used as substrates for the solar cells. They were successively cleaned in baths of a 2% mixture of Hellmanex (Sigma-Aldrich) in DI water, acetone, and isopropanol for 5min each in a sonicator. Then, they were exposed for 3min to oxygen plasma (March Plasmod) prior to spinning the electron transport material (ETM). The ETM was prepared from a titanium isopropoxide solution (Solaronix) to form the compact TiO_2 layer and a colloidal dispersion of TiO_2 nanoparticles of < 50 nm (Solaronix). The hole transport material (HTM) precursor was prepared from a solution of spiro-OMeTAD (288 mg, Sigma-Aldrich) in chlorobenzene (4 mL, Sigma-Aldrich) and doped with a 520 mg/mL solution of bis(trifluoromethane)sulfonimide lithium in acetonitrile (70 μL, Sigma-Aldrich) and 4-tert-Butylphenol (115.2 μL, Sigma-Aldrich).

3.3.5.2 Perovskite Precursor Preparation

The $MAPbI_3$ precursor was prepared from a solution of MAI (395 mg) and PbI_2 (1153 mg) in a 1:9 ratio of dimethylformamide (DMF, 2.25 mL) to dimethylsulfoxide (DMSO, 0.25 mL). The solution was stirred until completely homogeneous. All reagents were purchased from Sigma-Aldrich.

3.3.5.3 Solar Cell Fabrication

First, under low humidity conditions (<1 ppm H_2O), 100 μL of the titanium isopropoxide precursor was spun onto the ITO substrates at a speed of 5000 rpm and acceleration of 2000 rpm/s for 30s. Then, they were dried at 150°C for 10min on a metal top hotplate followed by a sintering step under atmospheric conditions at 500°C for 30min in a furnace to form the TiO_2 compact blocking layer. After the substrates have cooled back down to room temperature under atmospheric conditions, the colloidal dispersion of TiO_2 nanoparticles was spun on top of the blocking layer at 5000 rpm and 2000 rpm/s for 30s. They were subsequently dried at 150°C for 2min on a metal top hotplate followed by a sintering step at 475°C for 30min in a furnace to form the TiO_2 mesoporous layer. The substrates were moved to a nitrogen glovebox for the deposition of the perovskite layer.

100 μL of the perovskite precursor was spun under two consecutive regimes: regime 1 at 1000 rpm and 500 rpm/s for 10s and regime 2 at 6000 rpm and 3000 rpm/s for 25s. 10s into regime 2, droplets of cholorobenzene were deposited at a rate of 1 mL/min for a total volume of 100 μL using a digital syringe pump. Thereafter, the perovskite was annealed for 10min at 100°C on a metal top hotplate to form the active layer. Once cooled back down to room temperature, the HTM precursor was spun on top of the stack at 4000 rpm and 2000 rpm/s for 30s. Finally, 80 nm of gold were thermally evaporated, using a stainless steel mask, to form the top contact. The active area, defined as the overlap between the FTO and Au contacts, was 0.05 cm^2. This fabrication process was adapted from a report by Yi et al. [117].

3.3.5.4 Degradation Set-up

An environmental chamber (AES BHD-503) was used in conjunction with a custom set-up made for this study (See Figure 3.10). An incandescent light (150 W) was calibrated using a dimmer switch to deliver exactly 1 sun of irradiance to the device under testing (DUT). The DUT had a custom holder (See Figure 3.11) allowing for individual cells on a substrate to be connected to a 1 kΩ load (MPP) located outside the chamber. The holder consisted of a laser-cut piece of teflon with an opening in the center allowing light to penetrate the solar cells. Toothless copper alligator clips were attached to the teflon piece with aluminum wires, which doubled as leads to the electrical load. Teflon was chosen for its stability over the temperature and humidity ranges of the experiments. The toothless alligator clips were used to make direct contact with the gold anodes and the FTO cathode on the unencapsulated solar cells without significantly damaging them. Maintaining the load outside the chamber at atmospheric conditions ensured that the resistance was not varying over time. The PID controls of the environmental chamber were enabled to maintain constant temperature and humidity, especially when the incandescent light was on. Without them, the temperature in the chamber would overshoot the set value, for the light is also a heat source.

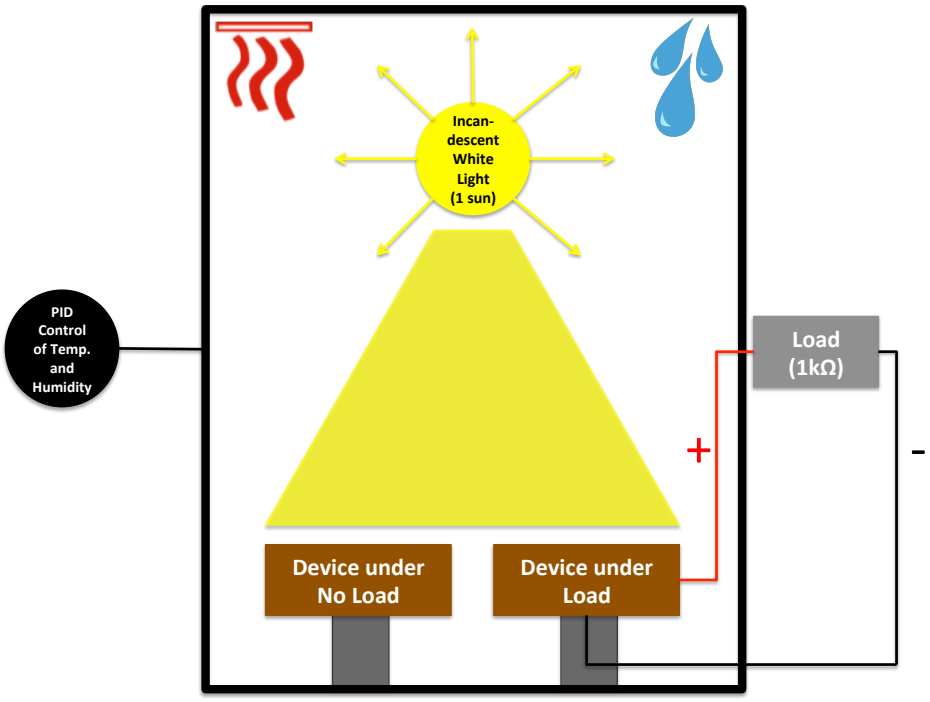

Figure 3.10: Schematic of the custom degradation set-up installed in the environmental chamber.

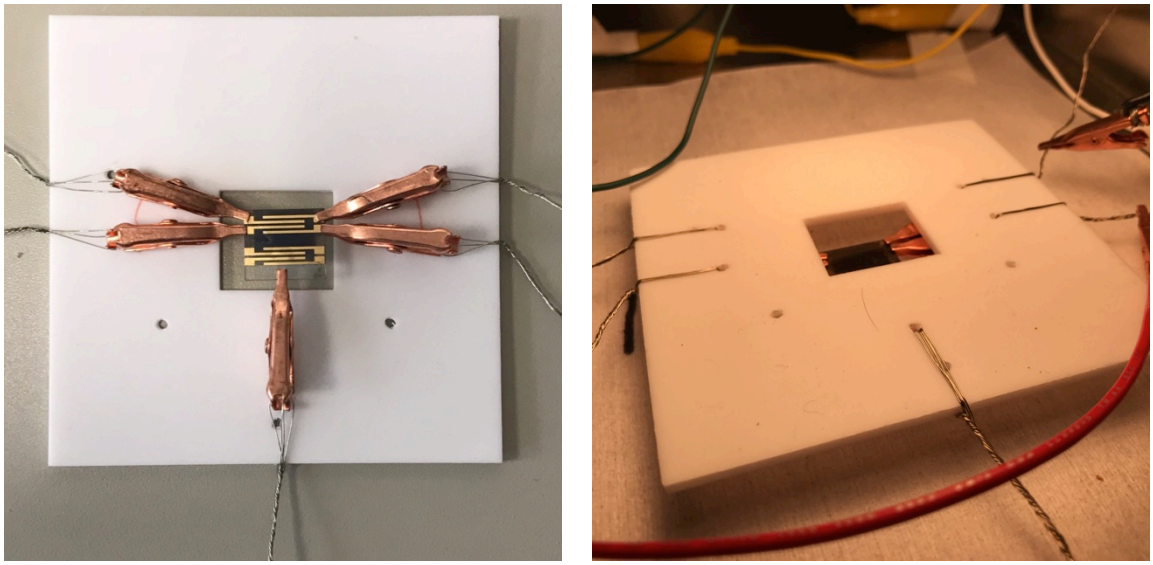

Figure 3.11: (**Left**) Top view of the teflon holder with the toothless alligator clips holding a non-encapsulated solar cell. (**Right**) DUT under illumination connected to a load.

3.3.5.5 Measurements

Post-fabrication and pre-degradation, the electrical, optical, and crystallographic characteristics of every cell were measured. Then, post-exposure, those characteristics were measured again and complemented by a PICTS measurement.

The electrical characteristics were measured using a solar simulator (Oriel-Sol1A) delivering an AM1.5 spectrum at 100mW/cm^2 and a Keithley-2400. To ensure the validity of the data collected, the standard solar simulator set-up was improved to limit unnecessary light exposure and speed up the measurements by fully automating the process. First, we built a new set-up that connected the data acquisition unit (DAQ) to an Arduino Mega 2560 via a computer. The Arduino microcontroller was in turn connected to low resistance electromagnetic relays (0.2Ω, 9002-05-00 Coto Technology), which fed into the DUTs. To synchronize this circuit, a new MATLAB code was written with a starting block coming from Zimmermann et al. [118]. With this software, we were able to completely measure the devices within 3min by performing both forward and reverse scans and shutting off the light while the software switched to the next cell to be tested. This system, illustrated in Figure 3.12, considerably improved the reliability of our measurements. The electrical characteristics were extracted from the forward bias scans, for they exhibited slightly lower performance values, and we perceived them as conservative figures of merit. Figure 3.13 shows typical current-voltage curves used in the analysis.

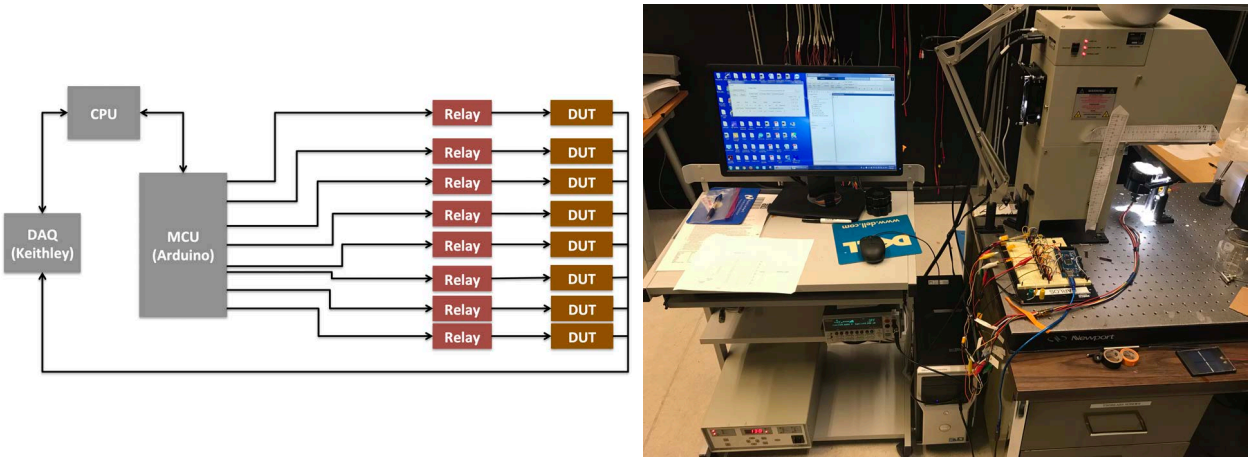

Figure 3.12: (**Left**) Schematic representation of the IV measurement set-up. (**Right**) Photograph of its physical implementation.

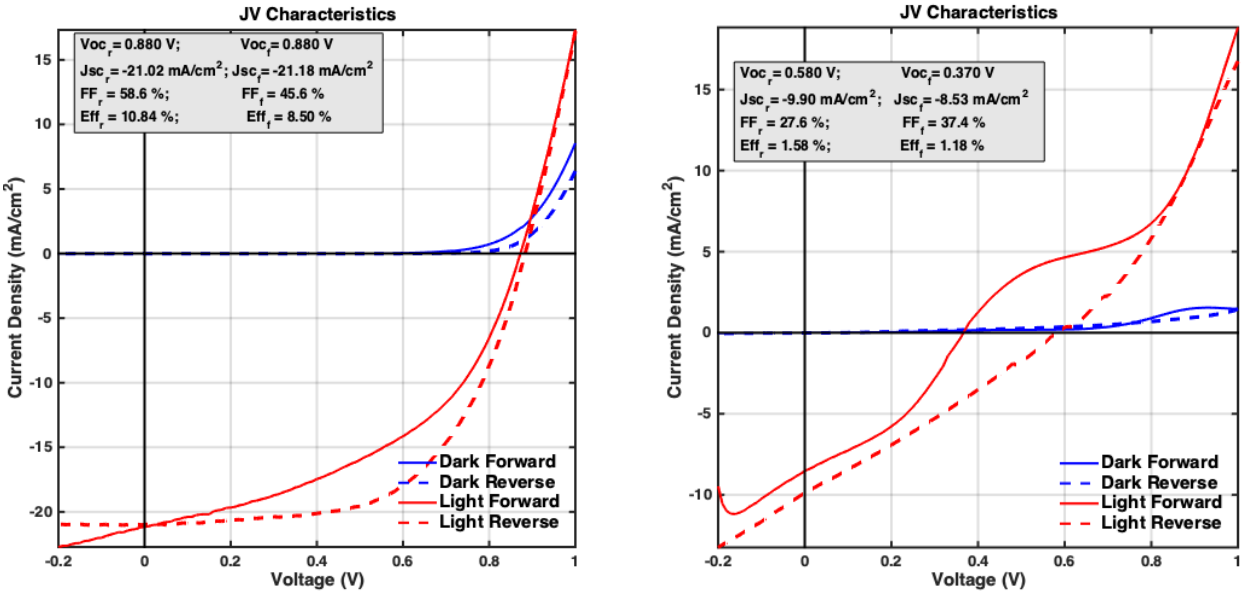

Figure 3.13: Typical JV characteristics (**Left**) pre and (**Right**) post degradation.

The absorption spectrum was measured with a UV-Vis spectrophotometer (Shimadzu UV-2600) for wavelengths ranging from 300 to 900 nm. The absorbance at 550 nm (A550) was promptly recorded, and the wavelength at the absorption band edge, the longest one at which there is a sharp increase in absorption, was converted to energy space using $E(eV) \approx 1240/\lambda(nm)$ (See Figure 3.14).

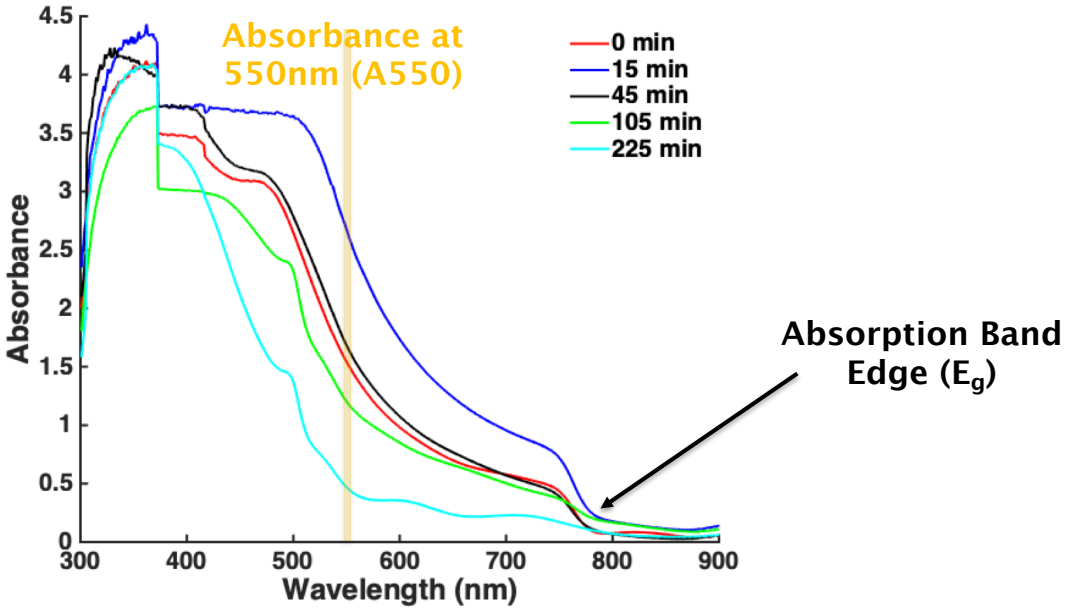

Figure 3.14: Typical absorption spectra tracked over several degradation periods.

The crystallographic characteristics were measured using a D8 Discover GADDS powder X-ray diffractometer. The crystallite size (L) and the microstrain ($\mu\epsilon$) were extracted using the following Sherrer equations [114]:

$$L = \frac{K\lambda}{B_{2\theta}\cos\theta} \quad \& \quad \mu\epsilon = \frac{B_{2\theta}}{4\tan\theta}$$

where K is Scherrer's constant, λ is the wavelength of the X-ray, and $B_{2\theta}$ is the peak broadening, approximated as the full width at half max (FWHM) at a given 2θ of the XRD spectrum. K varies from one instrument to the other, but is usually ~ 0.9. The x-ray source was Cu K-α of wavelength $\lambda = 1.5406$ Å. The crystallite size and microstrain were evaluated at the five main $MAPbI_3$ peaks and averaged for each sample. Those peaks are $2\theta \approx 14^o(110)$, $28.5^o(220)$, $31.5^o(210)$, $40.5^o(224)$, and $43^o(314)$ (See Figure 3.15).

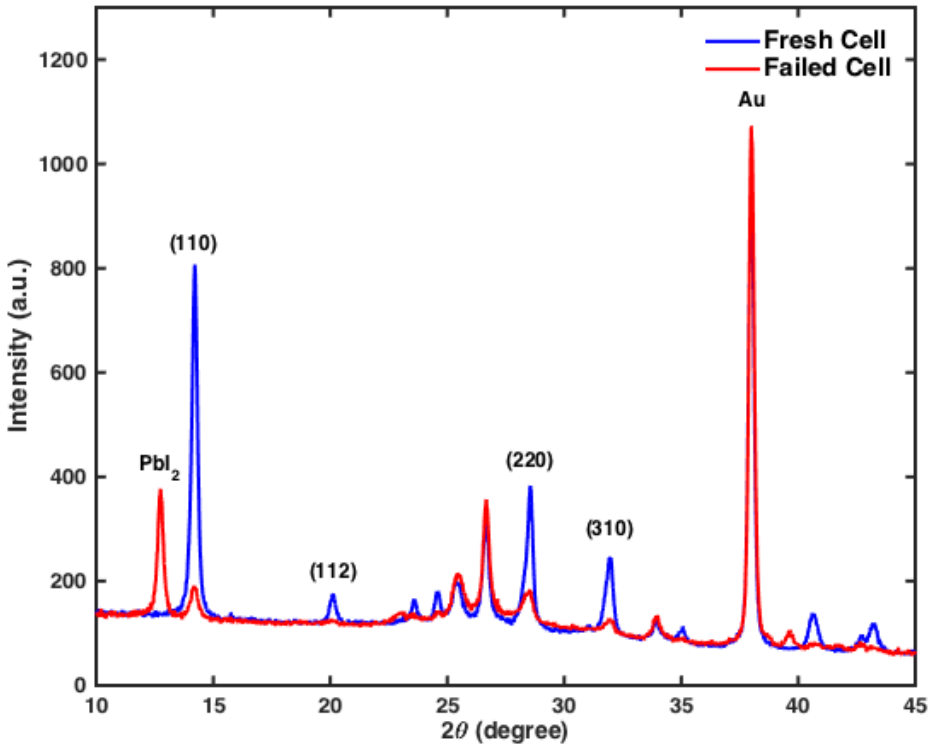

Figure 3.15: Typical XRD spectra pre and post degradation.

The electronic defect data were obtained using a PICTS measurement system (Sula Technologies). The device was placed in a cryostat (Janis) and connected to the PICTS measurement set-up. Then, a LED of wavelength 626 nm was pulsed (2000ms period) onto the device to generate carriers above the band gap of $MAPbI_3$ at 0 V bias. After pumping the pressure down below 10^{-5} Torr, the cryostat was turned on to cool down the device to 280K. The LabVIEW proprietary software controlling the set-up was programmed to record the spectrum of transient current at six different delays: 2, 5, 10, 20, 50 and 100ms. As soon

as the low set temperature was reached, the system recorded data by progressively heating the device at a rate of 2K/min until it reached its ultimate temperature of 400K. The device was immediately returned to RT after the run was completed to never allow it to dwell too long at high or low temperatures. This process was repeated as the filling pulse was varied from 1ms to 1000ms for every sample to uncover the nature of their defects. The trap activation energy (E_a) and capture cross-section (σ_a) were extracted after each temperature spectral run via an Arrhenius plot. Figure 3.16 shows an illustration of the system. The next chapter goes in depth on the theory behind this measurement and its significance.

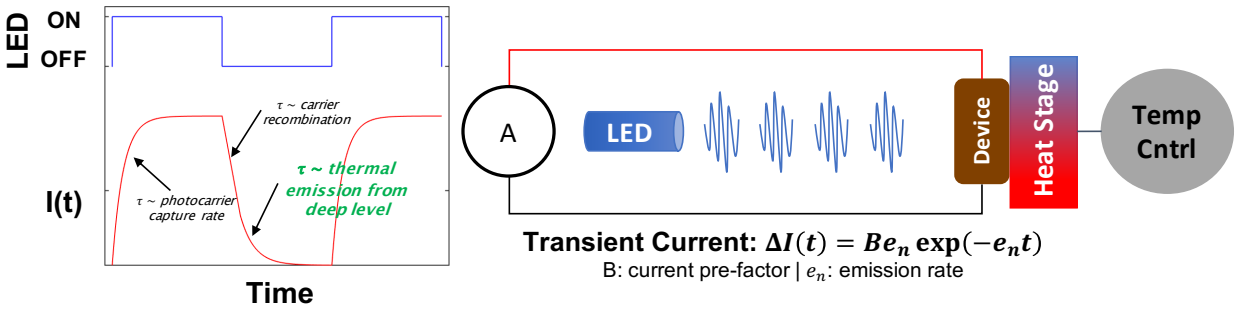

Figure 3.16: PICTS experimental set-up showing, on the **right**, a pulsing LED exciting a perovskite solar cell that is progressively heated from low to high temperature to extract trap information. The **left** shows how the pulsing light fills traps (steady state current), and that deep level traps are emitted after an initial steep decay in current while the LED is off.

3.3.6 Influence of Degradation Factors

The influence of temperature and electric load on the photovoltaic properties have been graphically reported in other studies [106]. However, we highlight the interaction terms that can only be revealed when performing degradation studies under a DOE framework. When considering the fill factor, the interaction plot in Figure 3.17 shows intersecting lines when controlling for temperature and load. In the same figure, the response contour plots show a change in concavity when switching from OC to MPP condition, which is significant when studying a categorical (and non-continuous) term like load condition. The half-normal plot does not show any significant deviation from Lenth's line for the Temp × Load term. However, a p-test reveals that the interaction between temperature and electric load ($p_{FF|Temp\times Load} = 0.07$) is below our significance level of $\alpha = 0.1$, whereas the individual influence of temperature and electric load are not ($p_{FF|Temp,Load} > 0.1$, Figure 3.21). In light of all these individual tests, we conclude that the interaction of temperature and electric load is relevant to the degradation of the fill factor in perovskites.

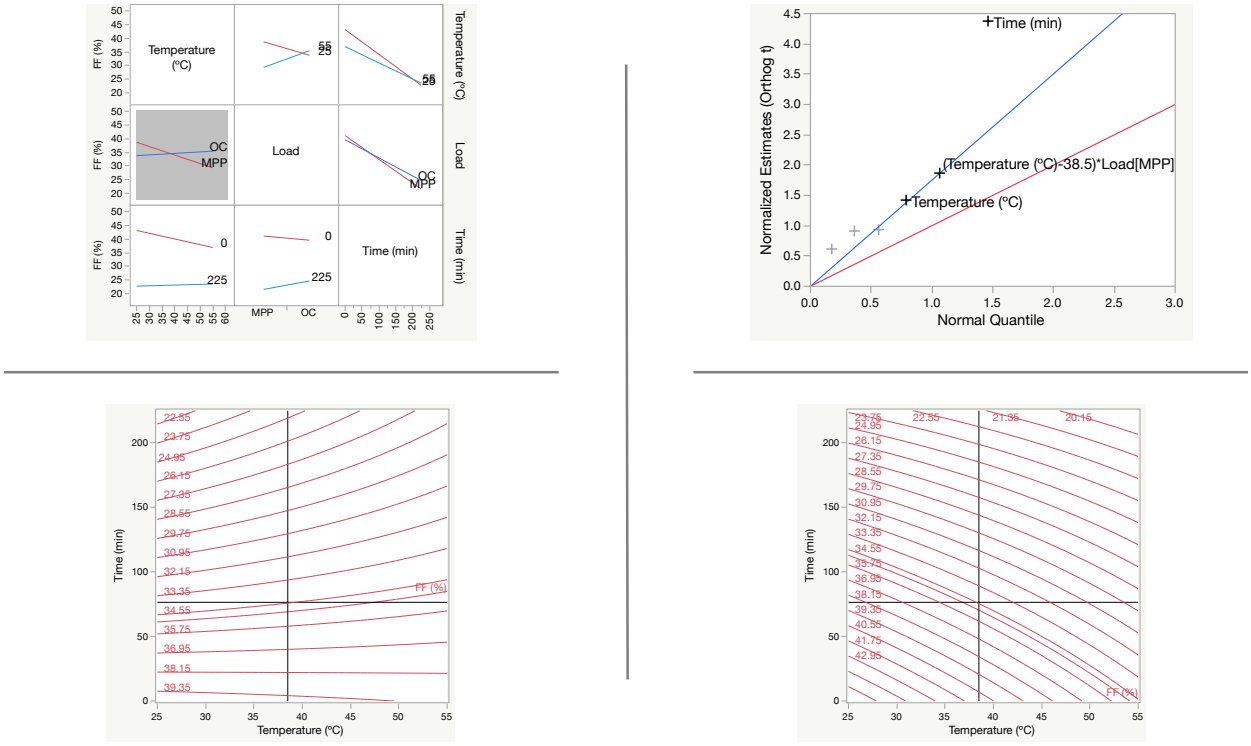

Figure 3.17: Diagnostic plots for evaluating the effects of confluent factors on the fill factor. (**Top Left**) Interaction plots with most significant interaction highlighted. (**Top Right**) Half-normal probability plot — the blue line has a slope equal to Lenth's PSE and the red line has a slope equal to 1. (**Bottom Left**) Response contour plot for open-circuit (OC) load condition. (**Bottom Right**) Response contour plot for maximum power point (MPP) load condition.

We undergo a similar analysis process to show that the interaction of temperature with time is significant in the change in the crystallite size (Figure 3.18), the absorbance at 550 nm (Figure 3.19), and the trap activation energy (Figure 3.20) – exposure time in this study should be understood as a confluence of atmospheric effects, illumination, and relative humidity (maintained at 5%) because we did not vary them. Figure 3.21 summarizes the p-test for the degradation factors studied. The relevance of these interaction terms highlights the importance of undergoing degradation studies with a systematic and holistic approach to extract all the salient effects and make educated decisions. Any stability model should properly account for these interaction factors for accuracy.

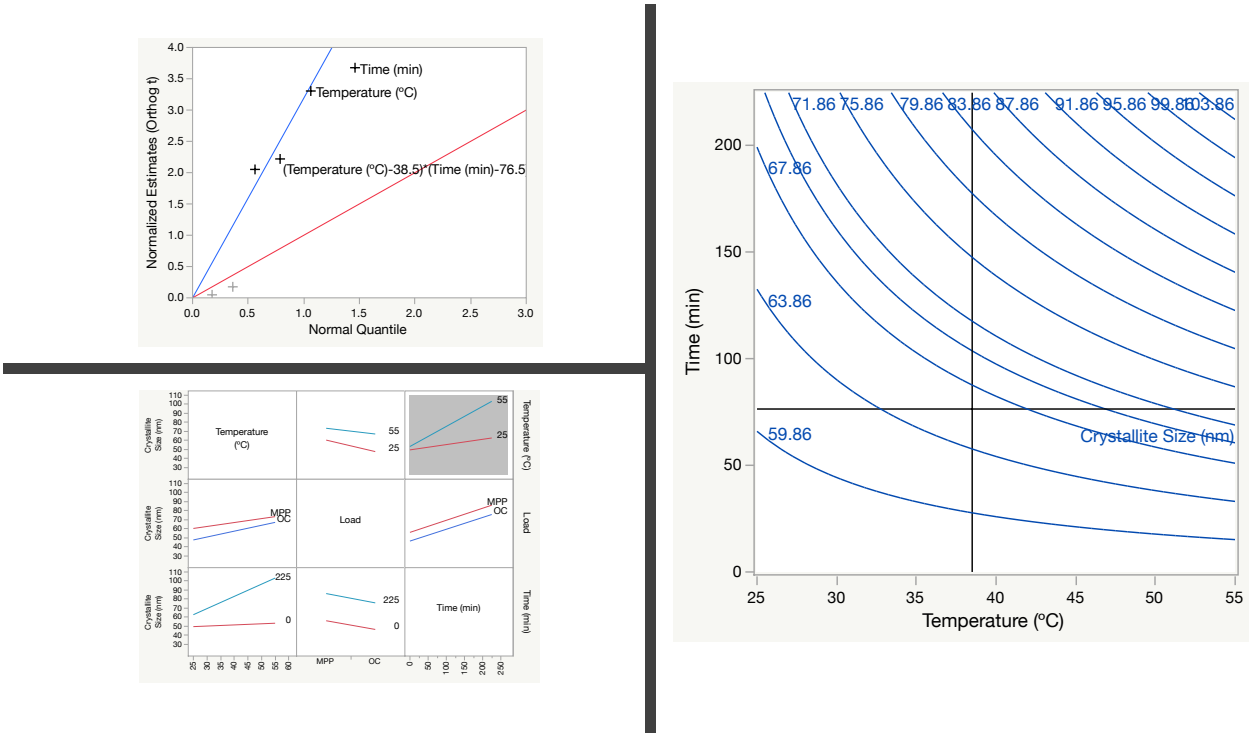

Figure 3.18: Diagnostic plots for evaluating the effects of confluent factors on the crystallite size. (**Top Left**) Half-normal probability plot — the blue line has a slope equal to Lenth's PSE and the red line has a slope equal to 1. (**Bottom Left**) Interaction plots with most significant interaction highlighted. (**Right**) Response contour plot showing curved lines indicating a significant interaction.

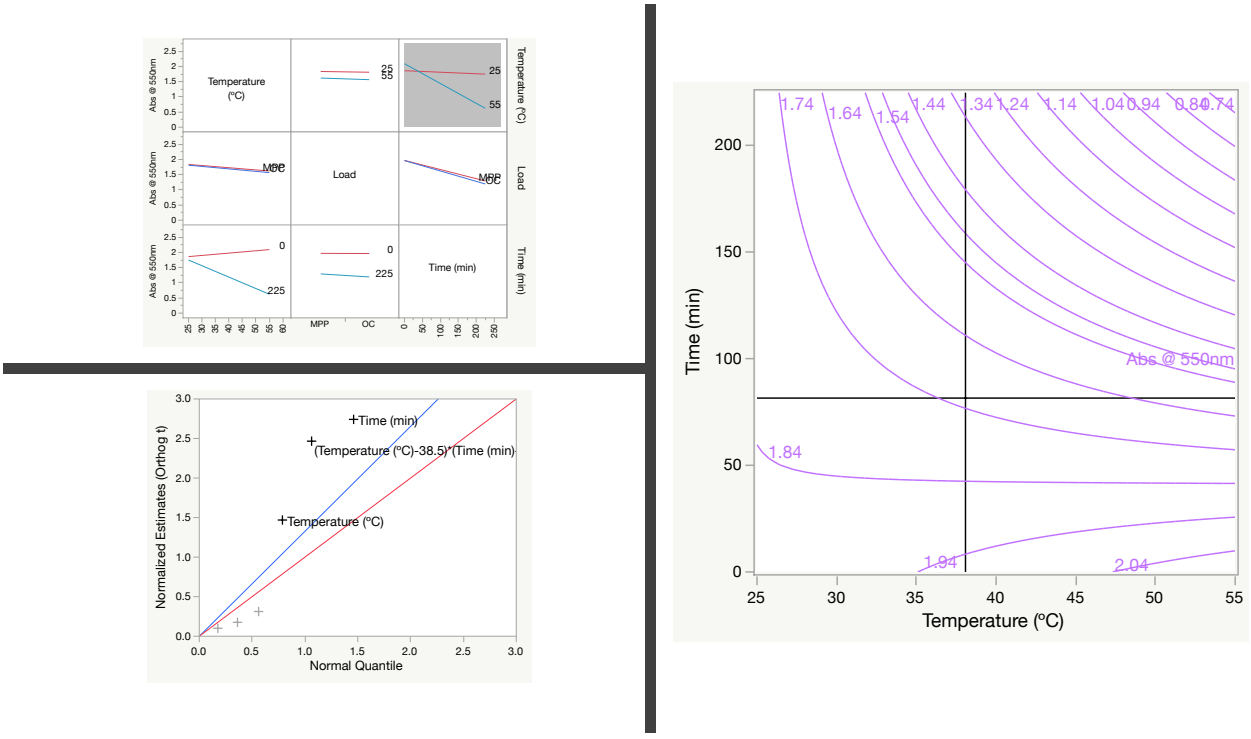

Figure 3.19: Diagnostic plots for evaluating the effects of confluent factors on the absorption at 550nm. (**Top Left**) Interaction plots with most significant interaction highlighted. (**Bottom Left**) Half-normal probability plot showing the interaction term deviating from Lenth's line (in blue) suggesting a significant effect — the red line has a slope equal to 1. (**Right**) Response contour plot showing curved lines indicating a significant interaction.

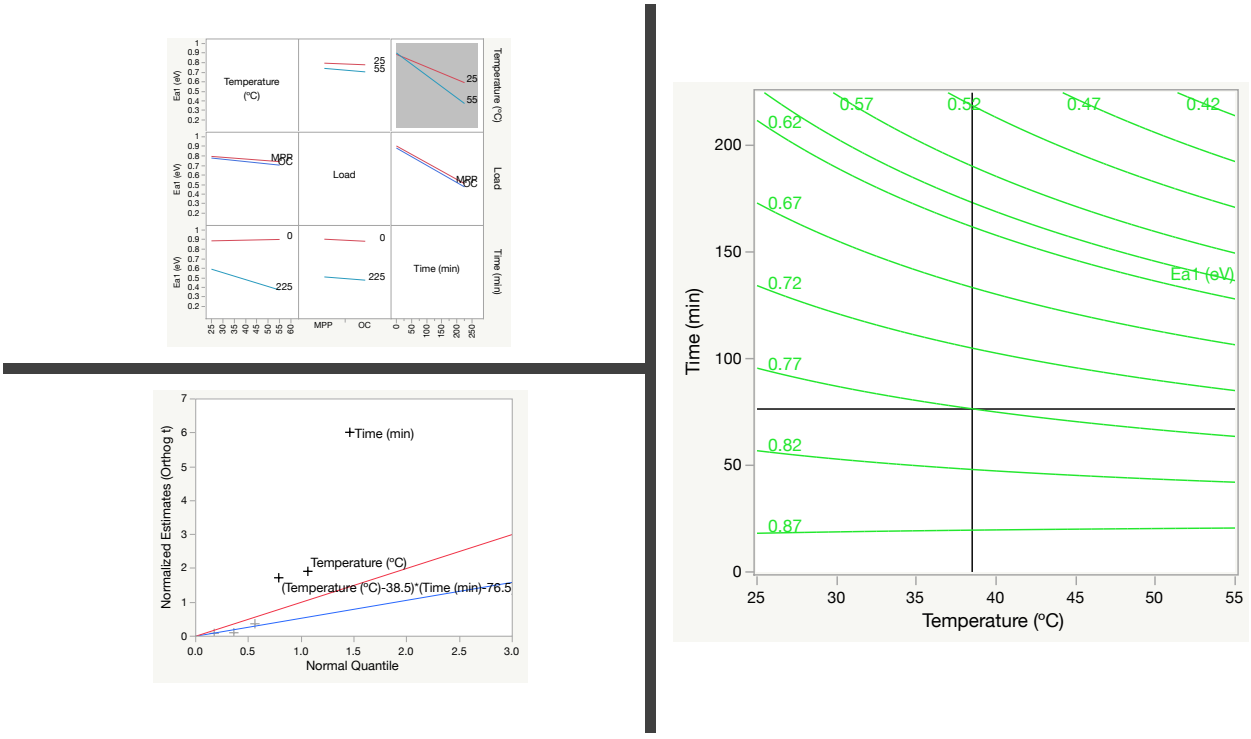

Figure 3.20: Diagnostic plots for evaluating the effects of confluent factors on the trap activation energy. (**Top Left**) Interaction plots with most significant interaction highlighted. (**Bottom Left**) Half-normal probability plot showing the interaction term deviating from Lenth's line (in blue) suggesting a significant effect — the red line has a slope equal to 1. (**Right**) Response contour plot showing curved lines indicating a significant interaction.

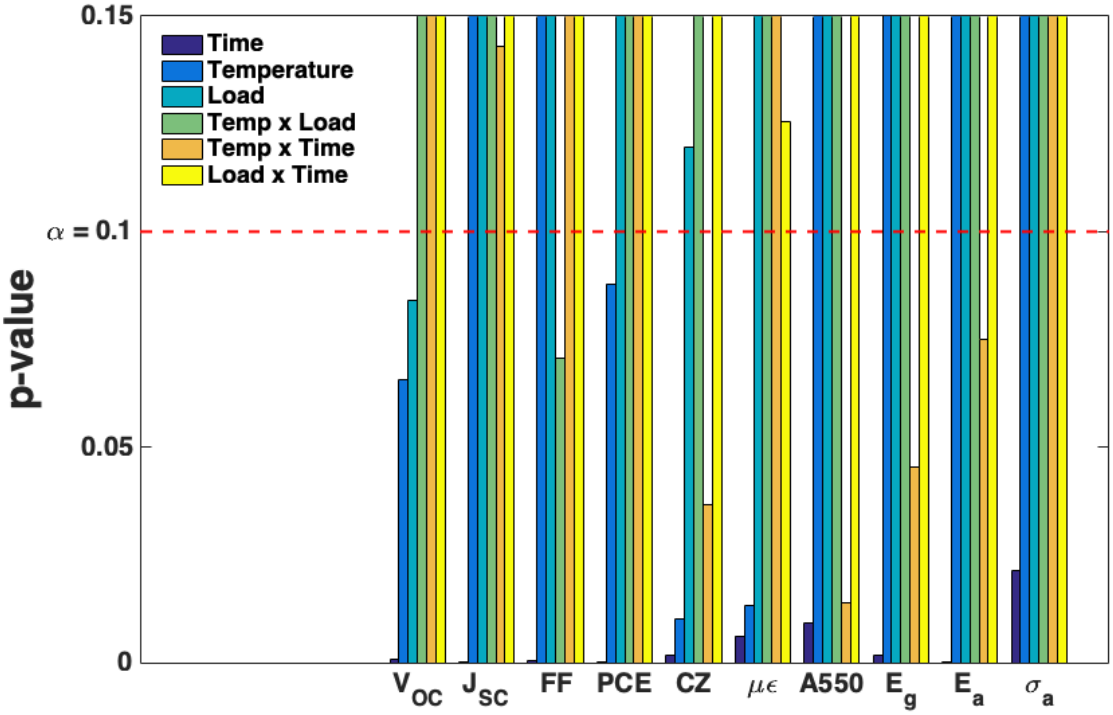

Figure 3.21: Summary of the p-test for all the responses tracked in this work. A factor is assigned significance when its p-value is below $\alpha = 0.1$, represented by the red dashed line.

3.4 Summary

In this chapter, we detailed the DOE methodology and showed why it is a robust statistical analysis framework. Then, we showed how we applied it to our study by using a $2^2 \times 5$ full factorial design with temperature, load, and exposure period as the factors. The chosen responses are the photovoltaic (J_{SC}, V_{OC}, FF & PCE), optical (A550 & E_g), crystallographic (L & $\mu\epsilon$), and deep level defect (E_a & σ_a) characteristics. We justified why choose our bounds and detailed our experimental procedure. Finally, we identified and quantified the influence of relevant interaction factors (Temperature × Load & Temperature × Time) in the degradation of $MAPbI_3$ cells. In the next chapter, we will explain the kinetics of deep level traps, how to measure them, and their evolution in degrading perovskites in chapter 4. Then, in chapter 5, we will tie the statistical observations from this chapter to physical mechanisms by focusing on the correlations between deep level traps and the other responses tracked in this study.

Chapter 4

Deep Level Trap Tracking in Degrading Perovskite Solar Cells

Impurity and defect states in semiconductors are usually divided into two classes: shallow and deep. Shallow states are ones at which the electron is weakly bound by a Coulomb potential in an extended state with the effective mass of the appropriate band edge. They are usually thermally ionized at room temperature. Deep states, on the other hand, are ones where the impurity potential is more strongly localized, causing electrons to be tightly bound. For most semiconductors, these levels are greater than 0.05 eV away from the band edges [119]. A very small concentration of deep states can influence carrier recombination lifetimes, which are critical for photocarrier generation in solar cells. It is therefore important to understand their behavior and influence on degrading perovskite solar cells. Techniques to appropriately characterize these deep states involve capturing transient signals while varying the temperature of the semiconductor. In this chapter, we discuss the general principles behind these techniques and describe the most widely used one, Deep Level Transient Spectroscopy (DLTS). Then, we discuss the technique we use for this work, Photo-Induced Conductivity Transient Spectroscopy (PICTS), and present the results from tracking the evolution of deep electronic states in degrading perovskite solar cells.

4.1 Deep Level Trap Kinetics

There are four processes defining the kinetics of a deep state: the individual emission and capture processes for electrons and holes. The capture process is characterized by a capture cross-section σ. In the presence of n free electrons per unit volume moving with rms thermal velocity $\langle v_n \rangle$, a deep state is exposed to a flux of $n\langle v_n \rangle$ electrons per unit area per unit time. If the total concentration of deep states is N_t, and if, at any instant, n_t of the states are occupied by electrons, the number of electrons captured by the $(N_t - n_t)$ unoccupied states in a further short time interval Δt is

$$\Delta n_t = \sigma_n \langle v_n \rangle n(N_t - n_t)\Delta t$$

and the capture rate per unoccupied state, defined as

$$c_n = \frac{\Delta n_t / \Delta t}{N_t - n_t}$$

is therefore

$$c_n = \sigma_n \langle v_n \rangle n$$

where the subscript n denotes electrons. A similar derivation can be done for holes [119]. The thermal dependence of the emission rate e_n of electrons is given by

$$e_n(T) = \gamma T^2 \sigma_a e^{-\frac{E_a}{kT}} \quad \text{with} \quad \gamma = 2\sqrt{3} M_c (2\pi)^{\frac{3}{2}} k^2 m^* h^{-3}$$

where M_c is the number of conduction band minima, k is Boltzmann's constant, m^* is the effective mass of the carrier, h is Planck's constant, and E_a is the trap's activation energy. An Arrhenius plot of $\ln(e_n/T^2)$ as a function of T^{-1} will be a straight line with E_a and pre-exponential factor defined by σ_a (See Figure 4.1). Experimentally, data for most traps fit an equation of that form over many orders of magnitude of e_n, although considerable care is required in the physical interpretation of E_a and σ_a. The linearity of the plot provides confirmation that the underlining assumptions for the measurement were correct. If, on the other hand, the plotted emission rates diverge strongly from linearity, the emission measured may not be from a single isolated trap and may require further characterization. In the formulation presented, the trap activation energy is given by $E_a = (E_c - E_t) + \Delta E_\sigma$, where ΔE_σ is related to changes in the lattice vibrational and electronic entropies with the deep center changing its charge state. Thus, E_a does not give the energy level of the trap directly yet can be used to characterize a trap's signature.

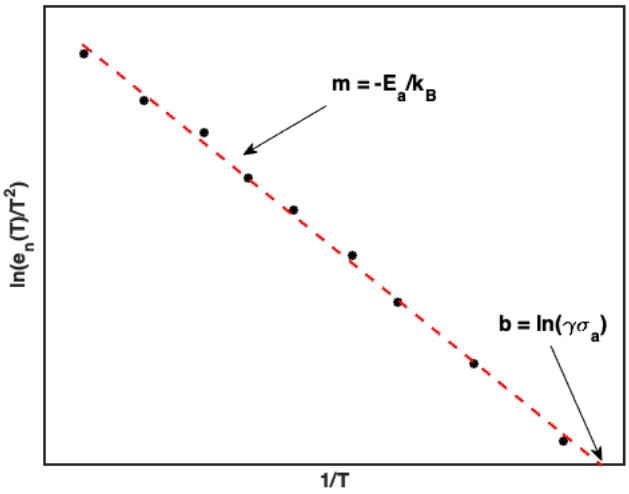

Figure 4.1: Sample Arrhenius plot obtained from a deep trap measurement technique [120].

4.2 Measuring Deep Level Traps

Generally, deep level studies seek to uncover the following semiconductor properties [120]:

- Number of distinct traps in the material
- Trap type: majority or minority carrier
- Trap concentration [cm^{-3}]
- Thermal activation energy of the trap [eV]
- Capture cross-section [cm^2]
- Nature and origin of the trap

Because of their underlying assumptions, some techniques are better suited at measuring some of those listed properties than others. All those techniques rely on measuring a transient signal (usually capacitance or current) from a heated semiconductor. We describe next the most widely used DLTS before discussing PICTS, the technique used in this work.

4.2.1 Deep Level Transient Spectroscopy (DLTS)

4.2.1.1 General Principles

DLTS is a technique that observes carrier emissions by means of a capacitance transient. In this description, we focus on majority carrier trap. The bias on the test diode is pulsed between a bias near zero and some reverse bias V_r with a period t_r. The zero bias condition is held for a time t_f during which traps are filled with majority carriers. In this interval, the capacitance signal contains no useful information and reaches steady state. During the reverse bias pulse, the trapped carriers are emitted at a rate e_n producing an exponential transient in the capacitance, which in its general form can be written as

$$C(t) = C(\infty) + \Delta C_o e^{-t/\tau}$$

The time constant τ is equal to e_n^{-1}, and ΔC_o is the initial transient capacitance measured with respect to the steady state capacitance $C(\infty)$ at $t = \infty$. The essence of the DLTS method is to feed this transient to a rate window which provides a maximum output when the time constant τ is equal to a known preset time constant τ_{ref}.

Imagine a test diode on a material containing two different traps, each characterized by a trap signature in the form of a linear plot of $\ln(\tau)$ versus T^{-1} with different values of E_a and σ_a. As the temperature of the diodes is increased, the emission rate increases and peaks in the rate window output as $\tau = e_n^{-1}(T)$ passes through τ_{ref} for each trap. For a given τ_{ref}, the peak temperatures (T_{pk}) T_1 and T_2 are characteristic of each trap, and the peak height is proportional to ΔC_o and gives the trap concentration N_t. Furthermore, by repeating the

scan with different values of τ_{ref}, sets of values of e_n and T_{pk} can be obtained from which Arrhenius plots of $\ln(e_n/T^2)$ versus T^{-1} can be generated, and E_a and σ_a can be deduced for each trap. The emission rate is determined by the instantaneous temperature, so the peaks are independent of the direction and rate of the temperature scan. Also, since the transient is not recorded directly, it is possible to take full advantage of the response time of the measuring instrument and work with time constants as short as a few μs. Therefore, the period can be a few ms short in order for e_n to be effectively constant over several cycles and for the output signal to be averaged without prolonging the scan time, if values of τ_{ref} are not too long. This allows DLTS to enjoy a high signal-to-noise ratio. Figure 4.2 summarizes the DLTS data collection process.

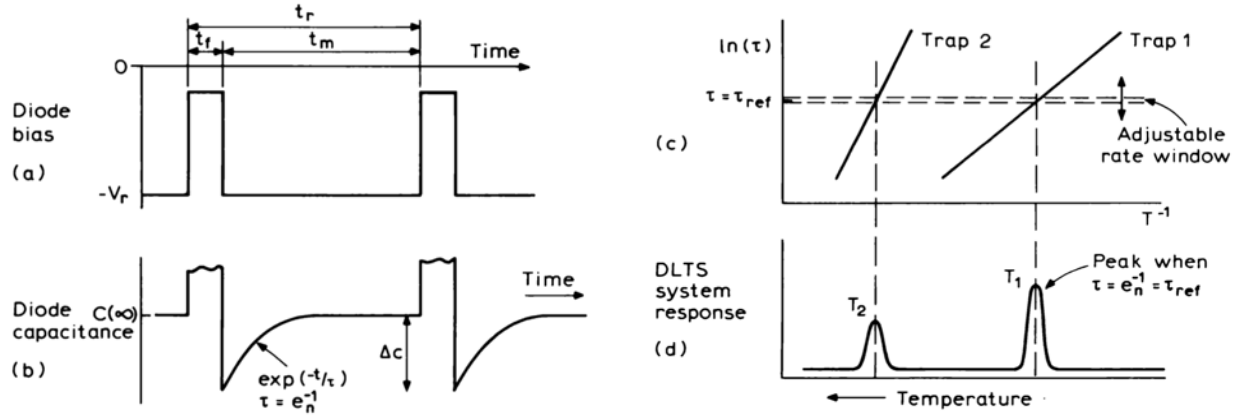

Figure 4.2: Illustration of the principles of DLTS. (**a**) Repetitive filling and reverse bias pulse sequence. (**b**) Corresponding transient capacitance as function of time. (**c**) Variation of the transient time constant $\tau = e_n^{-1}$ with reciprocal temperature for two different traps. (**d**) Deep level spectrum produced by a rate window τ_{ref} operating on the capacitance transient shown in (**b**) [119].

4.2.2 Photo-Induced Conductivity Transient Spectroscopy (PICTS)

Another reliable technique to measure traps, one better suited to photosensitive devices with relatively high leakage currents, is the powerful and sophisticated photo-induced conductivity transient spectroscopy (PICTS). It depends on transient currents generated from the device under testing (DUT) when excited by a pulsing light source and allows for the accurate extraction of E_a (as low as 0.1 eV depending on the coolant [121]) and σ_a. To perform such experiments, it is necessary to prime the traps repetitively, while the temperature is scanned, by illumination with photons of energy greater than the band gap. The excess electrons and holes are captured at trapping sites and subsequently released by thermal emission when the light is turned off, producing a current transient. A large photocurrent flows during the illumination period; then, when illumination stops, it decays rapidly, leaving a small

exponential transient, due to thermal emission from the traps, which is analyzed by a DLTS rate window (See Figure 4.3). In that sense, PICTS is similar to DLTS in that the peaks in the spectra are characteristic of thermal processes. We discuss next its principles and physical implementation.

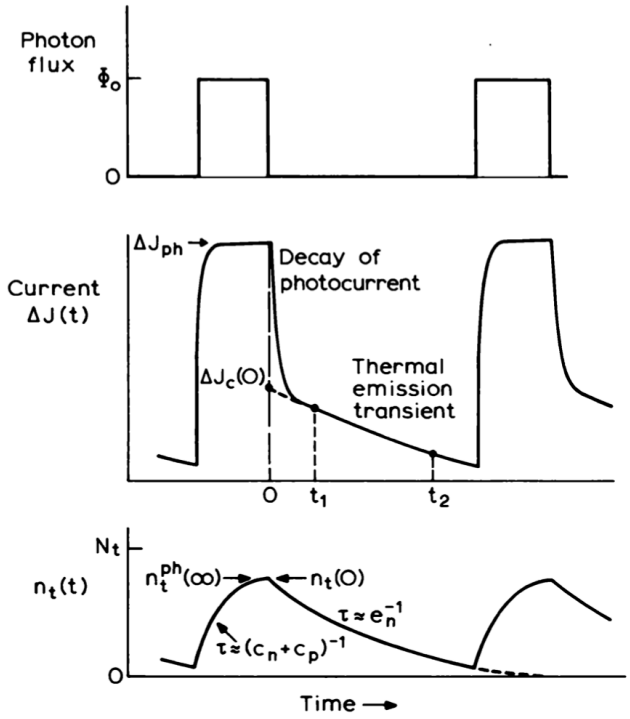

Figure 4.3: Time sequence of operations in a PICTS experiment. The light is pulsed on to generate electron-hole pairs, which fill the traps with a time constant $\tau \approx (c_n + c_p)^{-1}$. When the light is turned off, the photocurrent falls rapidly from its steady value under illumination (ΔJ_{ph}) eventually revealing an exponential thermal emission transient of amplitude $\Delta J_c(0)$. This is usually analyzed using a double box-car with gates set at t_1 and t_2. The lower part of the figure shows the density of trapped electrons $n_t(t)$ during the capture and emission periods [119].

4.2.2.1 General Principles

Illumination of a semiconductor with a flux Φ_o of photons of energy ($h\nu$) greater than the band gap generates free electron-hole pairs at a rate which depends upon the optical absorption coefficient $\alpha(h\nu)$, the distance below the surface of the sample (x), and the surface reflectivity R:

$$G(x) = (1 - R)\alpha(h\nu)\Phi_o e^{-\alpha(h\nu)x}$$

In a sample with ohmic contacts on the surface, the electric field is low and the steady state excess carrier density (Δn) is determined by the balance between generation, recombination

and diffusion which in the steady state is given by:

$$G(x) - \frac{\Delta n(x)}{\tau_n} + D_n \frac{\partial^2 \Delta n}{\partial x^2} = 0$$

where D_n is the diffusion coefficient for electrons. A similar equation can be written for holes [119]. Within the depletion region, the photogenerated electron-hole pairs are swept away by the depletion region field ($\mathscr{E}$) before they can recombine. This drift process dominates over diffusion, so the steady state carrier density is given by:

$$G(x) + \mu_n \mathscr{E}(x) \frac{\partial \Delta n}{\partial x} = 0$$

where μ_n is the electron mobility. Therefore, the effect of illumination is to produce excess carriers, which can be captured at deep states at rates

$$c_n = \sigma_n \langle v_n \rangle \Delta n$$

given $\Delta n \gg n_o$, where n_o is the equilibrium background electron concentration. These rates depend implicitly upon the distance x through the depth dependence of Δn. To effect significant changes in trap occupancy, it is necessary that Φ_o is sufficiently great that c_n exceeds the thermal emission rates.

After the traps are filled, the light is turned off, and the excess carrier populations in the bands decay rapidly at a rate determined by the carrier lifetimes in an undepleted sample and by the sweep-out rate in the depletion region. When this photocurrent has decayed away, a transient current remains due to the slower thermal emission of trapped carriers from the deep state (see Figure 4.3), which is given by:

$$\Delta J_c(t) = -e\mathscr{E}\tau_n \mu_n e_n n_t(0) e^{-e_n t}$$

Assuming the light pulse is of sufficient duration to reach a steady state during the filling period, $n_t(0)$ in these equations is given by $n_t^{ph}(\infty)$ (see Figure 4.3). The equation can be simplified as

$$\Delta J(t) = B(T) e_n \, e^{-e_n t}$$

where $B(T) = -e\mathscr{E}\tau_n \mu_n n_t(0)$. This transient can be processed using a DLTS rate window to produce a thermal emission spectrum as the traps are repetitively filled, and the temperature increased. B is inherently a function of temperature through $\mu_n \tau_n$, which is inconvenient since it is not included in standard calculations of τ_{ref}, and the form of its temperature dependency is not necessarily known. The presence of the e_n pre-exponential term adds to the complications. To overcome this issue, a four-gate rate window scheme can be employed (See Figure 4.4) [122]. Provided the $\mu_n \tau_n$ product is independent of time during the thermal emission transient, it is clear that the signal formed by

$$S(\tau) = \frac{\Delta J_c(t_1) - \Delta J_c(t_2)}{\Delta J_c(t_0) - \Delta J_c(t_3)}$$

is independent of $B(T)$ and any steady background current, and is given simply by

$$S(\tau) = \frac{e^{-t_1/\tau} - e^{-t_2/\tau}}{e^{-t_0/\tau} - e^{-t_3/\tau}}$$

This function depends only on the properties of the exponential function, and has a maximum dependent on τ provided t_0 and t_3 lie outside the interval $[t_1 \;\; t_2]$. A simplified expression for $\tau = \tau_{ref}$ is obtained if t_3 is chosen such that $t_3 \gg t_2 > t_1 > t_0$. Indeed, the peak output signal will occur at

$$\tau_{ref} = (t_2 - t_1)\left[\ln\left(\frac{t_2 - t_0}{t_1 - t_0}\right)\right]^{-1}$$

The disadvantage of this scheme is that by removing the signal's $B(T)e_n$ dependence, the peak height no longer depends upon $n_t(0)$, so the trap concentration N_t cannot be measured. This is a recognition of the difficulties in obtaining a value for N_t from a PICTS conductivity spectrum using the four-gate technique. Apart from that fact, the analysis of a PICTS signal is similar to that of DLTS with the Arrhenius plot.

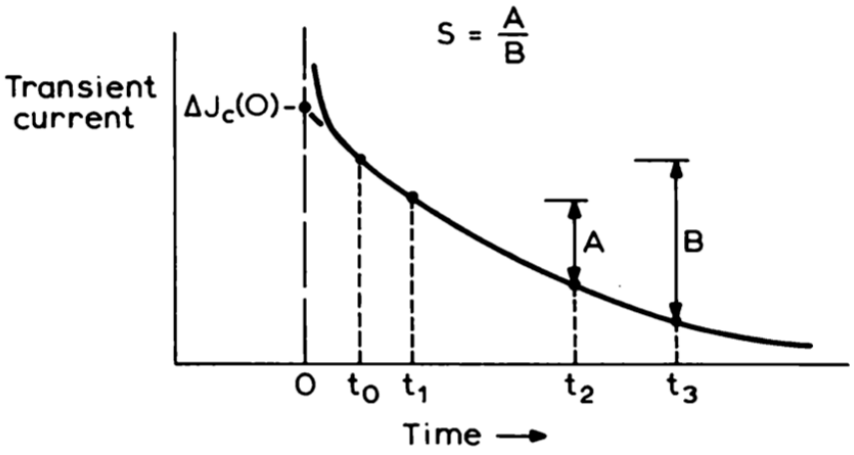

Figure 4.4: Gate positions in a four-gate sampling scheme for the conductivity transient in a PICTS experiment. The output signal S is formed by taking the ratio of the differential currents $A = \Delta J_c(t_1) - \Delta J_c(t_2)$ and $B = \Delta J_c(t_0) - \Delta J_c(t_3)$ [119].

4.2.2.2 Equipment

A block diagram of a simple PICTS system is shown in Figure 4.5. The transient current is measured with a highly sensitive ammeter since the signal is usually in the nA range. It is necessary to set the reverse bias, which may not necessarily be zero volts, with an external DC supply. A pulse generator is connected to the LED to provide the trap filling bias. The transients are analyzed by the rate window system triggered from the pulse generator, and the output signal is displayed on the recorder (computer screen). The pulse's period is

usually a few times τ_{ref}. The DUT is mounted in a variable temperature cryostat in intimate thermal contact with a temperature sensor, which provides the signal for the x-axis of the recorder, and, for convenience, can be linearized to give T directly.

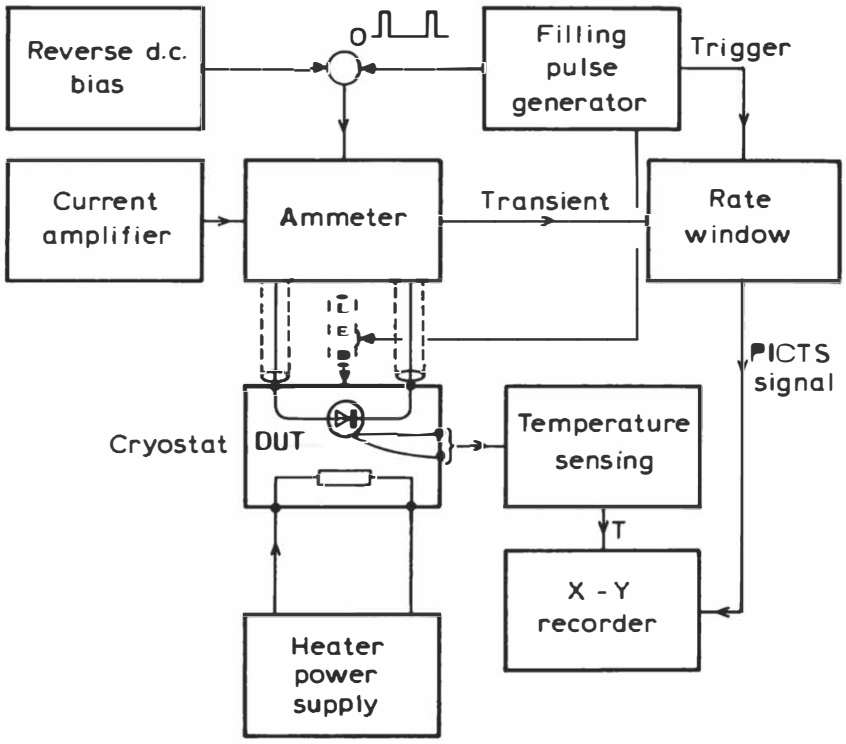

Figure 4.5: Block Diagram of a PICTS system (Adapted from [119]).

4.3 Evolution of Traps in Degrading Perovskites

Our experimental approach in measuring traps in $MAPbI_3$ perovskites was described in Section 3.3.5.5. We focus next on the analysis of our findings.

4.3.1 Results and Analysis

Figure 4.6 shows the PICTS spectra of a fresh (non-degraded) $MAPbI_3$ solar cell measured with a 1ms filling pulse. Using 6 rate windows (or delays), we constructed the Arrhenius plot from the spectra's peaks revealing an activation energy $E_a = 0.95$ eV and capture cross-section $\sigma_a = 4.50 \times 10^{-12}$ cm^2. This is a fairly deep trap, measured away from the conduction band, for a solar cell whose absorber material band gap is 1.58 eV. The linearity of the plot confirms the underlying assumptions of the measurement aforementioned in Sections 4.2.1.1 & 4.2.2.1. The corresponding current-voltage curve is available in Figure 4.7.

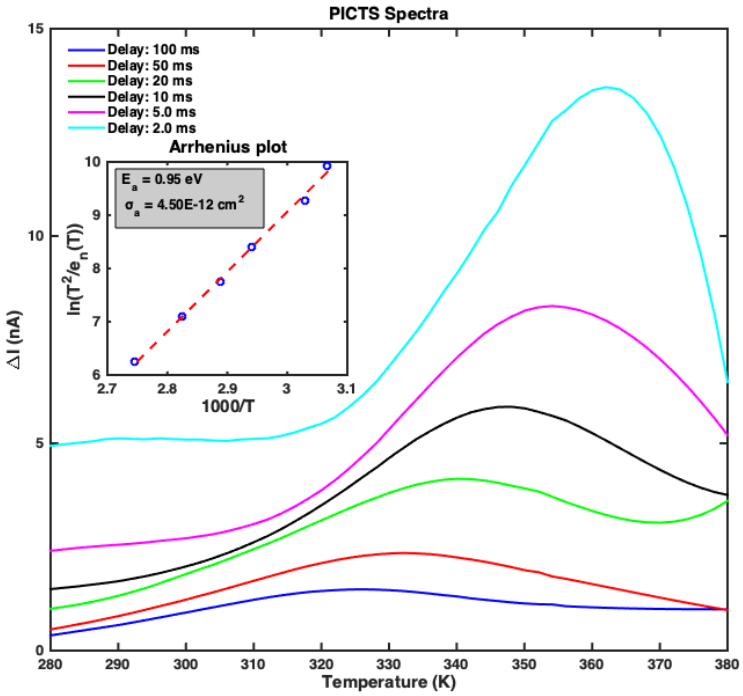

Figure 4.6: PICTS Spectra of a fresh $MAPbI_3$ solar cell with a 1ms filling pulse at 6 different rate windows (or delays). (**Inset**) Corresponding Arrhenius plot with extracted E_a and σ_a.

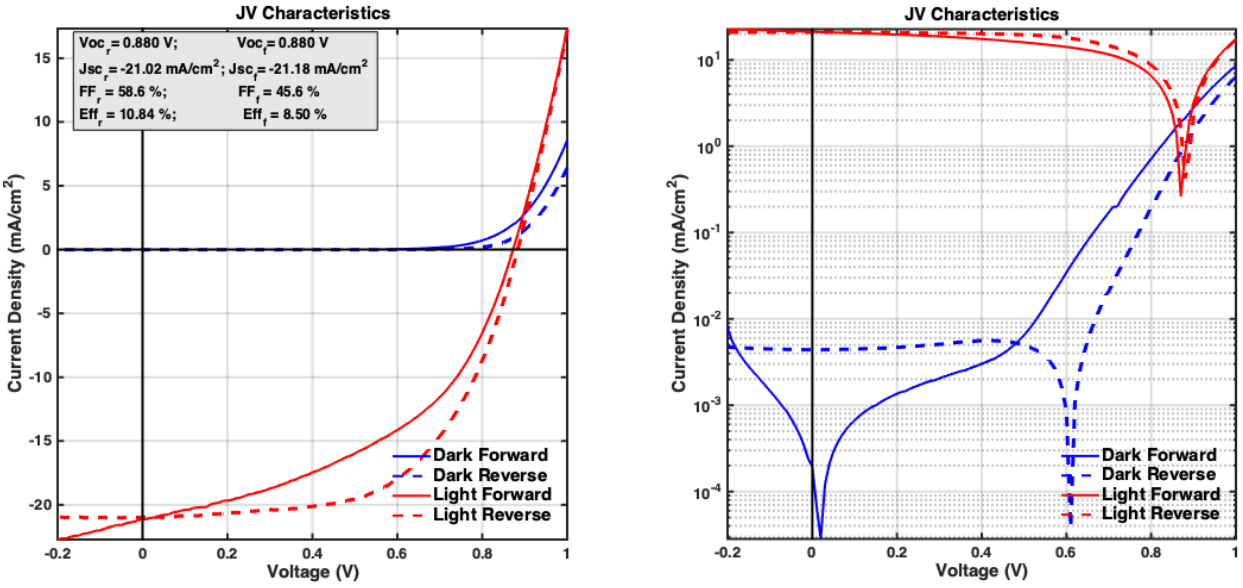

Figure 4.7: Photovoltaic characteristics in (**Left**) linear and (**Right**) semilog space for cell measured in Figure 4.6. Red curves are for illuminated cells under 100mW/cm^2 irradiance.

After successfully characterizing this fresh sample, we measured the trap signatures of $MAPbI_3$ solar cells degraded in the conditions described in Table 3.3. For each condition, the reported E_a and σ_a was the average calculated from the filling pulses ranging from 1 to 1000ms. Figure 4.8 shows that the average trap activation energy gets shallower as the device is degraded over time. The shift is exacerbated by degradation at higher temperature, where the rate of degradation is almost doubled at 55°C as compared to room temperature (25°C). The capture cross-section generally follows the same trends as E_a (See Figure 4.9).

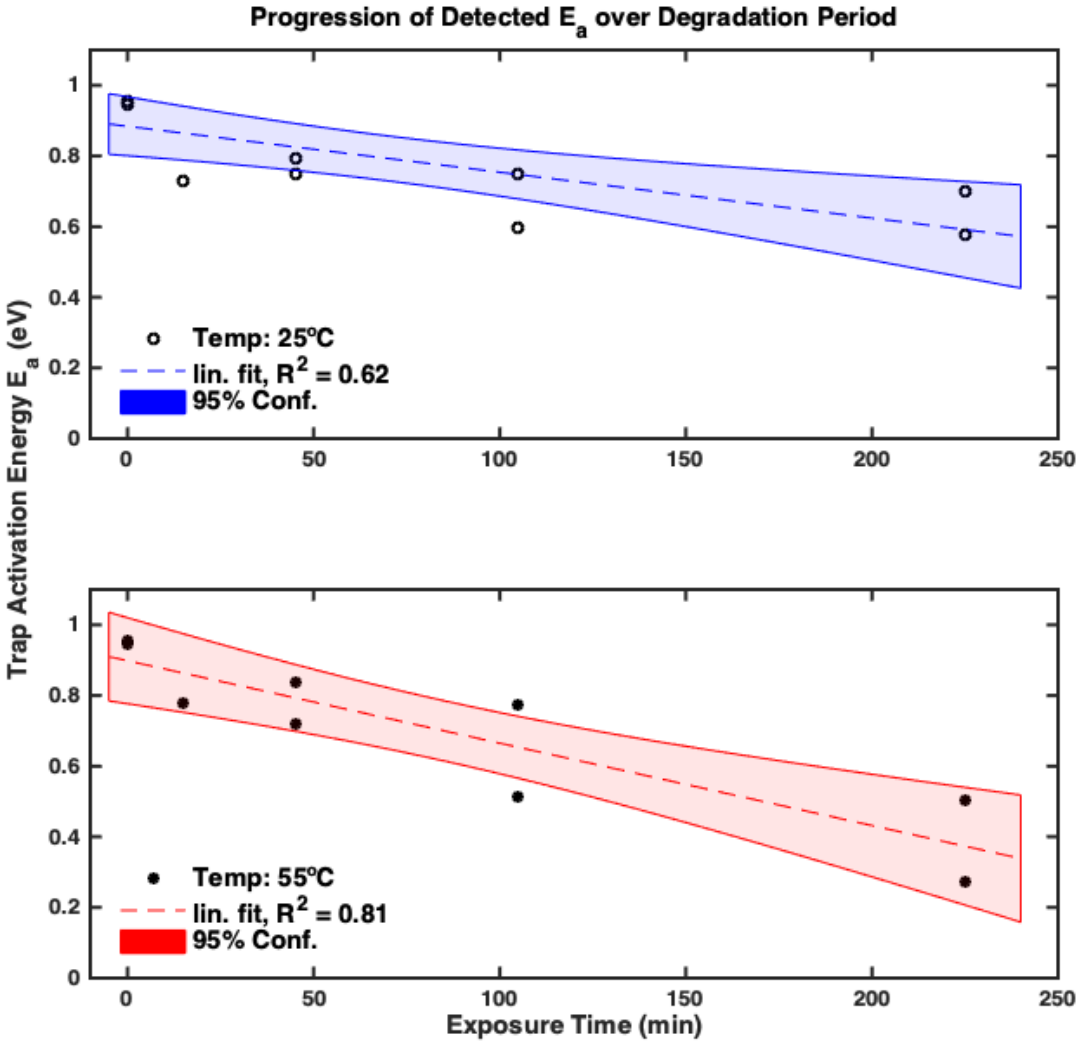

Figure 4.8: Evolution of the average trap activation energy over degradation time and condition. The linear fits for the top and bottom plots are is $\bar{E_a} = 0.88 - 1.3 \times 10^{-3}\ t$ and $\bar{E_a} = 0.90 - 2.3 \times 10^{-3}\ t$, respectively.

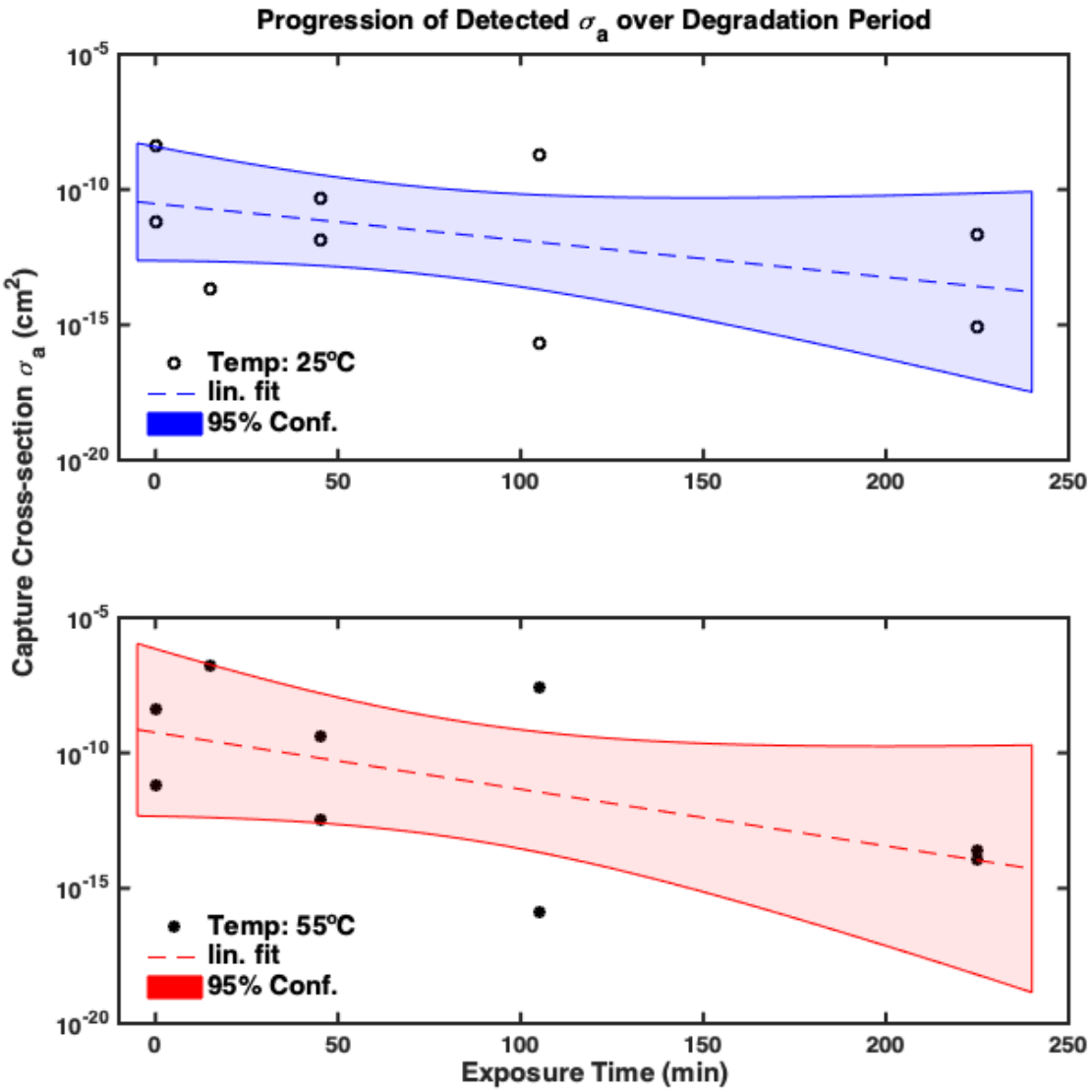

Figure 4.9: Evolution of the average capture cross-section over degradation time and condition.

To better understand why the average E_a got closer to the conduction band, we focused on the bottom plot of Figure 4.8 and plotted the raw activation energies instead of the averages. Figure 4.10 shows a range of states widening over the degradation period. Furthermore, inspecting the PICTS spectra of the $MAPbI_3$ solar cell degraded at 105min point of Figure 4.10, there is a general shift rightwards of the signal's peak as the filling pulse is increased (See Figure 4.11).

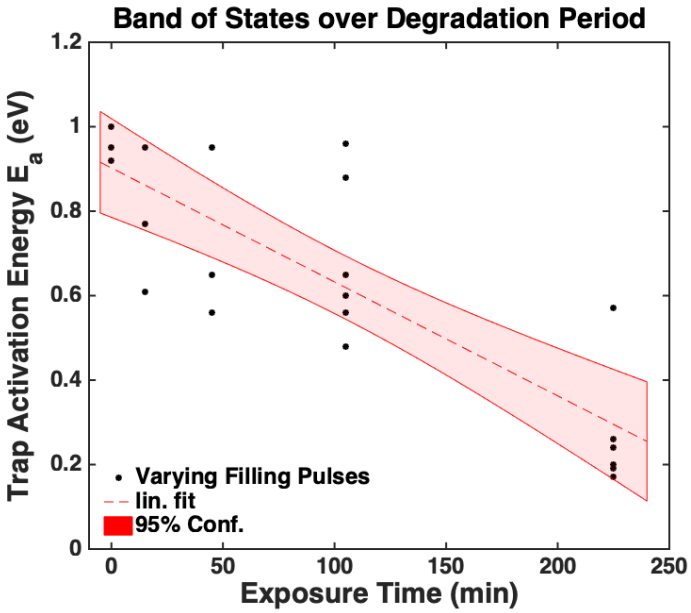

Figure 4.10: Evolution of raw trap activation energy with filling pulses, at each degradation point, ranging from 1 to 1000ms. Data extracted from Exp#11-15 of Table 3.3.

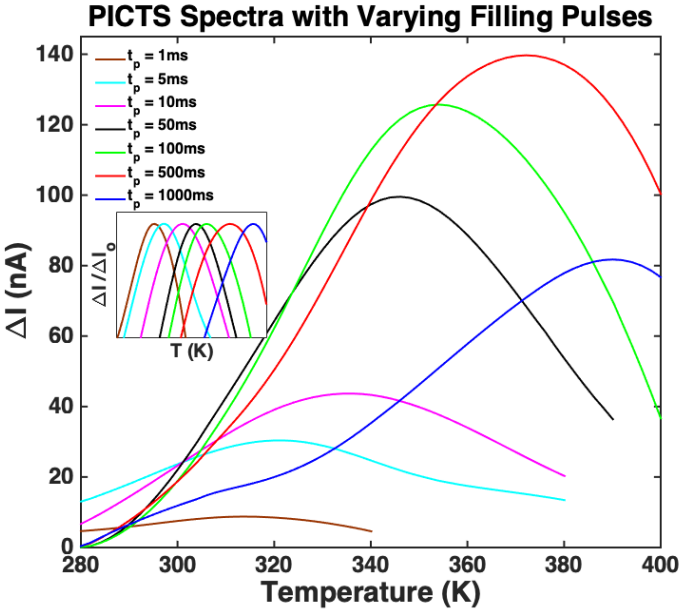

Figure 4.11: PICTS Spectra of sample from Exp#14 in Table 3.3 with varying pulses of period 2000ms. (**Inset**) Normalized plot of the same spectra highlighting the right shift of the signal peak with increasing pulse width.

Schröter et al. proposed two classifications of spatially extended defects in semiconductors: localized and band-like states [123]. This distinction lies in the comparison between the rate R_i at which the states reach their internal equilibrium and the emission (R_e) and capture (R_c) rates at which they reach equilibrium with the conduction band (See Figure 4.12). In this theory, defect states are band-like if $R_i \gg R_c, R_e$ and localized if $R_i \ll R_c, R_e$. Using simulated and measured DLTS spectra, they showed that localized states had isothermal peaks, whereas band-like states had shifting emission peaks.

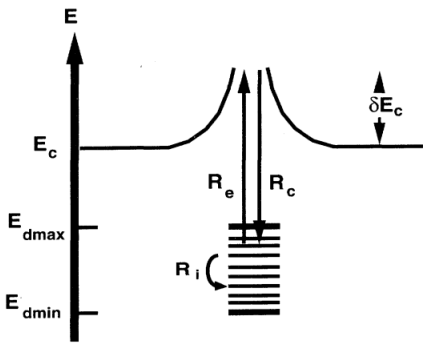

Figure 4.12: Extended defect with deep states in the band gap exchanging electrons with the conduction band by electrons emission (rate R_e) and electron capture (rate R_c) [123].

Based on this theory and our observations, we conclude that the degradation conditions of illumination and temperature combine to create spatially extended defects within the $MAPbI_3$ perovskite solar cells. These defects are characterized by band-like states since the PICTS spectra peaks shift with filling pulse. Prior to degradation, these states lie deep and narrow in the band gap with $0.92 \leqslant E_a \leqslant 1.0$ eV. By the end of the degradation period, they have widened to $0.17 \leqslant E_a \leqslant 0.57$ eV. It is very likely that we may have not measured the complete range of the band-like states post-degradation since we limited our study to filling pulses of maximum width 1000ms. Each trap may not have been completely filled with such pulses. This would explain why the range of the band-like states post-degradation does not fully overlap with the initial ones. We will tie this critical observation to physical mechanisms affecting the degradation of $MAPbI_3$ perovskite solar cells in the next chapter.

4.4 Summary

In this chapter, we explain the kinetics of deep level traps and discussed methods to effectively measure them. Then, we showed how fresh $MAPbI_3$ solar cells had traps deeply embedded within the band gap of the material. By varying the filling pulse width, we noticed that the band of trap states, initially highly localized deep within the band gap, was widening under increasing temperature and approaching the conduction band over the course of the degradation period. We will use this important observation in the next chapter to provide mechanisms tying deep level traps to photovoltaic, optical, and crystallographic data.

Chapter 5

Analysis of Degradation Data

After collecting the electrical, optical, crystallographic and electronic defect data, as described in Section 3.3 and summarized in Table 3.3, we discerned clear trends between the various responses and gained some understanding on the influence of the factors at play. In this chapter, we provide a discussion on the salient degradation mechanisms observed. We were aided in our analysis by the JMP Pro 15 statistical software package.

5.1 Observed Degradation Mechanisms

5.1.1 Photovoltaic Properties and Deep Level Defects

An examination of the correlation between the PV characteristics and the trap activation energy reveals that E_a's correlation to the PCE is mostly due to the J_{SC} and FF (See Figure 5.1). Given that the short-circuit current is a measure of the number of photocarriers extracted from the solar cell, and the fill factor is one for the efficiency of that extraction, it is logical that they track well with the trap activation energy. Indeed, if the traps are initially located deep in the band gap, they are less likely to interfere with the photogeneration process. However, as discussed in Section 4.3, as the trap's band of states widens over the course of the degradation process, they are more likely to capture generated carriers, prevent them from reaching the conduction band, and decrease the output of useful current. This is akin to an internal resistance process, which would also explain the decrease in fill factor (See Figure 5.2).

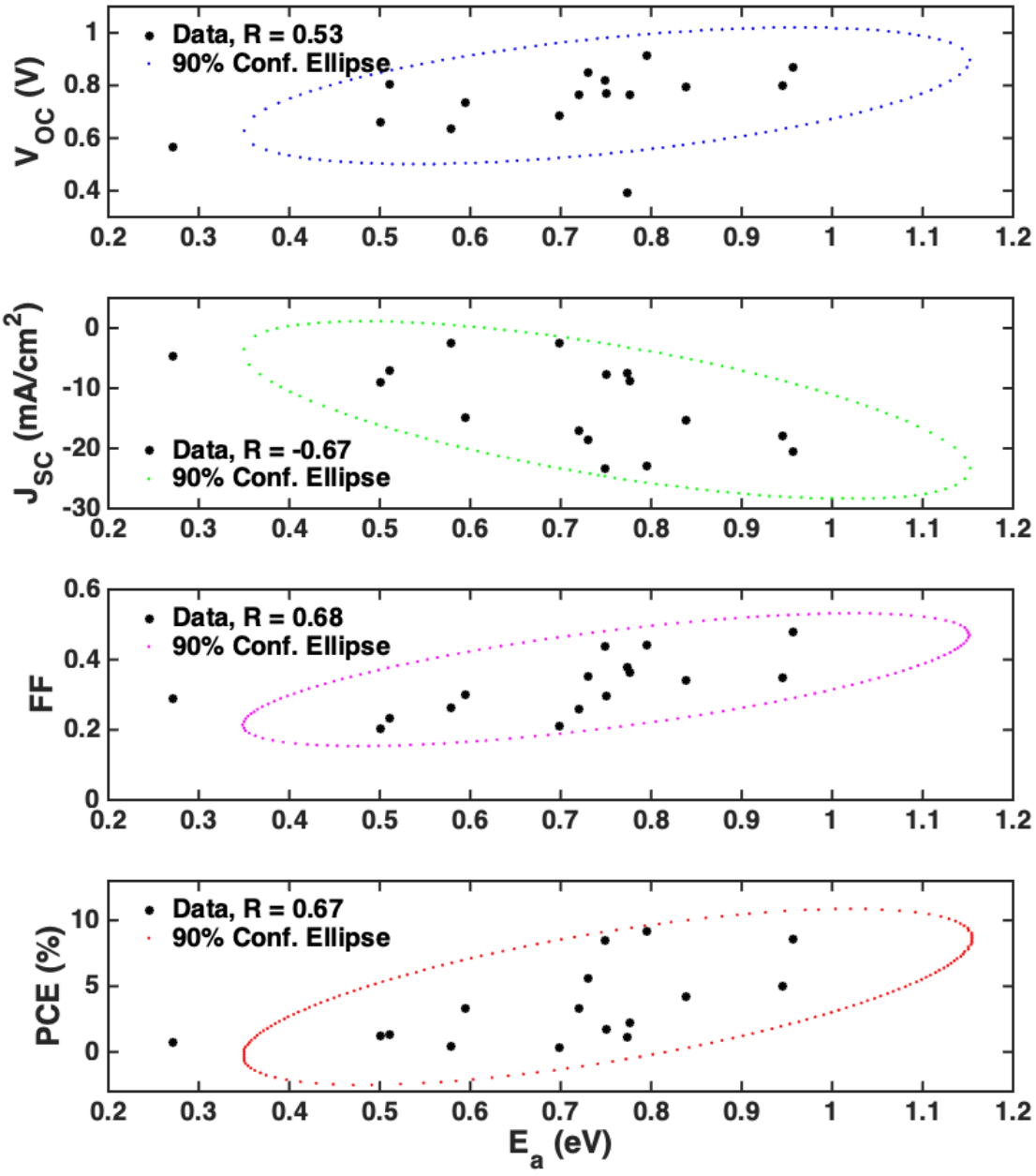

Figure 5.1: (**From Top to Bottom**) Correlation plots of the open-circuit voltage, the short-circuit current, the fill factor and the power conversion efficiency as functions of the trap activation energy. The 90% confidence ellipses of the dependent variables are included.

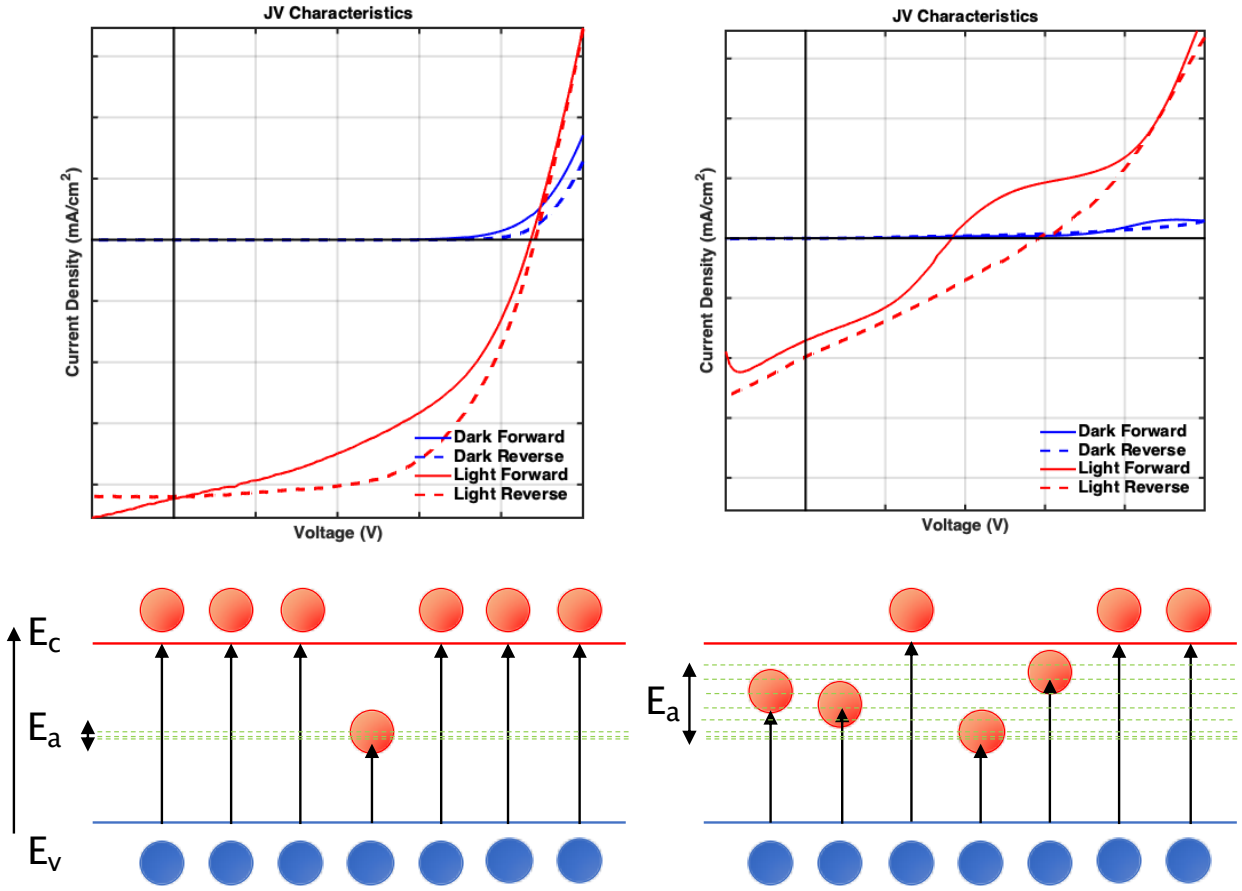

Figure 5.2: Illustration of the trap mechanism affecting the photovoltaic characteristics of perovskites. (**Left**) Pre-degradation, carriers are easily promoted to the conduction band upon illumination since the traps are located deep within the band gap. The corresponding JV characteristic shows an ideal exponential behavior. (**Right**) Post-degradation, more carriers are captured due to the widened band of trap states resulting in loss of current and increased internal resistance characterized by the more linear JV curve.

5.1.2 Crystals and Deep Traps

The correlation between the trap activation energy and the crystallographic data is also fascinating (See Figure 5.3). Indeed, E_a tracks well with the crystallite size as the larger it is, the shallower the traps. Focusing on the crystallites, our analysis shows that the degradation time (under illumination), the temperature and the interaction of both are significant factors driving the change in crystallite size ($p_{CZ|time} = 0.002$, $p_{CZ|Temp} = 0.01$, and $p_{CZ|Temp\times time} = 0.04$). This is consistent with the theory of crystal growth mainly driven by heat [124], which both the incident light of 1 sun and the temperature in the environmental chamber provided. This growth results in the reduction of the average grain boundary area, which in turn decreases the excess free energy associated with them. Because of the latter, the crystallite to crystallite microstrain will decrease, which is what we observe in our measurements (See Figure 5.4). Possible physical phenomena that drive this change may include (but may not be limited to) non-uniform lattice distortions, faulting, dislocations, antiphase domain boundaries, and/or grain surface relaxation [125].

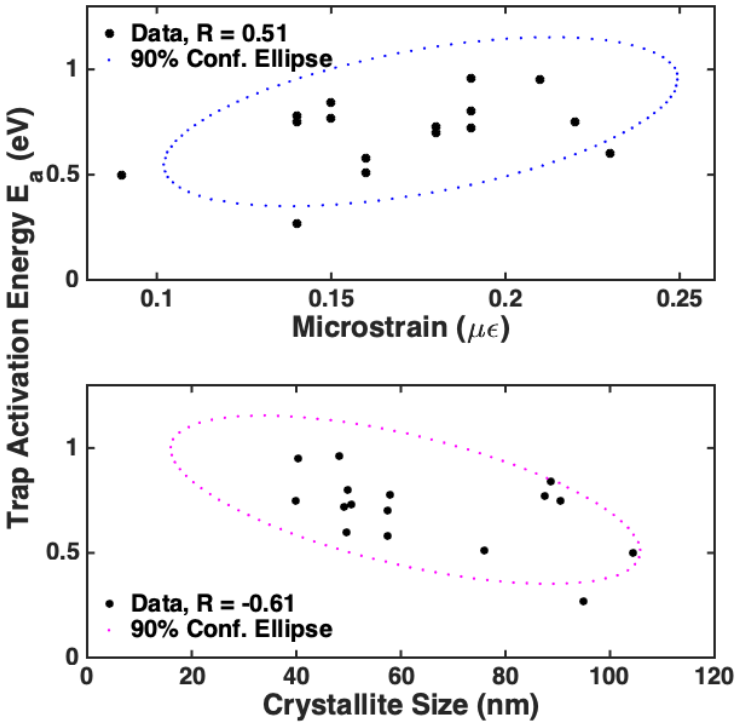

Figure 5.3: Correlation plots of the trap activation energy as a function of (**Top**) the microstrain and (**Bottom**) the crystallite size in the perovskite absorbing layer. The 90% confidence ellipses of the dependent variables are included.

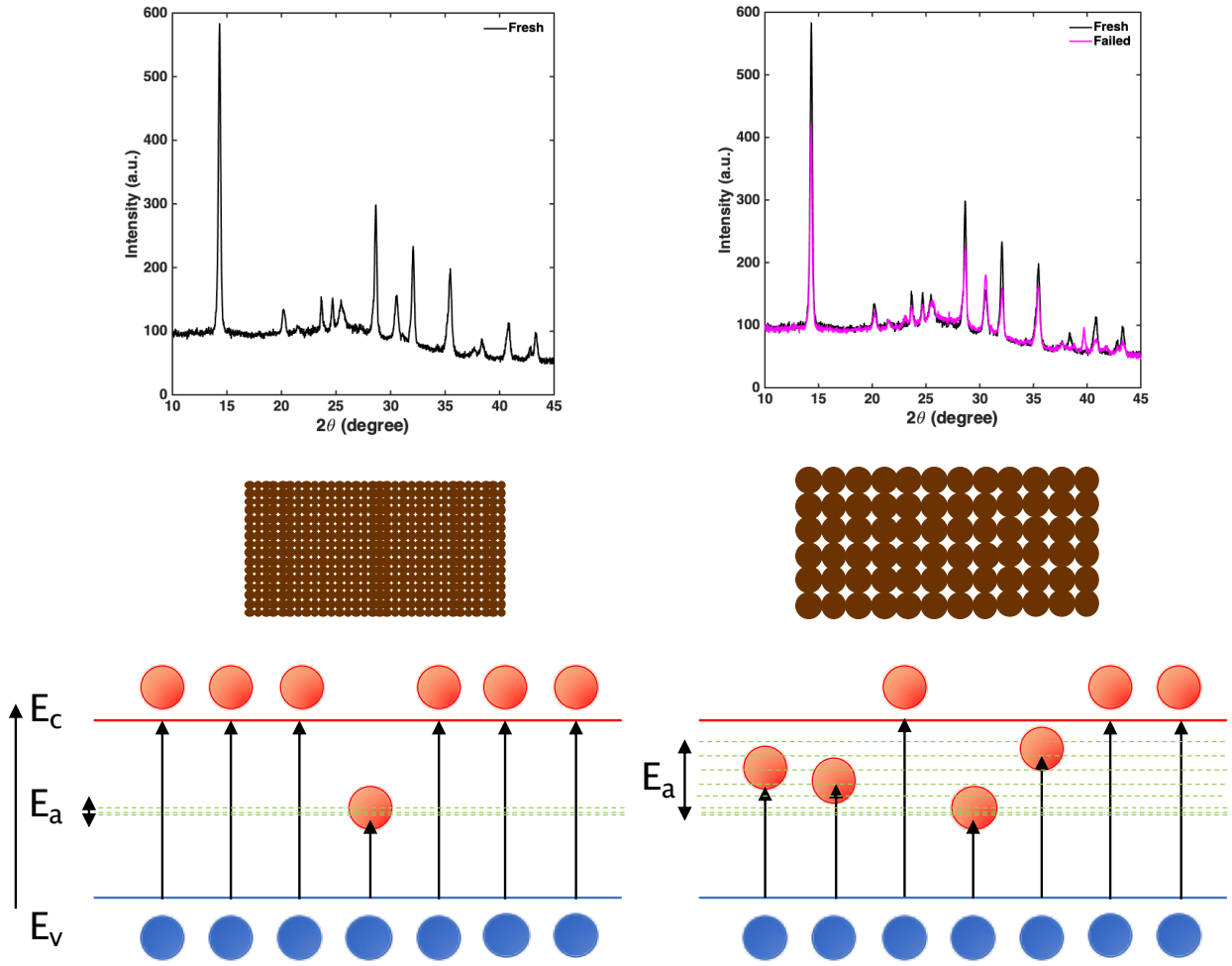

Figure 5.4: Illustration of the trap mechanism affected by the crystal properties of perovskites. (**Left**) Pre-degradation, the XRD indicates that smaller crystallites with high grain boundary area prevail in the perovskite with trap states localized deep within the band gap. (**Right**) Post-degradation, the crystallites are larger with reduced grain boundary area. This drives the widening of the band of trap states. The corresponding XRD shows the failed cells with generally narrower peaks than the fresh ones, thus confirming a net decrease in microstrain.

5.1.3 Optical Absorption and Traps

The correlation between the optical absorption and the trap activation energy becomes relevant once we control for temperature (See Figure 5.5). Our statistical test confirms these observations by revealing that the degradation period ($p_{A550|time} = 0.009$) and its interaction with temperature ($p_{A550|Temp\times time} = 0.01$) are the most influential factors in the decrease in absorption. This decrease can partly be explained by the widening of the defect band of states with temperature. Indeed, this evolution increases the probability of carriers getting captured in that band, which in turn would prevent photons from promoting carriers to the conduction band. The effect is therefore a loss in light absorption critical for the performance of the solar cell (See Figure 5.6).

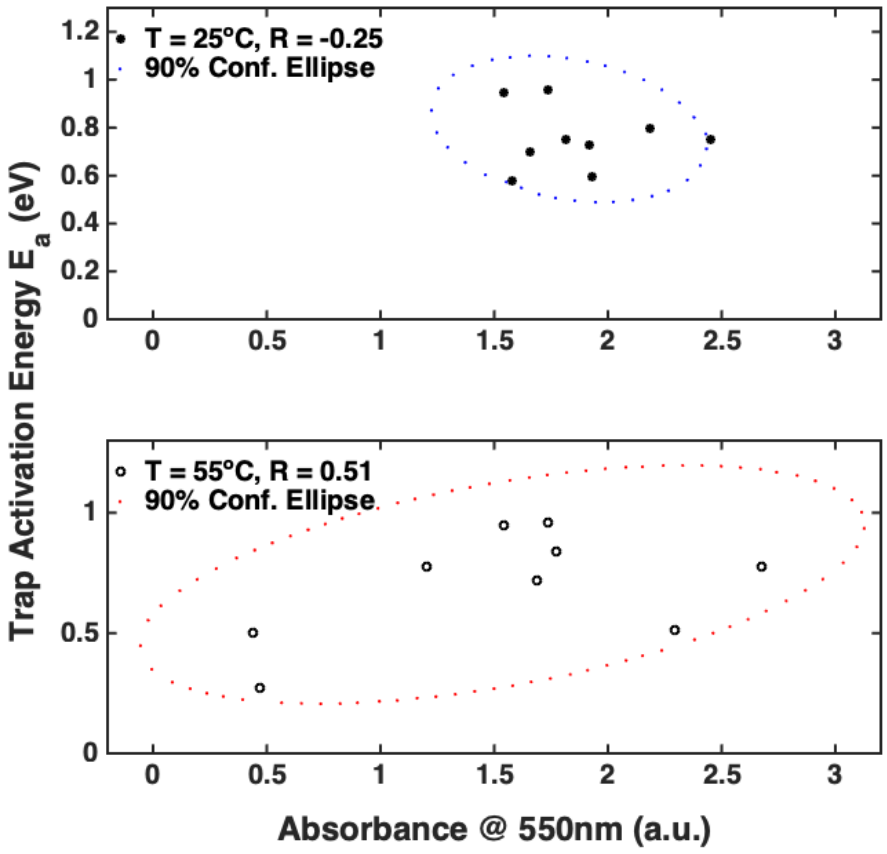

Figure 5.5: Correlation plots between the trap activation energy and the absorbance at 550nm at (**Top**) 25°C and (**Bottom**) 55°C. The 90% confidence ellipses of the dependent variables are included. Note how the top ellipse is almost circular, suggesting no relevant correlation. This is in sharp contrast with the bottom one.

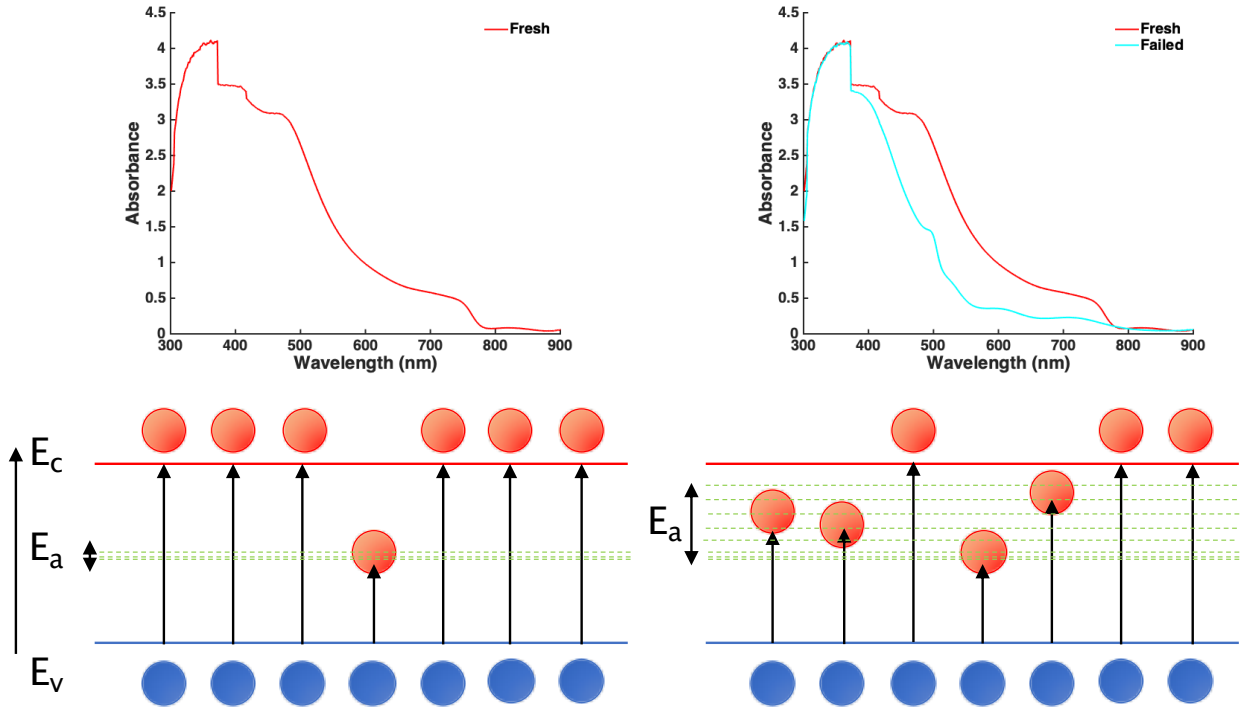

Figure 5.6: Illustration of the trap mechanism affecting the absorption properties of perovskites. (**Left**) Pre-degradation, most incoming photons of wavelength above the band gap are fully absorbed to promote the generation of photocarriers. (**Right**) Post-degradation, the extended band of trap states impedes the full absorption of photons thus reducing the visible range absorption properties of the perovskite.

5.2 Discussion

Our observations lead us to think that preventing the formation of a large number of new states closer to the band edges is an essential key to unlocking their long term stability. Indeed, extended traps impede the full absorption of photon and the generation & collection of photocarriers. This process is mainly driven by the growth of crystallites within the perovskite. Preventing that crystallite growth is essential in extending the lifetime of perovskite solar cells, and we think we can achieve it via two main methods. One would be to improve the formulation of the perovskite, especially at the A-site of its ABX_3 structure. Reducing the effective radius r_A of the A cation would shift the tolerance factor of the crystal structure toward the more desirable cubic lattice structure. It would also reduce its sensitivity to higher temperature, which is essential in promoting the crystallite's growth because heat is a significant driving factor. Optimizing r_A should be done by accounting for the narrow window in which functional and stable perovskite structures are expected to form. Indeed, Bartel et al. provided a predictive probabilistic model that portrays that opportunity window as a function of the cations' radii in the ABX_3 structure (See Figure 5.7) [126].

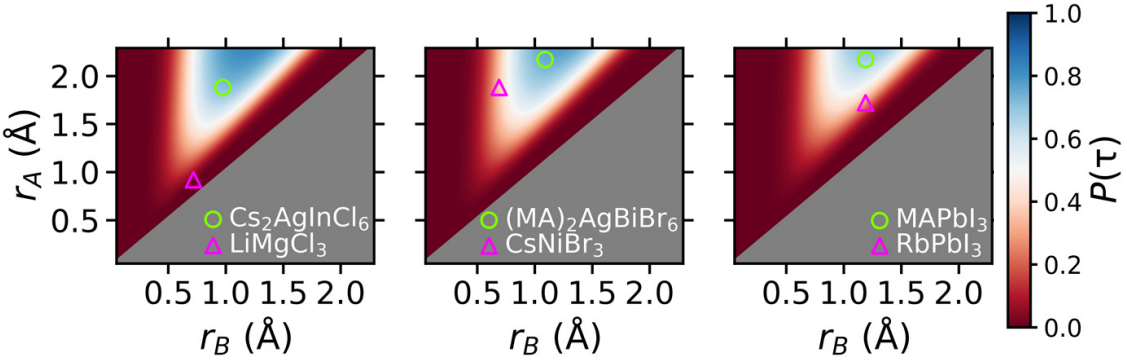

Figure 5.7: The effects of ionic radii on the stability of halide perovskites (from left to right, the halides used were Cl^-, Br^-, I^-). The radii r_A and r_B are the ones of the A and B cations of the ABX_3 perovskite structure. $P(\tau)$ is the probability that a perovskite will be stable as a function of Bartel's tolerance factor τ. The experimentally realized perovskites and nonperovskites are shown as open circles and triangles, respectively [126].

The other method for reducing the formation of extended states would be by doping the perovskite. For instance, the incorporation of divalent ions such as alkaline earth metals Sr and Mg in limited amounts can increase the microstrain in the perovskite and reduce its crystallite size. It will also maintain its Goldschimdt tolerance factor t between 0.8 and 1.0, which is necessary for forming a 3D perovskite structure. From DFT calculations, Phung et al. showed that the dopants could substitute either the A or B cation in the ABX_3 or be incorporated interstitially (See Figure 5.8) [127]. The increased microstrain in the low doping regime showed an increase in V_{OC} and improved stability under light exposure in an inert environment (See Figure 5.9).

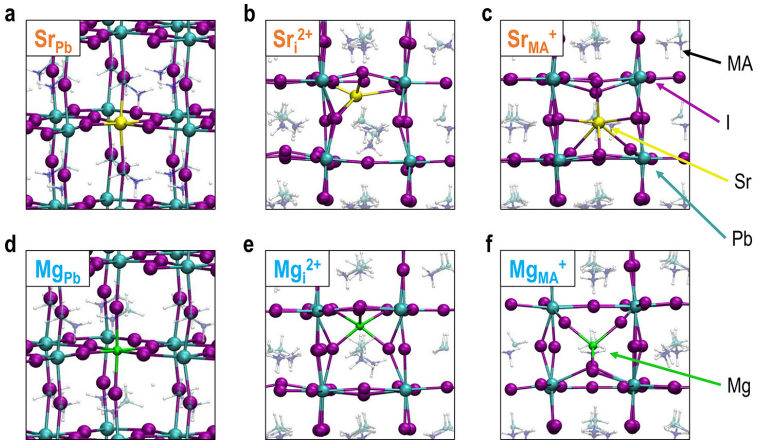

Figure 5.8: Potential doping mechanisms of $MAPbI_3$ calculated by DFT for Sr (top) and Mg (bottom). Visualization of (**a** & **d**) Pb^{2+} substitution, (**b** & **e**) interstitial incorporation, and (**c** & **f**) MA substitution [127].

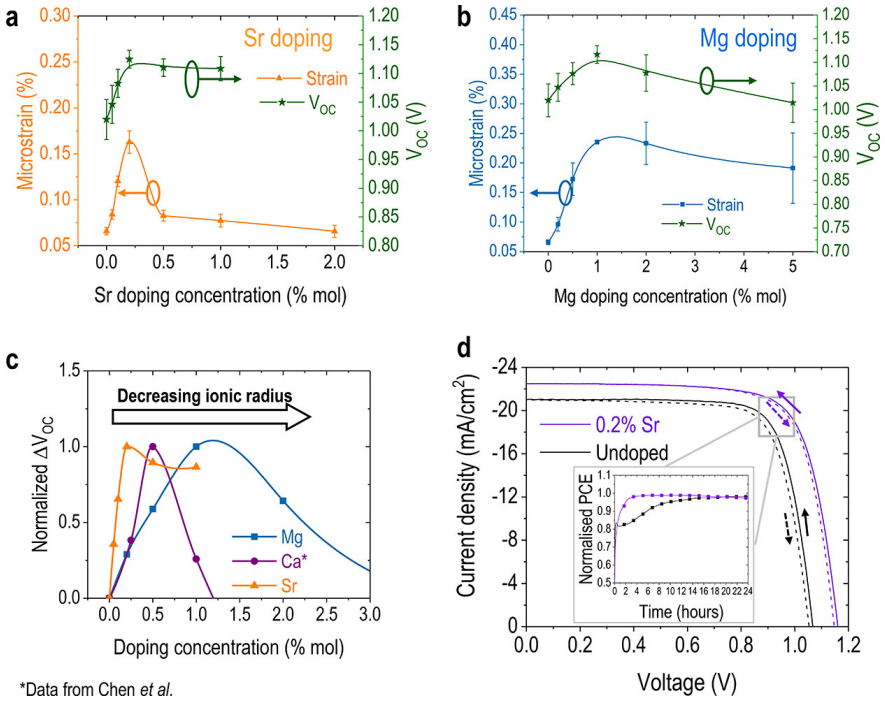

Figure 5.9: Device performance upon doping. Correlation between V_{OC} with microstrain from GIXRD refinement of (**a**) the Sr-doped and (**b**) Mg-doped $MAPbI_3$ devices. (**c**) V_{OC} trend with respect to nominal doping concentration of 3 alkaline earth metal ions. (**d**) J-V curve of the best 0.2% Sr-doped with antireflection coating and undoped $MAPbI_3$ device measured at standard AM1.5 1 sun equivalent condition with a 100mV/s scan rate. Arrows indicate scan direction. The inset is continuous MPP tracking in N_2 at 25°C in simulated global AM1.5 solar spectrum with UV cut-off at 380nm for 24h [127].

5.3 Summary

In this chapter, we analyzed the relationships between the evolution of deep level traps and the photovoltaic, crystallographic, and optical absorption properties of perovskites, summarized in Figure 5.10. We note that over the course of the degradation period of the $MAPbI_3$ solar cells, the average trap activation energy (E_a), PCE, and absorption at 550 nm (A550) decreased, while the average crystallite size (CZ) increased. With our significance level α set at 0.1, we found that all of these effects were significant as a function of time (from Figure 3.21, $p_{E_a|time} = 0.00001$, $p_{PCE|time} = 0.001$, $p_{A550|time} = 0.009$ & $p_{CZ|time} = 0.002$). We posited that the extension of the band of trap states over time, illumination, load, and temperature impeded the collection and generation of free carriers within the absorbing layer. We believe that process to be driven by the growth of crystallite. We thus concluded that reducing the formation of new trap states closer to the band edges could unlock longer stability. We finally discussed a couple of methods that could assist in that endeavor.

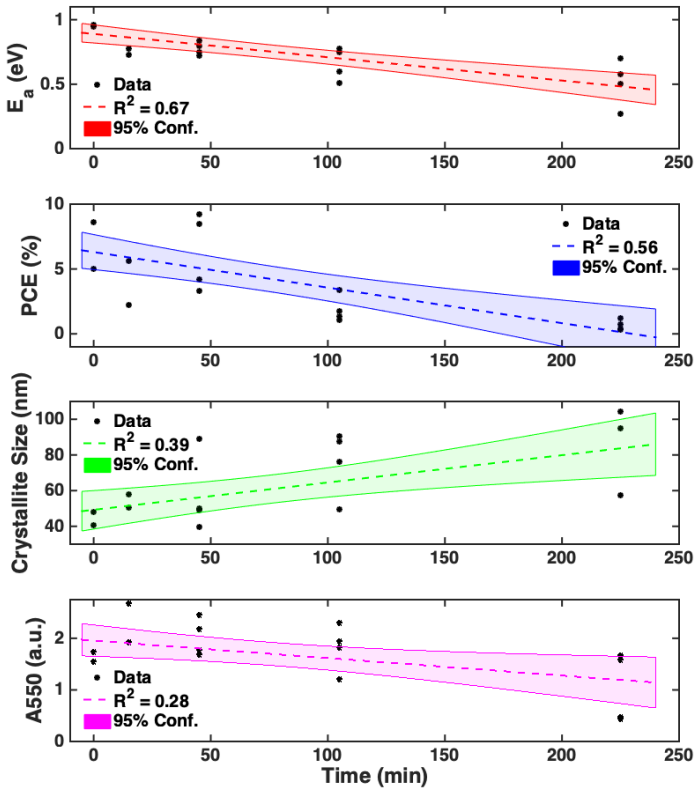

Figure 5.10: (**From Top to Bottom**) Evolution of the trap activation energy, power conversion efficiency, crystallite size and absorbance at $\lambda = 550$ nm over degradation time. The coefficient of determination R^2 of the linear fits are included along with their 95% confidence intervals.

Chapter 6

Conclusions, Recommendations & Future Work

6.1 Conclusions

In this work, we successfully applied the design of experiment (DOE) methodology to undergo a comprehensive multifactorial study of the degradation of perovskite solar cells in operation. We started by establishing how uncommon these multifactorial studies are in the perovskite community and highlighting the benefits of this approach to a device that still fails to meet the long-term stability standards necessary to making it a marketable product. These multifactorial studies show the usefulness of a holistic approach to the investigation of degradation in perovskite solar cells. Indeed, they allow the ranking of various degradation factors by relevance and the significance of their confluence. Then, we explained the DOE methodology and showed why it is a robust statistical analysis framework. We showed how we methodically built our own experimental space by using temperature, electric load, and time as the degradation factors. To understand their leverage, we tracked the photovoltaic, optical, crystallographic, and deep level defect properties of the $MAPbI_3$ solar cells. Our work confirmed the influence of interaction factors like Temperature×Load and Temperature×Time in the degradation of perovskite solar cells. These terms would not have been revealed in a one factor at a time study. We detailed how using PICTS as a method of measuring deep level defects was appropriate to studying photosensitive devices like ours. PICTS helped us uncover that a band of trap states, initially narrowly constricted deep in the band gap of $MAPbI_3$, widened over the course of the degradation period. From our DOE analysis, we found that this effect was significantly correlated with the degradation of the other responses tracked in this study. We posited that the extension of the band of trap states over time, load, and temperature impeded the collection and generation of free carriers within the absorbing layer. We believe that process to be driven by the growth of crystallites. We thus concluded that reducing the formation of these traps could unlock longer stability. Finally, we discussed improving the crystal structure to stabilize its crystallite growth by

changing its constituent compounds or by doping.

This work allowed us to gain a holistic understanding of concurrent degradation mechanisms under realistic atmospheric conditions for perovskite solar cells in operation. We demonstrated that higher order interaction factors must be considered in studying the stability of this technology experimentally or theoretically. Lastly, this study provides the framework for systematically investigating the degradation of novel solar cells.

6.2 Recommendations & Future Work

Follow-up studies to this work should first focus on collecting and analyzing humidity sensitive data for the evolution of crystallite size and trap activation energy over the course of the degradation period. We do not expect major deviations from the general trends observed in this work, but it will nonetheless complete the holistic picture we sought to paint. This will also serve as a basis for building predictive lifetime models, which can be enhanced once degradation data for properly encapsulated cells are also collected.

An attempt should also be made to confirm the physical phenomena discussed by, for example, correlating electron paramagnetic resonance (EPR) measurements with PICTS. Indeed, EPR is the most successful technique for the identification of lattice defects in semiconductors. Analysis of EPR signals can reveal whether the defects are due to dangling bonds in dislocations, point-defect clusters or a confluence of both. Omling et al. have employed this technique to suggest microscopic models for defect centers in plastically deformed silicon [128].

We also think that degradation studies as functions of fabrication techniques will be important as we move closer to commercialization. Indeed, this study has been entirely conducted on spin-coated 0.05 cm^2 devices, and the trade-offs in quality once a technique more suitable for larger area and throughput is employed, such as gravure printing, should not be accurately quantified. As the perovskite formulation is optimized, as discussed in Section 5.2, so should our understanding of the impact of those fabrication techniques. This knowledge will help the industry properly match the cost, quality and throughput of a given technique with its intended application.

Finally, we recommend studies linking the fabrication and degradation of perovskite cells to their cosmetic appearance. This is a major problem that the silicon solar industry is currently grappling with. Many residential customers are unwilling to install panels on their rooftops that are not aesthetically pleasing to the eye. In scientific terms, this can be expressed as seeking panels that are uniformly colored solar cells with excellent angular insensitivity while maintaining a high power conversion efficiency. This endeavor requires a high degree of control on the crystallization of process of the absorbing layer, potentially using of sensitizer to highlight preferred colors, and optimizing the absorption, transmission, and reflection of given wavelengths in the visible spectrum. Any technical improvement that can ease the wider adoption of solar technology should be thoroughly explored.

Appendix A

Solar Cell Operation

A solar cell is a photosensitive semiconducting device capable of generating electric power once incident photons impinge upon it. Light of energy $h\nu > E_g$, the band gap of the absorbing layer of the solar cell, allows for the establishment of two quasi-fermi levels: one for holes, the other for electrons. Concurrently, free electron-hole pairs are created and quickly promoted to either the conduction (E_C) or valence (E_V) band for extraction of useful current. When no bias is applied to the device, the current measured is called the short-circuit current (I_{SC}) or short-circuit current density (J_{SC}) when divided by unit area of the solar cell. The general equation for the current density in a solar cell is:

$$J = J_0(e^{\frac{qV}{nkT}} - 1) - J_L$$

where J_0 is a pre-exponential term dependent on the intrinsic properties of the semiconductor, q is the electron charge, n is the ideality factor (usually equal to unity), k is the Boltzmann constant, T is the temperature, and J_L is the photogenerated current or photocurrent. J_L is not equal to J_{SC}, but in practice, they are close enough in value that they are used interchangeably. Depending on the convention used, the J_{SC} may be reported as a positive or negative value. The potential bias measured under illumination but at zero current is called the open-circuit voltage (V_{OC}). Because the current-voltage curve is exponential, the fill factor (FF) is a metric used to gauge the squareness of the "knee" of the curve. It is obtained by dividing the maximum output power by the hypothetical optimal power obtained if the JV curve was perfectly squared. That is

$$FF = \frac{P_{max}}{J_{SC} \cdot V_{OC}}$$

By definition, $0 < FF < 1$. Finally, the power conversion efficiency (PCE) conveys the percentage of electric power generated by the cell from incident light. It is calculated as

$$PCE = \frac{P_{max}}{P_{in}} = \frac{V_{OC} \cdot J_{SC} \cdot FF}{P_{in}}$$

where P_{in} is the power of the incident light. The standard in reporting the PCE is to use $P_{in} = 100$ mW/cm^2 = 1 sun. Figure A.1 summarizes our brief description.

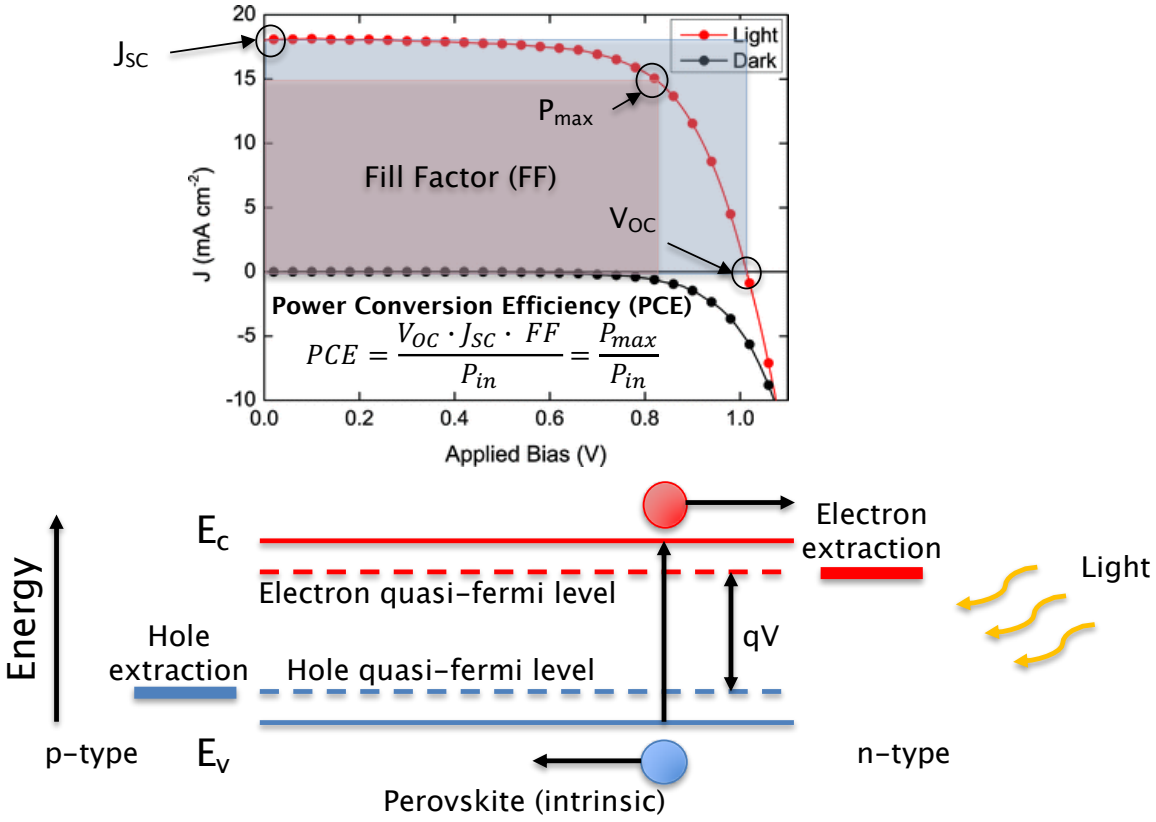

Figure A.1: (**Top**) Typical JV curve of a solar cell with the different figures of merit labelled. The curve here is inverted to report positive J_{SC}. In this work, we use non inverted curves with negative J_{SC}. (**Bottom**) Illustration of the carrier extraction process in an illuminated perovskite solar cell.

Appendix B

Perovskite Market

With more than 500 GW of PVs installed to date, silicon photovoltaics remain the incumbent technology with its cost now at \$0.25/W and declining capital expenditures (capex) [129]. Perovskites offer a strong alternative with the potential for extremely low manufacturing costs through solution processing that could compete with silicon. However, new cleantech technologies have historically struggled to scale-up, with their capital intensity resulting in long timelines for commercialization that are incompatible with traditional venture capital funding models, that lead to lower success rates for cleantech startups as compared to software and medical ventures. Today's leading PV module manufacturers drive down prices by producing modules at the GW/year scale, largely in regions with low labor costs, i.e. Asia. Nonetheless, according to Mathews et al. [130], there is a path to entry for newcomers via commercialization in the growing alternative markets such as the Internet of Things (IoT) applications, building-integrated photovoltaics (BIPV), telecommunications [131], vehicle integrated, and others where higher margins are possible [132, 133, 134, 135]. In their analysis, they show that such strategies can enable a sustainable route to scale, allowing perovskite manufacturing companies to leverage higher prices in alternative PV markets to overcome the capital intensity barrier for new cleantech products and reach significant scale before entering the wider solar power market. By focusing on the manufacture of flexible single-junction perovskite modules, a relatively low manufacturing cost can be achieved at small scales owing to the low capex contribution of roll-to-roll (R2R) tools to the final module cost for solution processed perovskites. Figure B.1**B** shows that the modeled minimum sustainable price (MSP) ranges from \$3.30/W for a small-scale annual production of 0.3 MW/year to \$0.53/W for an annual production capacity of 1 GW/year. The latter price is still not low enough to sell into residential or utility scale photovoltaic markets at a profit given that recent module prices have been in the \$0.20-\$0.40/W range [136], but advances in materials cost and efficiency ought to considerably reduce the price point. Indeed, Figure B.1**C**&**D** show that materials are the overwhelming burden in the cost of the module, while Figure B.1**E**&**F** show that the MSP is most sensitive to both the materials cost and the module efficiency. Figure B.2 highlights the potential growth rates for flexible perovskite manufacturing. Growth rates of 100% and greater are achievable for average selling prices obtainable

in alternative PV markets and show that perovskite manufacturing can be compatible with venture capital funds that typically look for growth opportunities with return on investments equivalent to $\sim$ 100% year-on-year growth. Still, the average selling price projected of \$0.72/W for a 1 GW/year plant is about double the typical price currently obtained for PV modules in the grid-connected residential, commercial, and utility PV markets.

Another route for perovskites to enter the market place is via expansion of the production line of current silicon PV modules. By leveraging the existing silicon cell and module facilities, tandem capacity can be added by only building the perovskite top cell manufacturing line, a significantly cheaper investment than building an entire tandem manufacturing line. The 4T configuration is ideal for this type of expansion since the top cell is fabricated entirely independently from the bottom cell, allowing the manufacturing lines to operate in parallel. Furthermore, assuming the perovskite top cell is to be fabricated in superstrate configuration onto the front glass, and then integrated as the front glass would be in a typical silicon module manufacturing process, the silicon module fabrication process would remain almost entirely unchanged. Mathews et al. modeled the manufacturing cost of these tandem modules onto a passivated emitter and rear cell (PERC) silicon bottom cell assuming a 2 GW/year plant [130]. Figure B.3**B** shows that the average MSP for the modules produced in such a factory would be \$63.33/m^2, assuming a tandem module PCE of 25.8% PCE and 18% for the single-junction modules. Figure B.4 models the growth rates of tandem manufacturing. In the fixed margin scenario, a 15% margin is used, where margin is defined as the percent of the selling price that exceeds manufacturing cost (materials, labor, depreciation, utilities, and operating expenses). For the efficiency-adjusted margin scenario, all single-junction modules use a 15% margin while the tandem module margin is increased to reflect the added value of high-efficiency. The tandem module selling price is set such that the dollar-per-watt price is equal to the dollar-per-watt of the silicon single-junction, resulting in a margin of 24%. The co-dependent growth scenario assumes an existing silicon manufacturing plant investing in perovskite-silicon 4T tandems by building top cell manufacturing capacity to combine with a portion of the silicon production as the bottom cell, thus producing both 4T tandems and silicon single-junctions as the tandem capacity is expanded. The independent growth model refers to a self-funded growth. Figure B.4**B** shows that the co-dependent growth with the efficiency adjusted margin leads to a rapid expansion of manufacturing capacity within a decade.

The models presented show the potential routes for perovskite market penetration assuming proper scaling and management of the issues of toxicity and stability. Nevertheless, Oxford PV, a company established in 2010, has completely embraced the tandem perovskite-silicon route. In December 2018, they announced a 1 cm^2 tandem cell of record 28% efficiency [61]. Swift Solar, established in 2019, is focused on the lightweight and flexible perovskite market [137]. Hunt Perovskite Technologies, Microquanta Semiconductor, Energy Materials are all companies that are focusing on producing large-area single-junction perovskite modules [138]. The perovskite industry is quickly taking shape.

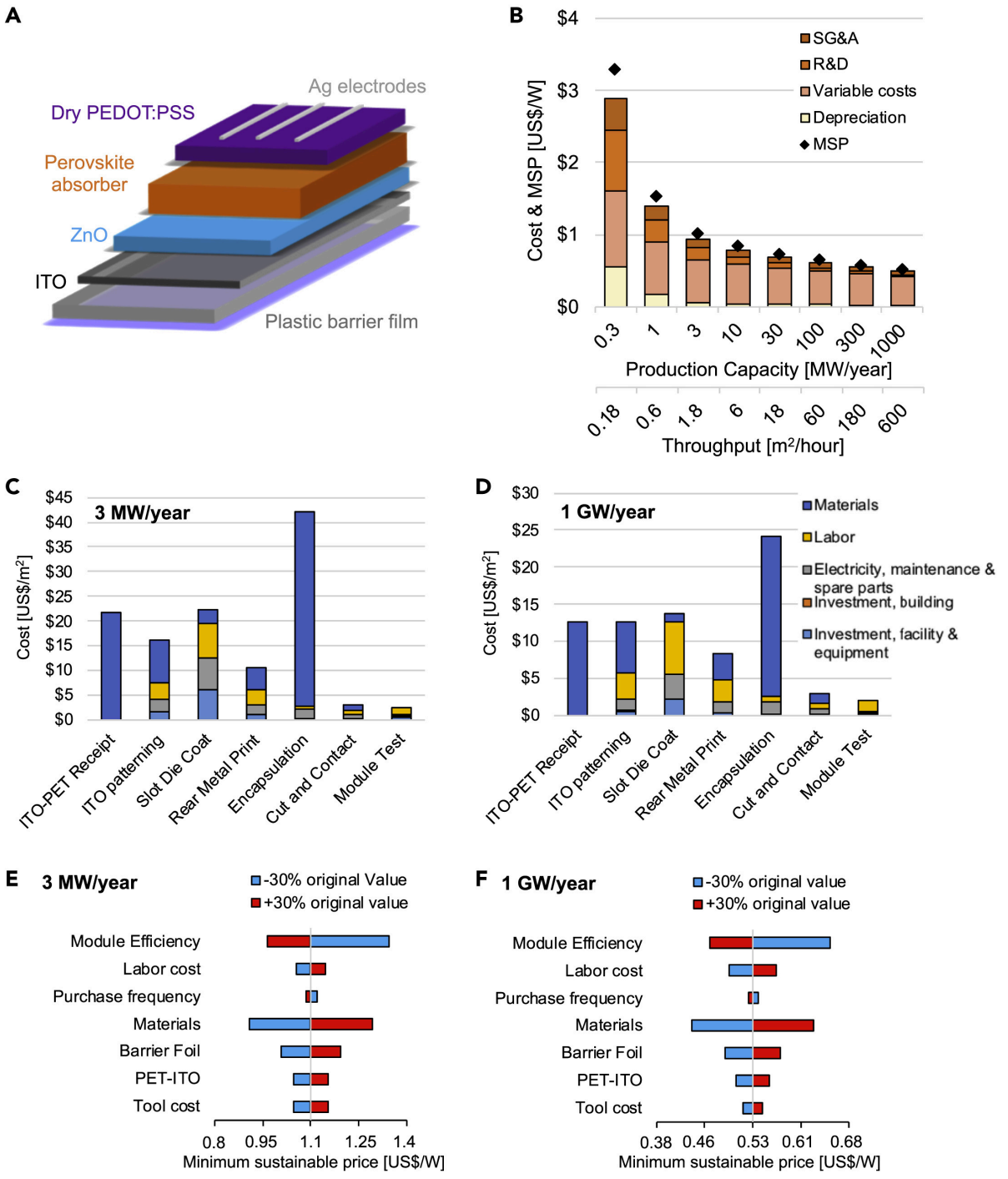

Figure B.1: (**A**) Schematic of the cell structure modeled; (**B**) Production cost and MSP for R2R perovskite modules vs scale; Breakdown of the costs per manufacturing step at a production capacity of (**C**) 3 MW/year & (**D**) 1 GW/year; Sensitivity of the module MSP to various parameters at a production capacity of (**E**) 3 MW/year & (**F**) 1 GW/year [130].

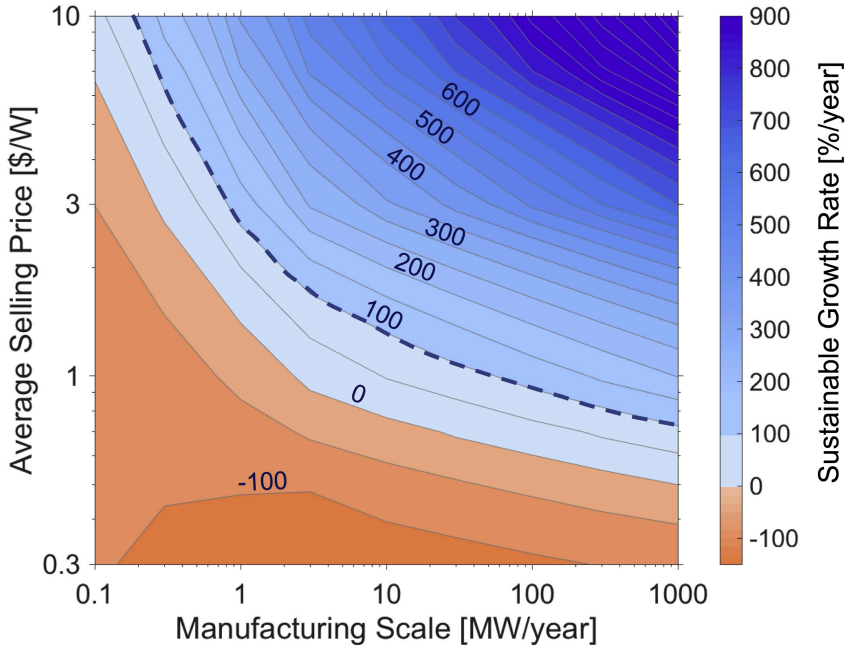

Figure B.2: The annual growth rate of a perovskite PV manufacturing plant vs. manufacturing scale and average selling price–the dashed blue line divides the regions above and below 100% year-on-year growth [130].

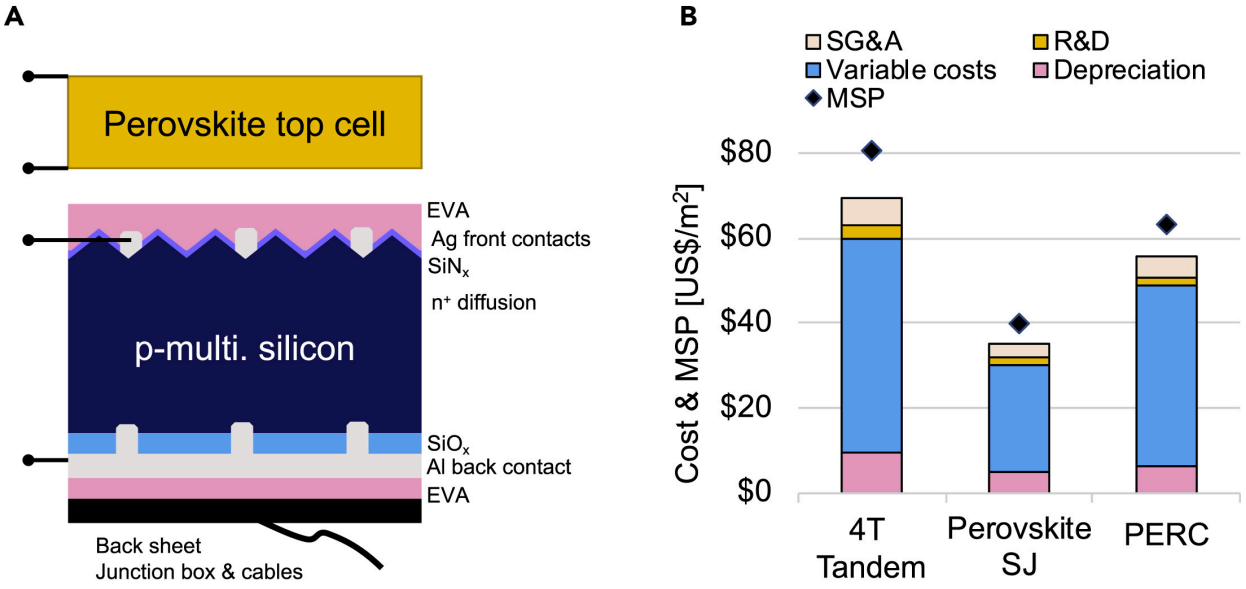

Figure B.3: (**A**) Schematic of the modeled 4-T perovskite-silicon tandem module and (**B**) the manufacturing cost and MSP of the individual sub-cells and the tandem module [130].

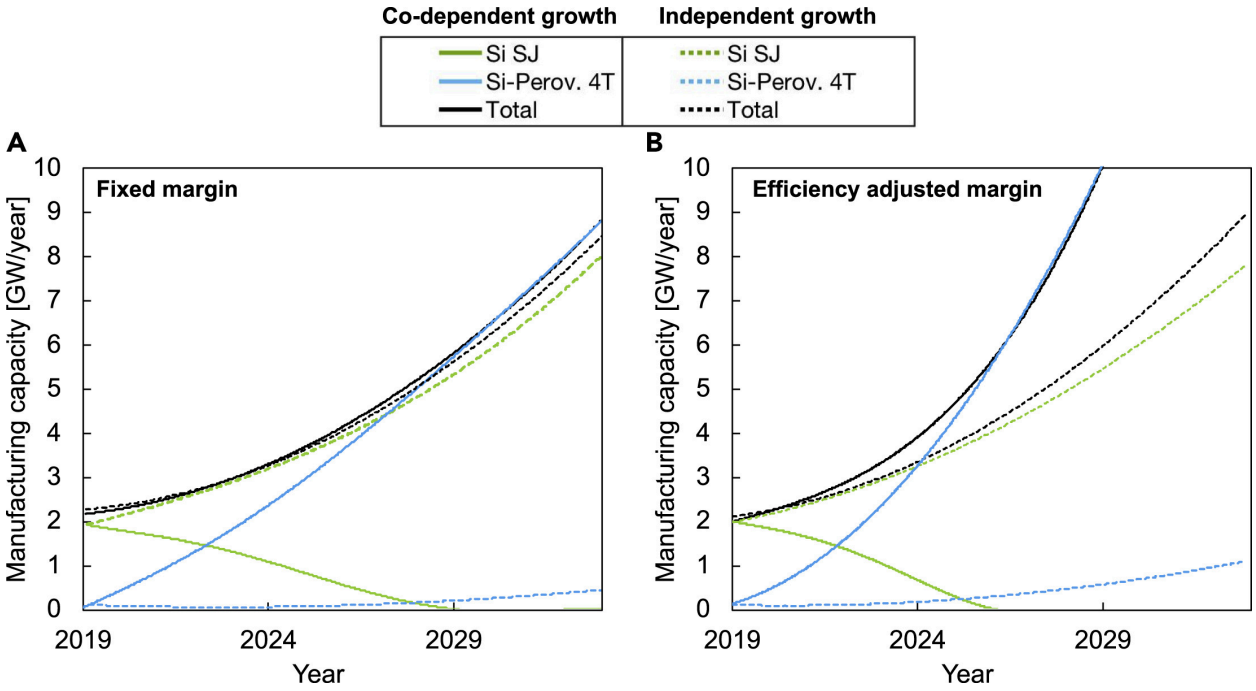

Figure B.4: The predicted growth in manufacturing capacity of a PERC silicon manufacturing facility that co-invests in perovskite-silicon tandem manufacturing using a (**A**) fixed margin or (**B**) efficiency-adjusted margin approach [130].

Appendix C

Building an Empirical Degradation Model

C.1 Degradation Model

In the final piece of this work, we sought to use the data we've collected to build an empirical model for the degradation of the unencapsulated $MAPbI_3$ perovskite solar cell. We envisioned the model to be of the form

$$Time = f(PCE) \tag{C.1}$$

Building this type of model is especially useful for field testing devices, providing warranties, and understanding the general state of the photovoltaic device from one measurement. However, to make it resilient, we cannot rely on a simple regression of time as a function of PCE from the data gathered in this work. Instead, we take advantage of knowing the influence of the deep level traps and the change in optical and crystallographic properties in the degradation of $MAPbI_3$ solar cells. The model will thus become

$$Time = f(PCE, E_a, CZ, A550) \tag{C.2}$$

and simplified into Equation C.1 by performing a regression between the PCE and each of the other responses. Ideally, we would have collected all the responses as functions of time, temperature, electric load, and relative humidity. We unfortunately were not able to collect the latter due to logistical issues caused by the coronavirus pandemic. To overcome this roadblock, we sought to model the missing responses based on data from our previous work [116]. Indeed, that study was a $2^3 \times 5$ factorial where the factors were temperature (25°C and 55°C), load (OC and MPP), relative humidity (RH = 30% and 60%), and time (0, 15, 45, 105, and 225 min). The responses for that study were the photovoltaic, absorption, and crystallographic characteristics. That experimental space matches well with our current one (see Table 3.3). Yet, there are four key differences that must be noted. First, we did not measure deep level trap data at the time. Second, the architecture of the solar cell, though

very similar to the current one (See Figure 3.9), differs in the use of FTO as its electron transport layer (ETL) instead of ITO here. Third, the XRD used for that study had a high noise floor, which made it difficult to extract reliable numerical data. Last, all data collected for this current work were at RH = 5%.

With those caveats in mind, we decided to model the crystallite size (CZ) and the average trap activation energy (E_a) for RH = 30 & 60% by using a weighted average of least squares linear regressions. That is,

$$E_a, CZ = \frac{\sum_n R^2_{adj,n}(a_n + b_n \cdot s_n + \epsilon_n)}{\sum_n R^2_{adj,n}} \tag{C.3}$$

where $R^2_{adj,n}$ is the adjusted coefficient of determination used here as a weight, a_n and b_n are respectively the y-intercept and slope of the linear regression, s_n is the signal on which the regression was performed on, and ϵ_n is the error associated with each regression estimated from the 95% confidence interval. The latter was implemented as

$$\epsilon_n = rand \cdot (Upper_{95\%} - Lower_{95\%}) + (Lower_{95\%} - (a_n + b_n \cdot s_n))$$

where $rand$ is the pseudorandom function with outputs between 0 and 1, and $Upper_{95\%}$ and $Lower_{95\%}$ refer to the upper and lower bounds of the 95% confidence interval of the linear regression, respectively. For the crystallite size, s_n = Time, V_{OC}, J_{SC}, FF and A550. For E_a, in addition to the aforementioned signals, we added the newly modelled crystallite size, for we found it essential for a close to accurate output. Finally, we built the regressions piecewise by controlling for temperature to maintain the effects previously observed in the physical experiments. The output is available in Appendix C.

Once the RH sensitive modelled responses were obtained, we built an empirical model of the form

$$\begin{aligned} Time = \beta_o + \sum_n \beta_n \cdot x_n + \sum_{n\neq m}\sum_{m\neq n} \beta_{nm} \cdot x_n \times x_m + \sum_{n\neq m,l}\sum_{m\neq n,l}\sum_{l\neq n,m} \beta_{nml} \cdot x_n \times x_m \times x_l \\ + \beta_{nmlk} \cdot x_n \times x_m \times x_l \times x_k + \epsilon \end{aligned} \tag{C.4}$$

where the β's are parameters estimated using a least squares regression, the x's are the variables used for the model (PCE, E_a, CZ, & A550), and ϵ is the error term. After removing all insignificant terms and analyzing the residuals, we settled on the factors presented in Figure C.1**b**. We choose ϵ to be ±RMSE, the root mean square error of the actual vs predicted plot (see Figure C.1**a**).

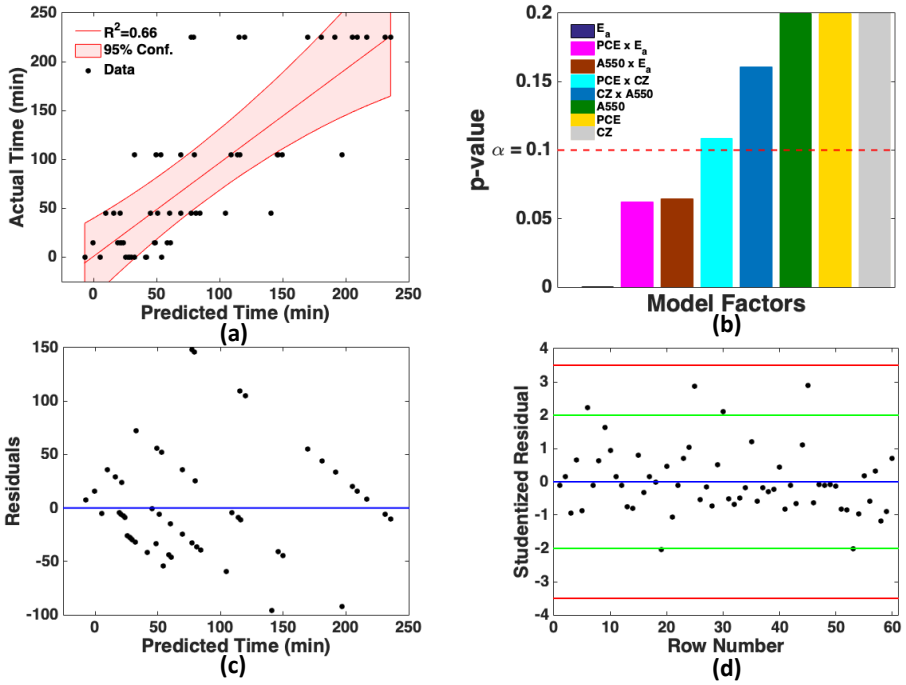

Figure C.1: (**a**) Actual vs predicted plot of the model (**b**) Significance levels for relevant factors. Main effects with $p > 0.1$ must be included when they are involved in significant interactions (**c**) Residual plot (**d**) Studentized residual plot showing normal distribution.

The last piece of the model was to determine the relationships binding E_a, CZ, and A550 to the PCE to reduce the four variables model to a single one as seen in Equation C.1. In our analysis, we decided to perform logarithmic fits instead of linear ones because of the physical behavior of our device. Indeed, there is a physical limit to the maximum crystallite size, absorption and trap activation energy that $MAPbI_3$ solar cells can reach. Moreover, our data suggest that there is a precipitous decrease in A550 and E_a and increase in crystallite size as the PCE approaches zero. The logarithmic regressions are presented in Figure C.2. When incorporating these fits in the degradation model, we inserted their respective RMSE as error terms.

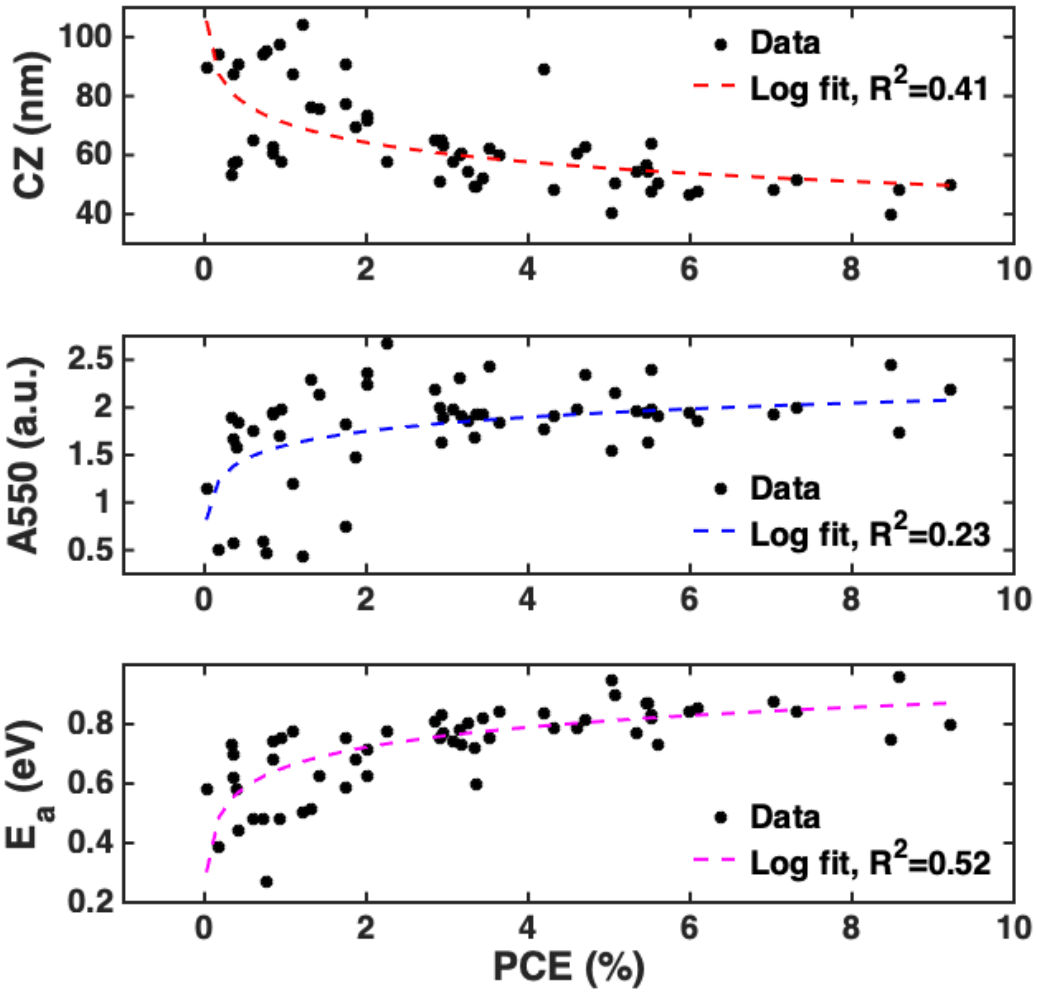

Figure C.2: (**From Top to Bottom**) Logarithmic fits to the crystallite size, the absorbance at 550 nm, and the trap activation energy as a function of PCE. Details are available in Appendix C.

All the pieces for the model now in place, we modeled the stability period of our unencapsulated $MAPbI_3$ perovskite solar cell in Figure C.3. We added the condition that the model must be monotonic since it would be very unlikely to have a cell with lower efficiency have a longer stability period than one with a higher PCE. The model converges near the temporal edge of our experimental space before diverging in predicting the degradation period. This is an expected effect because the coefficients for the interaction terms were estimated at the point of least uncertainty for each variable.

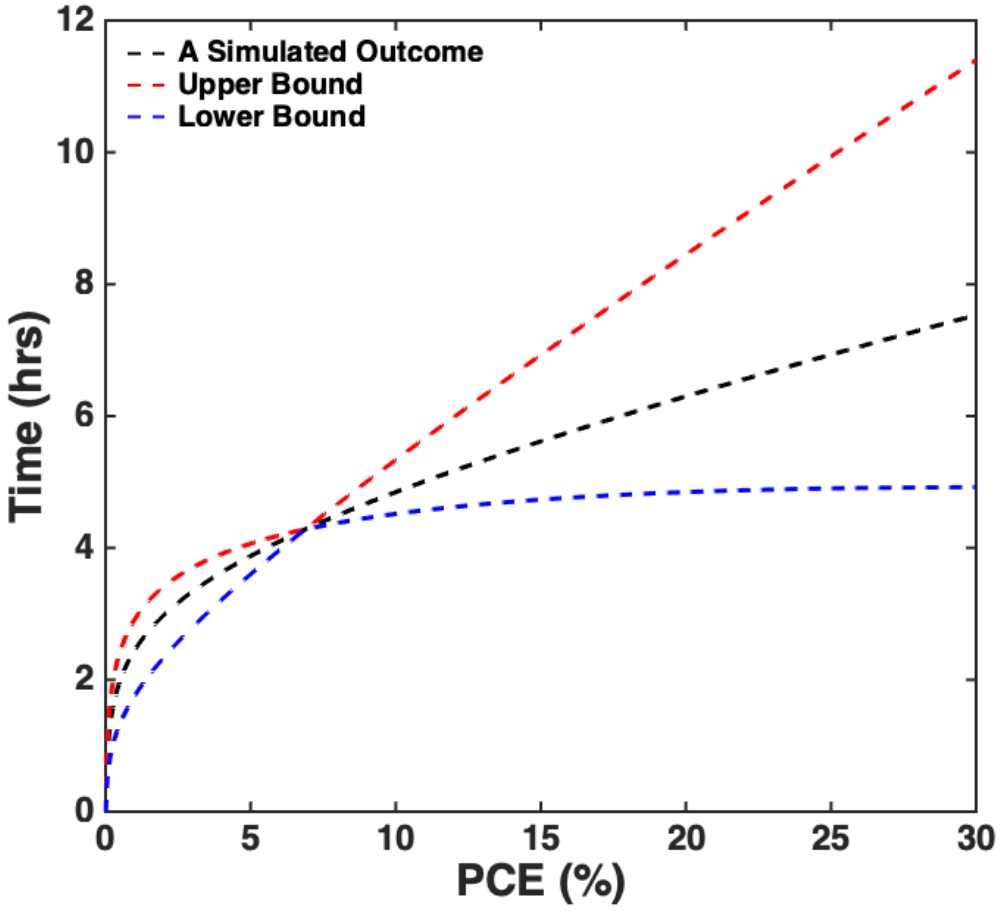

Figure C.3: Semi-empirical stability model for the unencapsulated $MAPbI_3$ solar cells studied in this work. Detailed equations are available in Appendix C.

In building this model, we found that the single most important factor in predicting the stability of the perovskite solar cell was the trap activation energy E_a (See Figure C.1). Techniques to maintain those traps localized deep in the band gap will be key in extending the stability of perovskite solar cells.

C.2 Supplementary Modeling Data

C.2.1 Regression Equations

C.2.1.1 Crystallite Size at T=25°C

$$CZ = 46.83 + 0.075 * Time \quad R^2_{adj} = 0.12$$
$$CZ = 69.28 + 1.12 * J_{SC} \quad R^2_{adj} = 0.30$$
$$CZ = 76.30 + 0.67 * FF \quad R^2_{adj} = 0.095$$

The dependencies on V_{OC} and A550 were insignificant and not used.

C.2.1.2 Crystallite Size at T=55°C

$$CZ = 52.78 + 0.23 * Time \quad R^2_{adj} = 0.68$$
$$CZ = 137.05 - 91.46 * V_{OC} \quad R^2_{adj} = 0.25$$
$$CZ = 106.41 + 2.87 * J_{SC} \quad R^2_{adj} = 0.42$$
$$CZ = 113.57 - 1.30 * FF \quad R^2_{adj} = 0.11$$
$$CZ = 100.48 - 18.60 * A550 \quad R^2_{adj} = 0.26$$

C.2.1.3 Trap Activation Energy at T=25°C

$$E_a = 0.88 + 0.0013 * Time \quad R^2_{adj} = 0.57$$
$$E_a = -0.13 + 1.16 * V_{OC} \quad R^2_{adj} = 0.38$$
$$E_a = 0.63 - 0.011 * J_{SC} \quad R^2_{adj} = 0.27$$
$$E_a = 0.43 + 0.01 * FF \quad R^2_{adj} = 0.35$$
$$E_a = 0.98 - 0.0036 * CZ \quad R^2_{adj} = 0.029$$

The dependency on A550 was insignificant and not used.

C.2.1.4 Trap Activation Energy at T=55°C

$$E_a = 0.90 + 0.0023 * Time \quad R^2_{adj} = 0.78$$
$$E_a = 0.25 + 0.63 * V_{OC} \quad R^2_{adj} = 0.05$$
$$E_a = 0.32 - 0.032 * J_{SC} \quad R^2_{adj} = 0.58$$
$$E_a = 0.085 + 0.019 * FF \quad R^2_{adj} = 0.44$$
$$E_a = 1.18 - 0.0067 * CZ \quad R^2_{adj} = 0.39$$
$$E_a = 0.46 + 0.16 * A550 \quad R^2_{adj} = 0.15$$

C.2.2 95% Confidence Intervals

C.2.2.1 Crystallite Size

Table Below

Time	Std_min	Std_max	Voc	Std_min	Std_max	Jsc	Std_min	Std_max	FF	Std_min	Std_max	Abs	Std_min	Std_max	Temperature
0	34.94	58.71	0.79	42.64	62.09	-16.31	42.86	59.21	33.30	44.20	63.48	1.90	41.16	62.17	25
15	37.06	58.84	0.80	42.13	61.53	-17.57	41.17	58.08	42.88	35.61	59.15	1.94	40.48	62.46	25
45	40.72	59.66	0.80	42.13	61.53	-16.53	42.59	58.99	53.05	20.14	60.91	1.92	40.85	62.29	25
105	44.79	64.56	0.79	42.64	62.09	-14.26	45.11	61.54	47.25	29.31	59.56	1.96	40.07	62.67	25
225	44.23	83.05	0.76	43.28	64.66	-11.35	47.29	65.87	36.83	42.22	60.70	1.91	41.01	62.22	25
0	34.94	58.71	0.82	40.63	60.88	-18.19	40.26	57.61	37.03	42.06	60.59	1.98	39.62	62.93	25
15	37.06	58.84	0.81	41.46	61.13	-17.59	41.14	58.06	51.33	22.92	60.45	2.00	39.14	63.22	25
45	40.72	59.66	0.82	40.63	60.88	-5.30	49.49	77.21	22.10	43.95	78.84	1.98	39.62	62.93	25
105	44.79	64.56	0.78	43.00	62.80	-8.47	48.61	71.00	44.20	33.80	59.19	2.00	39.14	63.22	25
225	44.23	83.05	0.64	38.68	82.12	-3.50	49.84	80.89	37.80	41.41	60.20	1.93	40.67	62.37	25
0	37.86	67.71	0.74	53.03	85.72	-13.03	54.73	83.25	29.53	56.99	93.53	2.18	38.31	81.53	55
15	42.51	69.81	0.65	60.08	95.13	-14.70	48.55	79.83	32.85	53.48	88.43	2.30	34.16	81.22	55
45	51.32	74.50	0.53	62.39	114.77	-12.56	56.25	84.42	29.27	57.15	94.05	2.23	36.60	81.38	55
105	65.67	87.16	0.55	62.32	111.18	-9.83	63.07	93.28	26.50	58.00	100.38	2.14	39.66	81.68	55
225	82.99	123.84	0.43	61.87	133.57	-7.74	66.34	102.02	26.23	58.01	101.07	1.70	52.49	85.21	55
0	37.86	67.71	0.82	41.88	82.23	-14.91	47.69	79.48	38.50	41.44	85.81	2.35	32.38	81.14	55
15	42.51	69.81	0.78	47.92	83.50	-15.20	46.49	79.01	46.35	18.16	88.72	2.40	30.58	81.08	55
45	51.32	74.50	0.73	54.12	86.45	-12.55	56.28	84.45	38.23	42.14	85.81	2.43	29.49	81.05	55
105	65.67	87.16	0.64	60.50	96.53	-10.03	62.68	92.52	31.30	55.48	90.45	2.36	32.02	81.13	55
225	82.99	123.84	0.34	60.73	151.18	-4.86	69.26	115.64	23.37	57.61	108.90	1.84	48.89	83.61	55
0	34.94	58.71	0.82	40.63	60.88	-12.16	46.79	64.56	34.80	43.54	62.12	1.92	40.85	62.29	25
15	37.06	58.84	0.79	42.64	62.09	-16.60	42.50	58.93	41.48	37.43	59.23	1.95	40.28	62.56	25
45	40.72	59.66	0.79	42.64	62.09	-4.54	49.65	78.75	23.00	44.15	77.43	1.94	40.48	62.46	25
105	44.79	64.56	0.76	43.28	64.66	-13.61	45.70	62.42	44.20	33.80	59.19	1.97	39.85	62.80	25
225	44.23	83.05	0.72	42.55	69.68	-11.23	47.36	66.07	37.90	41.32	60.16	1.97	39.85	62.80	25
0	34.94	58.71	0.85	37.39	60.91	-12.17	46.79	64.55	35.53	43.13	61.55	1.83	41.87	62.15	25
15	37.06	58.84	0.81	41.46	61.13	-16.58	42.52	58.95	45.68	31.66	59.32	1.86	41.65	62.08	25
45	40.72	59.66	0.78	43.00	62.80	-12.83	46.32	63.54	32.70	44.40	64.09	1.85	41.74	62.09	25
105	44.79	64.56	0.74	43.08	67.00	-1.90	50.09	84.22	23.87	44.33	76.07	1.88	41.43	62.10	25
225	44.23	83.05	0.40	23.03	123.46	-4.35	49.68	79.14	30.07	44.86	67.18	1.76	41.90	62.80	25
0	37.86	67.71	0.83	40.25	82.03	-9.32	64.00	95.29	37.98	42.79	85.81	1.62	54.30	86.39	55
15	42.51	69.81	0.72	55.14	87.26	-10.12	62.50	92.19	40.55	35.80	86.14	1.90	47.19	83.08	55
45	51.32	74.50	0.64	60.50	96.53	-0.26	72.23	139.11	16.68	54.39	129.47	1.15	60.92	97.25	55
105	65.67	87.16	0.41	61.66	137.45	-3.34	70.39	123.25	25.80	58.01	102.19	0.57	62.81	116.94	55
225	82.99	123.84	0.27	59.62	165.10	-2.63	70.86	126.86	21.18	56.80	115.39	0.51	62.82	119.17	55
0	37.86	67.71	0.89	29.86	81.44	-15.86	43.67	78.04	39.08	39.89	85.86	1.63	54.08	86.23	55
15	42.51	69.81	0.85	36.90	81.72	-16.24	41.99	77.54	36.75	45.83	85.96	2.16	38.99	81.60	55
45	51.32	74.50	0.68	58.41	91.31	-9.33	63.98	95.25	28.30	57.62	96.10	1.48	56.97	88.93	55
105	65.67	87.16	0.58	62.03	105.98	-11.76	58.60	86.66	25.25	57.98	103.65	0.74	62.66	110.77	55
225	82.99	123.84	0.37	61.15	145.27	-7.60	66.52	102.65	25.25	57.98	103.65	0.58	62.81	116.57	55

Figure C.4: 95% Confidence Interval for CZ.

C.2.2.2 Trap Activation Energy

Table Below

Time	Std_min	Std_max	Voc	Std_min	Std_max	Jsc	Std_min	Std_max	FF	Std_min	Std_max	Cz	Std_min	Std_max	Abs	Std_min	Std_max	Temp
0	0.80	0.97	0.79	0.71	0.86	-16.31	0.72	0.89	33.30	0.68	0.85	48.29	0.71	0.91	1.90	0.68	0.89	25
15	0.79	0.94	0.80	0.72	0.87	-17.57	0.73	0.90	42.88	0.76	0.96	46.42	0.71	0.92	1.94	0.67	0.89	25
45	0.76	0.89	0.80	0.72	0.87	-16.53	0.72	0.89	53.05	0.79	1.14	48.36	0.71	0.91	1.92	0.68	0.89	25
105	0.68	0.82	0.79	0.71	0.86	-14.26	0.70	0.87	47.25	0.78	1.04	54.57	0.69	0.88	1.96	0.67	0.89	25
225	0.46	0.73	0.76	0.67	0.84	-11.35	0.65	0.84	36.83	0.72	0.88	60.32	0.65	0.88	1.91	0.68	0.89	25
0	0.80	0.97	0.82	0.74	0.90	-18.19	0.73	0.91	37.03	0.72	0.88	47.69	0.71	0.91	1.98	0.66	0.89	25
15	0.79	0.94	0.81	0.73	0.89	-17.59	0.73	0.90	51.33	0.79	1.11	51.70	0.70	0.89	2.00	0.65	0.89	25
45	0.76	0.89	0.82	0.74	0.90	-5.30	0.54	0.83	22.10	0.50	0.80	57.70	0.67	0.88	1.98	0.66	0.89	25
105	0.68	0.82	0.78	0.70	0.85	-8.47	0.60	0.83	44.20	0.77	0.99	51.20	0.70	0.89	2.00	0.65	0.89	25
225	0.46	0.73	0.64	0.44	0.79	-3.50	0.50	0.82	37.80	0.73	0.89	60.56	0.65	0.88	1.93	0.67	0.89	25
0	0.78	1.02	0.74	0.54	0.90	-13.03	0.61	0.85	29.53	0.51	0.79	64.97	0.60	0.89	2.18	0.57	1.03	55
15	0.75	0.97	0.65	0.47	0.85	-14.70	0.65	0.92	32.85	0.58	0.85	59.79	0.62	0.94	2.30	0.57	1.07	55
45	0.70	0.89	0.53	0.30	0.87	-12.56	0.60	0.84	29.27	0.50	0.79	71.90	0.56	0.84	2.23	0.57	1.04	55
105	0.57	0.74	0.55	0.33	0.87	-9.83	0.50	0.76	26.50	0.43	0.76	75.71	0.53	0.82	2.14	0.57	1.01	55
225	0.21	0.54	0.43	0.13	0.92	-7.74	0.41	0.71	26.23	0.42	0.76	97.37	0.31	0.75	1.70	0.55	0.90	55
0	0.78	1.02	0.82	0.55	0.99	-14.91	0.66	0.93	38.50	0.65	1.00	62.92	0.61	0.91	2.35	0.57	1.08	55
15	0.75	0.97	0.78	0.55	0.94	-15.20	0.67	0.94	46.35	0.70	1.25	64.13	0.60	0.90	2.40	0.57	1.10	55
45	0.70	0.89	0.73	0.53	0.89	-12.55	0.60	0.84	38.23	0.65	0.99	62.06	0.61	0.92	2.43	0.57	1.11	55
105	0.57	0.74	0.64	0.46	0.85	-10.03	0.51	0.76	31.30	0.55	0.82	73.54	0.55	0.83	2.36	0.57	1.09	55
225	0.21	0.54	0.34	-0.03	0.97	-4.86	0.28	0.67	23.37	0.33	0.73	90.90	0.39	0.76	1.84	0.57	0.93	55
0	0.80	0.97	0.82	0.74	0.90	-12.16	0.67	0.85	34.80	0.70	0.86	51.91	0.70	0.89	1.92	0.68	0.89	25
15	0.79	0.94	0.79	0.71	0.86	-16.60	0.72	0.89	41.48	0.76	0.94	56.60	0.68	0.88	1.95	0.67	0.89	25
45	0.76	0.89	0.79	0.71	0.86	-4.54	0.53	0.82	23.00	0.52	0.80	62.50	0.63	0.88	1.94	0.67	0.89	25
105	0.68	0.82	0.76	0.67	0.84	-13.61	0.69	0.86	44.20	0.77	0.99	60.49	0.65	0.88	1.97	0.66	0.89	25
225	0.46	0.73	0.72	0.60	0.81	-11.23	0.65	0.84	37.90	0.73	0.89	57.43	0.67	0.88	1.97	0.66	0.89	25
0	0.80	0.97	0.85	0.76	0.95	-12.17	0.67	0.85	35.53	0.71	0.87	59.77	0.66	0.88	1.83	0.69	0.89	25
15	0.79	0.94	0.81	0.73	0.89	-16.58	0.72	0.89	45.68	0.77	1.01	47.62	0.71	0.91	1.86	0.69	0.89	25
45	0.76	0.89	0.78	0.70	0.85	-12.83	0.68	0.85	32.70	0.68	0.84	54.39	0.69	0.88	1.85	0.69	0.89	25
105	0.68	0.82	0.74	0.63	0.82	-1.90	0.47	0.82	23.87	0.53	0.81	52.94	0.69	0.89	1.88	0.69	0.89	25
225	0.46	0.73	0.40	-0.06	0.73	-4.35	0.52	0.82	30.07	0.64	0.83	65.22	0.61	0.88	1.76	0.70	0.90	25
0	0.78	1.02	0.83	0.54	1.00	-9.32	0.48	0.75	37.98	0.64	0.98	64.76	0.60	0.90	1.62	0.54	0.88	55
15	0.75	0.97	0.72	0.53	0.88	-10.12	0.52	0.76	40.55	0.67	1.06	63.24	0.61	0.91	1.90	0.57	0.94	55
45	0.70	0.89	0.64	0.46	0.85	-0.26	0.05	0.61	16.68	0.11	0.70	89.41	0.40	0.76	1.15	0.45	0.83	55
105	0.57	0.74	0.41	0.09	0.93	-3.34	0.20	0.65	25.80	0.41	0.75	87.08	0.43	0.77	0.57	0.27	0.83	55
225	0.21	0.54	0.27	-0.16	1.00	-2.63	0.17	0.64	21.18	0.26	0.72	94.13	0.35	0.75	0.51	0.24	0.84	55
0	0.78	1.02	0.89	0.53	1.10	-15.86	0.68	0.97	39.08	0.65	1.01	54.22	0.64	1.00	1.63	0.55	0.88	55
15	0.75	0.97	0.85	0.54	1.03	-16.24	0.69	0.98	36.75	0.63	0.95	50.15	0.65	1.04	2.16	0.57	1.02	55
45	0.70	0.89	0.68	0.50	0.86	-9.33	0.48	0.75	28.30	0.48	0.78	69.51	0.57	0.86	1.48	0.52	0.86	55
105	0.57	0.74	0.58	0.37	0.86	-11.76	0.57	0.81	25.25	0.39	0.75	77.11	0.52	0.81	0.74	0.32	0.83	55
225	0.21	0.54	0.37	0.02	0.95	-7.60	0.41	0.71	25.25	0.39	0.75	94.05	0.35	0.75	0.58	0.27	0.83	55

Figure C.5: 95% Confidence Interval for E_a.

C.2.3 Experimental Space with Modelled Data

Table on next page.

	Factors				**Responses**						
	2 Levels	3 Levels	2 Levels	5 Levels	Photovoltaic				Crystal	Absorption	Traps
Exp #	Temp.(°C)	RH (%)	Load	Time(min)	V_{OC}(V)	J_{SC}(mA/cm^2)	FF	PCE(%)	L(nm)	A550	E_a(eV)
1	25	5	OC	0	0.87	-20.58	0.48	8.58	48.16	1.74	0.96
2	25	5	OC	15	0.85	-18.65	0.35	5.61	50.56	1.92	0.73
3	25	5	OC	45	0.82	-23.27	0.44	8.47	39.86	2.45	0.75
4	25	5	OC	105	0.74	-14.99	0.30	3.35	49.50	1.93	0.60
5	25	5	OC	225	0.69	-2.56	0.21	0.36	57.35	1.66	0.70
6	25	5	MPP	0	0.80	-18.04	0.35	5.04	40.37	1.54	0.95
7	25	5	MPP	15	-	-	-	-	-	-	-
8	25	5	MPP	45	0.91	-22.87	0.44	9.21	49.79	2.18	0.80
9	25	5	MPP	105	0.77	-7.62	0.30	1.74	90.58	1.82	0.75
10	25	5	MPP	225	0.64	-2.50	0.26	0.40	57.56	1.58	0.58
11	55	5	OC	0	0.87	-20.58	0.48	8.58	48.16	1.74	0.96
12	55	5	OC	15	0.76	-8.78	0.36	2.26	57.94	2.68	0.78
13	55	5	OC	45	0.76	-17.05	0.26	3.34	49.16	1.69	0.72
14	55	5	OC	105	0.39	-7.46	0.38	1.09	87.44	1.20	0.77
15	55	5	OC	225	0.57	-4.67	0.29	0.76	94.96	0.47	0.27
16	55	5	MPP	0	0.80	-18.04	0.35	5.04	40.37	1.54	0.95
17	55	5	MPP	15	-	-	-	-	-	-	-
18	55	5	MPP	45	0.80	-15.38	0.34	4.19	88.77	1.77	0.84
19	55	5	MPP	105	0.80	-7.02	0.23	1.32	76.05	2.29	0.51
20	55	5	MPP	225	0.66	-9.12	0.20	1.21	104.36	0.44	0.50
21	25	30	OC	0	0.79	-16.31	0.33	4.32	48.29*	1.90	0.78*
22	25	30	OC	15	0.80	-17.57	0.43	5.99	46.42*	1.94	0.84*
23	25	30	OC	45	0.80	-16.53	0.53	7.03	48.36*	1.92	0.88*
24	25	30	OC	105	0.79	-14.26	0.47	5.34	54.57*	1.96	0.77*
25	25	30	OC	225	0.76	-11.35	0.37	3.17	60.32*	1.91	0.73*
26	25	30	MPP	0	0.82	-18.19	0.37	5.53	47.69*	1.98	0.83*
27	25	30	MPP	15	0.81	-17.59	0.51	7.31	51.70*	2.00	0.84*
28	25	30	MPP	45	0.82	-5.30	0.22	0.96	57.70*	1.98	0.75*
29	25	30	MPP	105	0.78	-8.47	0.44	2.91	51.20*	2.00	0.75*
30	25	30	MPP	225	0.64	-3.50	0.38	0.85	60.56*	1.93	0.68*
31	55	30	OC	0	0.74	-13.03	0.30	2.84	64.97*	2.18	0.81*
32	55	30	OC	15	0.65	-14.70	0.33	3.16	59.79*	2.30	0.78*
33	55	30	OC	45	0.53	-12.56	0.29	2.02	71.90*	2.23	0.71*
34	55	30	OC	105	0.55	-9.83	0.27	1.43	75.71*	2.14	0.63*
35	55	30	OC	225	0.43	-7.74	0.26	0.93	97.37*	1.70	0.48*
36	55	30	MPP	0	0.82	-14.91	0.39	4.71	62.92*	2.35	0.81*
37	55	30	MPP	15	0.78	-15.20	0.46	5.51	64.13*	2.40	0.82*
38	55	30	MPP	45	0.73	-12.55	0.38	3.52	62.06*	2.43	0.75*
39	55	30	MPP	105	0.64	-10.03	0.31	2.02	73.54*	2.36	0.63*
40	55	30	MPP	225	0.34	-4.86	0.23	0.42	90.90*	1.84	0.44*
41	25	60	OC	0	0.82	-12.16	0.35	3.44	51.91*	1.92	0.82*
42	25	60	OC	15	0.79	-16.60	0.41	5.46	56.60*	1.95	0.87*
43	25	60	OC	45	0.79	-4.54	0.23	0.85	62.50*	1.94	0.74*
44	25	60	OC	105	0.76	-13.61	0.44	4.60	60.49*	1.97	0.79*
45	25	60	OC	225	0.72	-11.23	0.38	3.08	57.43*	1.97	0.74*
46	25	60	MPP	0	0.85	-12.17	0.36	3.65	59.77*	1.83	0.84*
47	25	60	MPP	15	0.81	-16.58	0.46	6.10	47.62*	1.86	0.85*
48	25	60	MPP	45	0.78	-12.83	0.33	3.25	54.39*	1.85	0.80*
49	25	60	MPP	105	0.74	-1.90	0.24	0.34	52.94*	1.88	0.73*
50	25	60	MPP	225	0.40	-4.35	0.30	0.59	65.22*	1.76	0.48*
51	55	60	OC	0	0.83	-9.32	0.38	2.92	64.76*	1.62	0.83*
52	55	60	OC	15	0.72	-10.12	0.41	2.95	63.24*	1.90	0.77*
53	55	60	OC	45	0.64	-0.26	0.17	0.03	89.41*	1.15	0.58*
54	55	60	OC	105	0.41	-3.34	0.26	0.36	87.08*	0.57	0.62*
55	55	60	OC	225	0.27	-2.63	0.21	0.18	94.13*	0.51	0.38*
56	55	60	MPP	0	0.89	-15.86	0.39	5.49	54.22*	1.63	0.87*
57	55	60	MPP	15	0.85	-16.24	0.37	5.08	50.15*	2.16	0.90*
58	55	60	MPP	45	0.68	-9.33	0.28	1.86	69.51*	1.48	0.68*
59	55	60	MPP	105	0.58	-11.76	0.25	1.75	77.11*	0.74	0.58*
60	55	60	MPP	225	0.37	-7.60	0.25	0.73	94.05*	0.58	0.48*

Table C.1: Combined experimental space for the degradation model. In (*) are the modelled data, the rest were experimentally measured.

C.2.4 Validation Plots for the Combined Experimental Space

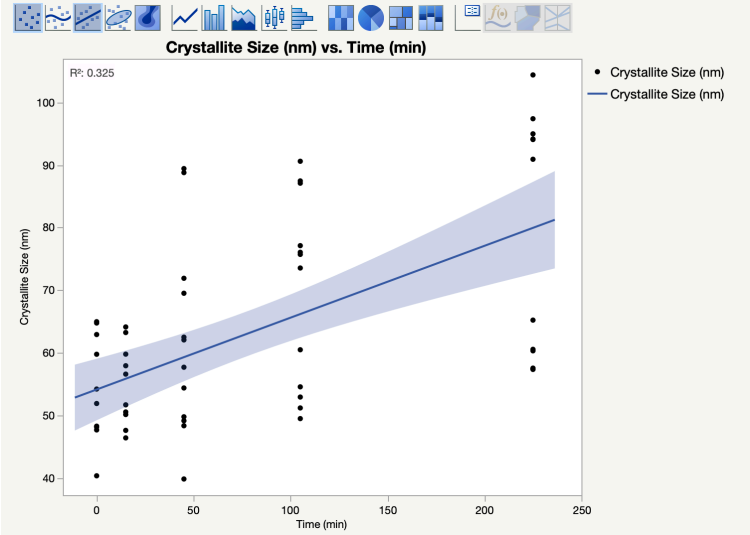

Figure C.6: Modelled CZ over time.

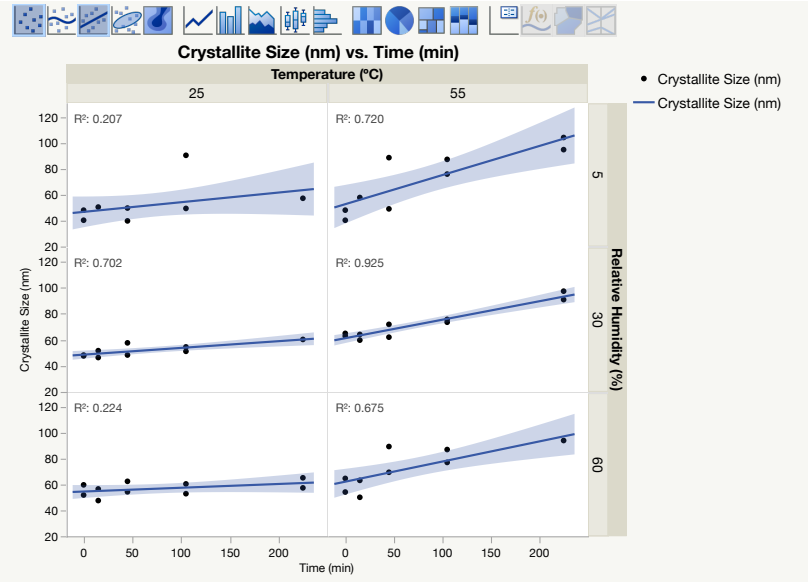

Figure C.7: Modelled CZ over time controlled for temperature and relative humidity.

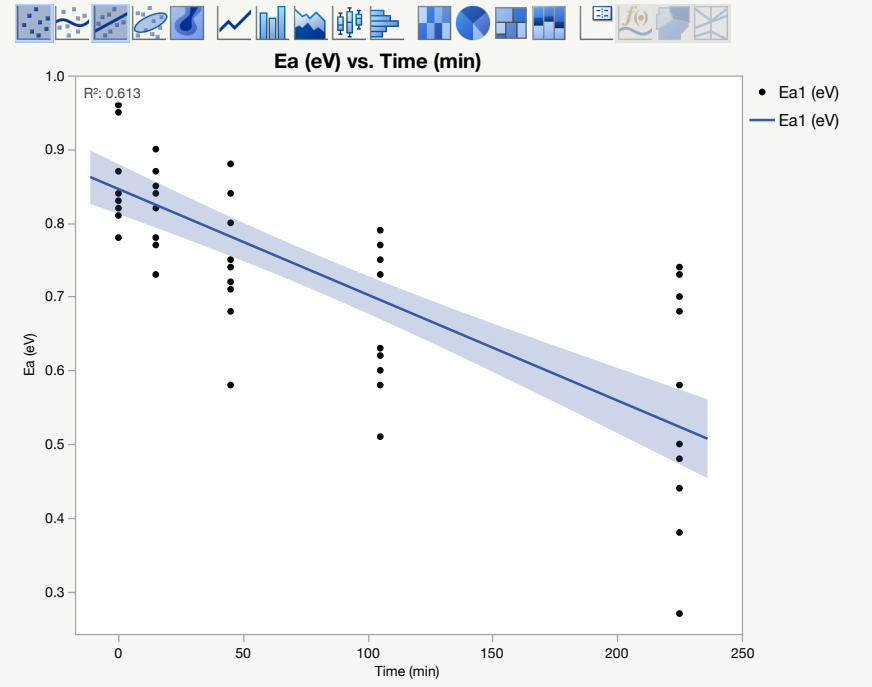

Figure C.8: Modelled E_a over time.

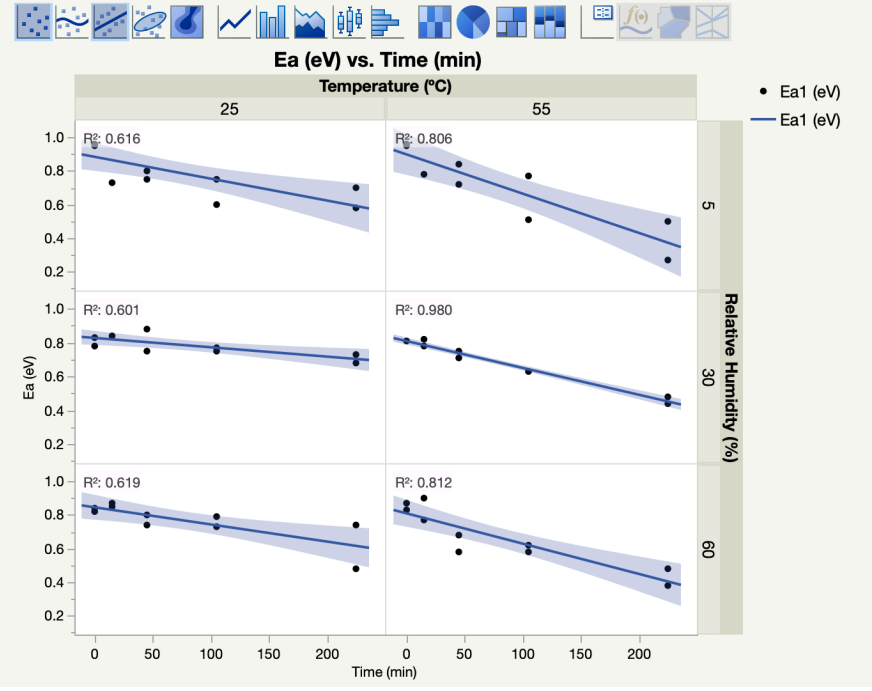

Figure C.9: Modelled E_a over time controlled for temperature and relative humidity.

C.2.5 Log Fits

$$CZ = 70.84 - 9.51 \ln(PCE) + \epsilon_{CZ}; \quad RMSE_{CZ} = 12.89$$

$$A550 = 1.60 + 0.213 \ln(PCE) + \epsilon_{A550}; \quad RMSE_{A550} = 0.44$$

$$E_a = 0.66 + 0.097 \ln(PCE) + \epsilon_{E_a}; \quad RMSE_{E_a} = 0.11$$

where $\epsilon = (2 * rand - 1) \cdot RMSE$

C.2.6 Semi-Empirical Degradation Model

$$Time = 423.37 - 2.011224 * PCE - 0.177547 * CZ - 13.68262 * A550 - 414.3237 * Ea$$

$$+0.6500754*(PCE-3.4475).*(CZ-63.035)-2.542503*(CZ-63.035).*(A550-1.7773333333)$$

$$+67.128356 * (PCE - 3.4475). * (Ea - 0.7348333333)$$

$$-304.8101 * (A550 - 1.7773333333). * (Ea - 0.7348333333) + \epsilon_{Time}$$

where $\epsilon_{Time} = (2 * rand - 1) \cdot RMSE_{Time}$, and $RMSE_{Time} = 51.939$ min. To obtain Figure C.3, the following transformation was performed: $f = min(Time) - Time$.

Appendix D

Supplementary Data

D.1 X-Ray Diffraction Plots

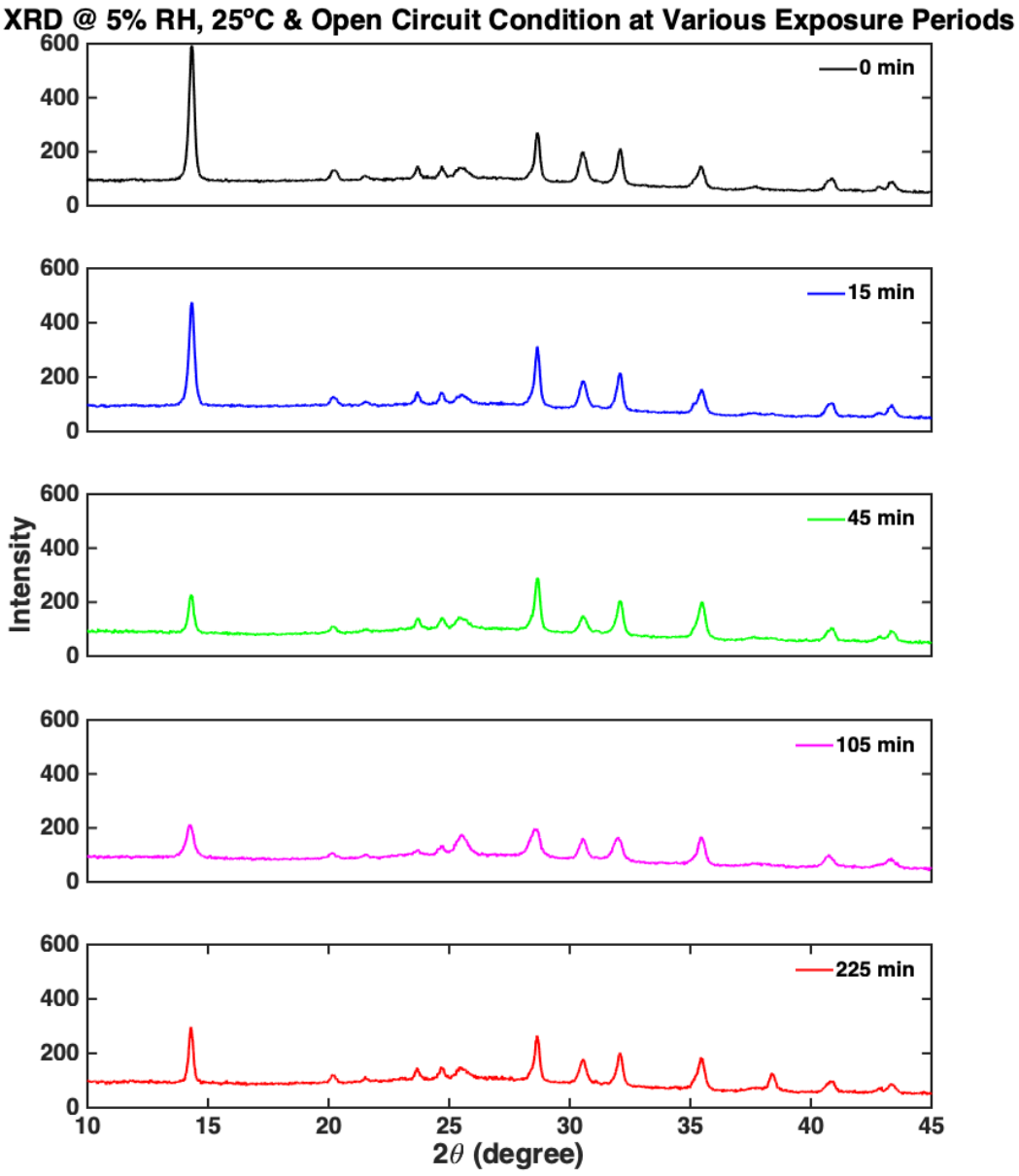

Figure D.1: XRD Condition: 25°C & OC.

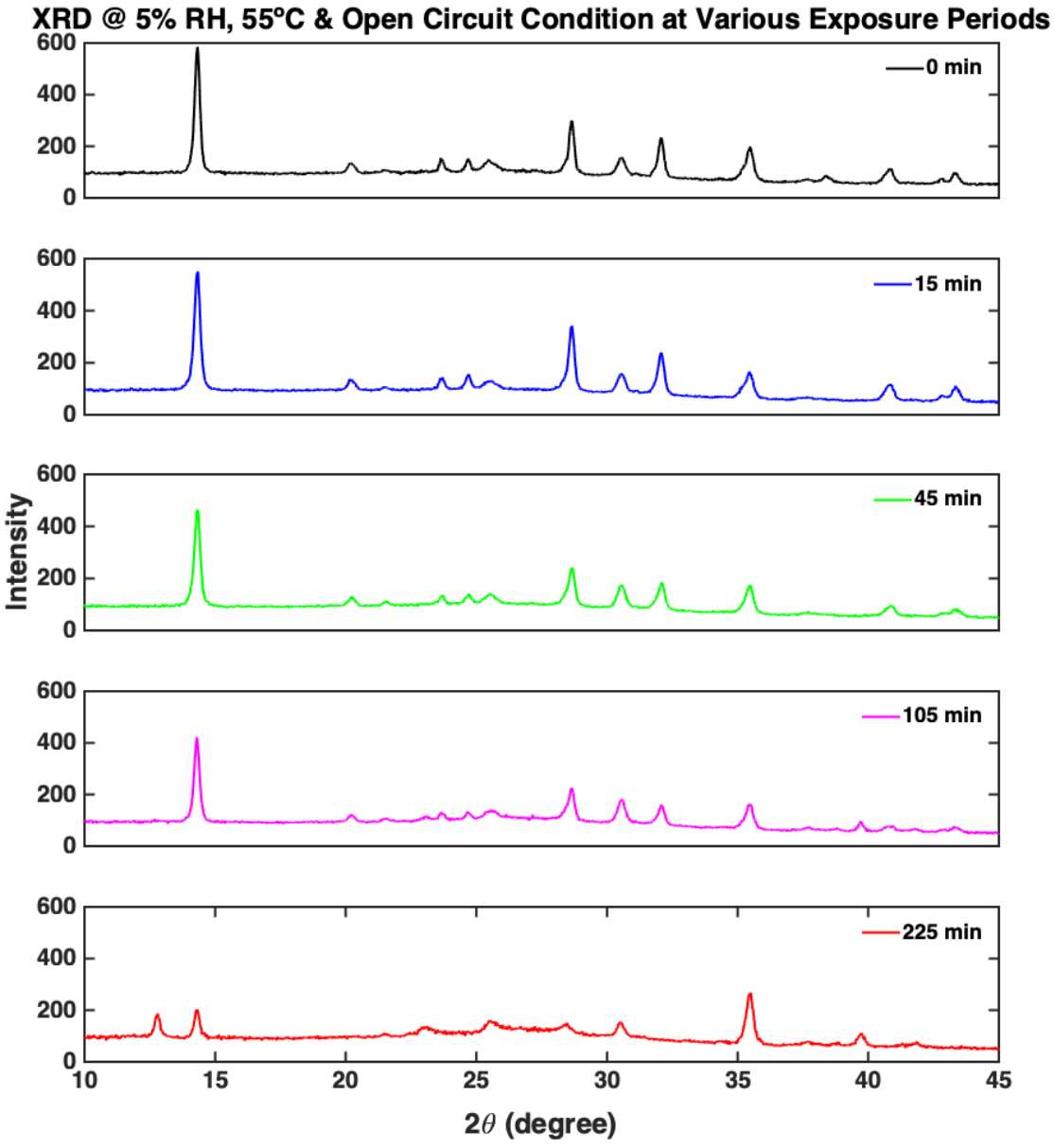

Figure D.2: XRD Condition: 55°C & OC.

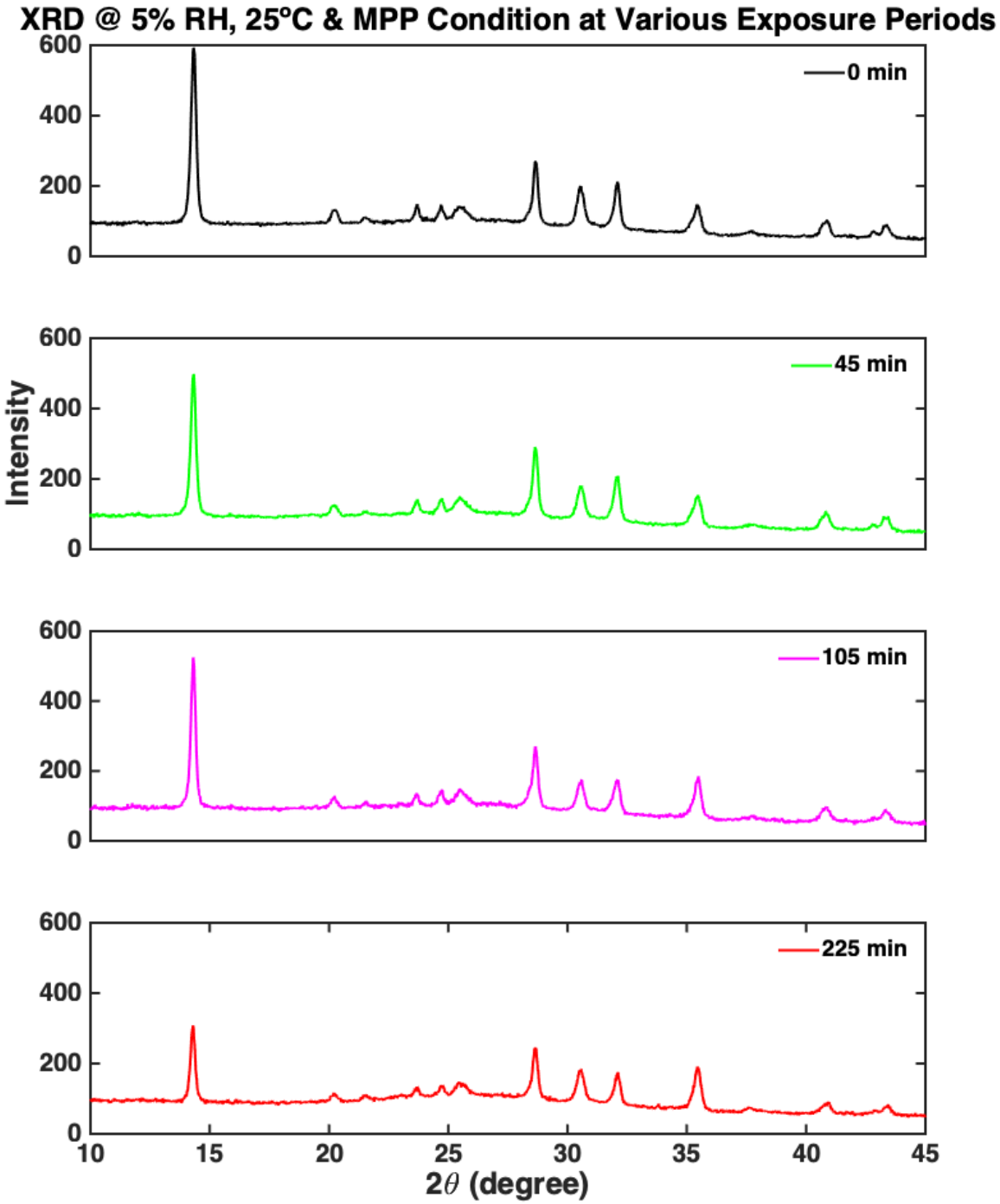

Figure D.3: XRD Condition: 25°C & MPP.

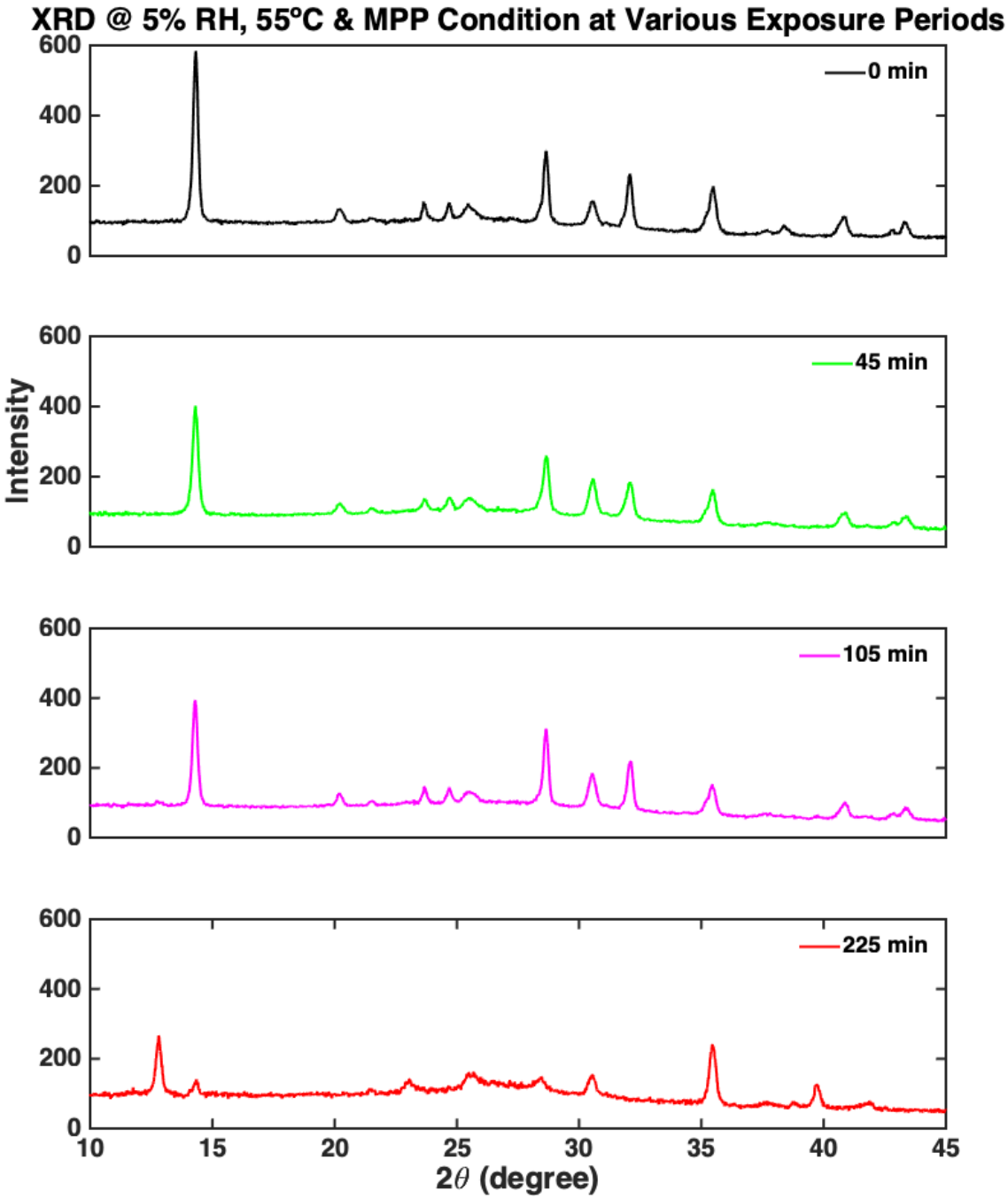

Figure D.4: XRD Condition: 55°C & MPP.

D.2 UV-Vis Absorption Plots

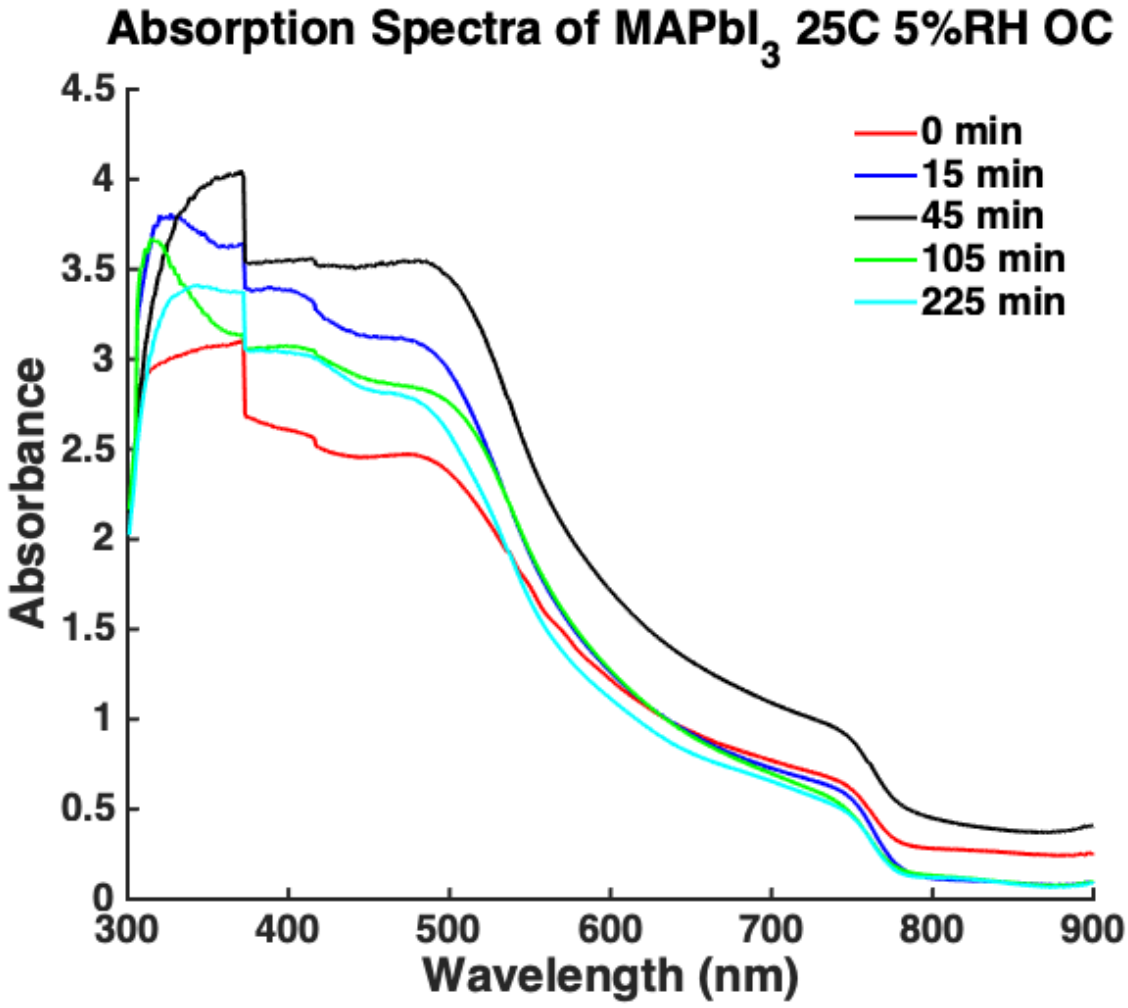

Figure D.5: UV-Vis Condition: 25°C & OC.

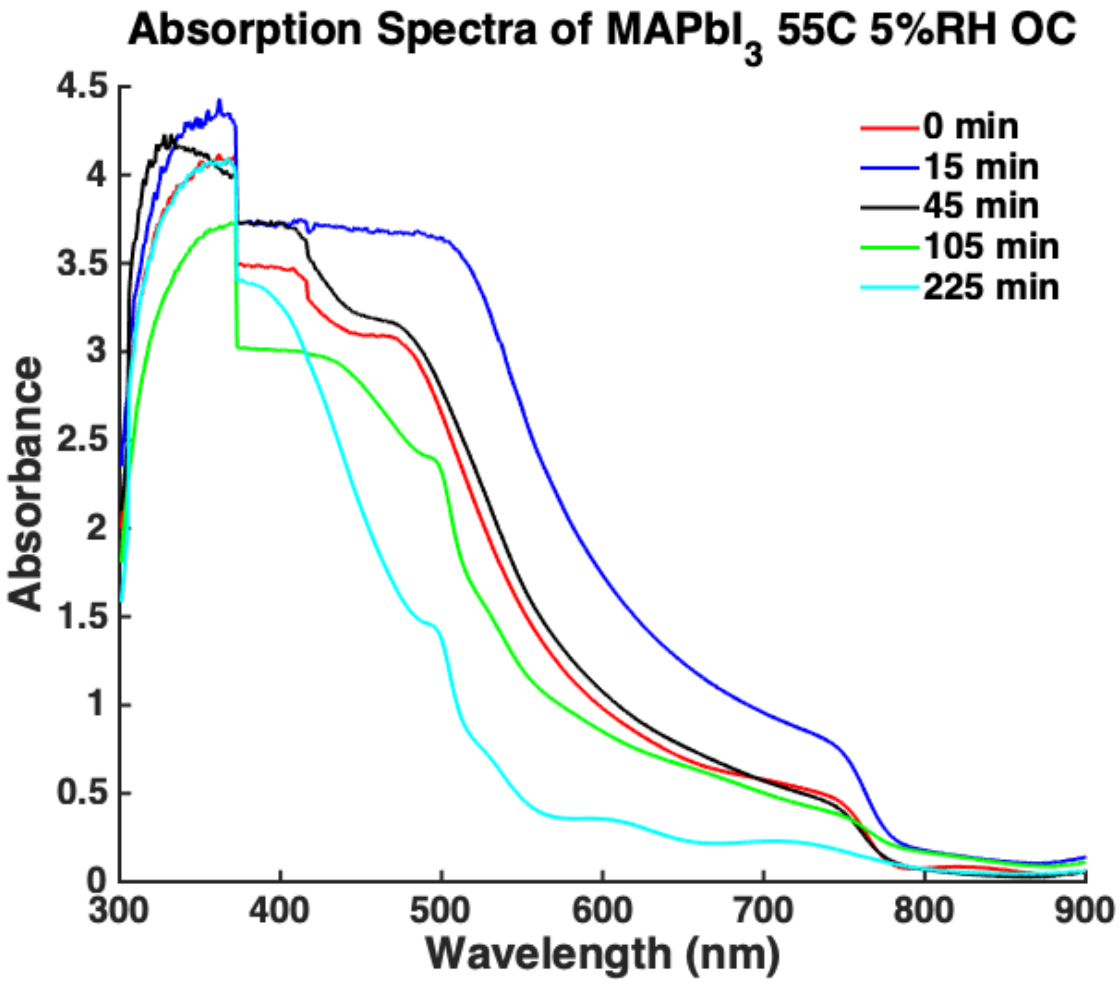

Figure D.6: UV-Vis Condition: 55°C & OC.

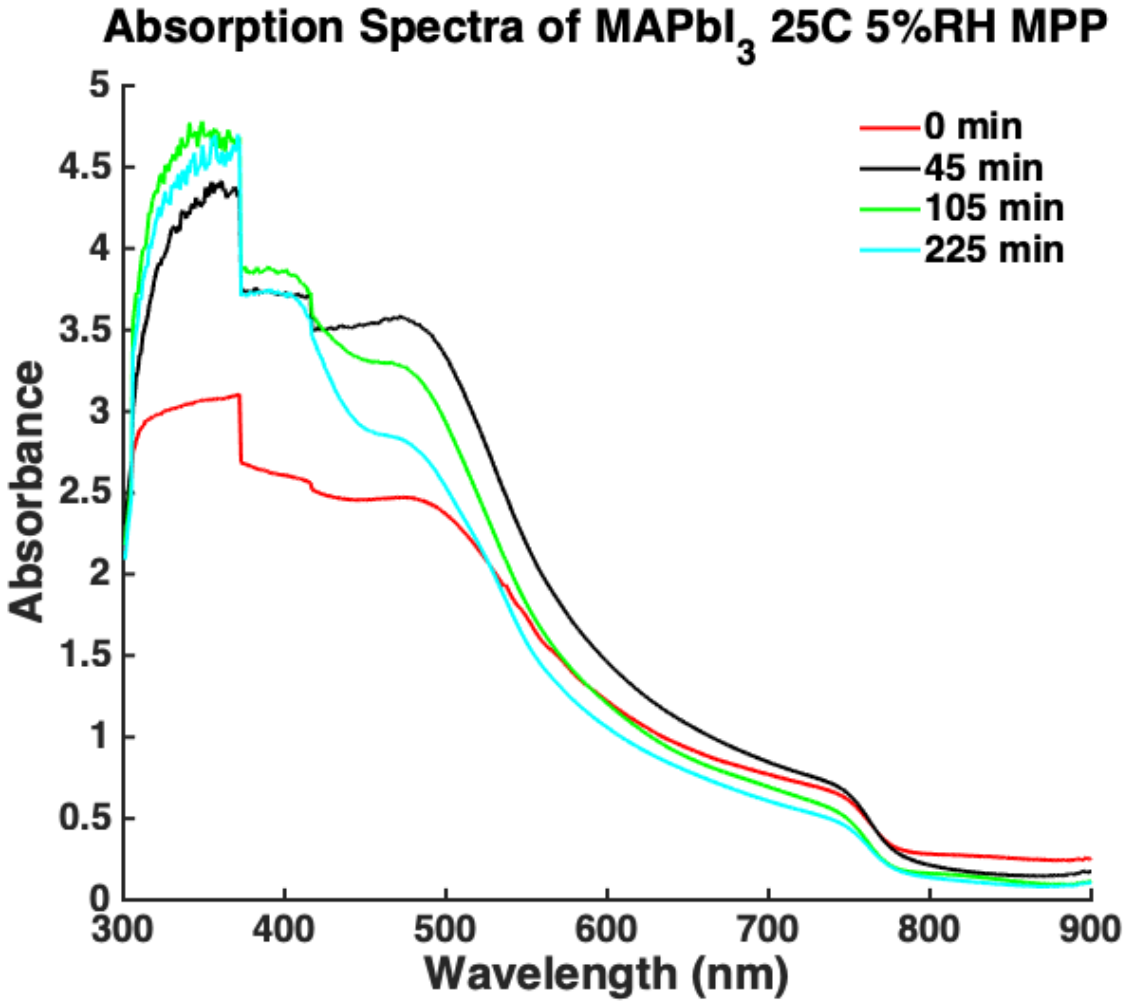

Figure D.7: UV-Vis Condition: 25°C & MPP.

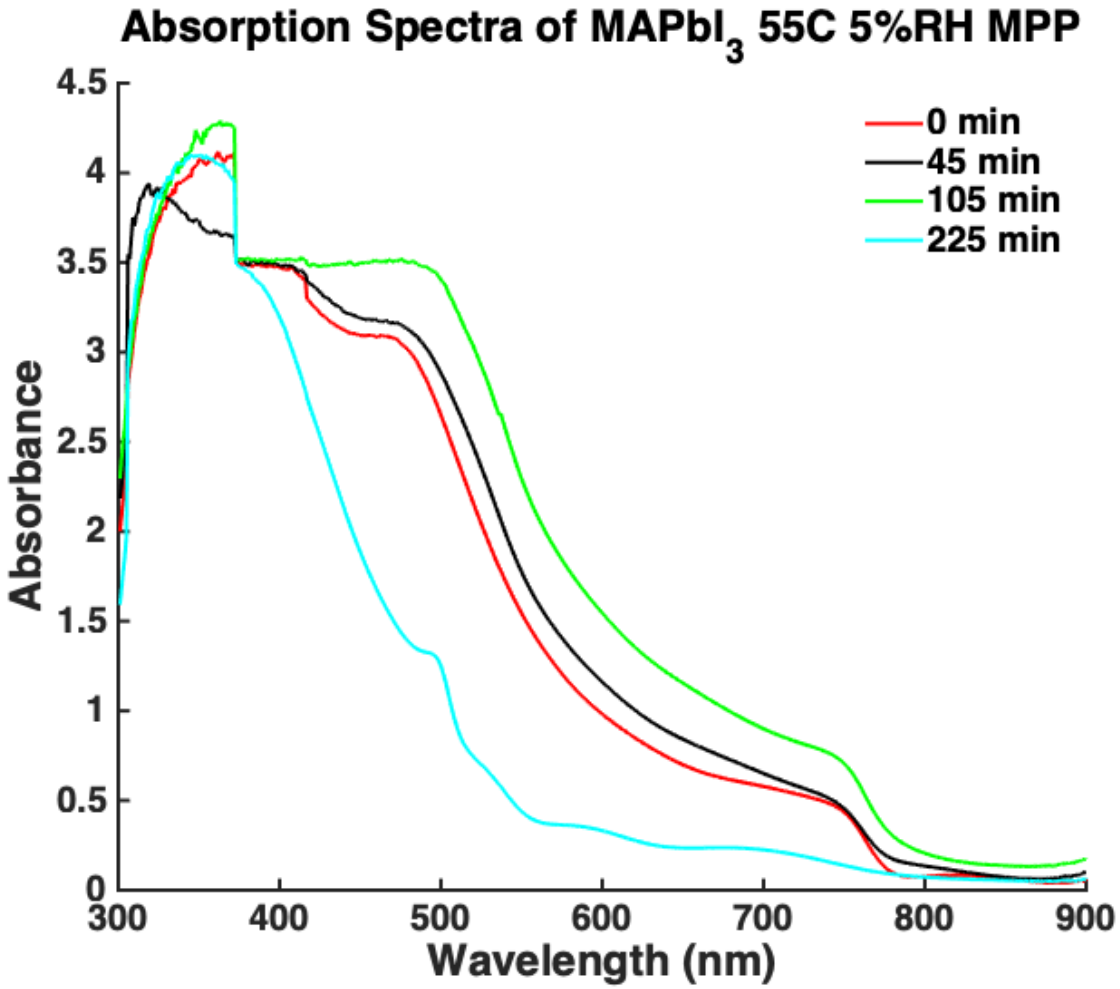

Figure D.8: UV-Vis Condition: 55°C & MPP.

Bibliography

[1] Nick Routley. *Mapped: The 1.2 Billion People Without Access to Electricity*. URL: https://www.visualcapitalist.com/mapped-billion-people-without-access-to-electricity/ (visited on 07/15/2020).

[2] Vijaya Ramachandran and Junaid Sadiq Masood. *How Tough Is It to Be a Tech Entrepreneur in Nigeria? Results from a New Survey*. URL: https://www.cgdev.org/blog/how-tough-it-be-tech-entrepreneur-nigeria-results-from-new-survey (visited on 07/15/2020).

[3] Charlie Zajicek. *How solar mini-grids can bring cheap, green electricity to rural Africa*. URL: https://www.odi.org/blogs/10730-how-solar-mini-grids-can-bring-cheap-green-electricity-rural-africa (visited on 07/15/2020).

[4] BP plc. *BP Statistical Review of World Energy 2019 — 68th edition*. URL: https://www.bp.com/content/dam/bp/business-sites/en/global/corporate/pdfs/energy-economics/statistical-review/bp-stats-review-2019-full-report.pdf (visited on 07/15/2020).

[5] National Oceanic and Atmospheric Administration. *Heating/Cooling Degree Days*. URL: https://www.nesdis.noaa.gov/content/heatingcooling-degree-days (visited on 07/15/2020).

[6] BP plc. *BP Statistical Review of World Energy 2020— 69th edition*. URL: https://www.bp.com/content/dam/bp/business-sites/en/global/corporate/pdfs/energy-economics/statistical-review/bp-stats-review-2020-full-report.pdf (visited on 07/15/2020).

[7] Akihiro Kojima et al. "Organometal Halide Perovskites as Visible-Light Sensitizers for Photovoltaic Cells". In: *Journal of the American Chemical Society* 131.17 (2009). PMID: 19366264, pp. 6050–6051. DOI: 10.1021/ja809598r.

[8] G. C. Papavassiliou. "Synthetic Three-and Lower-Dimensional Semiconductors Based on Inorganic Units". In: *Molecular Crystals and Liquid Crystals Science and Technology. Section A. Molecular Crystals and Liquid Crystals* 286.1 (1996), pp. 231–238. DOI: 10.1080/10587259608042291.

[9] Koji Yamada et al. "Structural Phase Transition and Electrical Conductivity of the Perovskite $CH_3NH_3Sn_{1-x}Pb_xBr_3$ and $CsSnBr_3$". In: *Bulletin of the Chemical Society of Japan* 63.9 (1990), pp. 2521–2525. DOI: 10.1246/bcsj.63.2521.

[10] M. Hirasawa et al. "Magnetoabsorption of the lowest exciton in perovskite-type compound $(CH_3NH_3)PbI_3$". In: *Physica B: Condensed Matter* 201 (1994), pp. 427–430. ISSN: 0921-4526. DOI: https://doi.org/10.1016/0921-4526(94)91130-4.

[11] Michael M. Lee et al. "Efficient Hybrid Solar Cells Based on Meso-Superstructured Organometal Halide Perovskites". In: *Science* 338.6107 (2012), pp. 643–647. ISSN: 0036-8075. DOI: 10.1126/science.1228604.

[12] Pablo Docampo et al. "Control of Solid-State Dye-Sensitized Solar Cell Performance by Block-Copolymer-Directed TiO2 Synthesis". In: *Advanced Functional Materials* 20.11 (2010), pp. 1787–1796. DOI: 10.1002/adfm.200902089.

[13] Constantinos C. Stoumpos, Christos D. Malliakas, and Mercouri G. Kanatzidis. "Semiconducting Tin and Lead Iodide Perovskites with Organic Cations: Phase Transitions, High Mobilities, and Near-Infrared Photoluminescent Properties". In: *Inorganic Chemistry* 52.15 (Aug. 2013), pp. 9019–9038.

[14] Ravi K. Misra et al. "Temperature- and Component-Dependent Degradation of Perovskite Photovoltaic Materials under Concentrated Sunlight". In: *The Journal of Physical Chemistry Letters* 6.3 (Feb. 2015), pp. 326–330.

[15] Eric T. Hoke et al. "Reversible photo-induced trap formation in mixed-halide hybrid perovskites for photovoltaics". In: *Chem. Sci.* 6 (1 2015), pp. 613–617. DOI: 10.1039/C4SC03141E.

[16] Farhad Fouladi Targhi, Yousef Seyed Jalili, and Faramarz Kanjouri. "$MAPbI_3$ and $FAPbI_3$ perovskites as solar cells: Case study on structural, electrical and optical properties". In: *Results in Physics* 10 (2018), pp. 616–627. ISSN: 2211-3797. DOI: https://doi.org/10.1016/j.rinp.2018.07.007.

[17] William Shockley and Hans J. Queisser. "Detailed Balance Limit of Efficiency of p-n Junction Solar Cells". In: *Journal of Applied Physics* 32.3 (1961), pp. 510–519. DOI: 10.1063/1.1736034.

[18] Giles E. Eperon et al. "Formamidinium lead trihalide: a broadly tunable perovskite for efficient planar heterojunction solar cells". In: *Energy Environ. Sci.* 7 (3 2014), pp. 982–988. DOI: 10.1039/C3EE43822H.

[19] Jin-Wook Lee et al. "High-Efficiency Perovskite Solar Cells Based on the Black Polymorph of $HC(NH_2)_2PbI_3$". In: *Advanced Materials* 26.29 (2014), pp. 4991–4998. DOI: 10.1002/adma.201401137.

[20] Nam Joong Jeon et al. "Compositional engineering of perovskite materials for high-performance solar cells". In: *Nature* 517.7535 (2015), pp. 476–480.

[21] Michael Kulbak, David Cahen, and Gary Hodes. "How Important Is the Organic Part of Lead Halide Perovskite Photovoltaic Cells? Efficient $CsPbBr_3$ Cells". In: *The Journal of Physical Chemistry Letters* 6.13 (July 2015), pp. 2452–2456.

[22] Christian Kn. Møller. "Crystal Structure and Photoconductivity of Cæsium Plumbohalides". In: *Nature* 182.4647 (1958), pp. 1436–1436.

[23] Yehonadav Bekenstein et al. "Highly Luminescent Colloidal Nanoplates of Perovskite Cesium Lead Halide and Their Oriented Assemblies". In: *Journal of the American Chemical Society* 137.51 (Dec. 2015), pp. 16008–16011.

[24] Michael Saliba et al. "Cesium-containing triple cation perovskite solar cells: improved stability, reproducibility and high efficiency". In: *Energy Environ. Sci.* 9 (6 2016), pp. 1989–1997. DOI: 10.1039/C5EE03874J.

[25] Victor Moritz Goldschmidt. "Die Gesetze der Krystallochemie". In: *Naturwissenschaften* 14.21 (1926), pp. 477–485. ISSN: 1432-1904. DOI: 10.1007/BF01507527.

[26] National Renewable Energy Laboratory. "Best Research-Cell Efficiencies". In: *nrel.gov* (2020). URL: https://www.nrel.gov/pv/assets/pdfs/best-research-cell-efficiencies.20200406.pdf (visited on 04/26/2020).

[27] Marc De Graef and Michael E. McHenry. "Ceramic Structures I". In: *Structure of Materials: An Introduction to Crystallography, Diffraction, and Symmetry*. Cambridge: Cambridge University Press, 2007. Chap. 22, pp. 671–672.

[28] A. Poglitsch and D. Weber. "Dynamic disorder in methylammoniumtrihalogenoplumbates (II) observed by millimeter-wave spectroscopy". In: *The Journal of Chemical Physics* 87.11 (1987), pp. 6373–6378. DOI: 10.1063/1.453467.

[29] Mingzhen Liu, Michael B. Johnston, and Henry J. Snaith. "Efficient planar heterojunction perovskite solar cells by vapour deposition". In: *Nature* 501.7467 (2013), pp. 395–398.

[30] Xianyu Jia et al. "Facile synthesis of organic–inorganic hybrid perovskite $CH_3NH_3PbI_3$ microcrystals". In: *Journal of Alloys and Compounds* 725 (2017), pp. 270–274. ISSN: 0925-8388. DOI: https://doi.org/10.1016/j.jallcom.2017.07.154.

[31] Qianqian Lin et al. "Electro-optics of perovskite solar cells". In: *Nature Photonics* 9.2 (2015), pp. 106–112.

[32] Atsuhiko Miyata et al. "Direct measurement of the exciton binding energy and effective masses for charge carriers in organic–inorganic tri-halide perovskites". In: *Nature Physics* 11.7 (2015), pp. 582–587.

[33] Samuel D. Stranks et al. "Electron-Hole Diffusion Lengths Exceeding 1 Micrometer in an Organometal Trihalide Perovskite Absorber". In: *Science* 342.6156 (2013), pp. 341–344. ISSN: 0036-8075. DOI: 10.1126/science.1243982.

[34] Guichuan Xing et al. "Long-Range Balanced Electron- and Hole-Transport Lengths in Organic-Inorganic $CH_3NH_3PbI_3$". In: *Science* 342.6156 (2013), pp. 344–347. ISSN: 0036-8075. DOI: 10.1126/science.1243167.

[35] Christopher L. Davies et al. "Bimolecular recombination in methylammonium lead triiodide perovskite is an inverse absorption process". In: *Nature Communications* 9.1 (2018), p. 293.

[36] Julian Burschka et al. "Sequential deposition as a route to high-performance perovskite-sensitized solar cells". In: *Nature* 499.7458 (2013), pp. 316–319.

[37] Zhengguo Xiao et al. "Efficient, high yield perovskite photovoltaic devices grown by interdiffusion of solution-processed precursor stacking layers". In: *Energy Environ. Sci.* 7 (8 2014), pp. 2619–2623. DOI: 10.1039/C4EE01138D.

[38] Qi Chen et al. "Planar Heterojunction Perovskite Solar Cells via Vapor-Assisted Solution Process". In: *Journal of the American Chemical Society* 136.2 (Jan. 2014), pp. 622–625.

[39] Alexander T. Barrows et al. "Efficient planar heterojunction mixed-halide perovskite solar cells deposited via spray-deposition". In: *Energy Environ. Sci.* 7 (9 2014), pp. 2944–2950. DOI: 10.1039/C4EE01546K.

[40] Brandon R. Sutherland et al. "Perovskite Thin Films via Atomic Layer Deposition". In: *Advanced Materials* 27.1 (2015), pp. 53–58. DOI: 10.1002/adma.201403965.

[41] Zhanhua Wei et al. "Inkjet Printing and Instant Chemical Transformation of a $CH_3NH_3PbI_3$/Nanocarbon Electrode and Interface for Planar Perovskite Solar Cells". In: *Angewandte Chemie International Edition* 53.48 (2014), pp. 13239–13243. DOI: 10.1002/anie.201408638.

[42] Matthew McPhail, Carlos Biaou, and Vivek Subramanian. "Ink Development and Airblade Drying for Gravure Printed Perovskite Solar Cells". unpublished. 2020.

[43] Olga Malinkiewicz et al. "Perovskite solar cells employing organic charge-transport layers". In: *Nature Photonics* 8.2 (2014), pp. 128–132.

[44] Fangchao Li et al. "A Universal Strategy to Utilize Polymeric Semiconductors for Perovskite Solar Cells with Enhanced Efficiency and Longevity". In: *Advanced Functional Materials* 28.15 (2018), p. 1706377. DOI: 10.1002/adfm.201706377.

[45] Fan Yang, Max Shtein, and Stephen R. Forrest. "Morphology control and material mixing by high-temperature organic vapor-phase deposition and its application to thin-film solar cells". In: *Journal of Applied Physics* 98.1 (2005), p. 014906. DOI: 10.1063/1.1941480.

[46] H. Sakata et al. "20.7% highest efficiency large area (100.5 cm^2) HIT/sup TM/cell". In: *Conference Record of the Twenty-Eighth IEEE Photovoltaic Specialists Conference - 2000 (Cat. No.00CH37036)*. 2000, pp. 7–12. DOI: 10.1109/PVSC.2000.915742.

[47] K. L. Chopra, P. D. Paulson, and V. Dutta. "Thin-film solar cells: an overview". In: *Progress in Photovoltaics: Research and Applications* 12.2-3 (2004), pp. 69–92. DOI: 10.1002/pip.541.

[48] Moritz Riede et al. "Efficient Organic Tandem Solar Cells based on Small Molecules". In: *Advanced Functional Materials* 21.16 (2011), pp. 3019–3028. DOI: 10.1002/adfm.201002760.

[49] Ossila Ltd. *How Humidity Affects Air-Processed Perovskite Films*. Apr. 2015. URL: https://www.ossila.com/pages/video-how-humidity-affects-air-processed-perovskite-films (visited on 05/18/2020).

[50] Sonia R. Raga et al. "Influence of Air Annealing on High Efficiency Planar Structure Perovskite Solar Cells". In: *Chemistry of Materials* 27.5 (Mar. 2015), pp. 1597–1603.

[51] Hyun-Seok Ko, Jin-Wook Lee, and Nam-Gyu Park. "15.76% efficiency perovskite solar cells prepared under high relative humidity: importance of PbI_2 morphology in two-step deposition of $CH_3NH_3PbI_3$". In: *J. Mater. Chem. A* 3 (16 2015), pp. 8808–8815. DOI: 10.1039/C5TA00658A.

[52] Giles E. Eperon et al. "The Importance of Moisture in Hybrid Lead Halide Perovskite Thin Film Fabrication". In: *ACS Nano* 9.9 (Sept. 2015), pp. 9380–9393.

[53] Sandeep Pathak et al. "Atmospheric Influence upon Crystallization and Electronic Disorder and Its Impact on the Photophysical Properties of Organic–Inorganic Perovskite Solar Cells". In: *ACS Nano* 9.3 (Mar. 2015), pp. 2311–2320.

[54] Alexis De Vos. "Detailed balance limit of the efficiency of tandem solar cells". In: *Journal of Physics D: Applied Physics* 13.5 (May 1980), pp. 839–846. DOI: 10.1088/0022-3727/13/5/018.

[55] Bo Chen et al. "Grain Engineering for Perovskite/Silicon Monolithic Tandem Solar Cells with Efficiency of 25.4%". In: *Joule* 3.1 (2019), pp. 177–190. ISSN: 2542-4351. DOI: https://doi.org/10.1016/j.joule.2018.10.003.

[56] Philipp Tockhorn et al. "Three-Terminal Perovskite/Silicon Tandem Solar Cells with Top and Interdigitated Rear Contacts". In: *ACS Applied Energy Materials* 3.2 (Feb. 2020), pp. 1381–1392.

[57] Florent Sahli et al. "Fully textured monolithic perovskite/silicon tandem solar cells with 25.2% power conversion efficiency". In: *Nature Materials* 17.9 (2018), pp. 820–826.

[58] Jin Hyuck Heo et al. "Efficient inorganic–organic hybrid heterojunction solar cells containing perovskite compound and polymeric hole conductors". In: *Nature Photonics* 7.6 (2013), pp. 486–491.

[59] Kevin A. Bush et al. "23.6%-efficient monolithic perovskite/silicon tandem solar cells with improved stability". In: *Nature Energy* 2.4 (2017), p. 17009.

[60] Eike Köhnen et al. "Highly efficient monolithic perovskite silicon tandem solar cells: analyzing the influence of current mismatch on device performance". In: *Sustainable Energy Fuels* 3 (8 2019), pp. 1995–2005. DOI: 10.1039/C9SE00120D.

[61] Oxford PV. *Oxford PV perovskite solar cell achieves 28% efficiency*. Dec. 2018. URL: https://www.oxfordpv.com/news/oxford-pv-perovskite-solar-cell-achieves-28-efficiency (visited on 05/19/2020).

[62] U.S. Energy Information Administration. *Levelized Cost and Levelized Avoided Cost of New Generation Resources in the Annual Energy Outlook 2020*. Feb. 2020. URL: https://www.eia.gov/outlooks/aeo/pdf/electricity_generation.pdf (visited on 05/20/2020).

[63] U.S. Department of Energy — Office of Indian Energy. *Levelized Cost of Energy (LCOE)*. Aug. 2015. URL: https://www.energy.gov/sites/prod/files/2015/08/f25/LCOE.pdf (visited on 05/20/2020).

[64] Zhaoning Song et al. "A technoeconomic analysis of perovskite solar module manufacturing with low-cost materials and techniques". In: *Energy & Environmental Science* 10.6 (2017), pp. 1297–1305.

[65] "Cost Analysis of Perovskite Tandem Photovoltaics". In: *Joule* 2.8 (2018), pp. 1559–1572. ISSN: 2542-4351. DOI: https://doi.org/10.1016/j.joule.2018.05.001.

[66] U.S. Department of Energy — Office of Energy Efficiency & Renewable Energy. *On the Path to SunShot*. 2011. URL: https://www.energy.gov/eere/solar/path-sunshot (visited on 05/20/2020).

[67] Nam-Gyu Park and Kai Zhu. "Scalable fabrication and coating methods for perovskite solar cells and solar modules". In: *Nature Reviews Materials* 5.5 (2020), pp. 333–350.

[68] Martin A. Green et al. "Solar cell efficiency tables (Version 53)". In: *Progress in Photovoltaics: Research and Applications* 27.1 (2019), pp. 3–12. DOI: 10.1002/pip.3102.

[69] Yehao Deng et al. "Surfactant-controlled ink drying enables high-speed deposition of perovskite films for efficient photovoltaic modules". In: *Nature Energy* 3.7 (2018), pp. 560–566.

[70] Francesco Di Giacomo et al. "Up-scalable sheet-to-sheet production of high efficiency perovskite module and solar cells on 6-in. substrate using slot die coating". In: *Solar Energy Materials and Solar Cells* 181 (2018). Thin film solar cells and applications, pp. 53–59. ISSN: 0927-0248. DOI: https://doi.org/10.1016/j.solmat.2017.11.010.

[71] Yue Hu et al. "Stable Large-Area (10×10 cm^2) Printable Mesoscopic Perovskite Module Exceeding 10% Efficiency". In: *Solar RRL* 1.2 (2017), p. 1600019. DOI: 10.1002/solr.201600019.

[72] Longbin Qiu et al. "Hybrid chemical vapor deposition enables scalable and stable Cs-FA mixed cation perovskite solar modules with a designated area of 91.8 cm^2 approaching 10% efficiency". In: *J. Mater. Chem. A* 7 (12 2019), pp. 6920–6929. DOI: 10.1039/C9TA00239A.

[73] Dong-Nyuk Jeong et al. "Perovskite Cluster-Containing Solution for Scalable D-Bar Coating toward High-Throughput Perovskite Solar Cells". In: *ACS Energy Letters* 4.5 (May 2019), pp. 1189–1195.

[74] Jueng-Eun Kim et al. "Slot die coated planar perovskite solar cells via blowing and heating assisted one step deposition". In: *Solar Energy Materials and Solar Cells* 179 (2018), pp. 80–86. ISSN: 0927-0248. DOI: https://doi.org/10.1016/j.solmat.2018.02.003.

[75] Mincheol Park et al. "Highly Reproducible Large-Area Perovskite Solar Cell Fabrication via Continuous Megasonic Spray Coating of $CH_3NH_3PbI_3$". In: *Small* 15.1 (2019), p. 1804005. DOI: 10.1002/smll.201804005.

[76] Yong Zhang et al. "Bifacial stamping for high efficiency perovskite solar cells". In: *Energy Environ. Sci.* 12 (1 2019), pp. 308–321. DOI: 10.1039/C8EE02730G.

[77] Juliane Borchert et al. "Large-Area, Highly Uniform Evaporated Formamidinium Lead Triiodide Thin Films for Solar Cells". In: *ACS Energy Letters* 2.12 (Dec. 2017), pp. 2799–2804.

[78] World Health Organization. *Exposure to Lead: A Major Public Health Concern*. 2010. URL: https://www.who.int/ipcs/features/lead..pdf?ua=1 (visited on 05/22/2020).

[79] Weijun Ke and Mercouri G. Kanatzidis. "Prospects for low-toxicity lead-free perovskite solar cells". In: *Nature Communications* 10.1 (2019), p. 965.

[80] Nakita K. Noel et al. "Lead-free organic–inorganic tin halide perovskites for photovoltaic applications". In: *Energy Environ. Sci.* 7 (9 2014), pp. 3061–3068. DOI: 10.1039/C4EE01076K.

[81] Efat Jokar et al. "Robust Tin-Based Perovskite Solar Cells with Hybrid Organic Cations to Attain Efficiency Approaching 10%". In: *Advanced Materials* 31.2 (2019), p. 1804835. DOI: 10.1002/adma.201804835.

[82] Feliciano Giustino and Henry J. Snaith. "Toward Lead-Free Perovskite Solar Cells". In: *ACS Energy Letters* 1.6 (Dec. 2016), pp. 1233–1240.

[83] Min Chen et al. "Highly stable and efficient all-inorganic lead-free perovskite solar cells with native-oxide passivation". In: *Nature Communications* 10.1 (2019), p. 16.

[84] Bert Conings et al. "Intrinsic Thermal Instability of Methylammonium Lead Trihalide Perovskite". In: *Advanced Energy Materials* 5.15 (2015), p. 1500477. DOI: 10.1002/aenm.201500477.

[85] Aslihan Babayigit et al. "Toxicity of organometal halide perovskite solar cells". In: *Nature Materials* 15.3 (2016), pp. 247–251.

[86] Dian Wang et al. "Stability of perovskite solar cells". In: *Solar Energy Materials and Solar Cells* 147 (2016), pp. 255–275. ISSN: 0927-0248. DOI: https://doi.org/10.1016/j.solmat.2015.12.025.

[87] Taame Abraha Berhe et al. "Organometal halide perovskite solar cells: degradation and stability". In: *Energy Environ. Sci.* 9 (2 2016), pp. 323–356. DOI: 10.1039/C5EE02733K.

[88] International Electrotechnical Commission. *IEC 61215-1:2016 - Terrestrial photovoltaic (PV) modules - Design qualification and type approval - Part 1: Test requirements*. Mar. 2016. URL: https://webstore.iec.ch/publication/24312 (visited on 05/23/2020).

[89] Qamar Wali et al. "Advances in stability of perovskite solar cells". In: *Organic Electronics* 78 (2020), p. 105590. ISSN: 1566-1199. DOI: https://doi.org/10.1016/j.orgel.2019.105590.

[90] Lei Shi et al. "Gas chromatography–mass spectrometry analyses of encapsulated stable perovskite solar cells". In: *Science* (2020). DOI: 10.1126/science.aba2412.

[91] Hairen Tan et al. "Efficient and stable solution-processed planar perovskite solar cells via contact passivation". In: *Science* 355.6326 (2017), pp. 722–726. ISSN: 0036-8075. DOI: 10.1126/science.aai9081.

[92] Zhiping Wang et al. "Efficient and Air-Stable Mixed-Cation Lead Mixed-Halide Perovskite Solar Cells with n-Doped Organic Electron Extraction Layers". In: *Advanced Materials* 29.5 (2017), p. 1604186. DOI: 10.1002/adma.201604186.

[93] Gi-Hwan Kim et al. "Fluorine Functionalized Graphene Nano Platelets for Highly Stable Inverted Perovskite Solar Cells". In: *Nano Letters* 17.10 (Oct. 2017), pp. 6385–6390.

[94] Seong Sik Shin et al. "Colloidally prepared La-doped BaSnO3 electrodes for efficient, photostable perovskite solar cells". In: *Science* 356.6334 (2017), pp. 167–171. ISSN: 0036-8075. DOI: 10.1126/science.aam6620.

[95] Kerttu Aitola et al. "High Temperature-Stable Perovskite Solar Cell Based on Low-Cost Carbon Nanotube Hole Contact". In: *Advanced Materials* 29.17 (2017), p. 1606398. DOI: 10.1002/adma.201606398.

[96] G. Grancini et al. "One-Year stable perovskite solar cells by 2D/3D interface engineering". In: *Nature Communications* 8.1 (2017), p. 15684.

[97] The Duong et al. "Light and elevated temperature induced degradation (LeTID) in perovskite solar cells and development of stable semi-transparent cells". In: *Solar Energy Materials and Solar Cells* 188 (2018), pp. 27–36. ISSN: 0927-0248. DOI: https://doi.org/10.1016/j.solmat.2018.08.017.

[98] Guangda Niu, Xudong Guo, and Liduo Wang. "Review of recent progress in chemical stability of perovskite solar cells". In: *J. Mater. Chem. A* 3 (17 2015), pp. 8970–8980. DOI: 10.1039/C4TA04994B.

[99] Jarvist M. Frost et al. "Atomistic Origins of High-Performance in Hybrid Halide Perovskite Solar Cells". In: *Nano Letters* 14.5 (May 2014), pp. 2584–2590.

[100] Jun Hong Noh et al. "Chemical Management for Colorful, Efficient, and Stable Inorganic–Organic Hybrid Nanostructured Solar Cells". In: *Nano Letters* 13.4 (Apr. 2013), pp. 1764–1769.

[101] Guangda Niu et al. "Study on the stability of CH3NH3PbI3 films and the effect of post-modification by aluminum oxide in all-solid-state hybrid solar cells". In: *J. Mater. Chem. A* 2 (3 2014), pp. 705–710. DOI: 10.1039/C3TA13606J.

[102] Michael Saliba et al. "Incorporation of rubidium cations into perovskite solar cells improves photovoltaic performance". In: *Science* 354.6309 (2016), pp. 206–209. ISSN: 0036-8075. DOI: 10.1126/science.aah5557.

[103] Tomas Leijtens et al. "Overcoming ultraviolet light instability of sensitized TiO2 with meso-superstructured organometal tri-halide perovskite solar cells". In: *Nature Communications* 4.1 (2013), p. 2885.

[104] Seigo Ito et al. "Effects of Surface Blocking Layer of Sb2S3 on Nanocrystalline TiO2 for CH3NH3PbI3 Perovskite Solar Cells". In: *The Journal of Physical Chemistry C* 118.30 (July 2014), pp. 16995–17000.

[105] Nicholas Aristidou et al. "Fast oxygen diffusion and iodide defects mediate oxygen-induced degradation of perovskite solar cells". In: *Nature Communications* 8.1 (2017), p. 15218.

[106] Konrad Domanski et al. "Systematic investigation of the impact of operation conditions on the degradation behaviour of perovskite solar cells". In: *Nature Energy* 3.1 (2018), pp. 61–67. ISSN: 2058-7546. DOI: 10.1038/s41560-017-0060-5.

[107] Wanyi Nie et al. "Light-activated photocurrent degradation and self-healing in perovskite solar cells". In: *Nature Communications* 7.1 (2016), p. 11574.

[108] Konrad Domanski et al. "Migration of cations induces reversible performance losses over day/night cycling in perovskite solar cells". In: *Energy Environ. Sci.* 10 (2 2017), pp. 604–613. DOI: 10.1039/C6EE03352K.

[109] Priyanka Tyagi et al. "Multivariate approach for studying the degradation of perovskite solar cells". In: *Solar Energy* 193 (2019), pp. 12–19. ISSN: 0038-092X. DOI: 10.1016/j.solener.2019.09.054.

[110] Douglas C. Montgomery. *Design and Analysis of Experiments*. Hoboken, New Jersey: Wiley, 2017.

[111] SAS Institute Inc. *jmp Statistical Discovery from SAS*. URL: https://www.jmp.com/en_us/home.html (visited on 07/07/2020).

[112] Cuthbert Daniel. "Use of Half-Normal Plots in Interpreting Factorial Two-Level Experiments". In: *Technometrics* 1.4 (1959), pp. 311–341. ISSN: 00401706. URL: http://www.jstor.org/stable/1266715.

[113] Russell V. Lenth. "Quick and Easy Analysis of Unreplicated Factorials". In: *Technometrics* 31.4 (1989), pp. 469–473. ISSN: 00401706. URL: http://www.jstor.org/stable/1269997.

[114] Paul Scherrer. "Bestimmung der inneren Struktur und der Größe von Kolloidteilchen mittels Röntgenstrahlen". In: *Kolloidchemie Ein Lehrbuch. Chemische Technologie in Einzeldarstellungen*. Berlin, Heidelberg: Springer, 1912.

[115] World Meteorological Organization. *WMO verifies 3rd and 4th hottest temperature recorded on Earth*. URL: https://public.wmo.int/en/media/press-release/wmo-verifies-3rd-and-4th-hottest-temperature-recorded-earth (visited on 07/14/2020).

[116] Carlos Biaou. "Towards a Better Mechanistic Understanding of the Degradation Processes of Perovskite Solar Cells". MA thesis. Berkeley, CA: University of California, Berkeley, Jan. 2018.

[117] Chenyi Yi et al. "Entropic stabilization of mixed A-cation ABX3 metal halide perovskites for high performance perovskite solar cells". In: *Energy Environ. Sci.* 9 (2 2016), pp. 656–662. DOI: 10.1039/C5EE03255E.

[118] Eugen Zimmermann et al. "Characterization of perovskite solar cells: Towards a reliable measurement protocol". In: *APL Materials* 4.9 (2016), p. 091901. DOI: 10.1063/1.4960759.

[119] P. Blood and J.W. Orton. *The Electrical Characterization of Semiconductors: Majority Carriers and Electron States*. London: Academic Press, 1992.

[120] Holland McTyeire Smith. "Characterization of Thallium Bromide (TlBr) for Room Temperature Radiation Detectors". PhD thesis. Berkeley, CA: University of California, Berkeley, 2013.

[121] M. Hage-Ali et al. "Microscopic defect level characterization of semi-insulating compound semiconductors by TSC and PICTS: Application to the effect of hydrogen in CdTe". In: *Applied Surface Science* 50.1 (1991), pp. 377–382. ISSN: 0169-4332. DOI: https://doi.org/10.1016/0169-4332(91)90202-U. URL: http://www.sciencedirect.com/science/article/pii/016943329190202U.

[122] J C Balland et al. "Investigation of deep levels in high-resistivity bulk materials by photo-induced current transient spectroscopy. II. Evaluation of various signal processing methods". In: *Journal of Physics D: Applied Physics* 19.1 (Jan. 1986), pp. 71–87. DOI: 10.1088/0022-3727/19/1/012.

[123] W. Schröter et al. "Bandlike and localized states at extended defects in silicon". In: *Phys. Rev. B* 52 (19 Nov. 1995), pp. 13726–13729. DOI: 10.1103/PhysRevB.52.13726.

[124] Carl V. Thompson and Roland Carel. "Stress and grain growth in thin films". In: *Journal of the Mechanics and Physics of Solids* 44.5 (1996). Mechanics and Physics of Layered and Graded Materials, pp. 657–673. ISSN: 0022-5096. DOI: https://doi.org/10.1016/0022-5096(96)00022-1.

[125] Scott A Speakman. *Estimating Crystallite Size Using XRD*. URL: http://prism.mit.edu/XRAY/oldsite/CrystalSizeAnalysis.pdf (visited on 07/31/2020).

[126] Christopher J. Bartel et al. "New tolerance factor to predict the stability of perovskite oxides and halides". In: *Science Advances* 5.2 (2019). DOI: 10.1126/sciadv.aav0693.

[127] Nga Phung et al. "The Doping Mechanism of Halide Perovskite Unveiled by Alkaline Earth Metals". In: *Journal of the American Chemical Society* 142.5 (Feb. 2020), pp. 2364–2374. DOI: 10.1021/jacs.9b11637.

[128] P. Omling et al. "Electrical properties of dislocations and point defects in plastically deformed silicon". In: *Phys. Rev. B* 32 (10 Nov. 1985), pp. 6571–6581. DOI: 10.1103/PhysRevB.32.6571.

[129] Nancy M. Haegel et al. "Terawatt-scale photovoltaics: Transform global energy". In: *Science* 364.6443 (2019), pp. 836–838. ISSN: 0036-8075. DOI: 10.1126/science.aaw1845.

[130] Ian Mathews et al. "Economically Sustainable Growth of Perovskite Photovoltaics Manufacturing". In: *Joule* 4.4 (2020), pp. 822–839. ISSN: 2542-4351. DOI: https://doi.org/10.1016/j.joule.2020.01.006.

[131] Justin Xiao. "Technoeconomic Analysis of Perovskite Photovoltaic Manufacturing for Powering Telecommunications Towers". MA thesis. Cambridge, MA: Massachusetts Institute of Technology, June 2018.

[132] Matthew O. Reese et al. "Increasing markets and decreasing package weight for high-specific-power photovoltaics". In: *Nature Energy* 3.11 (2018), pp. 1002–1012.

[133] S. N. R. Kantareddy et al. "Perovskite PV-Powered RFID: Enabling Low-Cost Self-Powered IoT Sensors". In: *IEEE Sensors Journal* 20.1 (2020), pp. 471–478.

[134] Ian Mathews et al. "Self-Powered Sensors Enabled by Wide-Bandgap Perovskite Indoor Photovoltaic Cells". In: *Advanced Functional Materials* 29.42 (2019), p. 1904072. DOI: 10.1002/adfm.201904072.

[135] Konrad Wojciechowski, Dávid Forgács, and Thomas Rivera. "Industrial Opportunities and Challenges for Perovskite Photovoltaic Technology". In: *Solar RRL* 3.9 (2019), p. 1900144. DOI: 10.1002/solr.201900144.

[136] pvXchange Trading GmbH. *Price Index*. Apr. 2020. URL: https://www.energy.gov/eere/solar/path-sunshot (visited on 05/21/2020).

[137] Swift Solar. *Swift Solar is building the next generation of solar technology*. URL: https://www.swiftsolar.com/ (visited on 05/21/2020).

[138] Yoana Cholteeva. *Record-breaking solar perovskites*. May 2020. URL: https://www.power-technology.com/features/record-breaking-solar-perovskites/ (visited on 05/21/2020).